Srinidhi Embar Ramanujam

Intermodulation Distortion Modelling and Measurement Techniques for GaN HEMT Characterization

kassel university press

This work has been accepted by the faculty of Electrical Engineering and Computer Science of the University of Kassel as a thesis for acquiring the academic degree of Doktor der Ingenieurwissenschaften (Dr.-Ing.).

Supervisers:

Prof. Dr.-Ing. G. Kompa
Prof. Dr.-Ing. A. Bangert

Defense day: 09th December 2008

Bibliographic information published by Deutsche Nationalbibliothek
The Deutsche Nationalbibliothek lists this publication in the Deutsche Nationalbibliografie; detailed bibliographic data is available in the Internet at http://dnb.d-nb.de.

Zugl.: Kassel, Univ., Diss. 2008
ISBN print: 978-3-89958-654-1
ISBN online: 978-3-89958-655-8
URN: urn:nbn:de:0002-6558

Printed by: Unidruckerei, University of Kassel
Printed in Germany

To my parents and my family

for their devotion and prayers

Acknowledgements

I wish to express my deep gratitude to Prof. Dr.-Ing. G. Kompa who supervised and nurtured me in becoming a researcher. His invaluable support and encouragement gave me confidence in overcoming difficult times.

My sincere thanks to Prof. Dr.-Ing. A. Bangert for accepting the task of being my second examiner. Further, I wish to thank Prof. Dr. sc. techn. B. Witzigmann and PD Dr.-Ing. R. Marklein for accepting to be members of the disputation committee.

I am thankful to all the members of the department of High Frequency Engineering for their constant support. I wish to express my gratitude to Mrs. H. Nauditt, Dipl.-Ing. J. Weide, Dr. -Ing. A. Z. Markos, Mr. R. Ma, Dipl.-Ing. B. Wittwer, Mr. S. Dahmani, Mr. A. Zamudio, Mr. S. Monsi, and Mr. A. A. Hussein. My sincere thanks to my parents, family members, and friends who are not mentioned by name for their unreserved encouragement and strong support over past several years.

This acknowledgement will most certainly be incomplete without thanking the German Research Foundation (DFG) and the European project TARGET (Top Amplifier Research Group in a European Team) for their financial support.

Srinidhi Embar Ramanujam
Kassel, December 2008

Contents

List of Abbreviations

3GPP	third generation partnership project
ACPR	adjacent channel power ratio
ADC	analog-to-digital converter
AM-AM	input amplitude modulation to output amplitude modulation conversion
AM-PM	input amplitude modulation to output phase modulation conversion
ANN	artificial neural network
CAD	computer aided design
CCDF	complementary cumulative distribution function
CW	continuous wave
DiVA	dynamic I(V) analyser
DMI	drain modulation index
DPCH	dedicated physical channel
DUT	device under test
EVM	error vector magnitude
FDD	frequency division duplex
FP	field-plate
GaAs	gallium arsenide
GaN	gallium nitride
GSM	global system for mobile communication
HEMT	high electron mobility transistor
MLP	multi-level perceptron
IF	intermediate frequency
IMD	intermodulation distortion
IM3L	3rd-order lower intermodulation distortion
IMR	intermodulation ratio
IP3	3rd-order intercept point
LDMOS	laterally diffused metal oxide semiconductor
LTE	long term evolution
MESFET	metal semiconductor field effect transistor
MTA	microwave transition analyser
OFDM	orthogonal frequency division multiplexing
PA	power amplifier
PAE	power added efficiency
PAR	peak-to-average ratio
QPSK	quadrature phase shift keying
RF	radio frequency
UMTS	universal mobile telecommunications system
VNA	vector network analyser
VSA	vector signal analyser
W-CDMA	wideband code division multiple access

List of Symbols

a_1	incident power wave at port-1	dBm
a_2	incident power wave at port-2	dBm
b_1	reflected power wave from port-1	dBm
b_2	reflected power wave from port-2	dBm
β	propagation coefficient	
C	capacitance	F
C_{gs}	intrinsic gate-source capacitance	F
C_{ds}	intrinsic drain-source capacitance	F
C_{gd}	intrinsic gate-drain capacitance	F
C/I3	3rd-order carrier-to-intermodulation ratio	dBc
Δf	carrier spacing	Hz
ΔIMD	IMD asymmetry	dB
ε_r	dielectric constant	
e_{00}	directivity	
e_{11}	port-1 match	
e_{10}	coupler tracking	
$e_{01}e_{10}$	reflection tracking	
e_{22}	port-2 match	
f_c	centre frequency	Hz
f_{env}	maximum baseband frequency	Hz
f_{SR}	series resonant frequency	Hz
Γ	reflection coefficient	
Γ_L	load reflection coefficient	
G	conductance	S
G_m	transconductance	S
G_{ds}	channel conductance	S
G_{m2}, k_{2gm}	2nd-order derivative of drain-source current	S/V
G_{m3}, k_{3gm}	3rd-order derivative of drain-source current	S/V²
h_n	time-domain nth-order Volterra kernel	
H_n	frequency-domain nth-order transfer function	
H_1	1st-order linear transfer function	
I_{ds}	intrinsic incremental drain current	A
i_{2NL}	2nd-order nonlinear current source	A
i_{3NL}	3rd-order nonlinear current source	A
$I_{DS,DC}$	self-biased DC drain current	A
I_{max}	channel saturation current	A
I_n	excitation vector (voltage-controlled current source)	
IP3	3rd-order intercept point	dBm
k_{2g}, k_{3g}	conductance nonlinearity coefficients	
k_{2c}, k_{3c}	capacitance nonlinearity coefficients	
ℓ	transmission line length	m

L_S	capacitor's parasitic inductance	H
M	number of phase states	
P_{in}	input power	W
P_{out}	output power	W
P_{1dB}	1 dB compression point	dBm
Q	quality factor	
Q_{gs}	gate-source charge	C
Q_{gd}	gate-drain charge	C
Q_g	gate depletion charge	C
R	resistance	Ω
t	time	sec
TF, TF_{XYZ}, TF_{XYZW}	transimpedance transfer function	
v_g	gate nodal voltage	V
v_d	drain nodal voltage	V
v_s	source nodal voltage	V
v_{gs}	incremental gate-source voltage	V
v_{ds}	incremental drain-source voltage	V
v_{gd}	incremental gate-drain voltage	V
V_{BR}	gate-drain breakdown voltage	V
V_{in}	input signal amplitude	V
V_{GS0}	extrinsic gate-source bias voltage	V
V_{DS0}	extrinsic drain-source bias voltage	V
V_{GS}	extrinsic gate-source voltage	V
V_{DS}	extrinsic drain-source voltage	V
V_k	knee voltage	V
V_{pi}	pinch-off voltage	V
V_t	threshold voltage	V
$v_x(t)$	input signal amplitude	
$v_{peak}(\Delta f)$	peak baseband drain bias voltage	V
ω	angular frequency	Hz
x(t)	input excitation	
X_L	inductive reactance	Ω
X_C	capacitive reactance	Ω
y(t)	output system response	
$y_{NL}(t)$	nonlinear output response	
$y_{ML}(t)$	memoryless output response	
$y_{QM}(t)$	quasi-memoryless output response	
z(t)	linear output response	
Z_0	characteristic impedance	Ω
Z_L	load impedance	Ω

Abstract

Growing demand for higher data rates and ever increasing users on the 3G network is forcing rapid system enhancements to meet the stringent linearity specifications. The implications of microwave power transistor semiconductor technology and design strategies, implemented in basestation power amplifiers (PAs), have become the core focus of research. This thesis offers relevant practical application of computer-aided design (CAD) based modelling and measurement techniques to tackle linearity enhancement issues in AlGaN/GaN HEMT technology.

Principle foundation for a successful linear power amplifier design lies in understanding the mechanism of intermodulation distortion (IMD) generation. In this thesis, a new approach for identification and minimization of distortion sources in AlGaN/GaN HEMTs has been analysed based on Volterra series technique. Volterra model based third-order IMD analysis is performed on an 8 x 125 μm AlGaN/GaN HEMT, depicting individual distortion contributors for direct interpretation of their key physical origins. The applicability of Volterra series technique for enhancing AlGaN/GaN HEMT's linearity has been demonstrated through the optimisation of gate field-plate technology. With the AlGaN/GaN HEMT technology development still in its early stages, this work has made an appeal that Volterra series analysis is a powerful tool for improving AlGaN/GaN HEMT technology.

The disagreement between the model prediction and measured data, in terms of AlGaN/GaN HEMT's broadband IMD behaviour, is commonly encountered, which restricts dynamic measurements to only narrowband excitation. Moreover, when characterizing AlGaN/GaN HEMTs using conventional testbench, device inherent true IMD characteristics such as the

low distortion sweet-spots are concealed by the measurement setup induced memory-effects. The reproducibility of the desired sweet-spots become more uncertain under realistic digitally modulated stimulus signals such as W-CDMA signal. This has subsequently forced power amplifier designers to rely on complex external linearization techniques for achieving 3G linearity specifications.

This thesis further addresses IMD characterization issues for reliable large-signal device characterization. A fully automated frequency-domain measurement setup has been established based on dual-channel vector signal analyser (VSA), supporting vector error-correction of RF measurements under multi-tone and W-CDMA test signal environment. The applicability of commercial bias tees become questionable when conducting broadband device characterization under modulated test signals due to the DC feed affecting bias tee's frequency dependent baseband impedance properties. This motivated the design of an optimal bias tee based on $\lambda/4$ open-circuited radial stub. Memory-effects in AlGaN/GaN HEMTs are experimentally analysed by providing the desired impedances at the device reference plane. Dramatic improvement in IMD contours is exemplified by fundamental load-pulling, supporting a straightforward application rule for tackling linearity-efficiency trade-off in power amplifier design. The proposed IMD characterization methodology represents a further refinement in the state-of-the-art source- and load-pull for precise evaluation of intrinsic linearity in GaN HEMTs for 3G broadband applications.

With the optimised testbench, the statistical process consistency in GaAs and GaN HEMT devices, from the perspective of the sweet-spot reproducibility in IMD and ACPR characteristics, is investigated. GaAs HEMTs, being matured technology, proved excellent sweet-spot repeatability in contrast with the developing GaN HEMT based devices. However, under multi-carrier W-CDMA stimuli, the experimental results on GaN HEMTs have justified the

practical applicability of IMD sweet-spots for UMTS basestation power amplifier design, minimizing the complexity of external linearization techniques.

Zusammenfassung

Steigende Datenraten und eine stetig wachsende Anzahl von Nutzern im 3G Netzwerk zwingen zu rasanten Weiterentwicklungen der Systeme, um den geforderten Linearitätsanforderungen gerecht zu werden. Die Implikation von Halbleitertechnologie und Entwurfstrategien für Mikrowellen-Leistungstransistoren, eingesetzt in Leistungsverstärkern (PAs) von Basisstationen, sind ein Hauptschwerpunkt der Forschung. Die vorliegende Arbeit zeigt relevante praktische Anwendungen im Bereich des computergestützten Entwurfs (CAD), basierend auf Modellierung und Messtechniken, zur Steigerung der Linearität der AlGaN/GaN HEMT Technologie.

Ein Verständnis der Mechanismen, die zur Entstehung von Intermodulationsverzerrungen (IMD) führen, ist von großer Bedeutung für den erfolgreichen Entwurf von linearen Leistungsverstärkern. In dieser Arbeit wurde ein neuer Ansatz zur Identifikation und Minimierung von Verzerrungsquellen in AlGaN/GaN HEMTs analysiert, basierend auf der Volterra Reihe. Eine Untersuchung der IMD-Produkte dritter Ordnung wurde an 8 x 125 μm AlGaN/GaN HEMTs durchgeführt, um einzelne Verzerrungsursachen für die direkte Interpretation ihrer physikalischen Entstehung aufzuzeigen. Die praktische Nutzbarkeit der Volterra Reihe zur Erhöhung der Linearität von AlGaN/GaN HEMTs wurde durch die Optimierung der Gate-Feldplattentechnik erfolgreich aufgezeigt. Die vorliegende Arbeit zeigt, dass die Anwendung und Analyse der Volterra-Reihe ein vielversprechender Ansatz zur Verbesserung der noch am Beginn ihrer Entwicklung stehenden AlGaN/GaN HEMTs ist.

Die widersprüchlichen Aussagen von Messdaten und Simulationsergebnissen bei Untersuchungen der breitbandigen IMD Eigenschaften von AlGaN/GaN

HEMTs sind allgemein bekannt, was Dynamikmessungen auf schmalbandige Signale beschränkt. Überdies werden durch den Aufbau des Messplatzes bauteilspezifische IMD Charakteristiken, wie die sich durch geringe Verzerrung auszeichnenden Sweet-Spots, durch vom Messplatz selber verursachte Memory-Effekte überdeckt. Die Reproduzierbarkeit der gewünschten Sweet-Spots wird durch die Verwendung digital modulierter Signale, z.B. WCDMA-Signale, noch geschmälert. Dies hat dazu geführt dass PA Designer auf komplexe externe Linearisierungstechniken zurückgreifen mussten, um die 3G Linearisierungsanforderungen zu erfüllen.

Weiterhin behandelt die vorliegende Arbeit das Thema IMD-Charakterisierung zur verlässlichen Großsignalcharakterisierung von Transistoren. Es wurde ein vollautomatisiertes Frequenzbereichsmesssystem erstellt, welches auf einem zweikanaligen Vektorsignalanalysator (VSA) basiert und eine Vektor- Fehlerkorrektur von Multiton- und WCDMA Testsignalen ermöglicht. Aufgrund frequenzabhängiger Beeinflussung der Basisbandimpedanzen durch die DC Versorgung ist die Einsetzbarkeit kommerzieller Bias-Tees fraglich, wenn Transistoren durch breitbandige modulierte Testsignale charakterisiert werden sollen. Diese Erkenntnis führte zur Entwicklung eines optimierten Bias-Tees basierend auf einer leerlaufenden $\lambda/4$ radialen Stichleitung. Durch Anbringen verschiedener erwünschter Impedanzen an der Referenzebene von AlGaN/GaN HEMTs wurden Memory Effekte experimentell untersucht. Durch ein fundamentales Load-Pull werden dramatische Verbesserungen bei IMD Konturen exemplarisch dargestellt, unterstützt durch einfache Anwendungsregeln zur gegenseitigen Bestimmung von Linearität und Effizienz bei der PA Entwicklung,. Die dargestellte Technik zur IMD Charakterisierung liefert eine weitere Verfeinerung der hochmodernen Source-/Load-Pull Technik zur präzisen Beurteilung der intrinsischen Linearität von GaN HEMTs für breitbandige 3G Anwendungen.

Mit dem optimierten Messplatz wurde die statistische Prozessbeschaffenheit in GaAs und GaN HEMTs aus der Perspektive der Sweet-Spot Reproduzierbarkeit in IMD und ACPR Charakteristika erforscht. Im Gegensatz zu den in der Entwicklung befindlichen GaN HEMTs zeigten die ausgereiften GaAs HEMTs eine exzellente Reproduzierbarkeit der gemessenen Sweet-Spots. Unter der Verwendung von Multiträger WCDMA Anregung rechtfertigen experimentelle Ergebnisse an GaN HEMTs jedoch die praktische Anwendbarkeit von IMD Sweet-Spots für das Design von UMTS Basisstations-Leistungsverstärkern durch Minimierung der Komplexität externer Linearisationstechniken.

Chapter 1

Introduction

The wireless industry has grown at a tremendous pace over the past decade. Today's mobile communication systems require high power for multi-carrier capability, broadband for high data rate, capacity and service quality, high linearity to meet adjacent channel power ratio (ACPR) requirements, and multi-band and multi-standard so that mobile phones can be used everywhere. A consequence of high spectral efficiency offered by 2nd-generation (2G) and 3rd-generation (3G) mobile communication systems is the requirement of highly linear power amplifier.

The function of a power amplifier in a transmitter basestation system is to boost a signal to a power level suitable for transmission. Such microwave power amplifiers operate most efficiently at saturation in the nonlinear range of their behaviour. The impact of nonlinearity strongly depends on the application employing a unique modulation scheme coupled with the specifications imposed on the spectral mask. In modern communication systems, the signals are amplitude and phase modulated to achieve better spectral efficiency under narrowband conditions to transmit the required information. In such circumstances, when a nonlinear power amplifier is

excited by a modulated carrier, the output will result in spectral regrowth, which is often considered to be a problem of adjacent channel interference. Eventually, this increases the demodulation error rates, which form the basis for evaluating transmitter power amplifier linearity [1].

Considering the initial voice-only services offered by 2G mobile networks that grew beyond expectations, a constant signal envelope due to non-zero crossing restriction, was beneficial for the power amplifier designers, thereby controlling the signal peak-to-average power ratio (PAR). This, however, reduced spectral efficiency in terms of channel capacity. Gaussian minimum shift keying (GMSK), used in global system for mobile communication (GSM) networks, is one classical example of a constant envelope digital modulation scheme.

With the growing demand for higher data rates and ever increasing users on the 3G network, linearity specifications have become acute in accomplishing the needed capacity. In this regard, the basestation power amplifier must be able to handle large peaks, which means that the power amplifier is usually operating well below its peak efficiency point. For instance, the Universal Mobile Telecommunications System (UMTS) power amplifier requirements according to 3G partnership project (3GPP) specifications are to have frequency band (FDD, downlink) from 2.11 to 2.17 GHz, with ACPR of -45 dBc at ±5 MHz and -50 dBc at ±10 MHz carrier offset [2]. Moreover, since the UMTS basestation power amplifiers are subjected to wideband code division multiple access (W-CDMA) signals, a PAR ranging from 3 dB up to 12 dB must be sustained. The proposed 3G UMTS-LTE (long term evolution), which is a recent development in 3G UMTS interface, would employ orthogonal frequency division multiplexing (OFDM) for downlink with scalable bandwidths ranging from 1.25 to 20 MHz [3]. This continuing developments in 3G radio interface towards broadband capabilities targeting up to 100 Mb/s is forcing rapid system enhancements.

Linear operation in conventional power amplifiers is achieved by reducing the RF input to a level sufficiently low to avoid saturation of the active devices [4]. When a high degree of linearity is required, back-off mode of operation inevitably degrades overall efficiency and output power. Consequently, as indicated in Figure 1.1, in modern RF power amplifier applications, fulfilling linearity for preserving fidelity of the signal together with high power amplifier efficiency, imposes two conflicting design requirements.

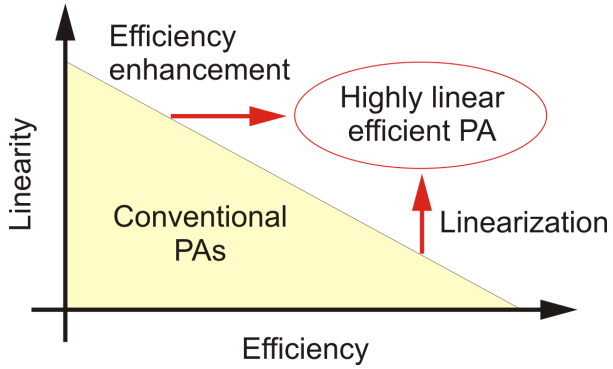

Figure 1.1 Linearity-efficiency trade-off in PA design [5].

Besides, by resorting to highly efficient power amplifier architecture, memory-effects cause bottleneck in realizing conventional linearization techniques. Memory-effects manifest as asymmetry behaviour between lower and upper distortion sidebands, which vary with signal bandwidth. An overview on such memory-effect behaviour is presented in Chapter 2 by introducing fundamental signal properties commonly adopted by amplifier designers for characterizing nonlinearity.

The success of device performance always depends on the semiconductor technology. The system, which demands very high linear power amplifier, in turn demands power transistors with very high compression point, excellent thermal stability and higher frequency response. In this regard, semiconductor materials that can fulfil high frequency and high power requirements are of enormous importance for 3G mobile communication. New compound

semiconductor devices, especially gallium-nitride (GaN) high-electron mobility transistors (HEMTs), have demonstrated high power, enhanced linearity and large power density at high frequencies, which make them attractive for basestation transmitter applications. Due to the key physical property of having wide bandgap material with high breakdown voltage, GaN HEMTs have the potential to operate at higher bias voltages and RF power levels [6].

1.1 Research Objectives

With the extensive use of sophisticated multi-carrier test signals, it is essential to enhance the intrinsic linearity of the power amplifiers in general, and transistors in particular. This further eliminates complex and expensive circuitries underlining the linearization techniques. This work is intended to provide pertinent practical application of computer-aided design (CAD) based modelling in circumventing linearity enhancement issues of AlGaN/GaN HEMT technology, supported by accurate measurement technique for reliable characterization of intermodulation distortion. FET devices which were experimentally analysed in this thesis, are listed below:

- GaN HEMTs with gate widths of 2 x 250 μm, 8 x 250 μm, and 8 x 400 μm manufactured at the Fraunhofer Institute for Applied Solid-State Physics (IAF), Freiburg, Germany.
- GaN HEMTs with gate widths of 8 x 125 μm and 8 x 500 μm manufactured at Ferdinand-Braun-Institute for High Frequency Technique (FBH), Berlin, Germany.
- GaN HEMTs with gate width of 10 x 200 μm manufactured by Nitronex, USA.
- GaAs HEMTs with gate width of 1.2 mm manufactured by TriQuint Semiconductors, USA.

CAD Modelling

The complexity in realizing successful power amplifier linearization techniques is growing rapidly to meet the figures of ever emerging 3GPP schemes. Some researchers have resorted to develop techniques capable of suppressing nonlinear IMD at the device-level rather than tackling the problem once the amplifier is designed. This has forced to develop methods for better understanding of IMD generation mechanism associated with the transistor. Commonly used CAD tools simulate overall IMD, providing no insight on the dominant distortion sources. As illustrated in Figure 1.2, such valuable information would subsequently aid the device manufacturer for making appropriate changes in the device process technology. This closed-loop between the device technology and sophisticated modelling and/or simulation tools would hence encourage more efficient approach to circumvent power amplifier linearity issues.

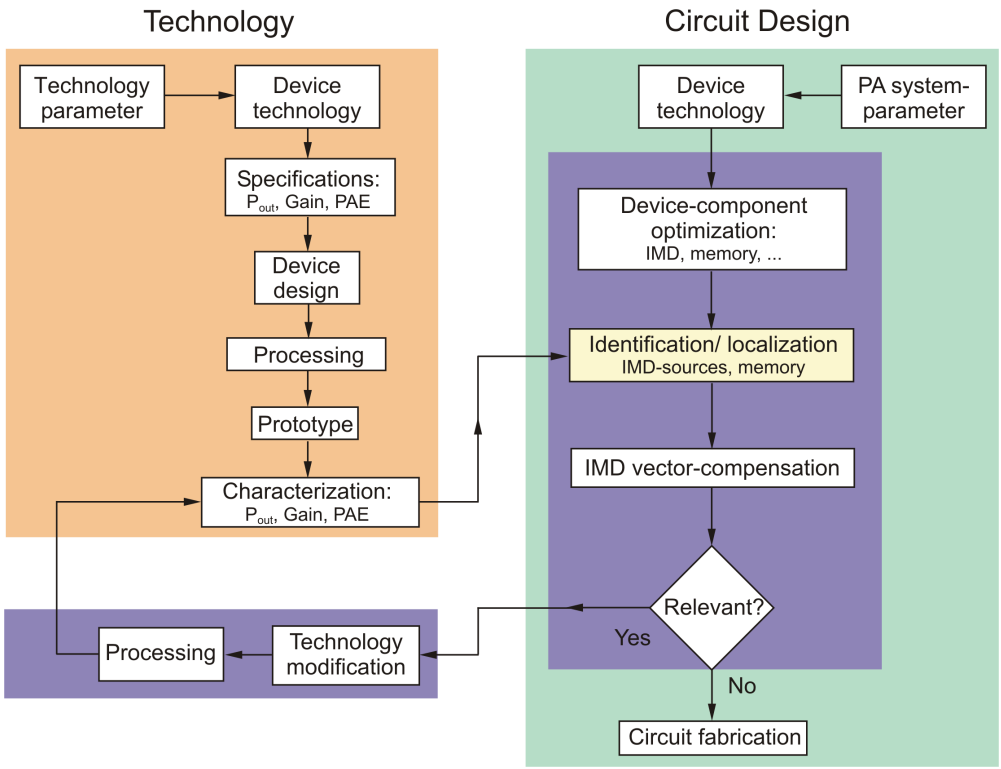

Figure 1.2 Closed-loop strategy between technologists and CAD modelling community for efficient circuit design optimisation.

In Chapter 3, frequency-domain Volterra model based IMD analysis strategy is discussed for obtaining insight into IMD generation mechanism. In this thesis, an 8 x 125 μm GaN HEMT is used to demonstrate third-order IMD vectorial analysis under two-tone excitation. Further, by interpreting key physical origins of the calculated distortion phasors, the influence of gate field-plate on IMD is investigated for possible GaN device linearity enhancement.

Measurement Techniques

Reliable large-signal device and/or power amplifier characterization techniques are essential for analysing RF and microwave circuits. Successful design of a high linear power amplifier requires accurate measurement data acquisition enabling straightforward CAD model verification and experimental design optimisation. Chapter 4 of this thesis focuses on fundamental issues encountered by microwave engineers in characterizing high power GaN HEMT devices.

The calibration techniques for error-correcting digitally modulated test signals are seldom treated by measurement experts. Under UMTS application, W-CDMA based device and power amplifier characterization is of high relevance, where the DUT is tested for its performance under realistic telecommunication environment. Often such measurements resort to power meters for output power measurements and spectrum analysers for ACPR measurements, by completely avoiding calibration routines. Consequently, such unreliable measurements strongly affect device model verification based on power sweep and source- and load-pull measurements. The established calibration routine for error-correcting the measured data under multi-tone and digitally modulated test signals is discussed in Chapter 4. In this work, frequency-domain based large-signal measurements are performed using a

dual-channel phase coherent vector signal analyser operating until 2.7 GHz.

Practical wide bandwidth considerations also become vital for designing highly linear power amplifiers with reduced memory-effects and implementing simple but efficient linearization techniques for operating the power amplifiers close to 1-dB compression point. In a 50Ω environment, broadband distortion measurements at the device-level should principally be reproducible, independent of the testbench properties. This aspect is very critical for CAD model verification, when the device is operated in the nonlinear regime, where disagreement between the model prediction and measured data in terms of IMD behaviour is very common. In such circumstances, the researchers are forced to either restrict the characterization to narrowband or emulate the measurement environment for broadband conditions in their simulation with respect to the termination properties, which is not practical. However, another alternative is to carefully optimise relevant testbench properties. In this regard, it becomes necessary to assess of the baseband termination properties of measurement setup that impact device's IMD characteristics.

Bias tees are one of the key components used in the measurement setup, which must be treated sensitively. The intervention of multi-carrier broadband test signals have re-emphasised the objective of bias network design in general, and bias tee design in particular, in addressing wider RF bandwidth and baseband termination issues. It is proven that compared to the second-harmonic termination, the envelope termination has significant impact on device's linearity and memory-effect behaviour. However, in reality to eliminate the undesired envelope component at the drain terminal, it is difficult to principally achieve broadband low baseband termination. This particular issue has been addressed in Chapter 4, emphasizing on the non-negligible DC-feed, which is often overlooked. In addition, Appendix C reports frequently encountered pitfalls in characterizing IMD, where a conventional testbench is used incorporating a commercial RF bias tee. This

particular issue accounts for misleading IMD results, leaving the power amplifier designers confused. There are many research works, which propose different bias network topologies for power amplifier design. However, the intension of this thesis work is to focus on device characterization issues and not on designing a bias network for high linear power amplifier design, though the knowledge is applicable for both cases.

As FETs are biased closer to pinch-off in order to reduce the drain current for improved efficiency, there is a general trend towards higher levels of IMD. However, there is a narrow range of bias point near pinch-off, where there is occurrence of a local minimum in the IMD characteristics. This IMD nulling behaviour is generally referred to as IMD sweet-spots. As a result, the power amplifier designers are encouraged to utilize this aspect by effectively overcoming linearity-efficiency trade-off. However, industries are sceptical about the consistency of sweet-spot occurrence, especially in AlGaN/GaN HEMTs. Thus, uncertainty still exists among several researchers whether sweet-spot characteristics could be utilized for practical applications. Chapter 5 thoroughly analyses the cause for the uncertainties by studying IMD sweet-spot behaviour in GaAs and GaN technologies through which the importance of the measurement setup is justified.

In this work, large-signal sweet-spot has been accepted as a yardstick for evaluating the measurement setup termination properties under modulated test signal environment. Ambiguity still exists in retaining the IMD nulling from wafer-to-wafer basis for a specific device technology and whether they are reproducible over an extended period of time. For this reason, following the improved RF characterization testbench, the sweet-spot reproducibility issues are investigated in matured GaAs technology and the upcoming and promising GaN technology. This is supported by analysing the statistical process consistency between GaAs and GaN HEMT semiconductor technologies in terms of their respective pinch-off voltages.

Chapter 2

Nonlinearity and Memory-Effect Characterization

In recent years, the development of cellular market has world-wide initiated researchers to investigate the implications of power amplifiers on the telecommunication system. With the increasing importance of spectral efficiency, an RF power amplifier, used in third generation (3G) mobile communication, needs to be highly linear to meet stringent spectrum emission requirements of 3GPP standards. This accounts for precise characterization of amplifier nonlinearity.

For a linear power amplifier, the output time-domain waveform will be identical to that of the input as shown in Figure 2.1. In the frequency-domain, no new spectral components are generated either within or outside the amplifier bandwidth [4]. Amplifying an input signal to levels required for reliable transmission using currently available power amplifier, introduces amplitude and phase distortion. In other words, when the amplifier is used in conditions such that the gain is not constant as a function of input signal, it is said to be an amplifier working in a nonlinear mode or the amplification is called nonlinear amplification. In such circumstances, a modulated carrier that has amplitude variations will exhibit a spread of the transmitted spectrum

(spectral regrowth) as a result of amplifier nonlinearities degrading the spectral efficiency of the system.

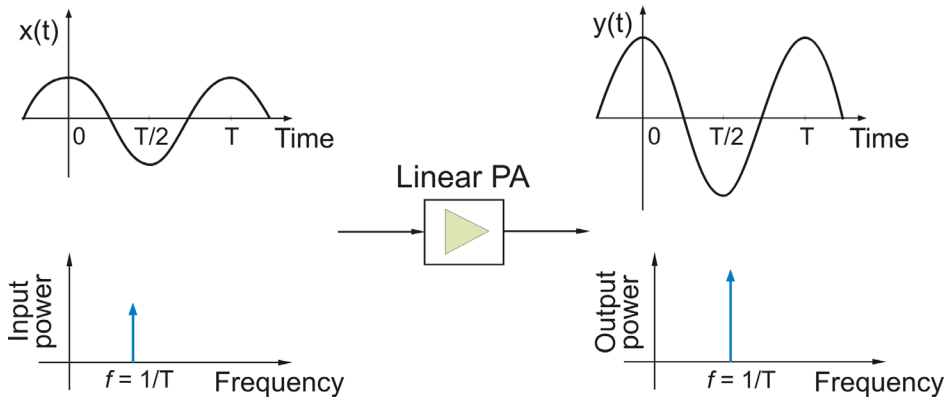

Figure 2.1 Linear power amplification.

It is very much essential to select a relevant stimulus to obtain valuable information on the distortion behaviour of the device. Immense development in the field of nonlinear characterization of microwave power devices and power amplifiers have been made under CW stimuli. At the device level, for instance, they provide key information on the fundamental and harmonic powers at the output together with power added efficiency (PAE) for the validation of transistor nonlinear models for computer aided design. Additionally, they provide experimental confirmations of the optimum operating conditions of active cells in terms of power, gain, and efficiency [7]. Test signals like two-tone or multi-tone stimuli, in general, provide additional information concerning linearity/efficiency trade-offs. Multi-tone characterization has proved to be an alternative test procedure closer to the system's final operating condition [8]. Realistic telecommunication signals, in contrast, usually constitute one or more carriers individually modulated by the baseband information signals, representing an aperiodic signal. Its frequency-domain counter part is a band-limited continuous spectrum. Bridging the gap between conventional test signals like single-tone (CW) or two-tone signals and telecommunication signals is still a major challenge, when considering nonlinear device and power amplifier characterization [9].

2.1 Nonlinear RF Characterization Techniques

2.1.1 Single-Tone Characterization

Indeed it is meaningful and straightforward to test the nonlinear system under realistic signal environment. However, since these signals are unpredictable in nature, it is rather difficult to interpret the system response behaviour. A simpler approach would be to approximate the total power distributed across the channel to a single frequency, giving rise to a single-tone test signal (Chapter 2 of [10]).

As illustrated in Figure 2.2, a nonlinear system subjected to a sinusoidal signal (f_c = 2 GHz) produces spectral components harmonically related to the input fundamental frequency. The presence of higher order harmonic components in the output power is evident due to the asymmetrical clipping of the drain current waveform along the loadline. As a matter of fact, CW tests only provide information on nonlinear static aspects through the well known AM-AM and AM-PM conversion characteristics [4], [10]. Nevertheless, CW measurements provide additive information on the frequency dependence of AM-AM and AM-PM characteristics performed on a frequency grid within the device operating bandwidth.

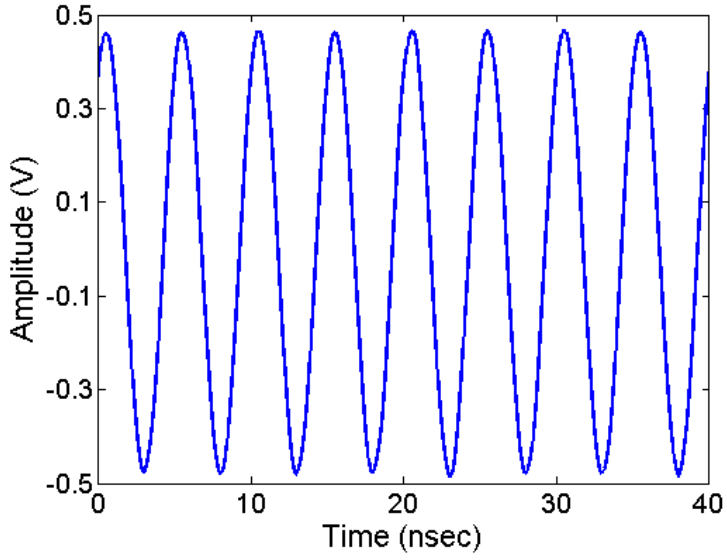

(a)

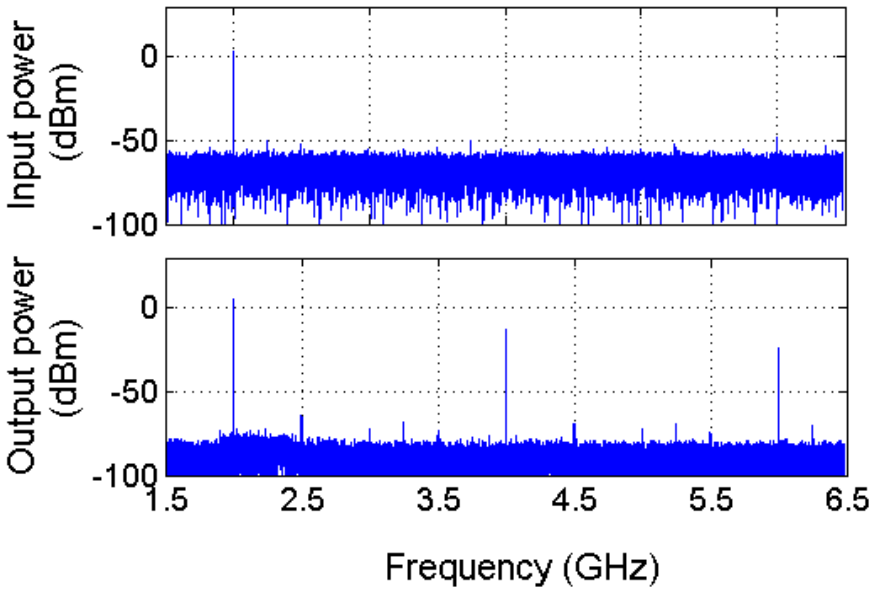

(b)

Figure 2.2 Measured (a) unmodulated single-tone (CW) time-domain waveform driving a 2-mm GaN HEMT into nonlinear operation, biased at deep class-AB (2% I_{DSS}, V_{DS0} = 15V) and measured (b) input-output spectrum using 12 GHz real-time oscilloscope.

2.1.2 Two-Tone Characterization

It is important to note that it is impossible to transmit any information using an unmodulated single carrier signal. Moreover, the system's spectral regrowth behaviour cannot be explored under static CW stimuli, which is a typical scenario observed in real telecommunication systems. This aspect is revealed by considering modulated signals, which are rather complex compared to the CW case. A better representation of a realistic telecommunication signal compared to CW is a two-tone signal, which has indeed, over the years, proved to be an efficient solution for evaluating the linearity properties of a nonlinear system.

Assuming a simple two-tone excitation signal x(t), as shown in Figure 2.3(a), with tones having equal amplitude and zero phase offset, x(t) can be expressed as

$$
\begin{aligned}
x(t) &= A \cdot \left[\cos(\omega_1 t) + \cos(\omega_2 t)\right] \\
&= 2A \cdot \cos\left(\frac{\omega_1 - \omega_2}{2} t\right) \cdot \cos\left(\frac{\omega_1 + \omega_2}{2} t\right) \\
&= 2A \cdot \cos\left(\omega_m t\right) \cdot \cos\left(\omega_c t\right)
\end{aligned} \tag{2.1}
$$

where $\omega_m = (\omega_1 - \omega_2)/2$ and $\omega_c = (\omega_1 + \omega_2)/2$ are the modulation and carrier frequencies. The corresponding nonlinear output $y_{NL}(t)$ would be

$$
y_{NL}(t) = \sum_{r=1}^{\infty} A_{o_r} \cdot \cos(\omega_r t + \phi_{o_r}) \tag{2.2}
$$

where $\omega_r = m\omega_1 + n\omega_2$ with m, n $\in$ Z, which shows that output would be composed of many mixing spectral components involving all possible combinations of $\pm\omega_1$ and $\pm\omega_2$ as shown in Figure 2.3(b) [10]. In particular, output of the device will have unwanted frequency components generated at frequencies $2\omega_1-\omega_2$ and $2\omega_2-\omega_1$, which are termed as lower and upper 3rd-order intermodulation distortion (IMD3) products, respectively. Also the lower and upper 5th-order intermodulation distortion (IMD5) products can be seen at frequencies $3\omega_1-2\omega_2$ and $3\omega_2-2\omega_1$, respectively, which become significant near compression.

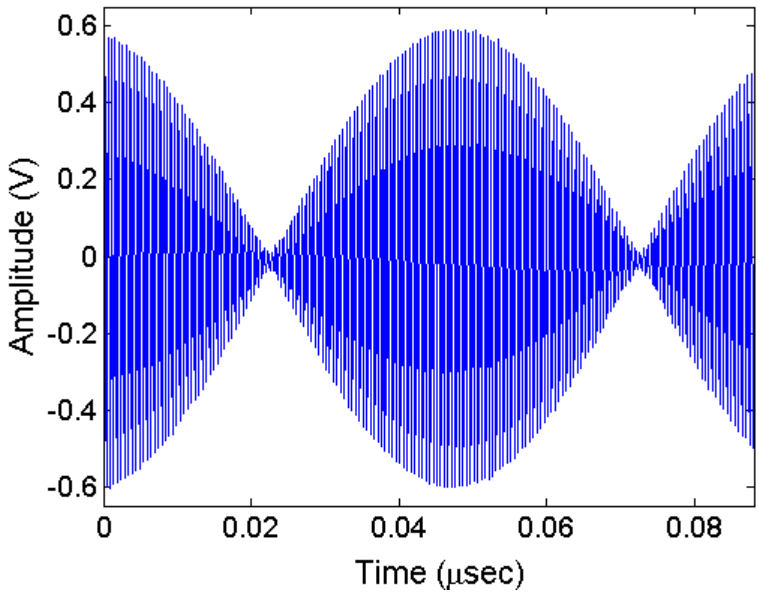

(a)

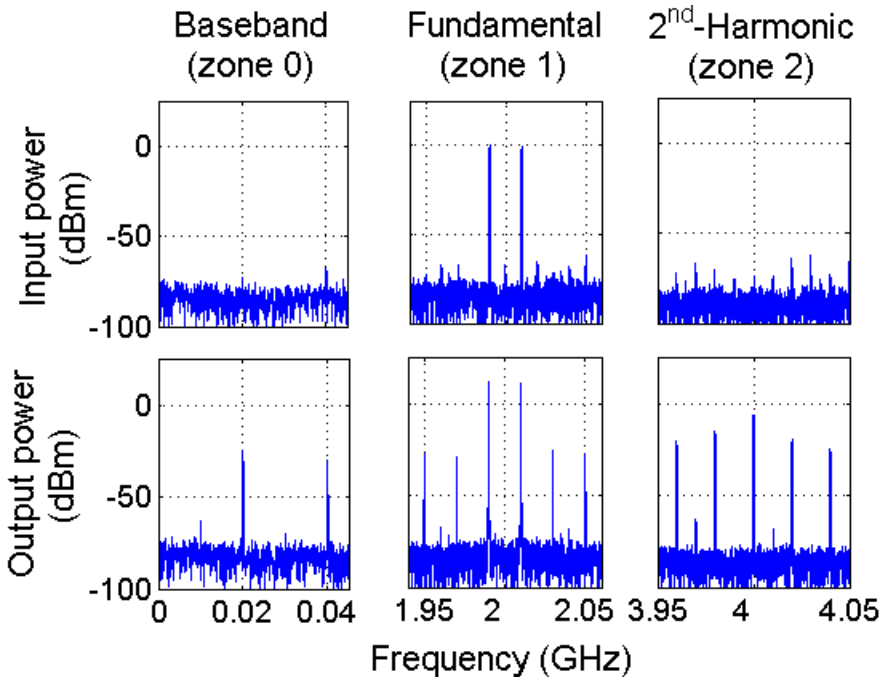

(b)

Figure 2.3 Measured (a) two-tone time-domain waveform with 5 MHz carrier spacing driving a 2-mm GaN HEMT into nonlinear operation, biased at deep class-AB (2% I_{DSS}, V_{DS0} = 15V) and measured (b) input-output spectrum using 12 GHz real-time oscilloscope.

Although gain compression is an evident problem for the amplifiers with 3rd-order nonlinearity, of greater concern are the IMD products appearing at $2\omega_1$-ω_2 and $2\omega_2$-ω_1 seen in Figure 2.4. These products appear in-band and hence will distort the desired waveshape of the fundamental signal component. Further, it is impossible to filter out these components, which appear within the band of interest, unlike the out-of-band products appearing across the baseband and harmonic zones. The compression and phase characteristics under two-tone excitation are strongly dependent on the modulation frequency. In particular, the process of AM-PM conversion of the fundamental tones can be understood by considering that at higher input levels, additional distortion products are generated at the fundamental frequency. When these vectorially contribute to the fundamental response, phase rotation occurs (Chapter 8 of [11]). The consequence of both AM-AM and AM-PM nonlinearities result in IMD asymmetry as illustrated in Figure 2.5, since components of IMD products originating from AM-AM conversion

will be in-phase whereas the components from AM-PM conversion tend to be 180° phase shifted [4].

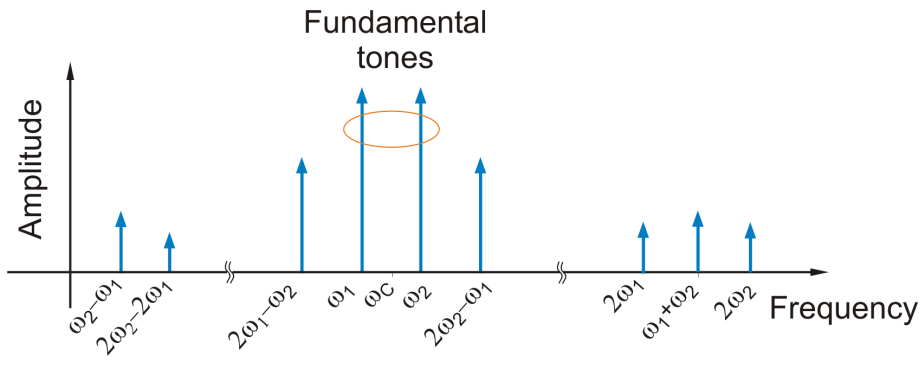

Figure 2.4 Typical two-tone output spectral response of a nonlinear system.

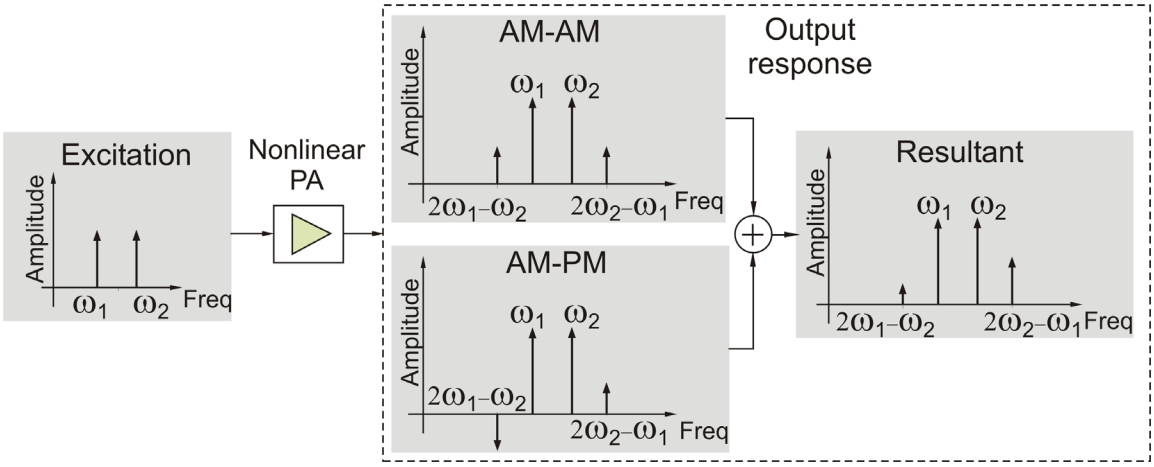

Figure 2.5 Effect of superposition of AM-AM and AM-PM conversions on the IMD products (after [4]).

2.1.3 Multi-Tone and Spread Spectra Excitation

Multi-tone characterization technique is another option for characterizing nonlinearity with more than two tones, which have gained importance in recent years as a substitute replacing the practical telecommunication signal. The measured time-domain waveform of ten-tone signal with equal amplitude and phase offset is depicted in Figure 2.6 along with the discrete input and output spectral components signifying the periodicity of the signal. In the fundamental band (zone 1) of the output spectrum of Figure 2.6(b), it can be

observed that the magnitude of the IMD products diminishes with the order, exhibiting the spectral regrowth behaviour. With the increase in the number of carriers n, the signal's peak-to-average ratio (PAR) increases by a factor of $10\log(n)$. This argument could be, however, extended to a digitally modulated test signal as shown in Figure 2.7, exhibiting an aperiodic time-domain behaviour and a corresponding spread spectrum in frequency-domain.

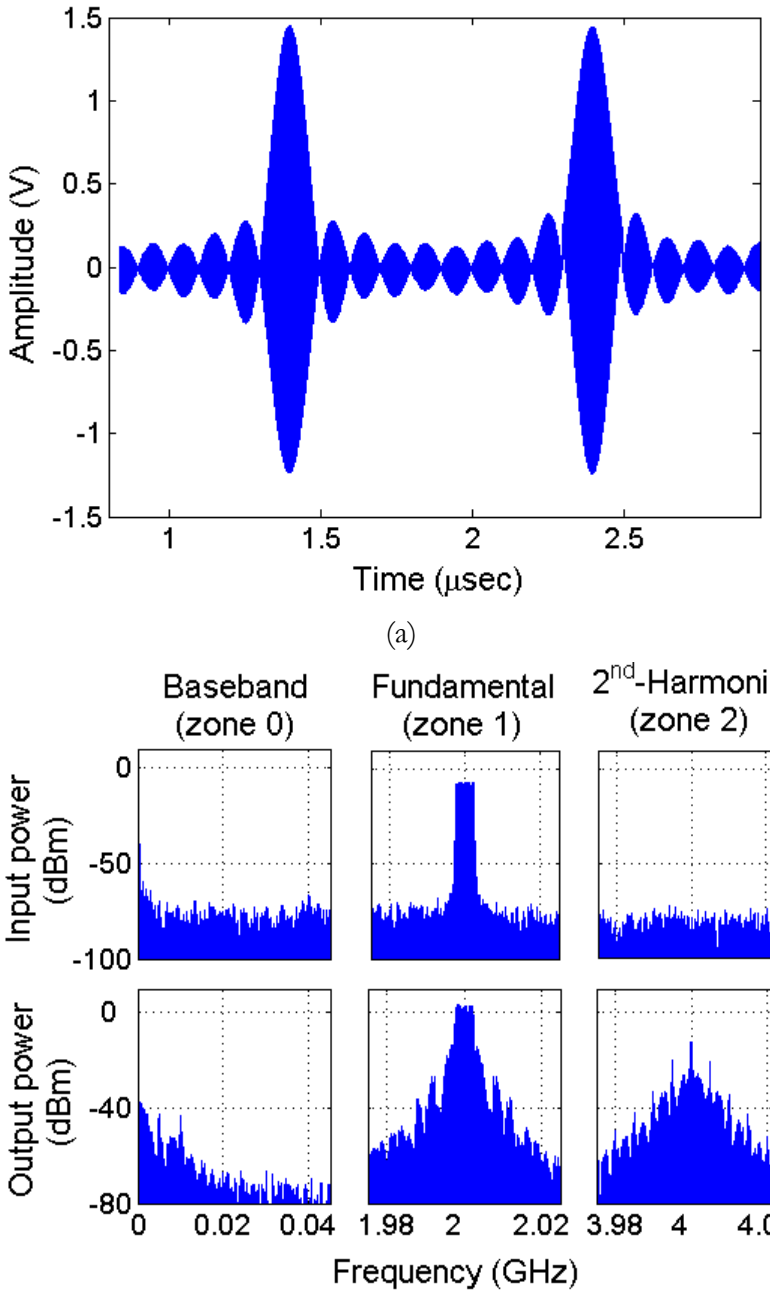

Figure 2.6 Measured (a) ten-tone time-domain waveform driving a 2-mm GaN HEMT into nonlinear operation, biased at deep class-AB (2% I_{DSS}, V_{DS0} = 15V) and measured (b) input-output spectrum using 12 GHz real-time oscilloscope.

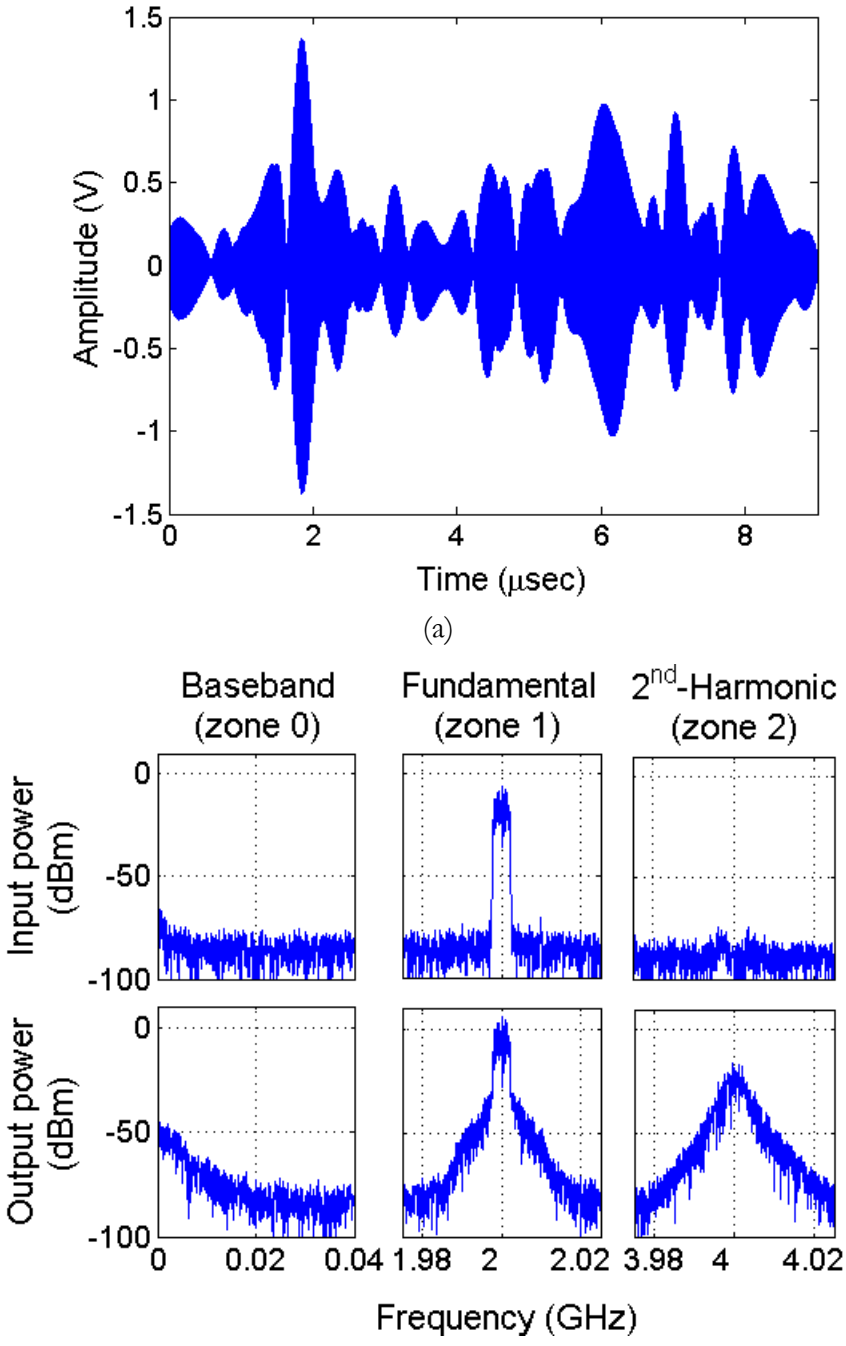

Figure 2.7 Measured (a) digitally modulated time-domain waveform [W-CDMA Test Model 1 -32 dedicated physical channel (DPCH)] driving a 2-mm GaN HEMT into nonlinear operation, biased at deep class-AB ($2\%I_{DSS}$, V_{DS0} = 15V) and measured (b) input-output spectrum using 12 GHz real-time oscilloscope.

Interpretation of power amplifier nonlinearity in terms of the time-domain waveforms of a digitally modulated signal is rather complicated. Nevertheless, amplifier linearity under digitally modulated test signal is characterized by

measuring the degree of output spectrum regeneration across the lower and upper sidebands. In all cellular systems it is necessary for the system design to impose specifications on maximum amount of distortion that can be introduced in adjacent channels. However, since it is impossible to practically design for absolute distortion levels, relative levels of power in the adjacent channel to power radiated in the main channel, is made obligatory, defining the most commonly used figure of merit (FoM) called adjacent channel power ratio (ACPR).

Figure 2.8 depicts important details of the spectral mask on an input-output power spectral density (PSD) measured using a commercial amplifier of type AMF-6B-020080-80-33P manufactured by Miteq.

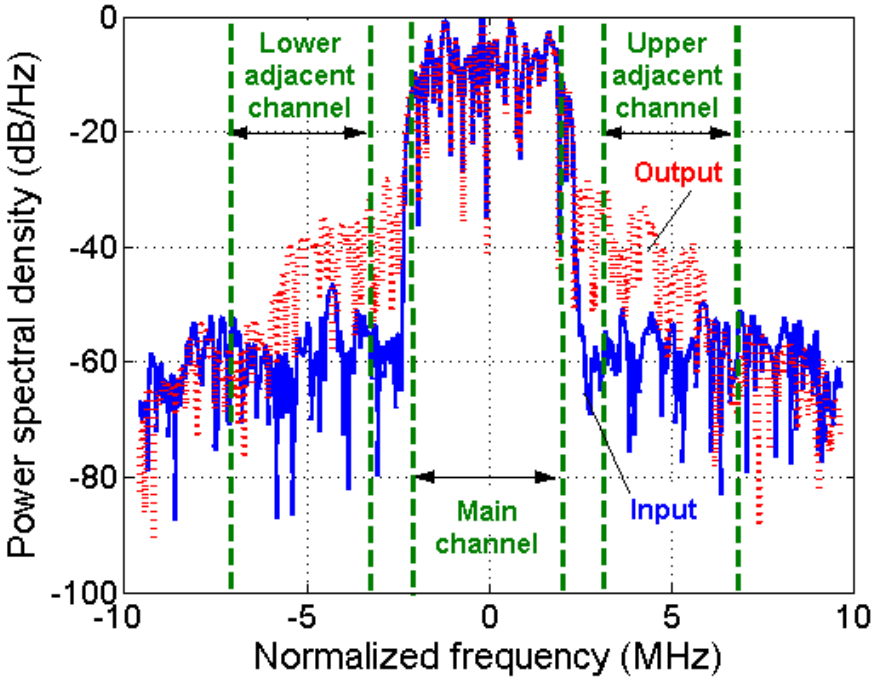

Figure 2.8 Input-output power spectral density encompassing the main channel with lower and upper adjacent channels measured with 2.7 GHz VSA.

At 1 dB compression point, 2W output power is measured under CW with an operational bandwidth from 2 to 8 GHz. The DUT was excited by a digitally modulated signal implementing quadrature phase shift keying (QPSK) modulation scheme. In QPSK, the carrier is modulated due to four phase

states (M = 4), which are 90° phase shifted from the neighbouring states. Subsequently, at any instant of time, the phase of the carrier is either 45°, 135°, 225° or 315° exhibiting 2 bits per symbol.

Figure 2.9 provides an alternate insight into the effect of AM-AM and AM-PM conversion of amplifier's nonlinearity from the perspective of the constellation diagram, obtained by plotting the in-phase (I) versus quadrature phase (Q) signal waveforms. The amplitude and phase distortion of the output signal is evident in the inset of Figure 2.9, where there is deformation of the constellation states.

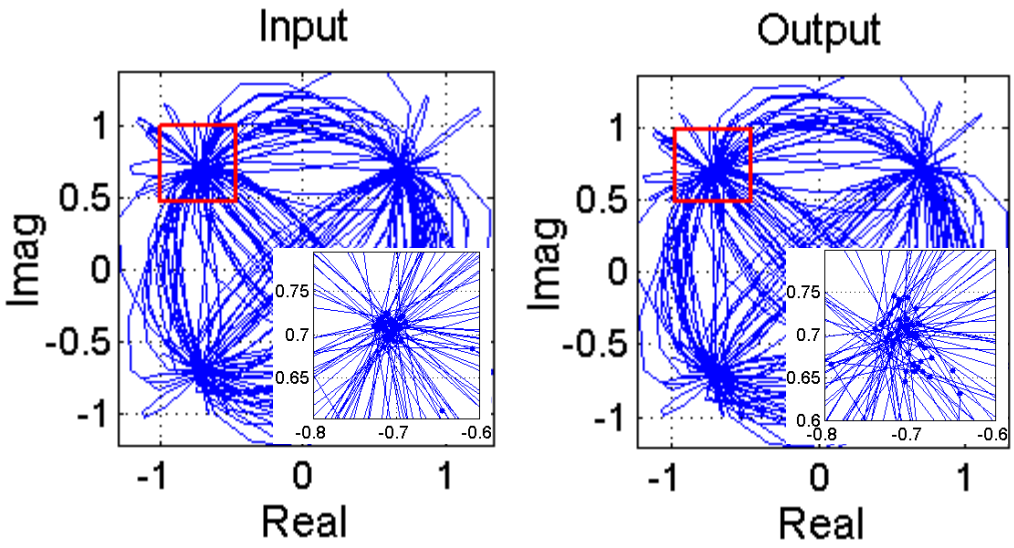

Figure 2.9 Constellation deformation of nonlinear power amplifier output illustrating amplitude and phase distortion.

2.2 Memory Properties of a Nonlinear System

In late 1980's, intensive research was carried out in designing a predistortion linearizer for IMD cancellation, whose AM-AM and AM-PM characteristics are inverse to that of power amplifiers to be linearized [12]. This approach was acceptable under the condition that predistortion circuits could reproduce the same characteristics for any signal envelope frequencies, which unfortunately could not be fulfilled. This unintentional behaviour, caused by the time constants of the linearizer circuit, is termed as *memory-effects*. As a result, there is

significant degradation in IMD cancellation performance followed by a more sophisticated implementation of linearization techniques.

At this point, it becomes rather interesting to rise the subject of nonlinear system classification with respect to the inherent memory property. Accordingly, nonlinear systems can be classified into memoryless system, quasi-memoryless system, and systems with memory. However, it is important to understand the type of excitation signal essential for characterizing system's memory behaviour.

From the application point of view, a static single-tone power sweep measurement is generally favoured during power amplifier characterization, additionally aiding the design of a linearizer. However, it is well known that a CW characterization does not provide sufficient information on the system's memory. Moreover, Bösch *et al.* [12] reported that a statically linearized amplifier (under single-tone stimuli) fails to show any improvement in IMD characteristics compared to nonlinearized power amplifier under dynamic two-tone excitation. This had prompted the presence of non-negligible memory, which forced the system response to vary with the envelope frequencies. As a result, such effects can be characterized only under modulated test signal environment.

Consider a sinusoidal input signal x(t) with an angular frequency of ω_c, which is modulated by amplitude A(t) and phase ϕ(t)

$$x(t) = A(t) \cdot \cos\left[\omega_c t + \phi(t)\right] \tag{2.3}$$

In order to simplify the analysis, in case of small-signal excitation, the linear system response of a memoryless system y_{ML}(t) can be expressed as

$$y_{ML}(t) = C\left(A\right) \cdot \cos\left(\omega_c t + \phi\right) \tag{2.4}$$

where C(A) is the amplitude conversion curve, commonly referred to AM-AM

curves, which is always defined at a specific amplitude or power level. The input-output response characteristics of a memoryless nonlinear systems is shown in Figure 2.10(a) as a single curve. Figure 2.10(b) clearly shows the absence of phase shift between the input and the output waveform.

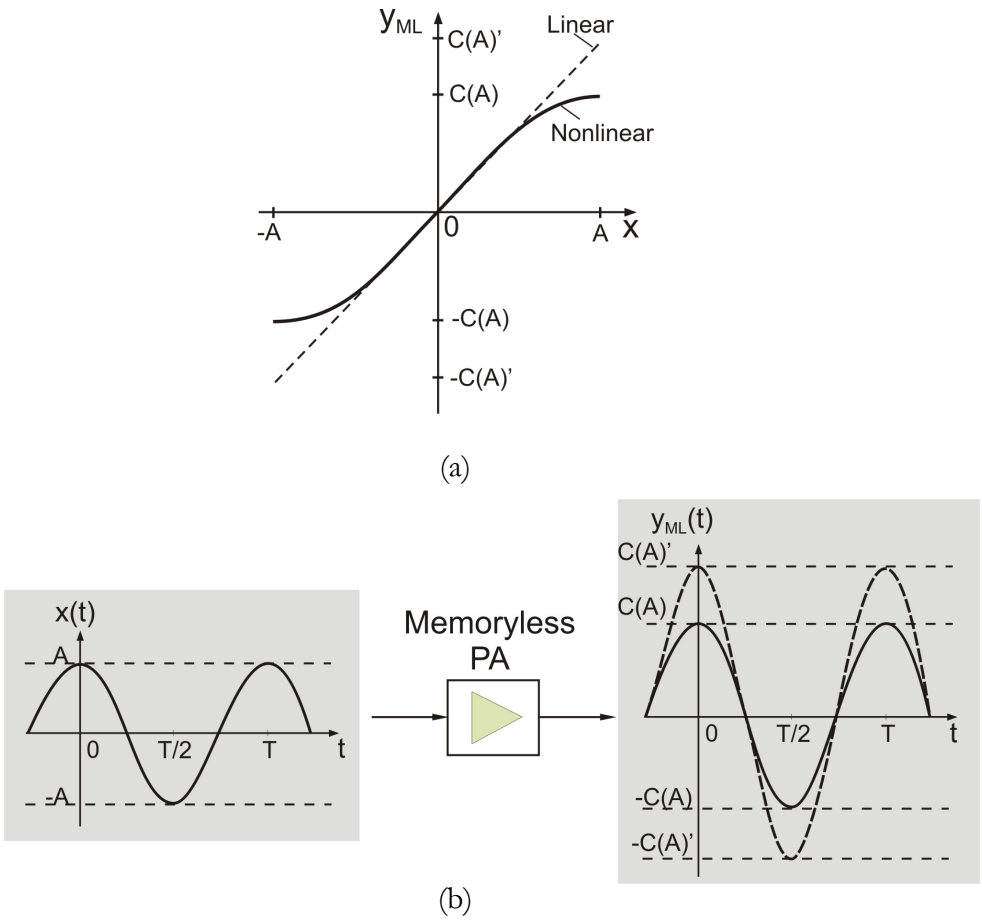

Figure 2.10 Memoryless system depicting (a) nonlinear input-output characteristics and (b) representing time-domain waveform [13].

For a quasi-memoryless system the output response $y_{QM}(t)$ takes the following form:

$$y_{QM}(t) = C(A) \cdot \cos\left[\omega_c t + \phi - \Phi(A)\right] \tag{2.5}$$

where $\phi(A)$ is the input amplitude dependent phase distortion additionally induced in a quasi-memoryless system due to AM-PM conversion. Thus, if phase distortion is present, the system must posses certain amount of memory. At any given time instant, the response amplitude C(A) and the

phase $\phi(A)$ are functions of only instantaneous input amplitude A as shown in Figure 2.11(a)-(b), respectively, with the assumption that A is time invariant. In case of a modulated single carrier, the system time constant $\tau \ll 1/f_{env}$, where f_{env} is the maximum baseband frequency indicating negligible memorizing time. In such systems, symptoms of memory-effect manifests mainly in terms of phase distortion.

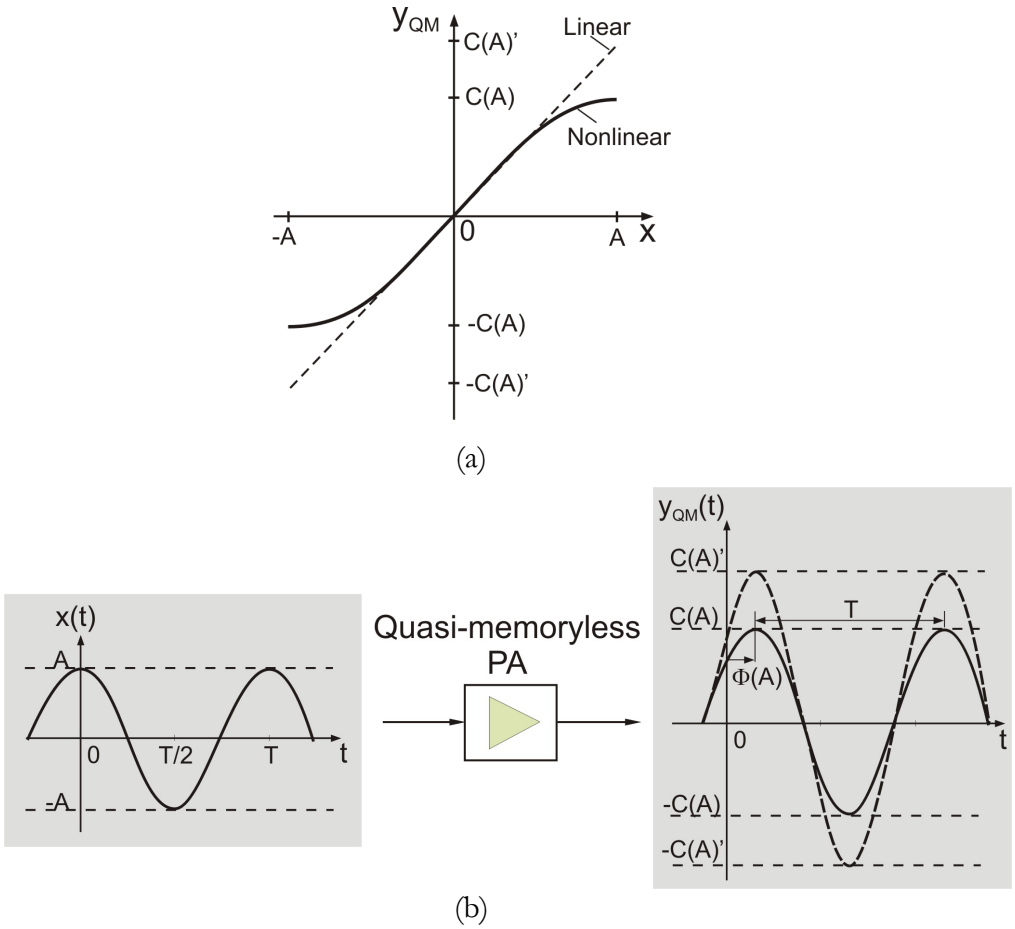

Figure 2.11 Quasi-memoryless system depicting (a) nonlinear input-output characteristics and (b) representing time-domain waveform [13].

A nonlinear system with memory constitutes a more realistic scenario, a consequence of which is that the output of the system will no longer respond instantaneously. As shown in Figure 2.12, which depicts the nonlinear time-domian input-output characteristics, a phenomenon of hysteresis emerges due to the system's memorizing effect preventing the overlap of input-output trajectory with the increase in signal swing. In other words, as indicated in

Figure 2.12, the rising curves from s' to s fail to maintain the same trajectory when the amplitude is increased from A' to A [13]. The hysteresis behaviour, hence, tends to show a strong dependence of memory-effect with input amplitude. In frequency-domain, the AM-AM and AM-PM characteristics become a function of the carrier frequency as shown in Table 2.1 of Section 2.3. In case of a modulated carrier, for instance, the system time constant τ will be comparable to $1/f_{env}$ indicating a significant amount of memorizing time.

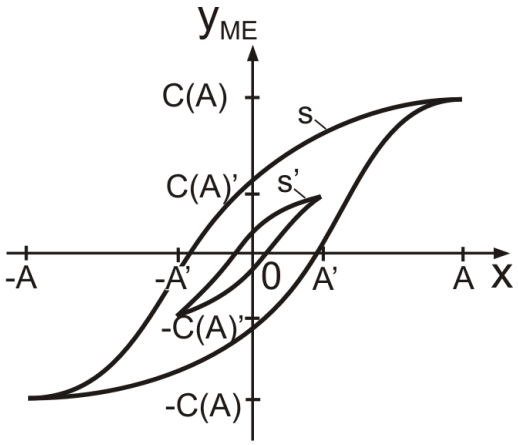

Figure 2.12 Nonlinear input-output characteristics for a system with memory representing the hysteresis behaviour [13].

2.3 Memory-Effect Manifestation

Pioneering work of Bösch and Gatti [12] led to better understanding of major consequences of memory-effects, introducing basic measurement techniques to characterize these effects. Indeed, success of a good linearizer design depends on precise characterization of amplitude and phase of IMD. Later, Vuolevi *et al.* [14] established an improved measurement system for investigating memory-effects, which could characterize complex IMD. Further, focusing on the envelope termination issues, which was a bottleneck for realizing conventional linearization techniques, Vuolevi *et al.* [15] established three techniques, namely, (i) envelope filtering, (ii) impedance optimisation, and (iii) envelope injection for efficient cancellation of memory-

effects. For high efficiency microwave power amplifier design, Meghadi [13] established a method for simulating nonlinear power amplifier behaviour, which could exhibit envelope memory-effects.

This thesis follows the definition of Vuolevi [14-15] in understanding nonlinear systems with memory. Subsequently, the memory-effects of such systems can be characterized under single-tone and two-tone stimuli:

- Single-tone excitation with AM-PM curves provides the memory-effect information, which is a function of the carrier frequency. This approach can be regarded as a narrowband approximation of a bandwidth dependent system.
- Two-tone excitation enables memory-effect characterization through IMD curves as a function of input modulation bandwidth.

In simple terms, at any time instant, the response of the system exhibiting memory-effects, not only depends on its instantaneous input but also on its past inputs. This is a direct consequence of energy-storing circuit elements, causing phase delay. Table 2.1 gives an overview of the simulated nonlinear characteristics, which are vulnerable to memory-effect phenomena under single-tone, two-tone, and digitally modulated excitation signals (Chapter 3 of [17]). Simulations are performed in ADS® using Motorola's MOSFET based amplifier. Under single-tone (CW) stimulus, the frequency dependent nonlinear static AM-AM and AM-PM characteristics are simulated by sweeping the carrier frequency from 845 MHz to 855 MHz in 5 MHz steps. A variation of 0.4 dB gain and 5° phase shift is observed for every 5 MHz change in carrier frequency. However, referring to Table 2.1, AM-AM and AM-PM conversion curves under single-tone can no longer reveal the bandwidth dependent distortions. This requirement is fulfilled, in general, by modulated test signals, wherein the output signal depends not only on the input envelope amplitude but also on its envelope frequency.

Table 2.1 Manifestation of memory-effects in nonlinear systems with memory on the basis of ADS® simulation performed on Motorola's MOSFET based amplifier [4], [17].

Single-tone (carrier frequency sweep)

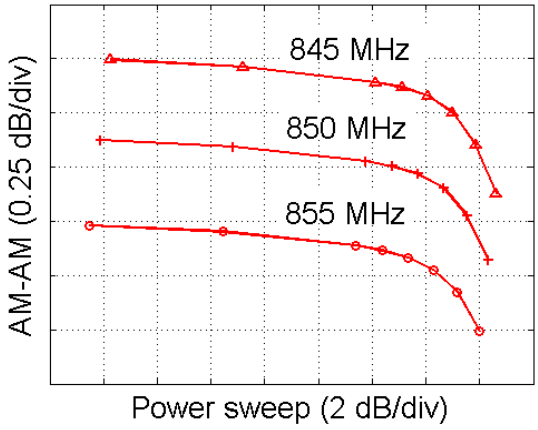

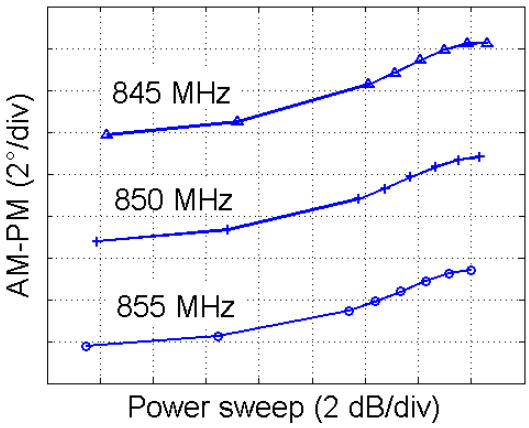

Two-tone (carrier spacing sweep)

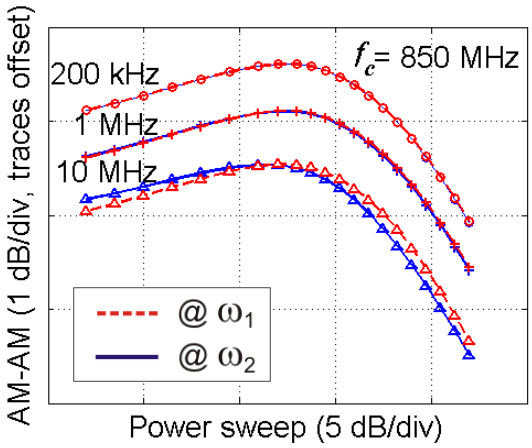

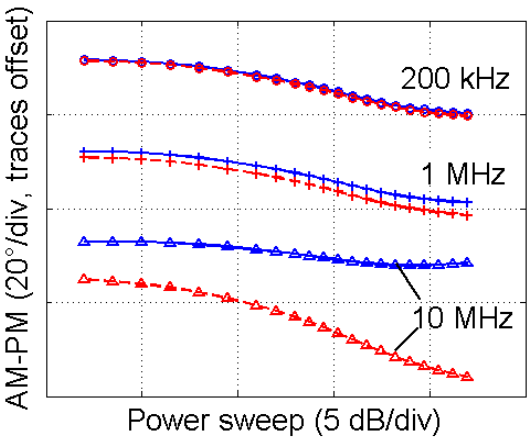

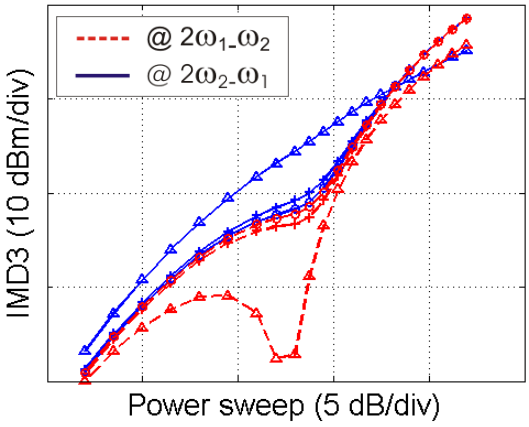

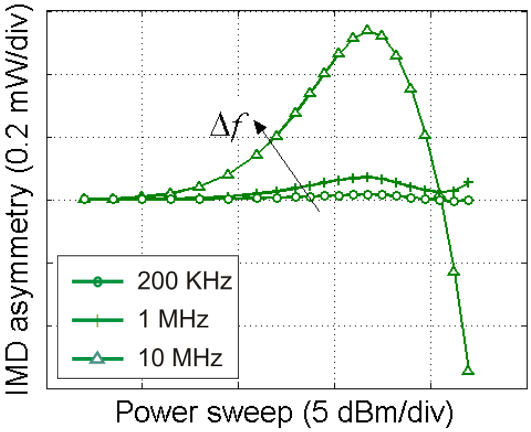

Digitally modulated QPSK signal

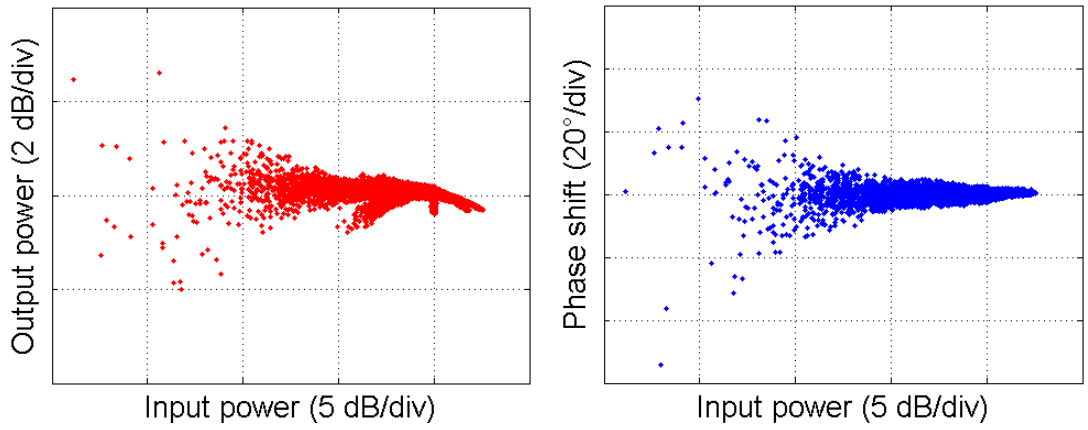

When the approach of measuring dynamic AM-AM and AM-PM conversions of the fundamental tone powers is followed, strong linear signals (1st-order) dominate over the higher order signal components [14-15]. Consequently, by measuring the fundamental signal component, it becomes impractical to evaluate any nonlinear effects caused by presence of memory. However, the in-band IMD products, originating from the device's nonlinearity, are more vulnerable to memory-effects than the fundamental signal. Thus, IMD characterization under two-tone excitation has been widely accepted as a conventional solution to investigate signal bandwidth dependent nonlinear effects. Under modulated stimuli, the memory-effects at the output manifest as asymmetric behaviour between lower and upper distortion sidebands, which vary with signal bandwidth. In Table 2.1, it can be seen that the IMD characteristics show pronounced dependence of carrier spacing, which is swept from 200 kHz to 10 MHz reaching 0.55 mW of IMD asymmetry for 10 MHz modulation bandwidth.

Depending on the origin, memory-effects are broadly categorized into (i) electro-thermal (long-term) memory effects caused by active device's temperature modulation for narrow bandwidth conditions [15-16] and (ii)

electrical memory-effects, mainly influenced by the external termination properties across all harmonics and intermodulation frequencies contributed by bias and matching networks [15]. These two classified memory-effect behaviours clearly explain the inability of CW signals to capture essential memory-effect induced parameters. It is, however, practically impossible to eliminate memory from a system. The condition of achieving constant IMD response with null asymmetry over a wide range of carrier spacing is not sufficient for a system to be memoryless since the system's phase distortion is inevitable.

It can be seen from Table 2.1 that the insight is lost in understanding memory-effect behaviour with the increase in the complexity of the test signal, for instance, under digitally modulated signals. The hysteresis behaviour becomes more evident in the AM-AM and AM-PM characteristics when the amplifier is driven by digitally modulated signal such as quadrature phase shift keying (QPSK) scheme having 12 dBm input power level with 850 MHz carrier frequency and a modulation bandwidth of 6 MHz.

Chapter 3

Volterra Model of AlGaN/GaN HEMT

The primary issue with basestation power amplifier performance is the amount of signal distortion generated by the used microwave field effect transistor (FET). Nonlinearities are easier to extract from highly sensitive intermodulation responses than changes in the fundamental signal. Hence, most of the nonlinearity analysis, simulations, and measurements give emphasis on IMD responses. In general, IMD can be attributed to device's strong nonlinearities or mild nonlinearities [18]. In the former case, signal distortion is due to the hard clipping of output waveform caused by cutoff, gate forward conduction, gate-to-drain breakdown, or linear-to-saturation region transition. This is common for operating classes other than class-A driven amplifiers and sometimes even for class-A amplifiers driven into deep compression. In contrast, under small-signal excitation, the signal waveform experiences weak or mild deviations in the I(V) characteristics around certain bias point resulting in low level IMD products.

Most of the developed nonlinear distortion analysis techniques only show the total amount of distortion, giving no assistance of their origin by which the distortion could be reduced. In such circumstances, the power amplifier

designers are unable to identify as to which circuit parameters should be optimised in order to achieve the desired design specification. As a result, the design tasks of complex power amplifier architectures become more challenging. Practically, such problems are tackled by optimising the design iteratively, which is expensive and time consuming.

It is, hence, essential to find efficient means of localizing or diagnosing the device distortion by which the basic nonlinearities that are responsible for the observed nonlinear behaviour, can be identified [19]. With this knowledge, the dominant distortion contributors can be suppressed or completely eliminated by suitably optimising the device process technology. Volterra series technique has been widely acknowledged over the years as a powerful tool in an effort to understand IMD generation mechanism. However, the price that is paid to such in-depth analysis is that this approach is restricted to only weakly nonlinear behaviour. A circuit is said to behave weakly nonlinear if, for the applied input, the response can be accurately described by first three terms of the converging Volterra series [19].

Volterra series method is an analytical procedure capable of describing the response of a certain class of nonlinear systems by closed form expressions. In general, through Volterra series approach, which is based on the direct calculation of component-level nonlinear response, it is therefore possible to draw a qualitative conclusion about the system.

Volterra series has been efficiently used for distortion calculation [19-35]. Narayanan [20] was one of few, who demonstrated for the first time that Volterra series technique was well suited for transistor distortion analysis, where the nonlinearities are weak but frequency dependent. Recently, Vuolevi *et al.* [21] analysed 3rd-order distortion (IMD3) in detail for GaAs MESFET amplifier, where it was shown to be a complex vector sum of several 3rd- and 2nd-order contributions and mixing products. Highlighting the advantages in

following Volterra series technique, Yum *et al.* [22] demonstrated 28 dB reduction in IMD outperforming typical predistortion of 5-10 dB based on compensating transistor pair module using SiGe bipolar transistor technology. Making effective use of vectorial analysis, Leung *et al.* [23] reported 6 dB improvement in adjacent channel power ratio (ACPR) by promoting distortion cancellation through envelope signal injection.

Exploiting the benefits of Volterra series technique, very few works have been published on optimising the device semiconductor properties for enhancing the overall device performance. Interestingly, concerning FET devices, much of the published works [24-26] resort to the optimisation of G_m, overlooking at the contributions from capacitive nonlinearities in general and gate-drain feedback capacitance C_{gd} in particular. This is because, typically a simplified formulation of Volterra series analysis is carried out by assuming an approximate equivalent circuit and especially neglecting the contributions from the feedback capacitance. Eventually, this leads to reduced analysis accuracy and any potential possibility of improving the device performance through C_{gd} optimisation is lost.

This chapter emphasises Volterra series technique on achieving insight into the interaction between different distortion contributors in GaN HEMT based device technology. One of the prime focus of this thesis work is in localizing the distortion behaviour, which degrades linearity performance, and to propose a possibility to tune relevant quasi-linear bias dependent intrinsic equivalent circuit elements causing intermodulation distortion in GaN HEMTs.

3.1 Small-Signal Distortion Analysis

Accurate CAD models are necessary to perform reliable analysis of active device's nonlinear behaviour. As reported by Maas [27], for reliable IMD

prediction, the model must satisfy the following conditions:

- For n^{th}-order distortion product calculation, the device's I(V) and Q(V) characteristics and its first n derivatives must be accurately modelled.
- The analysis is valid only over an operational range of currents or voltages within which individual nonlinear elements of the device are modelled.

Concerning FET devices, the most serious distortion products arise from those terms having an odd-power dependence on the gate signal, which generate new in-band components. Confining the study to only small-signal distortion, the two most standard analysis techniques used are (i) power series analysis, which describes a nonlinear memoryless system and (ii) Volterra series analysis, which describes a nonlinear dynamic system.

3.1.1 Power Series Characterized Memoryless System Analysis

As discussed in Section 2.2 of Chapter 2, a system whose output response depends only on the instantaneous input, is called a memoryless system or a zero memory system (Chapter 3 of [10]). A simple example of a linear memoryless system is the conductance, typically represented as $i(t) = G \cdot v(t)$, whose output current i(t) is a function of the input voltage v(t) at the same time instant.

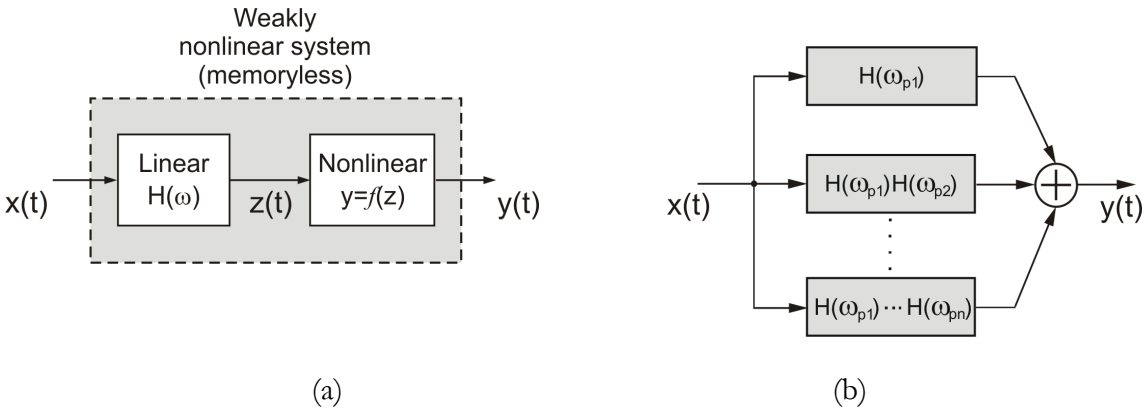

Figure 3.1 Weakly nonlinear system constituting (a) memoryless linear and nonlinear elements, (b) schematic of n^{th}-order system representation characterized by power series.

In case of a nonlinear system, which is more relevant in the present context, power series has been widely used for direct calculation of the response of a nonlinear device. Following the description of Maas [28], as shown in Figure 3.1(a), a memoryless weakly nonlinear system can be represented by a linear network, having a transfer function H(ω), in parallel with a set of nonlinear transfer functions described by the power series. Thus, the overall output response of the weakly nonlinear system can be expressed as

$$\begin{aligned} y(t) = f\left[z(t)\right] &= a_1 z(t) + a_2 z^2(t) + \ldots a_N z^N(t) \\ &= \sum_{n=1}^{N} a_n z^n(t) \\ &= \sum_{n=1}^{N} y_n(t) \end{aligned} \tag{3.1}$$

where $y_n(t) = a_n z^n(t)$. Let $v_x(t)$ denote an input signal, corresponding to x(t), with excitations at multiple frequencies (2P), which are small and non-commensurate (are not harmonics of a single frequency). Thus, under the assumption that the excitation does not include DC component ($p \neq 0$), the generalized form of the input signal can be represented as

$$\begin{aligned} v_x(t) &= \frac{1}{2} \sum_{p=1}^{P} V_{x,p} \exp(j\omega_p t) + V_{x,p}^{*} \exp(-j\omega_p t) \\ &= \frac{1}{2} \sum_{\substack{p=-P \\ p\neq 0}}^{P} V_{x,p} \exp(j\omega_p t) \end{aligned} \tag{3.2}$$

where $V_{x,-p} = V^{*}_{x,p}$ and $\omega_{-p} = -\omega_p$. As a result, the output of the linear block z(t) can be evaluated as

$$z(t) = v_z(t) = \frac{1}{2} \sum_{\substack{p=-P \\ p\neq 0}}^{P} V_{x,p} H(\omega_p) \exp(j\omega_p t) \tag{3.3}$$

Further, replacing z(t) from (3.3) in (3.1), the overall response of the system y(t) at the output of the nonlinear block will hence be

$$y(t) = \sum_{n=1}^{N} a_n v_z^n(t) \tag{3.4a}$$

$$a_n v_z^n(t) = a_n \left[\frac{1}{2} \sum_{\substack{p=-P \\ p\neq 0}}^{P} V_{x,p} H(\omega_p) \exp(j\omega_p t) \right]^n \tag{3.4b}$$

$$\begin{aligned} &= \frac{a_n}{2^n} \sum_{p1=-P}^{P} \sum_{p2=-P}^{P} \cdots \sum_{pn=-P}^{P} V_{x,p1} \cdot V_{x,p2} \cdots V_{x,pn} \\ &\cdot H(\omega_{p1}) H(\omega_{p2}) \ldots H(\omega_{pn}) \cdot \exp\left[j(\omega_{p1} + \omega_{p2} \ldots \omega_{pn}) t \right] \end{aligned} \tag{3.4c}$$

It is worth noting that in power series analysis, there exists only a single transfer function H(ω). Schematic of (3.4) is illustrated in Figure 3.1(b) showing the summation of parallel cascaded transfer functions for a system characterized by n^{th}-degree power series. However, despite the mathematical simplicity in representing a nonlinear system, the underlying assumption that the system's equivalent circuit contains only ideal memoryless transfer nonlinearities becomes often unrealistic. As an example, a classical two-tone stimulus x(t) can be represented as

$$x(t) = v\cos(\omega_1 t) + v\cos(\omega_2 t) \tag{3.5}$$

Applying x(t) to a weakly nonlinear system y(t), represented by a 3^{rd}-degree polynomial

$$y(t) = a_1 x(t) + a_2 x(t)^2 + a_3 x(t)^3 \tag{3.6}$$

yields IMD3 components at frequencies $2\omega_1$-ω_2 and $2\omega_2$-ω_1 with amplitudes proportional to $0.75a_3v^3$ [29]. Subsequently, the IMD3 products at the output are independent of signal bandwidth. In other words, power series approach fails to characterize bandwidth-dependent memory-effects under variable tone spacing, justifying the limitation of characterizing only a memoryless nonlinear system. Moreover, in a multi-port system, there is always more than one nonlinear mechanism present in an active device. Consequently, the input-

output relation neglects the fact that distortion components in one node generate new products at another node [15].

3.1.2 Volterra Series Characterized Dynamic System Analysis

In a dynamic system, the output response not only depends on the instantaneous input but also on its past inputs (Chapter 3 of [10]). Such systems, also termed as system with memory, may constitute linear and nonlinear resistive or reactive elements as shown in Figure 3.2(a), which are modelled using power series having a similar form expressed in (3.4). For a time-invariant system with memory, a classical example is a linear capacitance, where the output current is a function of the instantaneous and past input voltages, which can be expressed as

$$i(t) = \lim_{\Delta t \to 0} \frac{q(t) - q(t - \Delta t)}{\Delta t} = C \lim_{\Delta t \to 0} \frac{v(t) - v(t - \Delta t)}{\Delta t} = C \frac{dv(t)}{dt} \tag{3.7}$$

In this case, memory is actually denoted by the time derivative required to transform the storage charges into current i(t) across the capacitance [10].

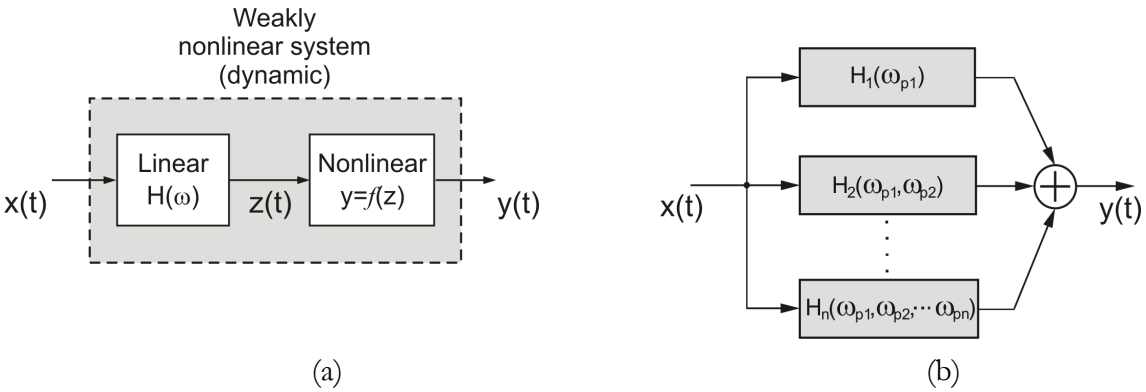

Figure 3.2 Weakly nonlinear system constituting (a) linear and nonlinear elements with memory, (b) schematic of n^{th}-order system representation characterized by Volterra series.

Retaining the same excitation signal (3.2), based on Volterra series, the output response takes the form

$$y(t) = \sum_{n=1}^{N} \frac{1}{2^n} \Bigg\{ \sum_{p1=-P}^{P} \sum_{p2=-P}^{P} \cdots \sum_{pn=-P}^{P} V_{x,p1} \cdot V_{x,p2} \cdots V_{x,pn} \cdot H_n(\omega_{p1}, \omega_{p2}, \ldots \omega_{pn}) \cdot \exp\Big[\big(j(\omega_{p1} + \omega_{p2} \ldots \omega_{pn}) \big) t \Big] \Bigg\} \tag{3.8}$$

where $H_n(\omega_{p1}, \omega_{p2},\ldots\omega_{pn})$ is referred to as the n^{th}-order transfer function. An analogy of (3.8) is shown as schematic in Figure 3.2(b), in which the block H_1 represents the transfer function of a linearized system (Chapter 4 of [19]). It is important to note the key difference between (3.4) and (3.8). With the possibility of determining transfer function separately for each order in (3.8), all orders of distortion generated from different nonlinear elements of the system can be individually described taking into account relevant mixing products [4].

Interestingly, it has been shown in [28] that the frequency-domain transfer function $H_n(\omega_{p1}, \omega_{p2},\ldots\omega_{pn})$ in (3.8), which is a product of linear transfer functions $a_nH(\omega_{p1})H(\omega_{p2})\ldots H(\omega_{pn})$ in (3.4), can be rewritten as convolution integral in the time-domain as

$$\begin{aligned} y(t) = & \sum_{n=1}^{N} \frac{1}{2^n} \sum_{p1=-P}^{P} \sum_{p2=-P}^{P} \cdots \sum_{pn=-P}^{P} V_{x,p1} \cdot V_{x,p2} \cdots V_{x,pn} \\ & \cdot \exp\Big[j(\omega_{p1} + \omega_{p2} \ldots \omega_{pn}) t \Big] \\ & \cdot \int_{-\infty}^{\infty} \int_{-\infty}^{\infty} \cdots \int_{-\infty}^{\infty} h_n(\tau_1, \tau_2, \ldots, \tau_n) \cdot \exp\Big[-j(\omega_{p1}\tau_1 + \omega_{p2}\tau_2 \ldots \omega_{pn}\tau_n) \Big] \\ & \cdot d\tau_1 d\tau_2 \ldots d\tau_n \end{aligned} \tag{3.9}$$

where $h_n(\tau_1, \tau_2,\ldots\tau_n)$ is called the n^{th}-order Volterra kernel or n^{th}-order nonlinear impulse response. Further rearranging (3.9), it is possible to arrive at a rather interesting expression, which reads

$$
\begin{aligned}
y(t) = & \int_{-\infty}^{\infty} h_1(\tau_1)x(t-\tau_1)d\tau_1 \\
& + \int_{-\infty}^{\infty} h_2(\tau_1,\tau_2)x(t-\tau_1)x(t-\tau_2)d\tau_1 d\tau_2 + \ldots \\
& + \int_{-\infty}^{\infty}\int_{-\infty}^{\infty}\ldots\int_{-\infty}^{\infty} h_n(\tau_1,\tau_2,\ldots,\tau_n)x(t-\tau_1)\ldots x(t-\tau_n)d\tau_1 d\tau_2 \ldots d\tau_n
\end{aligned}
\tag{3.10}
$$

which clearly indicates the possibility to model the output response as a function of both instantaneous input and past inputs. However, frequency-domain approach is the preferred choice for analysis and design of microwave circuits, in which case the harmonics and intermodulation products can be obtained from the knowledge of the Fourier transform of Volterra kernels.

3.1.2.1 Nonlinear Current Method

The nonlinear current technique is one of the method adopted to determine the transfer function of a circuit in the Volterra series form [15], [19], [30]. The analysis is carried out by, first, decomposing the system's quasi-linear conductances and capacitances into linear component in parallel combination with nonlinear voltage-controlled current sources as shown in Figure 3.3. This methodology is based on the substitution theorem [28]. The nonlinear current sources are functions of incremental control voltages, which can be expressed as

$$
\begin{aligned}
i_{cond}(v) &= k_{1g}v + k_{2g}v^2 + k_{3g}v^3 + \ldots k_{Ng}v^N \\
&= k_{1g}v + i_{2NLG}(v) + i_{3NLG}(v) + \ldots + i_{nNLG}(v) \\
&= k_{1g}v + i_{NLG}(v)
\end{aligned}
\tag{3.11}
$$

$$
\begin{aligned}
i_{cap}(v) &= \frac{\partial}{\partial t}\left(k_{1c}v + k_{2c}v^2 + k_{3c}v^3 + \ldots k_{Nc}v^N\right) \\
&= j\omega\left(k_{1c}v\right) + i_{2NLC}(v) + i_{3NLC}(v) + \ldots i_{nNLC}(v) \\
&= j\omega\left(k_{1c}v\right) + i_{NLC}(v)
\end{aligned}
\tag{3.12}
$$

where $i_{NLG}(v) = \sum_{n=2}^{N} k_{ng} v^n$ and $i_{NLC}(v) = \frac{\partial}{\partial t}\left(\sum_{n=2}^{N} k_{nc} v^n \right)$ are the incremental current components of nonlinear conductance and capacitance, respectively. In case of frequency-domain analysis, the differentiation of the charge source is replaced by jω. Further, in (3.11) and (3.12), the multiplication in time-domain corresponds to the convolution in frequency-domain. In other words, nonlinear current sources of different orders are determined by convolving voltage spectrums in the frequency-domain [31].

The linear operation is represented by $k_{1g}v$ and $k_{1c}v$ terms. However, the remaining terms denoted by $k_{ng}v^n$ and $k_{nc}v^n$ (n = 2,…N) are the distortion terms, which become significant only at higher signal levels. Subsequently, an analytical expression for the current of the nonlinear element can thus be obtained in an explicit form considering the interaction of different harmonics contributing to a specific frequency.

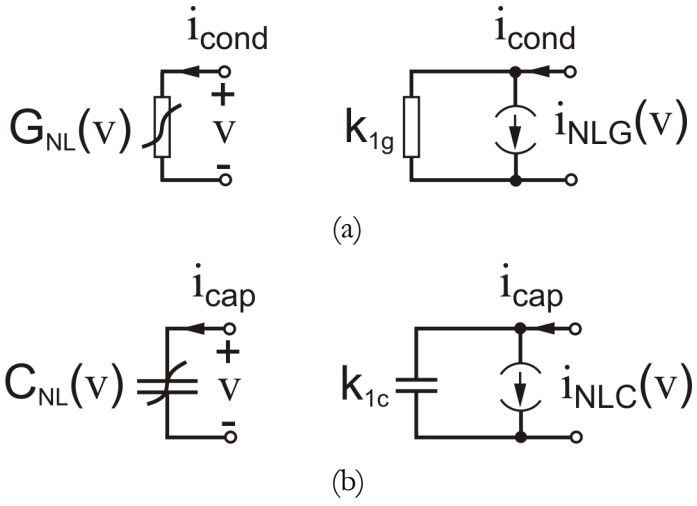

Figure 3.3 Equivalent model representation of quasi-static weakly nonlinear elements based on substitution theorem, (a) conductance, (b) capacitance (after [15], [28]).

Based on the nonlinear current method, the system's n^{th}-order transfer function $H_n(\omega_{p1}, \omega_{p2},\ldots\omega_{pn})$ can eventually be obtained by solving the linear nodal equations of the form

$$Y(\omega) \cdot H_n(\omega) = I_n \tag{3.13}$$

where Y is the nodal-admittance matrix calculated at frequency ω, and I_n is the vector of excitation, which in this case is a current source. For n = 1, external excitation is accounted as a current source, whereas for n > 1 the excitation I_n is calculated from the lower order circuit response. In other words, the higher order current sources are determined by the bias dependent Taylor series coefficients and by the lower order transfer function $H_i(\omega_{p1}, \omega_{p2},\ldots\omega_{pi})$ of orders i = 1,…(n-1).

A rigorous Volterra series approach involves a difficult task of generating Volterra kernels in algebraic form [32]. The analysis becomes very complex, when an arbitrary circuit with many nodes must be evaluated. Hence a simpler approach is to determine the n^{th}-order voltages directly, which is of actual importance, thereby avoiding the calculation of Volterra kernels [19], [31]. The solution lies in replacing H_n in (3.13) directly by n^{th}-order voltages by stimulating the network under n^{th}-order excitation. This approach is called as direct method, which is followed in this thesis. As shown in Figure 3.4, this enables a comprehensive description of IMD3 response of a microwave FET device by directly including relevant mixing products in the nonlinear current expressions.

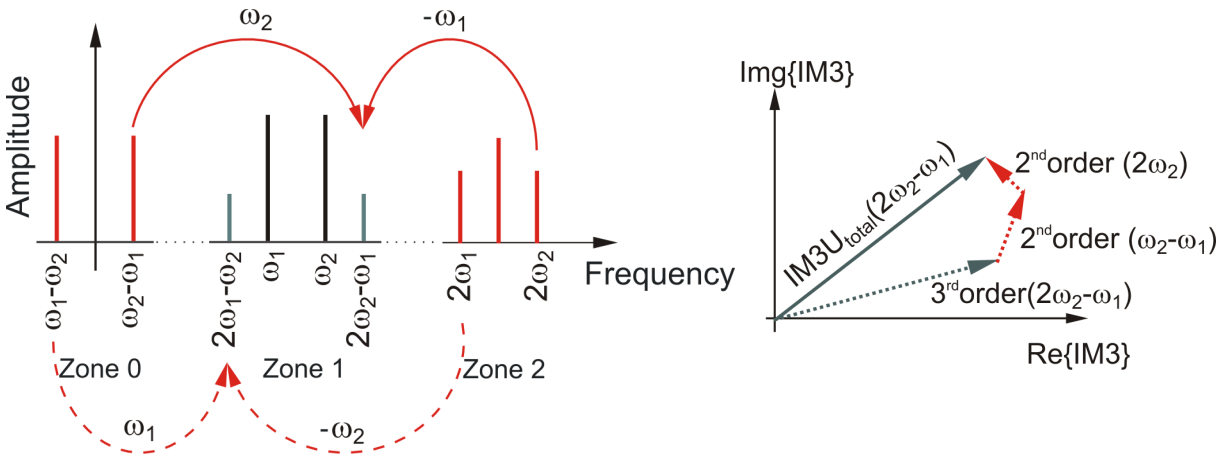

Figure 3.4 Mixing mechanism in IMD3 product.

To summarize, Volterra series technique has the following benefits:

- Volterra series technique adopts a convenient form of polynomial models to describe individual nonlinearities of a system, which is purely behavioural.
- Unlike the harmonic balance approach, Volterra-series analysis is non-iterative since it operates entirely in the frequency-domain.
- Due to the dynamic range limitation inherent in harmonic balance analysis, Volterra series approach is a method of choice for calculating small-signal IMD products [27].

However, the Volterra series technique imposes strong limitation on the input power level when the device leaves its quasi-linear mode of operation. Consequently, there is an increase in the numerical value of the higher order Volterra kernels forcing the series to diverge [30]. This is because of the implementation of truncated Taylor series, which limits the individual nonlinear components in describing their large-signal behaviour. A possible solution could be to simply extend the Taylor series expansion to higher degree. Section 3.6 exemplifies the complexity involved in deriving the IMD3 voltage phasor expressions by extending the Taylor series expansion from 3^{rd} to 5^{th}-degree.

Interestingly, Dimitriev *et al.* [33] has reported that substantial raise of the maximum order of the series does not necessarily guarantee any appreciable increase in the reliability of the calculation over a fixed range of signal swing. Pedro and Carlvalho (p. 132 of [10]) demonstrated this drawback by power series approximation of a node current up to 7^{th}-order, which resulted in an insignificant improvement in the model prediction at large input levels. Dimitriev *et al.* [33] proposed to represent the nonlinear element in the associated circuit by an additional parameter α, which takes into account the dynamic change in the admittance of the nonlinear element from the level of the input signal. Alternately, Krozer *et al.* [34] proposed to use a non-

stationary Volterra kernels, in which the nonlinear component's operating point and the kernels are functions of time. This modified Volterra series approach was implemented to analyse Schottky diode mixer as a nonlinear microwave circuit under large-signal excitation.

Nevertheless, under large-signal operation, harmonic balance complements Volterra series technique by circumventing the limitation of predicting only weak nonlinearities. On top of normal harmonic-balance simulation, Aikio *et al.* [35] used the simulated nonlinear voltage and current spectra of LDMOS for fitting a polynomial device model around the large-signal bias point. Similar approach based on power-dependent Volterra series was followed by Yum *et al.* [22], where table-based nonlinear component values were extracted from simulated multi-bias S-parameters under different RF power levels.

3.2 Quasi-Linear Small-Signal FET Equivalent Circuit Model

It is widely known that in a highly linear active device, nonlinear distortion products of the 3rd-order dominate the circuit's in-band IMD performance. In general, by using the Volterra series method, the nonlinear components are modelled using standard polynomial based Taylor series expansion around the bias point of interest. In other words, a quasi-static description [28] followed in a linear circuit theory assumes that all nonlinear elements change instantaneously with changes in their control voltages, which in turn limits the range of validity.

In this chapter, Volterra series analysis is performed based on the small-signal equivalent circuit of an 8 x 125 μm gate-width AlGaN/GaN HEMT on SiC substrate [N707-4 wafer manufactured by Ferdinand-Braun-Institute for High Frequency Technique (FBH), Germany]. Figure 3.5 shows the small-signal electrical equivalent circuit model of a FET, which reflects the physics of the device over a wide bias and frequency range. Following the conventional

parameter extraction procedure described in [36-38] the extrinsic parameters of the model topology are extracted from S-parameter measurements under cold pinch-off and gate-forward bias conditions. The bias-dependent intrinsic equivalent circuit elements are then de-embedded from multi-bias S-parameter measurement data.

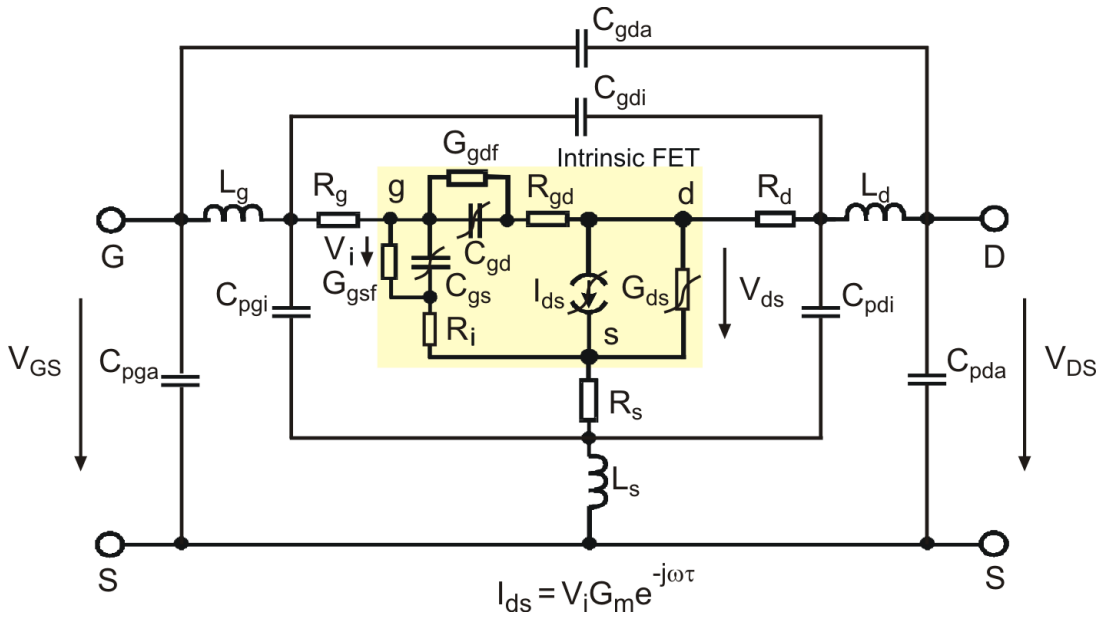

Figure 3.5 Quasi-linear electrical equivalent circuit model of a FET [36].

Under small-signal excitation, the incremental I(V) and C(V) characteristics extracted from RF measurements, are typically modelled on the basis of Taylor series. Multi-bias S-parameter measurements can be performed either by means of frequency swept CW signal or under pulsed conditions. Concerning drain current nonlinearity, there is a fundamental problem in FET devices related to traps causing differences in I(V) characteristics between DC and RF measurements. As a consequence, higher order derivatives of G_m, for instance, are often sensitive to these trapping effects [32]. Pulsed S-parameter characterization, which reflects real operating condition of the FET device, is however preferred in order to control the thermal and trap states while avoiding excessive self-heating [38].

3.2.1 Taylor Series Coefficient Extraction

In FET devices, the intrinsic nonlinearities of the transconductance $G_m(v_{gs}, v_{ds})$, channel conductance $G_{ds}(v_{gs}, v_{ds})$, gate-source capacitance $C_{gs}(v_{gs})$, and also the gate-drain capacitance $C_{gd}(v_{gs}, v_{ds})$, become major sources of IMD. Polynomial curve fitting of these nonlinearities is performed by following the classical Taylor series expansion. As an example, a truncated bi-dimensional power series of I_{ds} model can be represented using Taylor series expansion as follows:

$$\begin{aligned} I_{ds}(v_{gs}, v_{ds}) = {} & I_{ds0} \\ & + \frac{\partial I_{ds}}{\partial V_{gs}} v_{gs} + \frac{1}{2}\frac{\partial^2 I_{ds}}{\partial V_{gs}^2} v_{gs}^2 + \frac{1}{6}\frac{\partial^3 I_{ds}}{\partial V_{gs}^3} v_{gs}^3 \\ & + \frac{\partial I_{ds}}{\partial V_{ds}} v_{ds} + \frac{1}{2}\frac{\partial^2 I_{ds}}{\partial V_{ds}^2} v_{ds}^2 + \frac{1}{6}\frac{\partial^3 I_{ds}}{\partial V_{ds}^3} v_{ds}^3 \\ & + \frac{\partial^2 I_{ds}}{\partial V_{gs}\partial V_{ds}} v_{gs} v_{ds} + \frac{1}{2}\frac{\partial^3 I_{ds}}{\partial V_{gs}^2 \partial V_{ds}} v_{gs}^2 v_{ds} + \frac{1}{2}\frac{\partial^3 I_{ds}}{\partial V_{ds}^2 \partial V_{gs}} v_{ds}^2 v_{gs} \end{aligned} \tag{3.14}$$

where $v_{gs} = V_{gs} - V_{gs0}$ and $v_{ds} = V_{ds} - V_{ds0}$ are the deviations of V_{gs} and V_{ds} around V_{gs0} and V_{ds0} intrinsic bias voltages, respectively, with I_{ds0} denoting the DC component of the drain current [18], [28].

3.2.1.1 Modelling Conductance Nonlinearity

As a 1st-order linear approach, the intrinsic incremental drain-source current I_{ds} dependence on v_{gs} can be represented by k_{1gm} transconductance and the dependence on v_{ds} by k_{1gds} as output conductance. However, the distortion calculations are carried out by incorporating 3rd-degree polynomials describing mild nonlinearity. By confining the analysis to small-signal regime, the dual voltage controlled incremental intrinsic drain current is expressed as

$$
\begin{aligned}
I_{ds}(v_{gs}, v_{ds}) = I_{DC} &+ k_{1gm} v_{gs} + k_{2gm} v_{gs}^{\,2} + k_{3gm} v_{gs}^{\,3} \\
&+ k_{1ds} v_{ds} + k_{2ds} v_{ds}^{\,2} + k_{3ds} v_{ds}^{\,3} \\
&+ k_{2gmgds} v_{gs} v_{ds} + k_{3gm2gds} v_{gs}^{\,2} v_{ds} + k_{3gmgds2} v_{gs} v_{ds}^{\,2}
\end{aligned}
\tag{3.15}
$$

which yields

$$
\begin{aligned}
G_m(v_{gs}, v_{ds}) = \frac{\partial I_{ds}}{\partial v_{gs}} &= k_{1gm} + 2 \cdot k_{2gm} v_{gs} + 3 \cdot k_{3gm} v_{gs}^{\,2} \\
&+ k_{2gmgds} v_{ds} + 2 \cdot k_{3gm2gds} v_{gs} v_{ds} + k_{3gmgds2} v_{ds}^{\,2}
\end{aligned}
\tag{3.16}
$$

and

$$
\begin{aligned}
G_{ds}(v_{gs}, v_{ds}) = \frac{\partial I_{ds}}{\partial v_{ds}} &= k_{1gds} + 2 \cdot k_{2gds} v_{ds} + 3 \cdot k_{3gds} v_{ds}^{\,2} \\
&+ k_{2gmgds} v_{gs} + k_{3gm2gds} v_{gs}^{\,2} + 2 \cdot k_{3gmgds2} v_{gs} v_{ds}
\end{aligned}
\tag{3.17}
$$

where the coefficients correspond to the respective derivatives of (3.14). k_{2gmgds} and $k_{3gm2gds}$ represent the first and second order nonlinear dependence of G_{ds} on v_{gs}. Likewise, k_{2gmgds} and $k_{3gmgds2}$ represent the first and second order nonlinear dependence of G_m on v_{ds}. These terms are typically referred to as cross-terms [15], [18], [28]. It is important to note that the literatures commonly adopt the notations g_m and g_{ds} to describe the linear coefficients k_{1gm} and k_{1gds}, respectively.

Distortions are largely attributed to the dynamic variations of the current waveform over the device loadline. When following the Volterra series approach, the polynomial model of a nonlinear intrinsic FET element is locally fitted around a desired bias point. Consequently, the model becomes applicable only over a certain amplitude range. In this case, choosing a correct fitting range as a function of v_{gs} and v_{ds} coupled with a proper distribution of the data points are equally important in extracting meaningful Taylor series coefficients. Figure 3.6 shows a pulsed I(V) characteristics of a 2 x 250 µm GaN HEMT [manufactured by Fraunhofer Institute for Applied Solid-State Physics (IAF), Freiburg] measured using DiVA 265EP from V_{GS0} = -2.5V and

V_{DS0} = 15V with 1 μs pulse width and at 1 ms pulse repetition period. The rectangular box superimposed onto a pulsed I(V) characteristics, fulfils both the above mentioned conditions, for instance, when treating a two-dimensional nonlinearity such as $I_{ds}(v_{gs}, v_{ds})$ [15]. The diagonal of the rectangular box reflects the slope of an RF loadline describing the ratio between the voltage and the current swing.

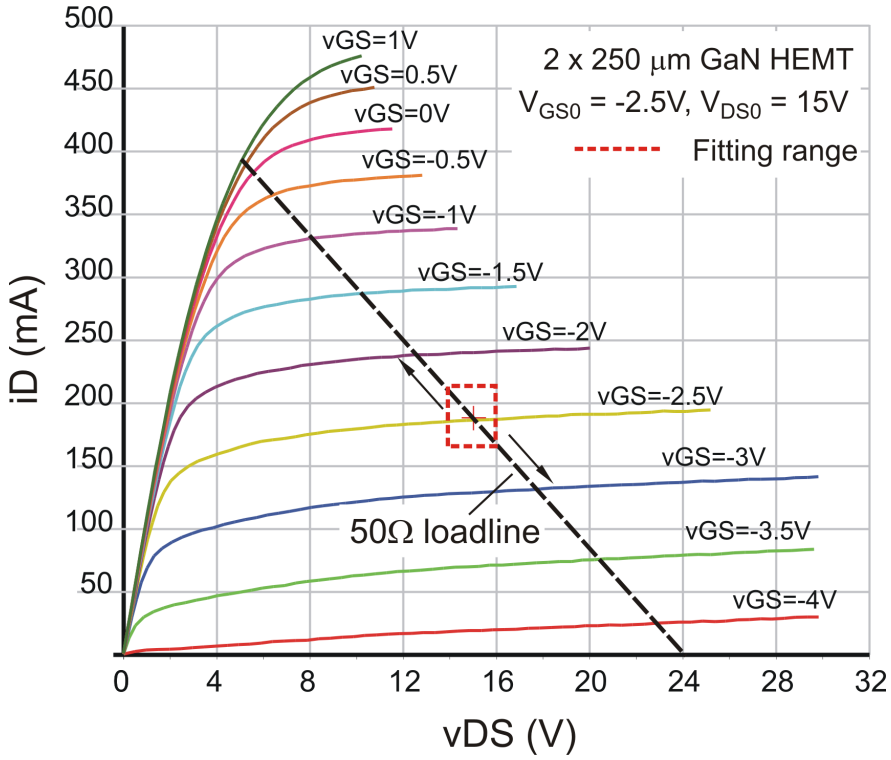

Figure 3.6 2 x 250 μm GaN HEMT pulsed-DC measurement depicting the fitting range enclosed by a box for extracting Taylor series coefficients. Quiescent bias of V_{GS0} = -2.5V and V_{DS0} = 15V with 1 μs pulse width and at 1 ms pulse repetition frequency.

The bias points were considered over a rectangular region for 7 V_{GS0} voltages and 10 V_{DS0} voltages with step-size of 0.2V resulting in a bias point grid of 7 x 10. In general, the unknown Taylor series coefficients of (3.15) are solved from N number of bias points measured on the I(V) characteristics.

Let the scalar matrix of the incremental drain current be represented as

$$I_{ds} = \begin{bmatrix} I_{ds1} & I_{ds2} & \cdots & I_{dsN} \end{bmatrix}^T \tag{3.18}$$

The corresponding incremental voltage matrix reads

$$v=\begin{bmatrix} 1 & v_{gs1} & v_{gs1}^{2} & v_{gs1}^{3} & v_{ds1} & v_{ds1}^{2} & v_{ds1}^{3} & v_{gs1}v_{ds1} & v_{gs1}^{2}v_{ds1} & v_{gs1}v_{ds1}^{2} \\ 1 & v_{gs2} & \cdots & & & & & & & \\ \vdots & \vdots & \vdots & \vdots & \vdots & \vdots & \vdots & \vdots & \vdots & \vdots \\ 1 & v_{gsN} & \cdots & & & & & & & v_{gsN}v_{dsN}^{2} \end{bmatrix} \tag{3.19}$$

The unknown Taylor series coefficients to be determined are represent as

$$K=\begin{bmatrix} I_{DC} & k_{1gm} & k_{2gm} & k_{3gm} & k_{1gds} & k_{2gds} & k_{3gds} & k_{2gmgds} & k_{3gm2gds} & k_{3gmgds2} \end{bmatrix}^{T} \tag{3.20}$$

Thus, the 10 unknown coefficients are solved by simple matrix equation read as

$$[I_{ds}]=[v]\cdot[K] \tag{3.21}$$

Thus [K] can be computed as

$$[K]=[v]^{-1}\cdot[I_{ds}] \tag{3.22}$$

In order to solve 10 unknowns parameters in (3.14), a minimum of N = 10 measurement points are essential, which are spread around the bias point of interest. However, accuracy can be enhanced by considering more than 10 data points, in which case, the unknown coefficients [K] can be solved by adopting least mean square error (LMSE [15], [19]) fitting expressed as

$$[K]=\left([v]^{T}\cdot[v]\right)^{-1}\cdot\left([v]^{T}\cdot[I_{ds}]\right) \tag{3.23}$$

Figure 3.7 shows polynomial fitting results of G_m and G_{ds} expressed in (3.16) and (3.17), respectively, extracted from an 8 x 125 μm GaN HEMT, for five gate voltages. Such excellent fitting hence offer reliable Taylor series coefficients as input for Volterra technique based intermodulation distortion prediction. Corresponding Taylor series coefficients are tabulated in Table 3.1.

Although, it is apparent from Table 3.1 that the cross-terms are usually much smaller than the terms involving v_{gs}; they are still significant compared to those involving v_{ds}. In the saturation region of I(V) characteristics, where the device operation is of actual interest, G_{ds} nonlinearity, in general, or the terms involving v_{ds}, in particular, rarely dominate. In other words, I_{ds} can be regarded mainly as a function of v_{gs}, presenting a residual dependence on v_{ds}. Nevertheless, for the completeness of the analysis, these parameters should not be neglected.

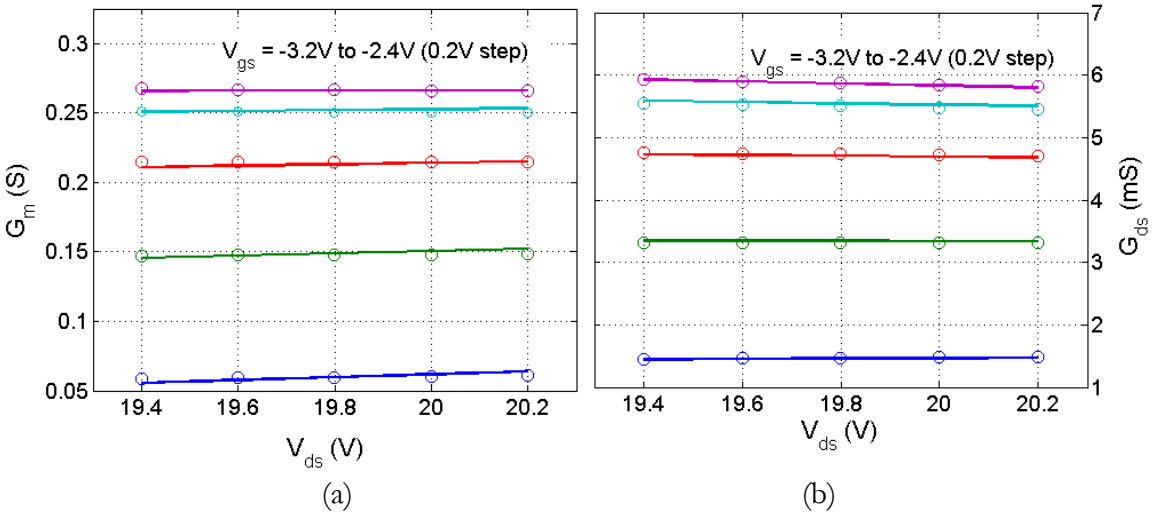

Figure 3.7 Comparison of measured (symbol) and modelled (line) bias dependent (a) intrinsic G_m and (b) intrinsic G_{ds} characteristics of the analysed 1-mm GaN HEMT around V_{gs0} = -2.8V and V_{ds0} = 19.8V quiescent point.

Table 3.1 Extracted Taylor series coefficients of incremental drain-source current I_{ds} nonlinearity for the analysed 1-mm GaN HEMT around V_{gs0} = -2.8V and V_{ds0} = 19.8V quiescent point..

	1st-deg.	2nd-deg	3rd-deg.
G_m	k_{1gm}	k_{2gm}	k_{3gm}
	0.2130	0.1290	-0.1044
G_{ds}	k_{1gds}	k_{2gds}	k_{3gds}
	0.0047	-0.00003	0.0
Cross-terms	k_{2gmgds}	$k_{3gm2gds}$	$k_{3gmgds2}$
	0.0055	-0.0065	-0.0001

3.2.1.2 Modelling Capacitance Nonlinearity

The gate-source capacitance C_{gs} and gate-drain capacitance C_{gd} of the FET small-signal equivalent circuit account for the main source of capacitive nonlinearity. Any change in V_{gs0} and V_{ds0} (or $V_{gd0}= V_{gs0}-V_{ds0}$) involves a change in the shape of the gate depletion region. The nonlinear capacitances C_{gs} and C_{gd} are derived from the associated gate depletion charge Q_g, which is composed of gate-source charge Q_{gs} and gate-drain charge Q_{gd} [28]. Since the capacitance surfaces are extracted from the S-parameter measurement, the Taylor series coefficients are determined directly from the C(V) curves. In the saturation region of operation, C_{gs} is predominantly dependent on only v_{gs}. Therefore it can be represented, with reasonable accuracy, by a one-dimensional Taylor series expansion of the input control voltage. The expression for the gate-source charge reads

$$Q_{gs}(v_{gs}) = k_{1cgs} \cdot v_{gs} + k_{2cgs} \cdot v_{gs}^{\,2} + k_{3cgs} \cdot v_{gs}^{\,3} \tag{3.24}$$

which yields

$$C_{gs}(v_{gs}) = \frac{\partial Q_{gs}}{\partial v_{gs}} = k_{1cgs} + 2 \cdot k_{2cgs} \cdot v_{gs} + 3 \cdot k_{3cgs} \cdot v_{gs}^{\,2} \tag{3.25}$$

In contrast, C_{gd} is modelled with a two-dimensional polynomial as a function of v_{gd} and v_{gs} incremental control voltages. The expression for gate-drain charge reads

$$\begin{aligned} Q_{gd}(v_{gd}, v_{gs}) = {} & k_{1cgd} \cdot v_{gd} + k_{2cgd} \cdot v_{gd}^{\,2} + k_{3cgd} \cdot v_{gd}^{\,3} \\ & + k_{1cgs} \cdot v_{gs} + k_{2cgs} \cdot v_{gs}^{\,2} + k_{3cgs} \cdot v_{gs}^{\,3} \\ & + k_{2cgdgs} \cdot v_{gs} \cdot v_{gd} + k_{3cgd2gs} \cdot v_{gd}^{\,2} \cdot v_{gs} + k_{3cgdgs2} \cdot v_{gs}^{\,2} \cdot v_{gd} \end{aligned} \tag{3.26}$$

which yields

$$\begin{aligned} C_{gd}(v_{gd}, v_{gs}) = \frac{\partial Q_{gd}}{\partial v_{gd}} = {} & k_{1cgd} + 2 \cdot k_{2cgd} \cdot v_{gd} + 3 \cdot k_{3cgd} \cdot v_{gd}^{\,2} \\ & + k_{2cgdgs} \cdot v_{gs} + 2 \cdot k_{3cgd2gs} \cdot v_{gd} \cdot v_{gs} + k_{3cgdgs2} \cdot v_{gs}^{\,2} \end{aligned} \tag{3.27}$$

The unknown coefficients of (3.24) and (3.26) are determined using least mean square error fitting similar to (3.22) expressed in the form

$$\begin{bmatrix} C_{gs1} \\ C_{gs2} \\ \vdots \\ C_{gsN} \end{bmatrix} = \begin{bmatrix} 1 & 2 \cdot v_{gs1} & 3 \cdot v_{gs1}^{\,2} \\ 1 & 2 \cdot v_{gs2} & 3 \cdot v_{gs2}^{\,2} \\ \vdots & \vdots & \vdots \\ 1 & 2 \cdot v_{gsN} & 3 \cdot v_{gsN}^{\,2} \end{bmatrix} \cdot \begin{bmatrix} k_{1cgs} \\ k_{2cgs} \\ k_{3cgs} \end{bmatrix} \tag{3.28}$$

which can be rewritten as

$$[C_{gs}] = [v] \cdot [K] \tag{3.29}$$

The unknown coefficient matrix [K] of the C_{gs} polynomial can be hence determined as

$$[K] = \left([v]^T \cdot [v] \right)^{-1} \cdot \left([v]^T \cdot [C_{gs}] \right) \tag{3.30}$$

Figure 3.8 shows the polynomial curve fitting of C_{gs} and C_{gd} curves, and their corresponding Taylor series are tabulated in Table 3.2.

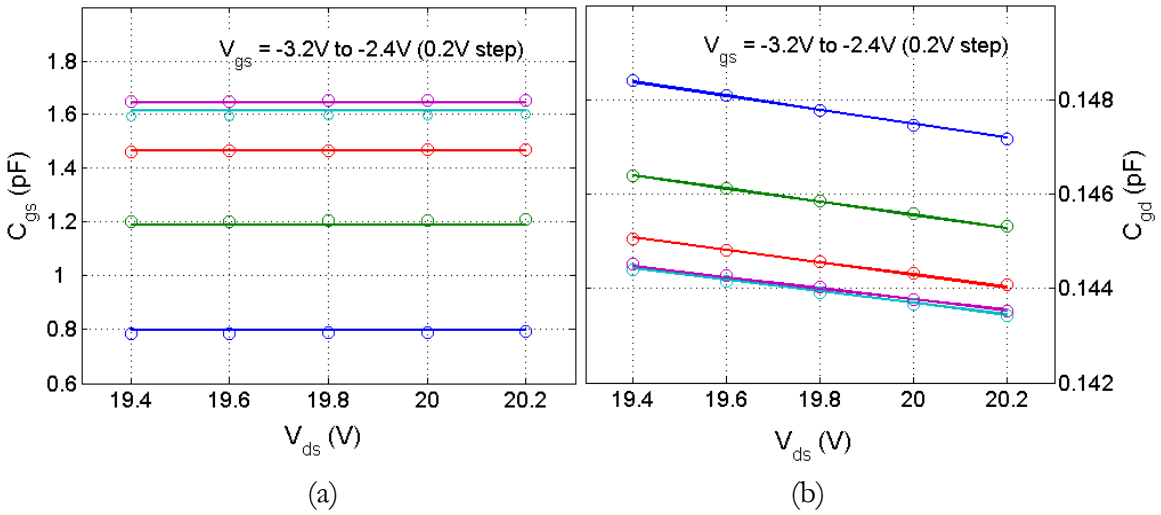

Figure 3.8 Comparison of measured (symbol) and modelled (line) bias dependent (a) intrinsic C_{gs} and (b) intrinsic C_{gd} characteristics of the analysed 1-mm GaN HEMT around V_{gs0} = -2.8V and V_{ds0} = 19.8V quiescent point.

Table 3.2 Extracted Taylor series coefficients of gate-source C_{gs} and gate-drain capacitance C_{gd} nonlinearity for the analysed 1-mm GaN HEMT around V_{gs0} = -2.8V and V_{ds0} = 19.8V quiescent point.

	1st-deg. (pF)	2nd-deg. (pF/V)	3rd-deg. (pF/V²)
C_{gs}	k_{1cgs}	k_{2cgs}	k_{3cgs}
	0.2710	-0.0002	-0.0171
C_{gd}	k_{1cgd}	k_{2cgd}	k_{3cgd}
	0.1464	-0.0016	0.0
Cross-terms	k_{2cgdgs}	$k_{3cgd2gs}$	$k_{3cgdgs2}$
	-0.0151	0.0005	0.0220

3.3 IMD Modelling

With the extracted Taylor series coefficients, the next step is to derive higher order current sources and their corresponding voltage components at each node of FET equivalent circuit. The nonlinear nodal equations of the FET equivalent circuit model are successively solved using the same linearized circuit by first determining the lower order nodal voltages. The 1st-order linearized circuit is analysed with the external excitation applied. For higher order circuit response, the same linearized circuit is analysed with the excitations from higher-order voltage-controlled current sources computed from the lower order circuit analysis. As briefly introduced in Section 3.1.2.1, applying nonlinear current method, 2nd-order and 3rd-order voltage-controlled current expressions are determined at relevant frequencies, whose parameters are higher-order Taylor series extracted coefficients. The 3rd-order IMD (at $2\omega_1-\omega_2$ or $2\omega_2-\omega_1$) at the drain node can then be derived step-wise as follows:

(i) First, the fundamental node voltages $v_1(\omega) = [v_g(\omega) \quad v_d(\omega) \quad v_s(\omega)]^T$ are evaluated using linear ac analysis.

(ii) Nonlinear analysis starts with the evaluation of 2nd-order distortion currents $i_{NL2}[v_1(\omega)]$ using 1st-order fundamental voltage amplitudes

across each intrinsic nonlinear elements. The relevant frequencies of interest are envelope ($\omega_{1,2}$ - $\omega_{2,1}$) and 2nd-harmonic ($2\omega_{1,2}$).

(iii) The 2nd-order distortion currents are further transformed to 2nd-order distortion voltages $v_2(\omega)$ at each node through transimpedance transfer functions.

(iv) With the 1st and 2nd-order voltages, 3rd-order distortion currents $i_{NL3}[v_1(\omega), v_2(\omega)]$ at $2\omega_1$-ω_2 and/or $2\omega_2$-ω_1 are calculated across each intrinsic nonlinear element.

(v) Finally all the 3rd-order distortion current sources from all the three nodes are transformed to 3rd-order voltage across the load (drain terminal) to obtain the final IMD3 response.

Eventually the analysis would result in a vectorial sum of 3rd-order (cubic) and 2nd-order mixing components (envelope and 2nd-harmonic) to produce the total IMD3.

3.3.1 1st-order Volterra Kernel

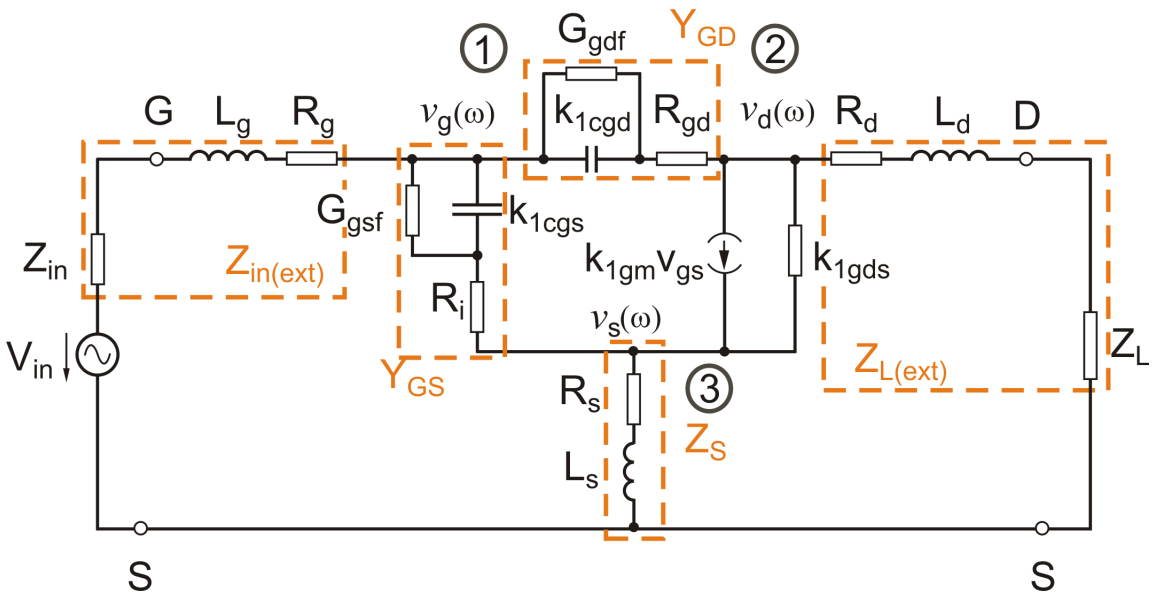

Figure 3.9 Bias dependent linearized 1st-order equivalent circuit of the analysed 1-mm GaN HEMT.

In this step, each intrinsic nonlinearity is replaced by its linearized equivalent as shown in Figure 3.9. The intension of linear analysis is to obtain the fundamental voltage amplitudes $v_1(\omega_{1,2})$ at nodes 1-3 depicted in Figure 3.9. By defining an input two-tone signal with signal amplitude of V_{in} at fundamental frequencies ω_1 and ω_2, Kirchhoff's current law is applied on the linear network. The 1st-order node voltages $v_g(\omega)$, $v_d(\omega)$, $v_s(\omega)$ at nodes 1, 2 and 3, respectively, are determined using Cramer's rule which reads

$$\begin{bmatrix} I_{in} \\ 0 \\ 0 \end{bmatrix} = \begin{bmatrix} Y_{in}+Y_{GS}+Y_{GD} & -Y_{GD} & -Y_{GS} \\ k_{1gm}-Y_{GD} & k_{1gds}+Y_{GD}+Y_L & -k_{1gm}-k_{1gds} \\ -k_{1gm}-Y_{GS} & -k_{1gds} & Y_{GS}+k_{1gds}+Y_S+k_{1gm} \end{bmatrix} \cdot \begin{bmatrix} v_g \\ v_d \\ v_s \end{bmatrix} \tag{3.31}$$

assuming $Z_{L(ext)} \approx Z_L$, $Z_{in(ext)} \approx Z_{in}$, and $I_{in} = Y_{in} \cdot V_{in}$. The nodal voltages $v_g(\omega)$, $v_d(\omega)$, and $v_s(\omega)$ reduce to linear transfer functions H_{1g}, H_{1d}, and H_{1s} when V_{in} is unity. In other words, the matrix expression (3.31) can be rewritten in the form of (3.13) as

$$\begin{bmatrix} Y_{in} \\ 0 \\ 0 \end{bmatrix} = \begin{bmatrix} Y_{in}+Y_{GS}+Y_{GD} & -Y_{GD} & -Y_{GS} \\ k_{1gm}-Y_{GD} & k_{1gds}+Y_{GD}+Y_L & -k_{1gm}-k_{1gds} \\ -k_{1gm}-Y_{GS} & -k_{1gds} & Y_{GS}+k_{1gds}+Y_S+k_{1gm} \end{bmatrix} \cdot \begin{bmatrix} H_{1g}(\omega) \\ H_{1d}(\omega) \\ H_{1s}(\omega) \end{bmatrix} \tag{3.32}$$

However, in this work, the nodal voltages are directly calculated avoiding the need to determine the transfer function or the Volterra kernel H_n.

3.3.2 2nd-order Volterra Kernel

The 2nd-order Volterra kernel is determined by first setting the external excitation of the linearized equivalent circuit to zero (short-circuiting the voltage source $V_{in} = 0$) as shown in Figure 3.10. The circuit is now excited by 2nd-order voltage-controlled current sources $i_{2NL}(\omega)$, which are in parallel

with the linearized circuit elements and are functions of 1st-order Volterra kernel. The 2nd-order current expressions for the conductance and capacitance nonlinearity at the envelope (ω_2-ω_1) and 2nd-harmonic ($2\omega_2$) frequencies, contributing to the final upper-IMD3, are listed in Table 3.3.

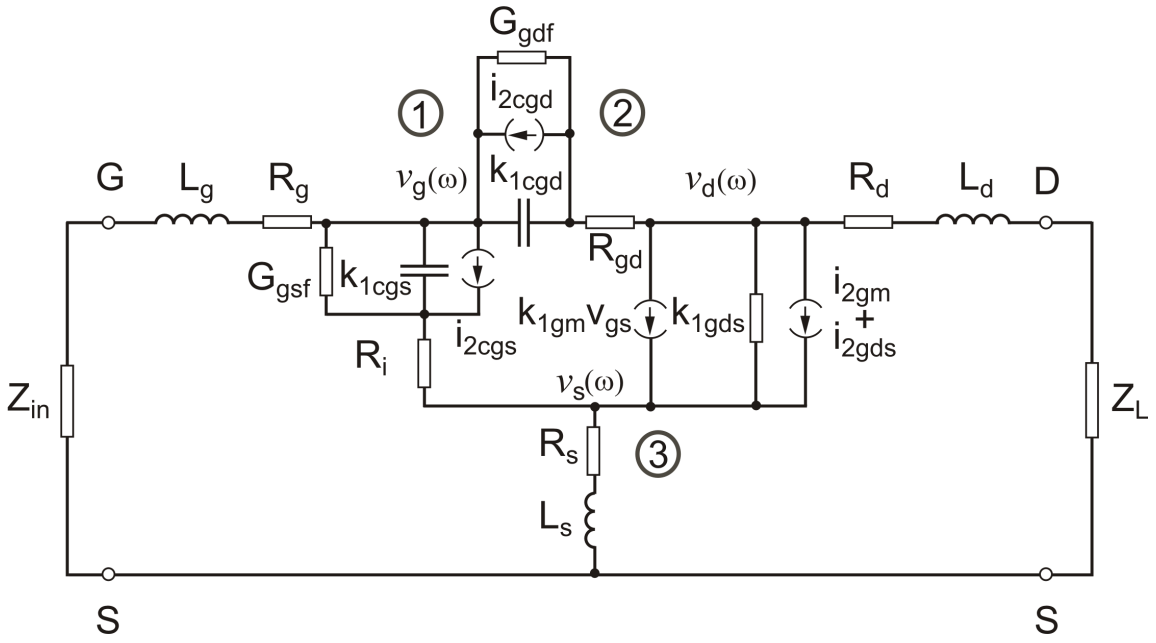

Figure 3.10 2nd-order linearized equivalent circuit of the analysed 1-mm GaN HEMT with 2nd-order current sources (i_{2NL}).

Table 3.3 2nd-order nonlinear current sources $i_{2NL}(\omega)$ under 2-tone excitation contributing towards upper-IMD3 at $2\omega_2$-ω_1 [15], [19].

Nonlinearity	$i_{2NL}(\omega_2-\omega_1)$	$i_{2NL}(2\omega_2)$
Transconductance	$k_{2\,gm}\cdot v_{gs}(\omega_2)\cdot v_{gs}(-\omega_1)$	$\frac{1}{2}\cdot k_{2\,gm}\cdot v_{gs}(\omega_2)^2$
Channel conductance	$k_{2\,gds}\cdot v_{ds}(\omega_2)\cdot v_{ds}(-\omega_1)$	$\frac{1}{2}\cdot k_{2\,gds}\cdot v_{ds}(\omega_2)^2$
Capacitor	$j(\omega_2-\omega_1)\cdot k_{2cgs(cgd)}\cdot v_{gs(gd)}(\omega_2)\cdot v_{gs(gd)}(-\omega_1)$	$\frac{j2\omega_2}{2}\cdot k_{2cgs(cgd)}\cdot v_{gs(ds)}(\omega_2)^2$
Conductance cross-terms	$\frac{1}{2}k_{2\,gmgds}\left[\begin{matrix}v_{gs}(\omega_2)\cdot v_{ds}(-\omega_1)\\+v_{gs}(-\omega_1)\cdot v_{ds}(\omega_2)\end{matrix}\right]$	$\frac{1}{2}\cdot k_{2\,gmgds}\cdot v_{gs}(\omega_2)\cdot v_{ds}(\omega_2)$
Capacitance cross-terms	$\frac{j(\omega_2-\omega_1)}{2}k_{2cgdgs}\left[\begin{matrix}v_{gd}(\omega_2)\cdot v_{gs}(-\omega_1)\\+v_{gs}(-\omega_1)\cdot v_{gd}(\omega_2)\end{matrix}\right]$	$\frac{j2\omega_2}{2}\cdot k_{2cgdgs}\cdot v_{gd}(\omega_2)\cdot v_{gs}(\omega_2)$

Since G_m, G_{ds} and C_{gd} are 2-dimensional functions of v_{gs} and v_{ds} (or v_{gd}), the corresponding 2nd-order distortion currents should also additionally incorporate expressions with cross-terms. It is clearly seen from Table 3.3 that the current sources are functions of bias-dependent 2nd-order Taylor series coefficients (k_{2gm}, k_{2gds}, k_{2gmgds}, k_{2cgs}, k_{2cgd}, k_{2cgdgs}) and the fundamental 1st-order voltages (v_{gs}, v_{ds}) determined from (3.31), where $v_{gs} = v_g - v_s$ and $v_{ds} = v_d - v_s$. Moreover, every 2nd-order nonlinearity in the circuit combines two 1st-order components of the controlling voltages to produce the 2nd-order signal.

An example is considered to show how a 2nd-order nonlinearity in a FET equivalent circuit contributes to the 2nd-harmonic at the output terminal. Using Table 3.3, the 2nd-harmonic current sources of gate-source capacitance nonlinearity and transconductance nonlinearity can be expressed as

$$i_{NL2cgs}(2\omega_2) = j\omega_2 k_{2cgs} v_{gs}(\omega_2)^2 \tag{3.33}$$

$$i_{NL2gm}(2\omega_2) = \frac{1}{2}\left[k_{2gm} v_{gs}(\omega_2)^2 + k_{2gmgds} v_{gs}(\omega_2) v_{ds}(\omega_2) \right] \tag{3.34}$$

The calculated 2nd-order current sources are converted to the voltage phasor at all the three nodes with the help of transimpedance transfer function [15], [19]. The transfer function TF_{XYZ} denotes the transformation of the current source i_{XY} across nodes X and Y to the voltage vector v_Z at node Z. These transfer functions are determined by short (open)-circuiting 1st-order linear voltage (current) sources. The transfer function can be derived from (3.31) by replacing i_{in} with a test current i_{XY} between nodes X and Y. With i_{XY} as the excitation signal at relevant frequencies, Kirchhoff's current law is applied on the linearized circuit at nodes 1, 2 and 3. The transimpedance transfer functions are hence determined using Cramer's rule (3.31).

The transfer functions essential for converting higher order current sources across respective branches to the gate, drain and source nodal voltages are

expressed as

$$TF_{GSG}(\omega)=\frac{v_g}{i_{gs}}$$

$$=-\left[Y_S\cdot Y_L+Y_{ds}\cdot Y_S+Y_{ds}\cdot Y_L+k_{1gm}\cdot Y_L+j\omega\cdot k_{1cgd}\cdot Y_S\right]\cdot\frac{1}{\det(\omega)} \quad (3.35)$$

$$TF_{GSS}(\omega)=\frac{v_s}{i_{gs}}$$

$$=\left[Y_{in}\cdot Y_L+Y_{ds}\cdot Y_{in}-k_{1gm}\cdot Y_L+j\omega\cdot k_{1cgd}\cdot\left(Y_L+Y_{in}\right)\right]\cdot\frac{1}{\det(\omega)} \quad (3.36)$$

$$TF_{GSD}(\omega)=\frac{v_d}{i_{gs}}$$

$$=\left[Y_{ds}\cdot Y_{in}+k_{1gm}\cdot Y_{in}+k_{1gm}\cdot Y_S-j\omega\cdot k_{1cgd}\cdot Y_S\right]\cdot\frac{1}{\det(\omega)} \quad (3.37)$$

$$TF_{DSG}(\omega)=\frac{v_g}{i_{ds}}$$

$$=\left[Y_{GS}\cdot Y_L+j\omega\cdot k_{1cgd}\cdot Y_S\right]\cdot\frac{1}{\det(\omega)} \quad (3.38)$$

$$TF_{DSS}(\omega)=\frac{v_s}{i_{ds}}$$

$$=\left[Y_{in}\cdot Y_L+Y_{GS}\cdot Y_L+j\omega\cdot k_{1cgd}\cdot\left(Y_{in}+Y_L\right)\right]\cdot\frac{1}{\det(\omega)} \quad (3.39)$$

$$TF_{DSD}(\omega)=\frac{v_d}{i_{ds}}$$

$$=-\left[Y_{in}\cdot Y_S\cdot+Y_{GS}\cdot Y_{in}+Y_{GS}\cdot Y_S+j\omega\cdot k_{1cgd}\cdot Y_S\right]\cdot\frac{1}{\det(\omega)} \quad (3.40)$$

$$TF_{GDG}(\omega)=TF_{DSG}(\omega)-TF_{GSG}(\omega) \quad (3.41)$$

$$TF_{GDS}(\omega)=TF_{DSS}(\omega)-TF_{GSS}(\omega) \quad (3.42)$$

$$TF_{GDD}(\omega)=TF_{DSD}(\omega)-TF_{GSD}(\omega) \quad (3.43)$$

where

$$\begin{aligned}\det(\omega) = \Big[& Y_{GS} \cdot Y_{ds} \left(Y_L + Y_S + Y_{in} \right) + Y_{in} \cdot Y_L \left(Y_{GS} + Y_{ds} + k_{1gm} + Y_S \right) + Y_{ds} \cdot Y_S \cdot Y_{in} \\ & + Y_{GS} \cdot Y_L \cdot Y_S + Y_{GD} \left(Y_{GS} \cdot Y_{in} + Y_{ds} \cdot Y_{in} + Y_S \cdot Y_{in} + Y_{GS} \cdot Y_S + Y_{GS} \cdot Y_L \right. \\ & \left. + Y_{ds} \cdot Y_L + Y_S \cdot Y_L + Y_{ds} \cdot Y_S + k_{1gm} \cdot Y_L + k_{1gm} \cdot Y_{in} + k_{1gm} \cdot Y_S \right) \Big]\end{aligned} \tag{3.44}$$

When calculating the difference between two nodal voltages Z and W, the below presented formulation of the transimpedance transfer function is adopted [15].

$$TF_{XYZW}(\omega) = TF_{XYZ}(\omega) - TF_{XYW}(\omega) \tag{3.45}$$

TF_{XYZW} denotes the transformation of the current source i_{XY} across nodes X and Y to the voltage vector v_{ZW} across the nodes Z and W. Taking into account the nonlinearities across all circuit branches indicated in Figure 3.10, the 2nd-order nodal voltages can be expressed as

$$\begin{aligned}v_{2g}(\omega) = & TF_{GSG}(\omega) \cdot \left[i_{NL2cgs} \right] + TF_{DSG}(\omega) \cdot \left[i_{NL2gm} + i_{NL2gds} \right] \\ & + TF_{GDG}(\omega) \cdot \left[i_{NL2cgd} \right]\end{aligned} \tag{3.46}$$

$$\begin{aligned}v_{2d}(\omega) = & TF_{GSD}(\omega) \cdot \left[i_{NL2cgs} \right] + TF_{DSD}(\omega) \cdot \left[i_{NL2gm} + i_{NL2gds} \right] \\ & + TF_{GDD}(\omega) \cdot \left[i_{NL2cgd} \right]\end{aligned} \tag{3.47}$$

$$\begin{aligned}v_{2s}(\omega) = & TF_{GSS}(\omega) \cdot \left[i_{NL2cgs} \right] + TF_{DSS}(\omega) \cdot \left[i_{NL2gm} + i_{NL2gds} \right] \\ & + TF_{GDS}(\omega) \cdot \left[i_{NL2cgd} \right]\end{aligned} \tag{3.48}$$

where $\omega = 2\omega_{1,2}$ (2nd-harmonic) or $\omega_{1,2} - \omega_{2,1}$ (envelope). By substituting the expressions for the current sources from Table 3.3 into (3.46) - (3.48), the 2nd-order voltage vectors $v_{gs}(\omega)$, $v_{ds}(\omega)$ and $v_{gd}(\omega)$ at envelope and 2nd-harmonic can be derived as

$$
\begin{aligned}
v_{gs}(\omega_2-\omega_1) &= v_g(\omega_2-\omega_1)-v_s(\omega_2-\omega_1)\\
&= TF_{GSGS}(\omega_2-\omega_1)\cdot\left[j(\omega_1-\omega_2)\cdot k_{2cgs}\cdot v_{gs}(\omega_1)\cdot v_{gs}(-\omega_2)\right]+\\
&\quad TF_{DSGS}(\omega_2-\omega_1)\cdot\left\{k_{2gm}\cdot v_{gs}(\omega_1)\cdot v_{gs}(-\omega_2)+k_{2gds}\cdot v_{ds}(\omega_1)\cdot v_{ds}(-\omega_2)\right.\\
&\quad \left.+k_{2gmgds}\left[v_{gs}(\omega_2)\cdot v_{ds}(-\omega_1)+v_{gs}(-\omega_1)\cdot v_{ds}(\omega_2)\right]\right\}+TF_{GDGS}(\omega_2-\omega_1)\\
&\quad \left\{j(\omega_1-\omega_2)\cdot k_{2cgd}\cdot v_{gd}(\omega_1)\cdot v_{gd}(-\omega_2)+\frac{j(\omega_1-\omega_2)}{2}\cdot k_{2cgdcgs}\right.\\
&\quad \left.\cdot\left[v_{gd}(\omega_1)\cdot v_{gs}(-\omega_2)+v_{gd}(-\omega_2)\cdot v_{gs}(\omega_1)\right]\right\}
\end{aligned}
\tag{3.49}
$$

$$
\begin{aligned}
v_{ds}(\omega_2-\omega_1) &= v_d(\omega_2-\omega_1)-v_s(\omega_2-\omega_1)\\
&= TF_{GSDS}(\omega_2-\omega_1)\cdot\left[j(\omega_1-\omega_2)\cdot k_{2cgs}\cdot v_{gs}(\omega_2)\cdot v_{gs}(-\omega_1)\right.\\
&\quad +TF_{DSDS}(\omega_2-\omega_1)\left\{k_{2gm}\cdot v_{gs}(\omega_2)\cdot v_{gs}(-\omega_1)+k_{2gds}\cdot v_{ds}(\omega_2)\cdot v_{ds}(-\omega_1)\right.\\
&\quad \left.+k_{2gmds}\left[v_{gs}(\omega_2)\cdot v_{ds}(-\omega_1)+v_{gs}(-\omega_1)\cdot v_{ds}(\omega_2)\right]\right\}+TF_{GDDS}(\omega_2-\omega_1)\\
&\quad \left\{j(\omega_1-\omega_2)\cdot k_{2cgd}\cdot v_{gd}(\omega_2)\cdot v_{gd}(-\omega_1)+\frac{j(\omega_1-\omega_2)}{2}k_{2cgdcgs}\right.\\
&\quad \left.\cdot\left[v_{gd}(\omega_1)\cdot v_{gs}(-\omega_2)+v_{gd}(-\omega_2)\cdot v_{gs}(\omega_1)\right]\right\}
\end{aligned}
\tag{3.50}
$$

$$
\begin{aligned}
v_{gd}(\omega_2-\omega_1) &= v_g(\omega_2-\omega_1)-v_d(\omega_2-\omega_1)\\
&= TF_{GSGD}(\omega_2-\omega_1)\cdot\left[j(\omega_1-\omega_2)\cdot k_{2cgs}\cdot v_{gs}(\omega_1)\cdot v_{gs}(-\omega_2)\right.\\
&\quad +TF_{DSGD}(\omega_2-\omega_1)\left\{k_{2gm}\cdot v_{gs}(\omega_1)\cdot v_{gs}(-\omega_2)+k_{2gds}\cdot v_{ds}(\omega_1)\cdot v_{ds}(-\omega_2)\right.\\
&\quad \left.+k_{2gmds}\left[v_{gs}(\omega_1)\cdot v_{ds}(-\omega_2)+v_{gs}(-\omega_2)\cdot v_{ds}(\omega_1)\right]\right\}+TF_{GDGD}(\omega_2-\omega_1)\\
&\quad \cdot\left\{j(\omega_1-\omega_2)\cdot k_{2cgd}\cdot v_{gd}(\omega_1)\cdot v_{gd}(-\omega_2)+\frac{j(\omega_1-\omega_2)}{2}k_{2cgdcgs}\right.\\
&\quad \left.\cdot\left[v_{gd}(\omega_1)\cdot v_{gs}(-\omega_2)+v_{gd}(-\omega_2)\cdot v_{gs}(\omega_1)\right]\right\}
\end{aligned}
\tag{3.51}
$$

$$
\begin{aligned}
v_{gs}(2\omega_2) &= v_g(2\omega_2)-v_s(2\omega_2)\\
&= TF_{GSGS}(2\omega_2)\cdot\left[j(\omega_2)\cdot k_{2cgs}\cdot v_{gs}(\omega_2)^2\right]+TF_{DSGS}(2\omega_2)\left\{0.5\left[k_{2gm}\cdot v_{gs}(\omega_2)^2\right.\right.\\
&\quad \left.\left.+k_{2gds}\cdot v_{ds}(\omega_2)^2+2\cdot k_{2gmds}\cdot v_{gs}(\omega_2)\cdot v_{ds}(\omega_2)\right]\right\}+TF_{GDGS}(2\omega_2)\left[j(\omega_2)\right.\\
&\quad \left.\cdot\left\{k_{2cgd}\cdot v_{gd}(\omega_2)^2+k_{2cgdcgs}v_{gd}(\omega_2)v_{gs}(\omega_2)\right\}\right]
\end{aligned}
\tag{3.52}
$$

$$
\begin{aligned}
v_{ds}(2\omega_2) &= v_d(2\omega_2) - v_s(2\omega_2) \\
&= TF_{GSDS}(2\omega_2)\cdot\left[j(\omega_1)\cdot k_{2cgs}\cdot v_{gs}(\omega_2)^2\right] + TF_{DSDS}(2\omega_2)\left\{0.5\left[k_{2gm}\cdot v_{gs}(\omega_2)^2\right.\right. \\
&\quad \left. + k_{2gds}\cdot v_{ds}(\omega_2)^2 + 2\cdot k_{2gmds} v_{gs}(\omega_2)\cdot v_{ds}(\omega_2)\right]\Big\} + TF_{GDDS}(2\omega_2)\left[j(\omega_2)\right. \\
&\quad \left.\cdot\left\{k_{2cgd}\cdot v_{gd}(\omega_2)^2 + k_{2cgdcgs} v_{gd}(\omega_2) v_{gs}(\omega_2)\right\}\right]
\end{aligned}
\tag{3.53}
$$

$$
\begin{aligned}
v_{gd}(2\omega_2) &= v_g(2\omega_2) - v_d(2\omega_2) \\
&= TF_{GSGD}(2\omega_2)\cdot\left[j(\omega_1)\cdot k_{2cgs}\cdot v_{gs}(\omega_2)^2\right] + TF_{DSGD}(2\omega_1)\left\{0.5\left[k_{2gm}\cdot v_{gs}(\omega_2)^2\right.\right. \\
&\quad \left. + k_{2gds}\cdot v_{ds}(\omega_2)^2 + 2\cdot k_{2gmgds} v_{gs}(\omega_2)\cdot v_{ds}(\omega_2)\right]\Big\} + TF_{GDGD}(2\omega_2)\left[j(\omega_2)\right. \\
&\quad \left.\cdot\left\{k_{2cgd}\cdot v_{gd}(\omega_2)^2 + k_{2cgdcgs} v_{gd}(\omega_2) v_{gs}(\omega_2)\right\}\right]
\end{aligned}
\tag{3.54}
$$

Schematic of a simplified FET equivalent circuit in Figure 3.11 shows the transformation mechanism of the 2nd-order current sources from gate-source and drain-source terminal to the drain voltage v_d at 2nd-harmonic frequency $2\omega_2$. The total 2nd-order voltage phasor at the drain node accounts for the contributions from 2nd-order branch currents across gate-source and drain-source terminals are taken into account.

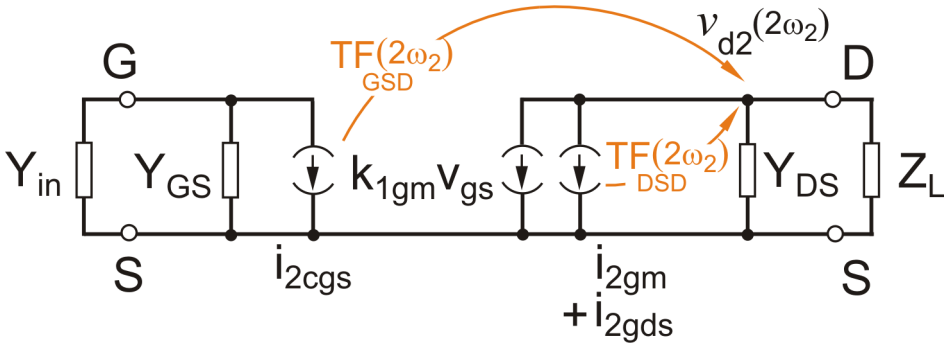

Figure 3.11 An example of a transformation mechanism from 2nd-order nonlinear current source to voltage at the drain node through transimpedance transfer function. The transformation is carried out at $2\omega_2$.

3.3.3 3rd-order Volterra Kernel

The 3rd-order nodal voltage in general, and the drain potential in particular, can be determined in a similar manner as described in Section 3.3.2. Figure 3.12 shows the 3rd-order linearized circuit schematic of the FET, which is excited by the 3rd-order current sources.

The closed-form analytical expressions of the 3rd-order current sources the conductance and capacitance nonlinearity contributing to the upper-IMD are listed in Table 3.4. The current equations consist of terms, which combine the nonlinearity of (i) 1st-order voltage phasors (ω_2, ω_2, $-\omega_1$), often referred to as a cubic nonlinearity, together with the quadratic mixing products of (ii) the envelope (ω_2-ω_1, ω_2) and (iii) 2nd-harmonic ($2\omega_2$, $-\omega_1$) voltage phasors.

As an example, using Table 3.4, the lower-IMD current sources generated by the gate-source capacitance nonlinearity and transconductance nonlinearity can be expressed as

$$\begin{aligned} i_{NL3cgs}(2\omega_2-\omega_1) = j(2\omega_2-\omega_1)\cdot\Big[& k_{2cgs}\cdot v_{gs}(\omega_2-\omega_1)\cdot v_{gs}(-\omega_1) \\ & + k_{2cgs}\cdot v_{gs}(2\omega_2)\cdot v_{gs}(-\omega_1) + \frac{3}{4}\cdot k_{3cgs}\cdot {v_{gs}}^2(\omega_2) v_{gs}(-\omega_1)\Big] \end{aligned} \tag{3.55}$$

$$\begin{aligned} i_{NL3gm}(2\omega_2-\omega_1) = & \frac{3}{4}\cdot k_{3gm}\cdot v_{gs}^2(\omega_2)\cdot v_{gs}(-\omega_1) + k_{2gm}\cdot v_{gs}(\omega_2) \\ & \cdot v_{gs}(\omega_2-\omega_1) + k_{2gm}\cdot v_{gs}(-\omega_1)\cdot v_{gs}(2\omega_2) \\ & + \frac{1}{2}\cdot k_{2gmgds}\cdot\Big[v_{gs}(-\omega_1)\cdot v_{ds}(2\omega_2) + v_{gs}(\omega_2)\cdot v_{ds}(\omega_2-\omega_1) \\ & + v_{gs}(\omega_2-\omega_1)\cdot v_{ds}(\omega_2) + v_{gs}(2\omega_2)\cdot v_{ds}(-\omega_1)\Big] \\ & + \frac{1}{4}k_{3gm2gds}\cdot\Big[2v_{gs}(-\omega_1)\cdot v_{gs}(\omega_2)\cdot v_{ds}(\omega_2) + v_{gs}^2(\omega_2)\cdot v_{ds}(-\omega_1)\Big] \\ & + \frac{1}{4}k_{3gmgds2}\cdot\Big[2v_{gs}(\omega_2)\cdot v_{ds}(-\omega_1)\cdot v_{ds}(\omega_2) + v_{gs}(-\omega_1)\cdot v_{ds}^2(\omega_2)\Big] \end{aligned} \tag{3.56}$$

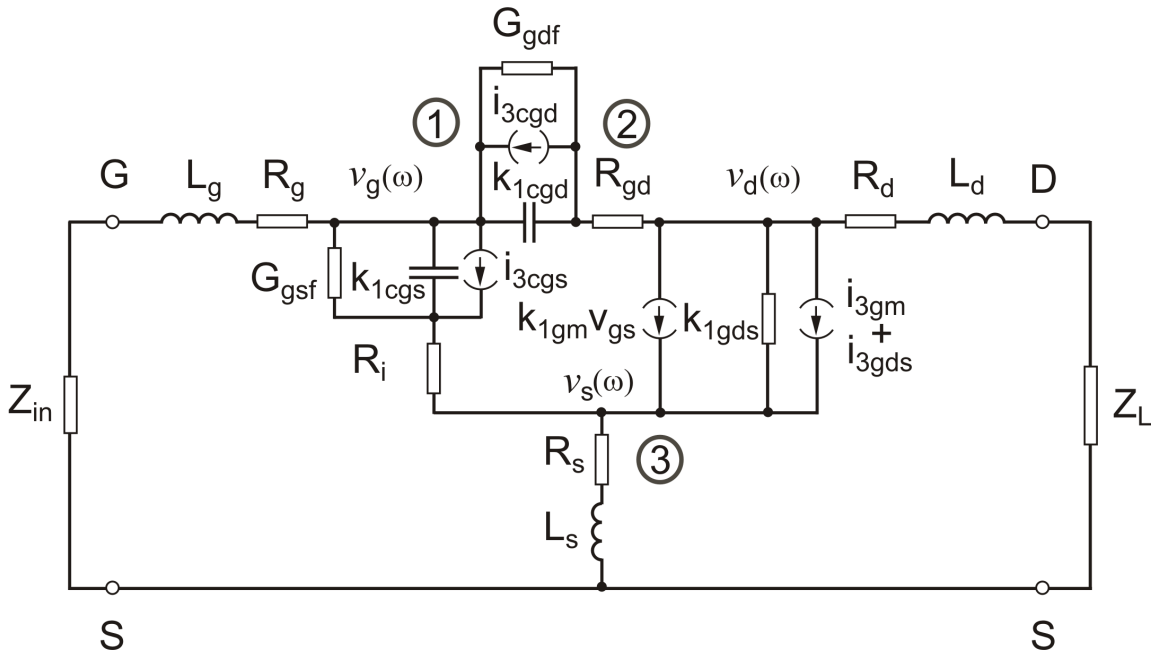

Figure 3.12 Linearized equivalent circuit of the analysed 1-mm GaN HEMT with the nonlinear elements decomposed into linear element and 2nd- and 3rd-order distortion current sources.

Similar to the 2nd-order transimpedance transfer function, the 3rd-order transimpedance transfer function is calculated to transform the current sources i_{3NLcgs}, i_{3NLgm} and i_{3NLgds} to voltage phasor at the drain node (v_{3d}) as shown in Figure 3.13. As a result, the IMD voltage phasor at the drain node can be expressed as

$$v_{3d}(2\omega_2-\omega_1) = TF_{GSD}(2\omega_2-\omega_1)\cdot i_{3NLcgs} + TF_{DSD}(2\omega_2-\omega_1)\cdot\left[i_{3NLgm}+i_{3NLgds}\right] \tag{3.57}$$

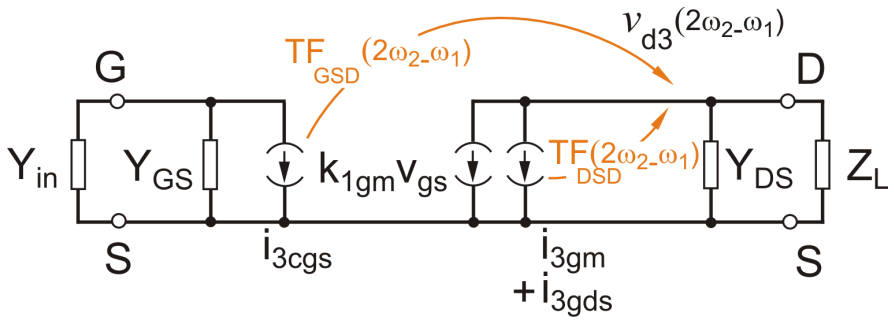

Figure 3.13 An example of a transformation mechanism from 3rd-order nonlinear current source to voltage at the drain node through transimpedance transfer function. The transformation is carried out at $2\omega_2-\omega_1$.

The derived IMD equations for a FET device in terms of v_{gs}, representing individual vectorial components, are given in Appendix A.

Table 3.4 3rd-order nonlinear current sources $i_{3NL}(\omega)$ under 2-tone excitation contributing towards upper IMD3 at $2\omega_2-\omega_1$ (after [15], [19]).

Nonlinearity	$i_{3NL}(2\omega_2-\omega_1)$
Transconductance	$\frac{3}{4}k_{3\,gm}\cdot v_{gs}^2(\omega_2)\cdot v_{gs}(-\omega_1)+k_{2\,gm}\cdot v_{gs}(\omega_2)\cdot v_{gs}(\omega_2-\omega_1)$ $+k_{2\,gm}\cdot v_{gs}(2\omega_2)\cdot v_{gs}(-\omega_1)$
Channel conductance	$\frac{3}{4}k_{3\,gds}\cdot v_{ds}^2(\omega_2)\cdot v_{ds}(-\omega_1)+k_{2\,gds}\cdot v_{ds}(\omega_2)\cdot v_{ds}(\omega_2-\omega_1)$ $+k_{2\,gds}\cdot v_{ds}(2\omega_2)\cdot v_{ds}(-\omega_1)$
Capacitor	$j(2\omega_2-\omega_1)\cdot\left[\frac{3}{4}\cdot k_{3cgs(cgd)}\cdot v_{gs(gd)}^2(\omega_2)\cdot v_{gs(gd)}(-\omega_1)\right.$ $+k_{2cgs(cgd)}\cdot v_{gs(gd)}(2\omega_2)\cdot v_{gs(gd)}(-\omega_1)$ $\left.+k_{2cgs(cgd)}\cdot v_{gs(gd)}(\omega_2)\cdot v_{gs(gd)}(\omega_2-\omega_1)\right]$
Conductance cross-terms	$\frac{1}{4}\cdot k_{3\,gm2\,gds}\cdot\left[2\cdot v_{gs}(\omega_2)\cdot v_{gs}(-\omega_1)\cdot v_{ds}(-\omega_1)+v_{gs}^2(\omega_2)\cdot v_{ds}(-\omega_1)\right]$ $+\frac{1}{4}\cdot k_{3\,gmgds2}\cdot\left[2\cdot v_{gs}(\omega_2)\cdot v_{ds}(-\omega_1)\cdot v_{ds}(-\omega_1)+v_{ds}^2(\omega_2)\cdot v_{gs}(-\omega_1)\right]$ $+\frac{1}{2}\cdot k_{2\,gmgds}\cdot\begin{bmatrix}v_{ds}(2\omega_2)\cdot v_{gs}(-\omega_1)+v_{gs}(\omega_2)\cdot v_{ds}(\omega_2-\omega_1)\\+v_{ds}(\omega_2)\cdot v_{gs}(\omega_2-\omega_1)+v_{gs}(2\omega_2)\cdot v_{ds}(-\omega_1)\end{bmatrix}$
Capacitance cross-terms	$j(2\omega_2-\omega_1)\cdot\left\{\frac{1}{4}\cdot k_{3cgd2cgs}\cdot\begin{bmatrix}2\cdot v_{gd}(\omega_2)\cdot v_{gd}(-\omega_1)\cdot v_{gs}(-\omega_1)\\+v_{gd}^2(\omega_2)\cdot v_{gs}(-\omega_1)\end{bmatrix}\right.$ $+\frac{1}{4}\cdot k_{3cgdcgs2}\cdot\left[2\cdot v_{gd}(\omega_2)\cdot v_{gs}(-\omega_1)\cdot v_{gs}(-\omega_1)+v_{gs}^2(\omega_2)\cdot v_{gd}(-\omega_1)\right]$ $+\frac{1}{2}\cdot k_{2cgdcgs}\cdot\left[v_{gs}(2\omega_2)\cdot v_{gd}(-\omega_1)+v_{gd}(\omega_2)\cdot v_{gs}(\omega_2-\omega_1)\right.$ $\left.\left.+v_{gs}(\omega_2)\cdot v_{gd}(\omega_2-\omega_1)+v_{gd}(2\omega_2)\cdot v_{gs}(-\omega_1)\right]\right\}$

3.3.4 Model Verification

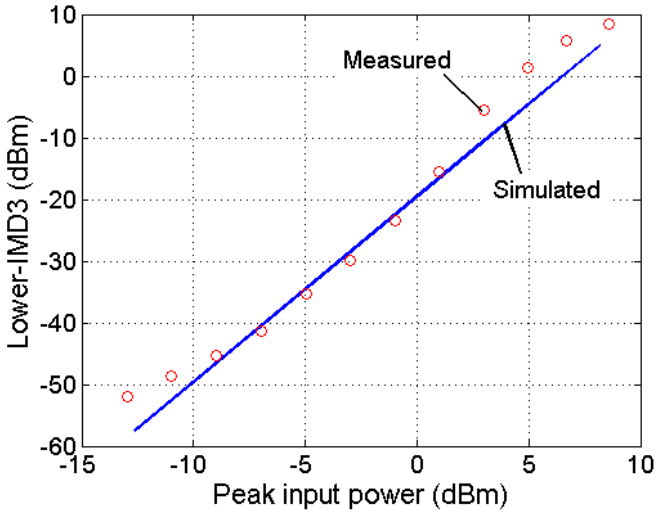

Figure 3.14 Measured and simulated IMD3 characteristics based on Volterra series analysis for a 2-tone input signal with f_c = 2.15 GHz, Δf = 100 kHz at V_{GS0} = -2V, V_{DS0} = 20V.

Volterra series prediction of IMD3 is validated by characterizing a 1-mm AlGaN/GaN HEMT under two-tone excitation as shown in Figure 3.14. With f_c = 2.15 GHz and Δf = 100 kHz, the device was biased for class-A operation (-2V, 20V). At lower input power level the measured IMD characteristics tend to show a constant behaviour due the dynamic range limitation of the vector signal analyser used as receiver. On the other hand, at higher power levels, as the fundamental gain characteristics begin to compress, the IMD curves show a typical expansion behaviour, which is evident from the measurements seen in Figure 3.14. Since the model is derived from the small-signal equivalent circuit parameters, a monotonously increasing lower-IMD3 (IM3L) curve is predicted with an expected 3 dB slope [39], which is valid until the device enters compression region.

3.4 IMD Vectorial Analysis

A further insight into the 3rd-order lower IMD across the load Z_L at the drain node for 0.3V input voltage level ($P_{in,\,peak}$= -6 dBm) is demonstrated in Figure

3.15(a)-(c), in the form of individual distortion vectors derived from the 3rd-order cubic term ($\omega_1+\omega_1-\omega_2$), the 2nd-order envelope term [($\omega_1-\omega_2$)+ ω_1] and the 2nd-order harmonic term [($2\omega_1$)-ω_2]. Referring to Figure 3.15(d), the IM3L vector begins at the origin and 3rd-order cubic distortion vectors add up to reach the point (-0.37+j0.08) mV. Further, 2nd-order distortion vectors, which are envelope frequency dependent ($\omega_1-\omega_2$), contribute to the IM3L vector to reach the co-ordinate (-0.45+j0.14) mV. Finally, the harmonic frequency ($2\omega_1$) dependent 2nd-order distortion vectors add up to reach the value (-0.58+j0.21) mV, which is the final complex value of IM3L.

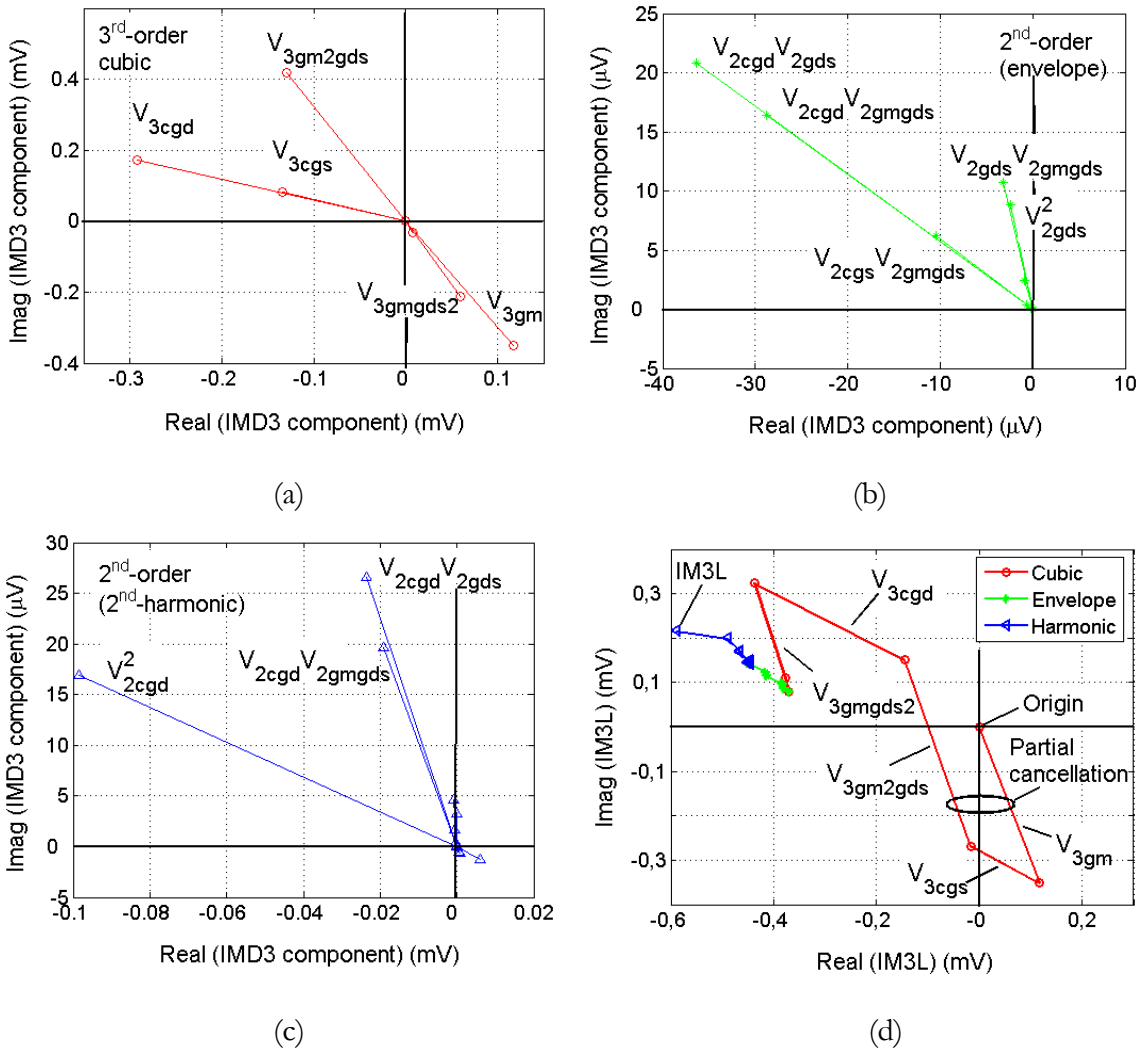

Figure 3.15 Vector representation of individual IMDL components in the analysed 1-mm GaN HEMT.

In Figure 3.15(d), 3rd-order distortion phasors, which are symbolically depicted as V_{3Y}, have significant influence on total IM3L, especially the dominant V_{3cgd} vector. The partial cancellation phenomena can be observed between vectors V_{3gm} and $V_{3gm2gds}$ in Figure 3.15(d). Although, in general, the nonlinear drain current source has major contribution towards IMD3, such a contribution is partially cancelled by another distortion vector originating from 3rd-order cross-terms ($V_{3gm2gds}$). On the other hand, the vector V_{3cgd} dominates over the total IM3L apart from minor influence from V_{3cgs}. Such detailed vectorial representation of IMD3 could encourage deep investigations on improving GaN HEMT technology by tuning the device parameters appropriately. Moreover, one of the primary advantages of this procedure is that it preserves phase information, which is critical in analyzing partial cancellation mechanism.

3.5 AlGaN/GaN Linearity Optimisation

Device-level linearity improvement techniques have focused on minimizing the higher order derivatives of G_m, G_{ds}, and C_{gs} nonlinearities. These nonlinearities depend to a great extent on the shape of the channel doping profile. This is because the gate bias dependence of the depletion layer boundary governs the bias dependence of the I(V) characteristics and the gate capacitance [40]. The solution for reducing distortion, however, lies in obtaining linear conductance and capacitive nonlinearities by suitably optimising the device semiconductor thereby minimizing higher order derivatives [25], [40]. This will not only eliminate the 3rd-order term but also remaining higher-order terms.

Early works of Pucel [40], Williams and Shaw [41] and later on deepened by Pedro [25], focused on reducing 3rd-order derivative of G_m by suitably tailoring the channel doping profile in MESFETs. Pucel [40] also proposed that by

following this approach, even the C_{gs} nonlinearity, which is proved to be proportional to G_m behaviour, could also be simultaneously linearized. With a similar notion, Chu *et al.* [24] attempted to maintain the depletion width in MESFETs to a rather constant value by varying the gate voltage swing, thereby preserving a linear G_m and C_{gs} characteristics. This was achieved by adopting spike-doped MESFET. G_m optimisation by doping profile engineering typically applies to MESFETs. However, in case of HEMTs, engineering is much more complex and requires, for instance, introducing multiple channels.

In yet another approach, Nakasha *et al.* [26] showed that by increasing the value of G_m in GaAs power FETs, device linearity could be effectively enhanced. Two possibilities were proposed to fulfil this requirement, either by decreasing the thickness of AlGaAs barrier layer, which increases the threshold voltage V_t or by increasing the donor concentration in the n-GaAs channel and simultaneously decreasing the thickness of the channel layer.

In the vectorial analysis presented in Section 3.4, C_{gd} nonlinearity was shown to be predominant. C_{gd} can be effectively controlled to suppress distortion by means of the gate field-plate (FP) technology, originally intended to improve current collapse and breakdown characteristics [42-44].

3.5.1 Gate Field-Plate Based IMD Minimization

Drain current collapse is a major problem encountered in the fabrication of conventional HEMTs, which reduce the available current swing as well as degrade the knee voltage [43]. The surface trap induced current dispersion is generally explained by the carrier freeze-out due to the surface states, which act as electron traps between the gate and the drain [45].

SiN film is mostly used as a surface passivation layer, since it reduces the

response of the surface traps, suppressing the effect of current collapse [45]. Collapse-free devices using SiN passivation, however, exhibit significant drop in the gate-drain breakdown voltage (V_{BR}), imposing restrictions on realizing high power operation in FET technology. This led to the implementation of field-modulating plate, which is primarily used to improve V_{BR} and to suppress the surface trap effects [46].

Suppression of drain current dispersion observed in field-plate based FET devices suggested that field-modulating plate effectively controls the depletion layer in the gate-drain region under large-signal RF operation, resulting in the removal of channel constriction effect caused by surface traps. The improvement in the V_{BR} is attributed to the reduction of electric field near the gate by introducing the field-plate [42-47]. This method was used effectively in AlGaAs/GaAs [46] and AlGaN/GaN [42], [45] based power devices.

The influence of field-plate on linearity in AlGaN/GaN HEMTs is however seldom discussed [43]. Wu *et al.* [47] carried out experiments on a 30 W/mm GaN HEMT by introducing field-plate to primarily improve the power performance, but had also claimed that it offered some linearization effect. The field-plate adds additional capacitance to the feedback capacitance C_{gd}. Since the field-plate increases the clipping-free signal range, an improvement in the 3rd-order carrier-to-intermodulation ratio C/I3 can be obtained in the power saturation region with the same input power as the conventional design (without field-plate). However, also in the small-signal regime an improvement in C/I3 can be achieved.

In fact, noting that the investigated GaN HEMT (Section 3.4) had no field-plate, the extracted value of $C_{gd(w/o\ FP)}$ (175 fF) was scaled to a practical value of $C_{gd(FP)}$ ($1.5*C_{gd(w/o\ FP)}$ = 262.5 fF) [44] to simulate the introduction of a field-plate structure and study its influence on IMD3. Figure 3.16 shows the simulation results, where the theoretically optimized IMD3 phasor, which

represents the device with field-plate, gradually approaches the origin, thus implying a reduction in distortion with the increase in $C_{gd(FP)}/C_{gd(w/o\ FP)}$ ratio. Quantitatively, if X_a (-0.58 + j0.21 mV) and X_b (-0.36 + j0.24 mV) are the complex IMD3L voltages before and after field-plate implementation, then an IMD3 suppression of $20\log_{10}\{abs(X_a/X_b)\}$ = 3.03 dB can be obtained after device optimization.

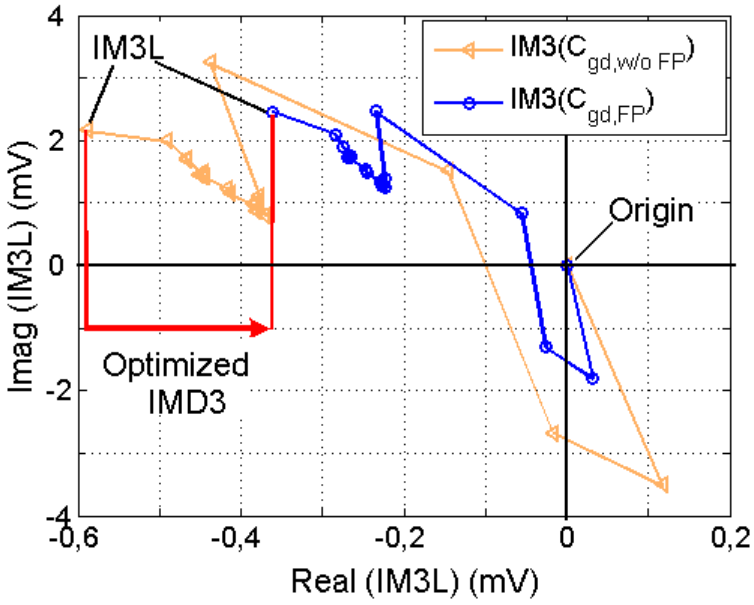

Figure 3.16 Gradual improvement of lower IMD3 in the analysed 1-mm GaN HEMT by increasing the value of C_{gd} [48].

Indeed, the amount of intermodulation distortion improvement for a given transistor technology depends on the methodology of fabrication, structure type, device characterization environment, and, importantly, the extrinsic (frequency dependent) and intrinsic (bias dependent) small-signal equivalent circuit parameter extraction procedure.

3.6 5th-Degree Extension of Volterra Model

In RF power amplifiers, higher-degree nonlinear effects not only become significant at 1-dB compression point but also dominate the nonlinear

behaviour. In this region, IMD curves exhibit more complex behaviour such as low distortion IMD sweet-spots. Further, the slope of the 3rd-order distortion products will no longer follow 3 dB/dB trend. In the context of modelling IMD3 using Volterra series technique, it is hence necessary to extend the Taylor series polynomial from 3rd-degree to higher degree polynomial to describe complex nonlinear effects [17]. 5th-degree channel current model was adopted by Kim *et al.* [49] and Heiskanen *et al.* [50] to predict IMD in MESFET and LDMOS transistors.

In recent years IMD sweet-spot effects have become interesting subject of discussion, which demonstrate a possible means to tailor device properties for promoting inherent cancellation mechanism at the desired operating conditions. Although Chapter 5 gives a detail description on the origin and controlling mechanisma of IMD sweet-spots, a better insight into such complex behaviour could alternately be obtained through Volterra series technique, implementing higher degree polynomials. Indeed, odd-order Taylor series coefficients of all nonlinear small-signal equivalent circuit elements play an important role in achieving IMD3 cancellation. It is evident that a 5th-degree polynomial is imperative in order to investigate the phenomena of IMD cancellation. As a result, a 3rd-degree polynomial of the channel current can be extended to 5th-degree as follows,

$$\begin{aligned} I_{ds}(v_{gs},v_{ds})^{(5)} = I_{ds}(v_{gs},v_{ds})^{(3)} + k_{4gm}{v_{gs}}^4 + k_{5gm}{v_{gs}}^5 + k_{4ds}{v_{ds}}^4 + k_{5ds}{v_{ds}}^5 \\ + k_{5gm3gds2}v_{gs}^3 v_{ds}^2 + k_{5gm2gds3}v_{gs}^2 v_{ds}^3 \end{aligned} \tag{3.58}$$

where $I_{ds}^{(3)}(v_{gs}, v_{ds})$ is equivalent to $I_{ds}(v_{gs}, v_{ds})$ of (3.15). Figure 3.17 shows the extracted bias dependent odd-order Taylor series coefficients obtained from polynomial expression (3.58) at V_{ds0} = 20V. Further, using Table 3.5, the 3rd-order Volterra kernel can be derived, as described in Section 3.3.3, which now includes the 5th-degree nonlinearity.

Table 3.5 3rd-order nonlinear current sources $i_{3NL}(\omega)$ caused by 5th-degree nonlinearity under two-tone excitation contributing towards upper IMD3 at $2\omega_2 - \omega_1$.

Nonlinearity	$i_{3NL}^{(5)}(2\omega_2 - \omega_1)$
Transconductance	$\frac{1}{16} k_{5\,gm}\Big[30 v_{gs}^2(\omega_2)\cdot v_{gs}(\omega_1)\cdot v_{gs}(-\omega_1)^2 +20\cdot v_{gs}^3(\omega_2)\cdot v_{gs}(-\omega_2)\cdot v_{gs}(-\omega_1)\Big]$
Channel conductance	$\frac{1}{16} k_{5\,gds}\Big[30 v_{ds}^2(\omega_2)\cdot v_{ds}(\omega_1)\cdot v_{ds}(-\omega_1)^2 +20\cdot v_{ds}^3(\omega_2)\cdot v_{ds}(-\omega_2)\cdot v_{ds}(-\omega_1)\Big]$
Capacitor	$\frac{j(2\omega_2-\omega_1)}{16} k_{5\,cgs(cgd)}\Big[30 v_{gs(gd)}^2(\omega_2)\cdot v_{gs(gd)}(\omega_1)\cdot v_{gs(gd)}(-\omega_1)^2 +20\cdot v_{gs(gd)}^3(\omega_2)\cdot v_{gs(gd)}(-\omega_2)\cdot v_{gs(gd)}(-\omega_1)\Big]$
Conductance cross-terms	$\frac{1}{16} k_{5\,gm3\,gds2}\Big[3 v_{gs}^2(\omega_2)\cdot v_{gs}(\omega_1)\cdot v_{ds}(-\omega_1)^2 + 12 v_{gs}(\omega_2)\cdot v_{gs}(-\omega_1) \cdot v_{gs}(\omega_1)\cdot v_{ds}(\omega_2)\cdot v_{ds}(-\omega_1) + 6 v_{gs}^2(\omega_2)\cdot v_{gs}(-\omega_1)\cdot v_{ds}(-\omega_1)\cdot v_{ds}(\omega_1) +6 v_{gs}(-\omega_1)^2\cdot v_{gs}(\omega_2)\cdot v_{ds}(\omega_2)\cdot v_{ds}(\omega_1) + 3 v_{gs}(-\omega_1)^2\cdot v_{gs}(\omega_2)\cdot v_{ds}(\omega_2)^2\Big]$ $\frac{1}{16} k_{5\,gm2\,gds3}\Big[6 v_{gs}^2(\omega_2)\cdot v_{ds}(\omega_2)\cdot v_{ds}(-\omega_2)\cdot v_{ds}(-\omega_1) + 6 v_{gs}(\omega_2)\cdot v_{gs}(-\omega_2) \cdot v_{ds}^2(\omega_2)\cdot v_{ds}(-\omega_1) + 6 v_{gs}(\omega_2)\cdot v_{gs}(-\omega_1)\cdot v_{ds}^2(\omega_2)\cdot v_{ds}(-\omega_2) +2 v_{gs}(-\omega_2)\cdot v_{gs}(-\omega_1)\cdot v_{ds}(\omega_2)^3\Big]$
Capacitance cross-terms	$\frac{j(2\omega_2-\omega_1)}{16} k_{5\,cgd3\,cgs2}\Big[3 v_{gd}^2(\omega_2)\cdot v_{gd}(\omega_1)\cdot v_{gs}(-\omega_1)^2 + 12 v_{gd}(\omega_2) v_{gd}(-\omega_1) \cdot v_{gd}(\omega_1)\cdot v_{gs}(\omega_2)\cdot v_{gs}(-\omega_1) + 6 v_{gd}^2(\omega_2)\cdot v_{gd}(-\omega_1)\cdot v_{gs}(-\omega_1)\cdot v_{gs}(\omega_1) +6 v_{gd}(-\omega_1)^2\cdot v_{gd}(\omega_2)\cdot v_{gs}(\omega_2)\cdot v_{gs}(\omega_1) + 3 v_{gd}(-\omega_1)^2\cdot v_{gd}(\omega_2)\cdot v_{gs}(\omega_2)^2\Big]$ $\frac{1}{16} k_{5\,cgd2\,cgs3}\Big[6 v_{gd}^2(\omega_2)\cdot v_{gs}(\omega_2)\cdot v_{gs}(-\omega_2)\cdot v_{gs}(-\omega_1) + 6 v_{gd}(\omega_2) \cdot v_{gd}(-\omega_2)\cdot v_{gs}^2(\omega_2)\cdot v_{gs}(-\omega_1) + 6 v_{gd}(\omega_2)\cdot v_{gd}(-\omega_1)\cdot v_{gs}^2(\omega_2)\cdot v_{gs}(-\omega_2) +2 v_{gd}(-\omega_2)\cdot v_{gd}(-\omega_1)\cdot v_{gs}(\omega_2)^3\Big]$

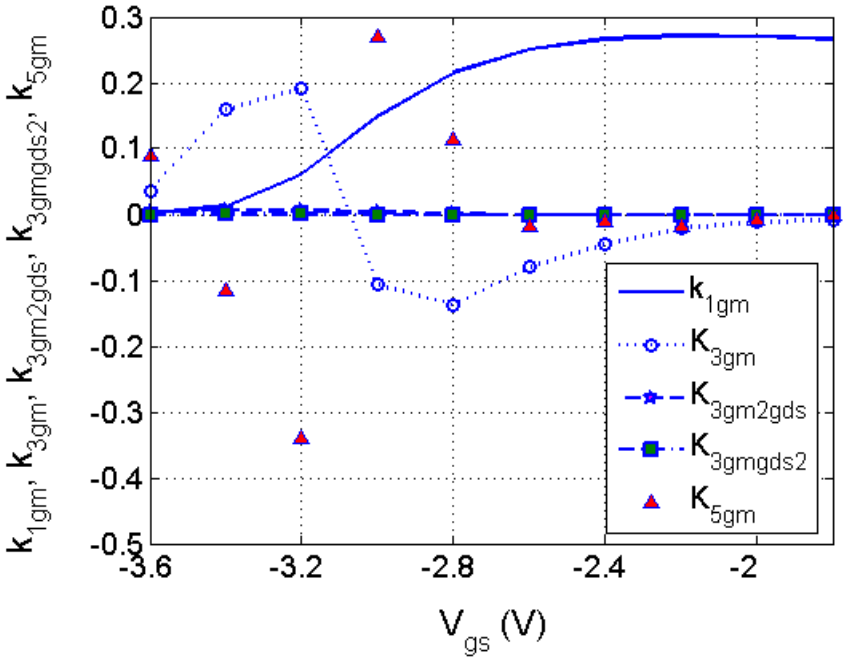

Figure 3.17 Bias dependent odd-order Taylor series coefficients of the analysed 1-mm GaN HEMT obtained from 5th-degree nonlinear $I_{ds}^{(5)}(v_{gs}, v_{ds})$ polynomial at V_{ds} = 20V [51].

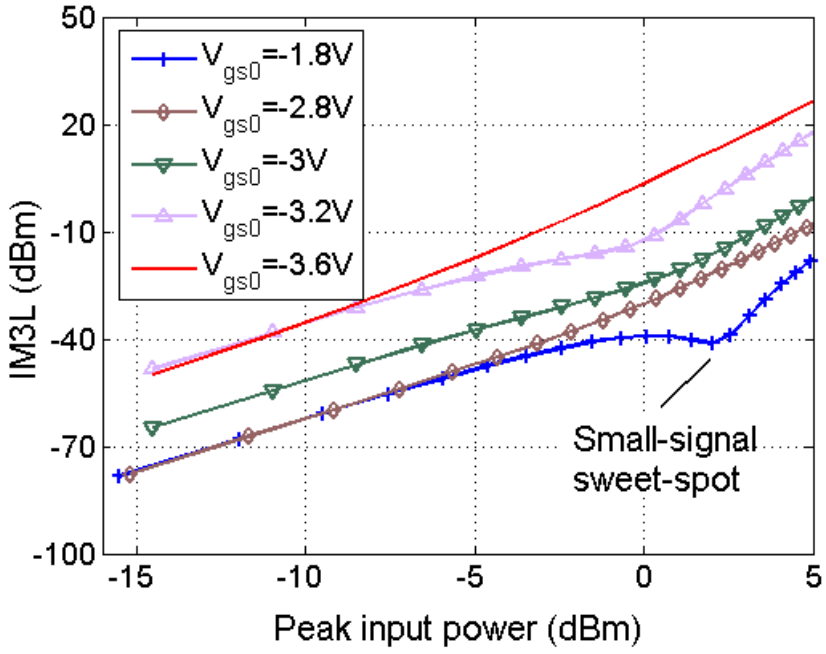

Figure 3.18 Simulated IMD3 characteristics of the analysed 1-mm GaN HEMT based on 5th-degree nonlinearity extension of Volterra series analysis for varying bias points.

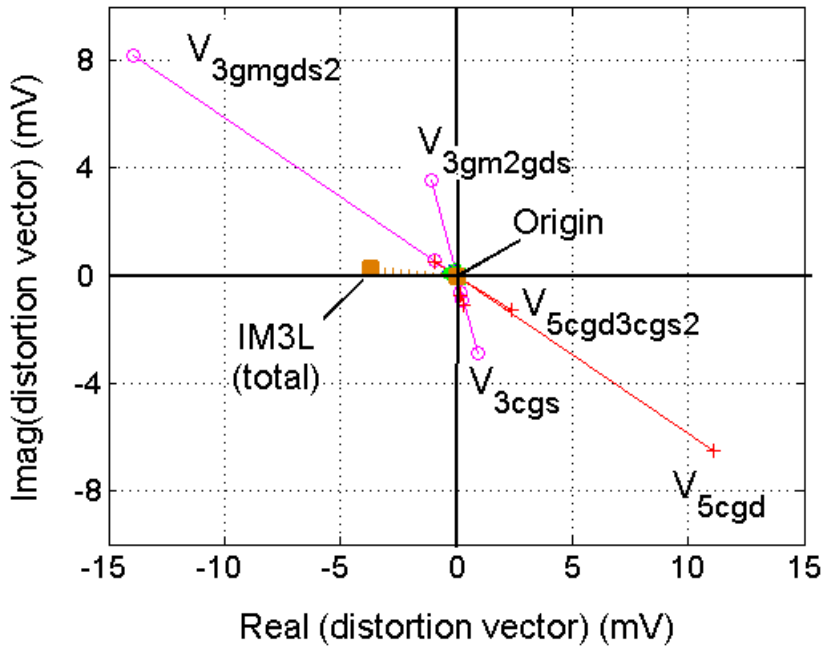

Figure 3.19 Distortion phasors of IM3L components of the analysed 1-mm GaN HEMT at small-signal sweet-spot (P_{in} = 2 dBm) indicating the cancellation between 3rd and 5th-degree IM3L contributors.

The simulation results of IMD3L are illustrated in Figure 3.18, wherein the small-signal IMD3 cancellation occurs for particular bias conditions. For instance, at P_{in} = 2 dBm (V_{gs0} = -1.8V), Figure 3.19 illustrates individual complex distortion vectors indicating the cancellation between 3rd- and 5th-degree IM3L contributors due to the opposite phase relationship between $V_{3gmgds2}$ and V_{5cgd}.

Chapter 4
Large-Signal Measurement Techniques

Several software and hardware tools are available for efficient design of microwave circuits. Characterization testbench together with the calibration techniques used are part of hardware tools, which ensure precise measurement data acquisition [52-56]. The measurement system has always been a tool for providing better insight into the device behaviour. Reliable large-signal device and/or power amplifier characterization techniques with broadband and high dynamic range capabilities are indeed desired. In particular, concerning linearity aspect, modelling nonlinear active device's large-signal IMD and ACPR curves are still a great challenge, whose importance is equally shared by the model verification data delivered. Thus, an accurate data acquisition will enable straightforward CAD model verification involving higher order IMD products. This further facilitates the design of high linear power amplifier with suppressed memory-effects followed by a simple and efficient linearization techniques.

Due to the advancement in the type of test signals used in practical telecommunication scenario (e.g. W-CDMA), in recent years there has been a dramatic shift to frequency-domain based measurement systems (receivers, in

particular) supporting periodic and aperiodic test signal environment [55]. Although the traditional way of viewing signals is in time-domain, it becomes often difficult to interpret a complex non-sinusoidal signal response. Besides, measurements based on time-domain sampling using sampling oscilloscope and microwave transition analyser (MTA) are restricted to periodic stimulus. However, since any waveform can be decomposed into sum of discrete sinusoidal signals, with the help of Fourier transform, the amplitude and phase at the corresponding frequency components can be simply acquired in frequency-domain. Thus, the low power small-signal components can be individually resolved out of the large-signal component. For microwave applications, frequency domain measurements become critical in distinctly characterizing distortion products and higher order harmonics along with the fundamental component. In part, this is because regulations require control of spurious spectral emissions to strictly restrict any interference with other wireless systems. However, as the semiconductor technology progresses, more detailed RF analysis is required to precisely evaluate and optimise the device performance [56].

4.1 Fundamental System Requirements

To concretise the requirements particularly pertaining to this research work, the measurement system must be capable of characterizing a power device or a power amplifier to fulfil the requirements of 3G UMTS spectral mask. This demands the need of a vector signal generator, which could produce UMTS based test signals (e.g. wideband code division multiple access W-CDMA) and a broadband receiver, capable of capturing vectorial raw data. However, the system should also support multi-tone modulated signals to study the memory-effect behaviour of the DUT. The means to model and characterize the nonlinear behaviour depends on the properties of the input signal. The introduction of two-tone test signal revolutionized the perception of

nonlinearity, simultaneously setting up stringent rules on the measurement system requirement. A basic two-tone test setup is shown in Figure 4.1. Two discrete tones of equal power that fall within the passband of the DUT, are applied as excitation signal. The resulting harmonic and IMD components are then measured using a spectrum analyser.

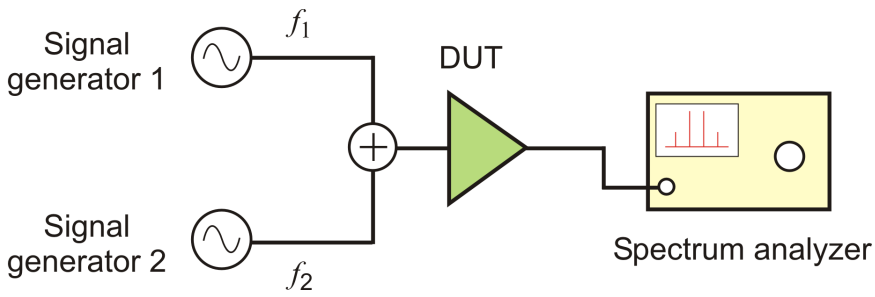

Figure 4.1 Basic two-tone test setup for IMD characterization.

A trivial method of generating the excitation signal is by combining the output signals from two RF sources [12], [14], [57]. However, it is difficult to practically maintain uniform amplitude and phase of both tones [58]. Further, as the number of tones increase, complexity of the system augments due to large number of signal generators coupled with synchronization problems between the tones [59]. To avoid these problems, modern signal generators are currently preferred, which are capable of generating CW, multi-tone with randomised phase-offset and 3GPP defined W-CDMA stimuli. The electronic signal generator of type ESG 4438C manufactured by Agilent [60] has built-in arbitrary waveform generator (AWG) with an IQ modulator to produce the required modulation on the carrier signal.

At microwave frequencies, it is important to take into account the errors introduced by the frequency response of the measurement system. Finite coupler directivity and connector mismatches can result in significant errors in the measured RF power [61-62]. Thus, the measured raw data must be vector error-corrected at both ports of the DUT. It is evident that to carry out vectorial error-correction, receiver should fundamentally be capable of

measuring both amplitude and phase information of the test signal. Conventional intermodulation distortion (IMD) measurement systems use either a power meter or spectrum analyser as receivers, which are restricted to only scalar correction. Demmler *et al.* [63] used the network analyser for vector error-correction of spectrum analyser measurements for attaining higher IMD measurement accuracy. Sophisticated error-correction algorithms have been carried out earlier for periodic bandpass signal measurements using time-domain sampling oscilloscope [62] and microwave transition analyser (MTA) [54-55] based systems. In this thesis, the well established calibration routine [55] has been implemented in frequency-domain based on dual-channel phase coherent vector signal analyser (VSA) system capable of error-correcting periodic and aperiodic signal types.

The frequency-domain measurement setup developed by Ahmed [64], for characterization of memory-effects in power amplifiers as well as active power devices, is based on single-channel Agilent VSA 89640A [65]. An added advantage of frequency-domain measurement setup is the possibility of selective power measurements at the frequencies of interest, which will in turn enable direct frequency-domain error-correction of the measured vectors. However, this feature was not fully exploited in [64] where calibration was limited to only frequency tracking. This work overcomes the deficiency prevailing in [64] by extending the measurement setup having the following key features:

- Using dual-channel VSA as receiver, the frequency-domain measurement setup is fully automated for characterizing nonlinear RF devices and power amplifiers.
- By introducing a second channel in the receiver, coaxial and on-wafer vector error-correction routine is developed for reliable absolute power and relative phase measurements. The second channel enabled two-path two-port SOLT calibration, which is the fundamental requirement

towards fulfilling power calibration. The control software including the calibration routine and large-signal measurements were developed using MATLAB® software.

- Static and dynamic AM-AM and AM-PM characterization can be performed under multi-tone and digitally modulated test signals (e.g. W-CDMA). Additionally, by measuring in-band distortion products, important figures of merit such as intermodulation ratio (IMR) and adjacent channel power ratio (ACPR) can be analysed.
- Bandwidth dependent memory-effects can be characterized by sweeping the modulation bandwidth of the test signal at the input. Insight into the measured memory-effect behaviour of GaN HEMTs led to the development of in-house bias tees specially designed for UMTS based applications. This has led to a more meaningful interpretation of the measured IMD.

4.1.1 System Description

The frequency-domain measurement setup established in this work is shown in Figure 4.2. It incorporates dual-channel 89600 series VSA as receiver. This system is intended for measuring and analysing active device and/or amplifier nonlinearity within the frequency range from DC to 2.7 GHz, with an instantaneous bandwidth of 36 MHz. The dual directional coupler (Amplifier Research DC7420 with operational bandwidth of 0.8 to 18 GHz) imposes 50W (CW) limitation in the measured output power.

As depicted in Figure 4.2, the transmitted and reflected complex travelling waves a_1 and b_1 at the input port 1 and b_2 and a_2 at the output port 2 are monitored by the VSA using dual directional coupler. A 100W driver amplifier (Amplifier Research 100S1G4M8 with operational bandwidth of 0.8 to 4.2 GHz) is inserted to generate high linear input power to drive high power DUTs until 1-dB compression point. Envelope source-/load-pull

measurements are established by using a combination of RF and LF bias tees, cascaded along the low frequency DC path. It is hence possible to present an arbitrary impedance at the envelope frequency, while being simultaneously decoupled from the impedance at the fundamental and harmonics.

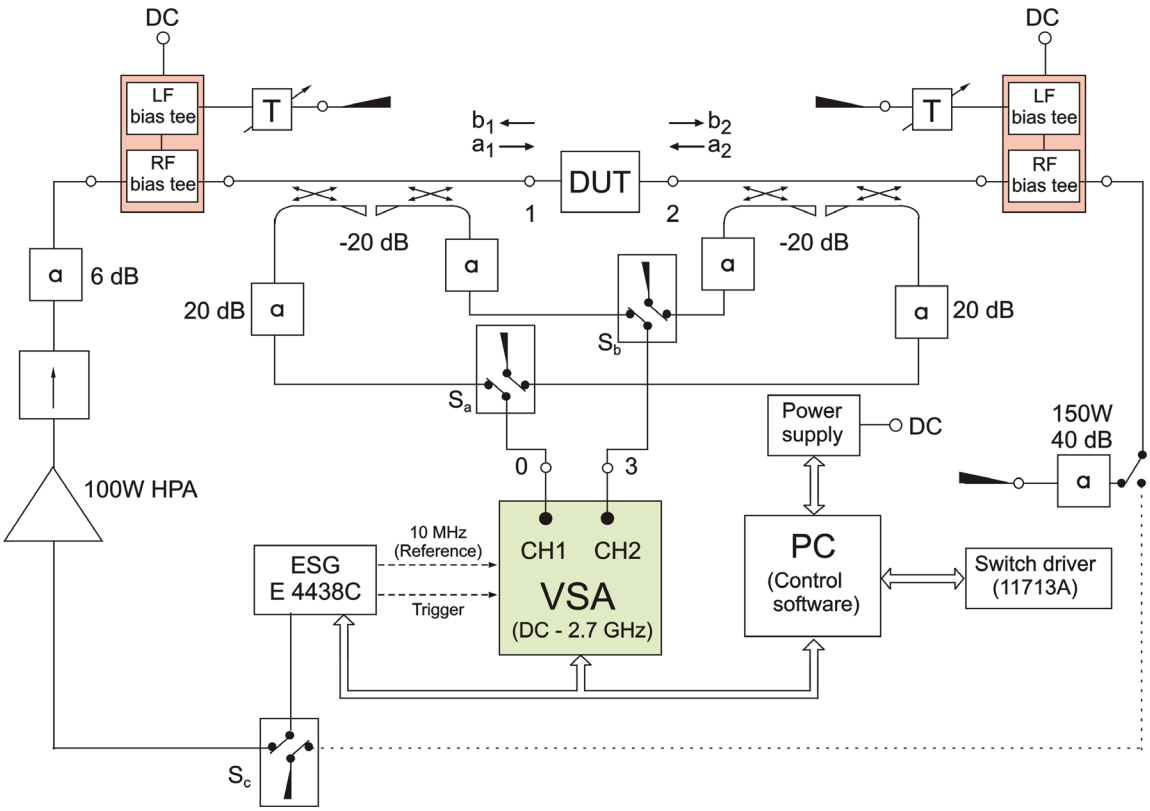

Figure 4.2 Frequency-domain measurement setup for distortion characterization facilitating passive envelope load-pull characterization.

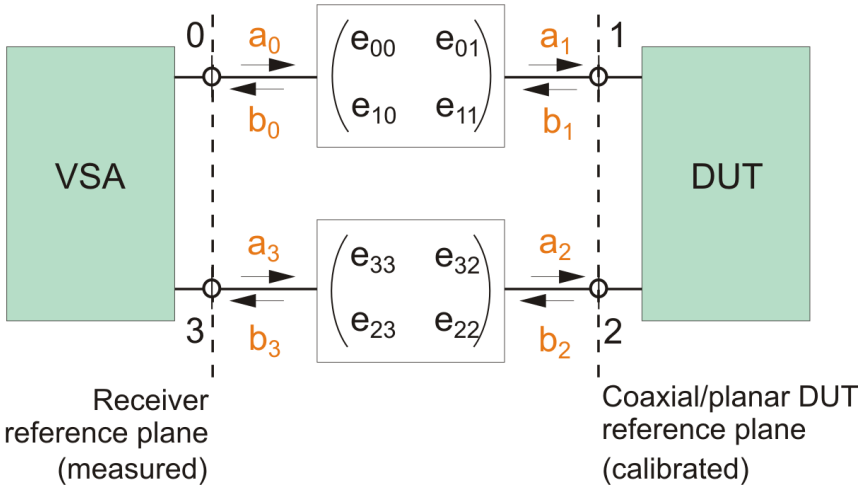

Figure 4.3 Simplified 8-term error-model of a 2-port VSA based testbench.

4.1.2 System Calibration

The calibration is essential to primarily remove systematic errors of the testbench at the intended measurement frequencies. The systematic errors are often represented using an error model of the measurement system. As shown in Figure 4.3, the raw data measured by the receiver must be transformed to the DUT reference plane by de-embedding the linear test-set parameters.

Kruppa and Sodomsky [52] established system calibration procedures for wave ratio (S-parameter) measurements in early 1970s. In fact, the main objective was to improve the measurement accuracy and to establish a well defined measurement reference plane. However, it was equally essential to determine the absolute values (magnitude and phase) of the measured power waves. Lott [53] fulfilled this requirement by introducing the concept of power calibration.

The calibration routine followed in this work is based on the method proposed by Benedikt *et al.* [55]. The entire control software including the calibration routine, measurement process and the post-data processing are programmed using Matlab® software. The error-correction is principally achieved in two stages with relevant closed-form equations. To outline the steps, first, with the help of source switching (switch S_c in Figure 4.2), a two-path two-port SOLT calibration (using short, open, matched 50Ω load and through standards) is performed in forward and reverse direction. From the ratio measurements, the standard 12-term systematic error-model of the measurement setup's test-set is determined [66]. The need for two sets of error models for the forward and reverse direction is to overcome the source switching issues inherent in nonideal reflectometers. The analytical expressions, derived by Rehnmark [67], was implemented for correcting the scattering parameters of the unknown test-set.

The inherent limitation in implementing merely full two-port SOLT calibration is that only complex travelling wave ratios can be determined accurately but not the absolute power and phase of the travelling waves. This restriction is due to the unknown transfer function present between the dependent node a_1 and the independent node a_0, called as coupler tracking e_{10} shown in Figure 4.4. This is conventionally scaled down to unity during error model extraction process.

Power Calibration

The second step, referred to as power calibration, is mainly intended to determine the scaling parameter e_{10} or the coupler tracking [55]. In case of on-wafer measurements, for instance, the linear test-set includes probe heads, directional coupler, cables and switches along the path from the DUT reference plane to the receiver's measurement reference plane. In order to determine e_{10}, neglecting the forward and reverse leakage errors (generally included in classical 12-term systematic error model), a simplified 8-term error model has been considered as shown in Figure 4.4 for obtaining error-corrected large-signal complex travelling waves. The error model coefficient e_{10} can be extracted separately by measuring the wave ratio a_1/a_0 with $b_1 = 0$ [55].

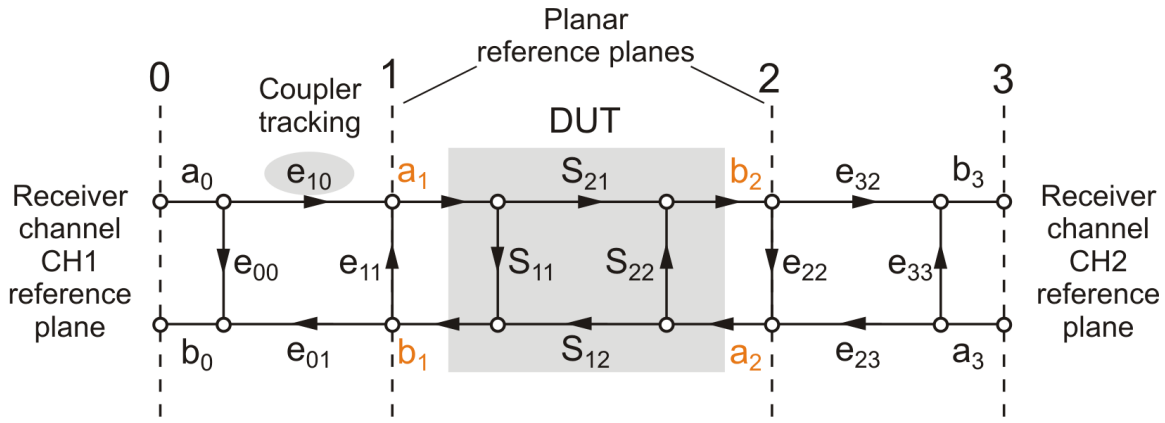

Figure 4.4 Simplified 8-term systematic-error model for vector error-corrected large-signal measurements.

One possibility to measure a_1 in case of on-wafer measurements is to directly connect port 1 (coplanar reference plane) in Figure 4.4 to receiver's CH2 (coaxial reference plane), which is impossible [54]. Alternately, with a coplanar through between port 1 and port 2 and considering the coaxial reference plane near to port 2, Benedikt *et al.* [55] proposed to shift port 2 reference plane by inserting a flexible coaxial cable between port 2 and receiver's CH2. The signal flow diagram for the corresponding setup is shown in Figure 4.5, wherein the complex S-parameters of the coaxial cable is predetermined at the required frequency points.

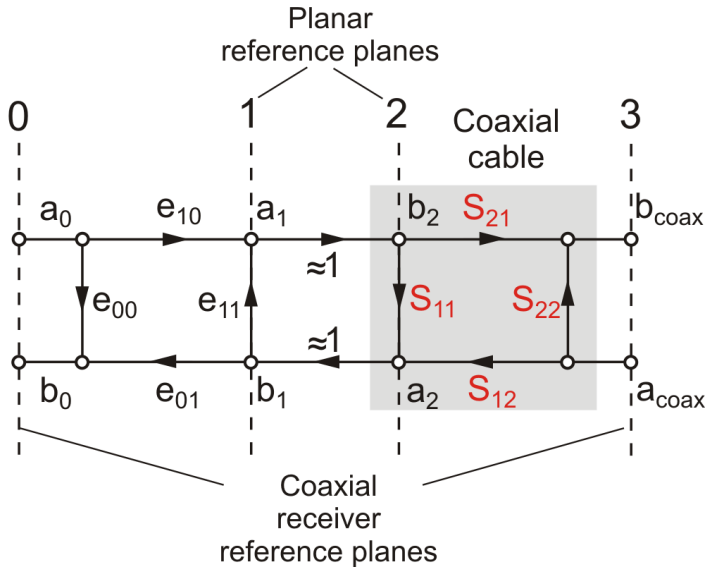

Figure 4.5 Modified error model after coaxial cable insertion. (Planar reference planes 1-2 are connected by a co-planar through line with 200 µm length.)

Further, with the measured complex wave ratio measurements of b_{coax}/a_0 ($a_{coax}= 0$), e_{10} can be computed as

$$e_{10} = \frac{S_{30}\left(1 - e_{11}S_{11}\right)}{S_{21}} \tag{4.1}$$

where

$$S_{30} = \left.\frac{b_{coax}}{a_0}\right|_{a_{coax}=0} \tag{4.2}$$

Subsequently, the complex power waves at port 1 and port 2, shown in Figure

4.4, can be calculated by using the following expressions:

$$a_1 = e_{10}a_0 + e_{11}b_1 \tag{4.3}$$

$$a_2 = e_{23}a_3 + e_{22}b_2 \tag{4.4}$$

$$b_1 = \frac{b_0 - e_{00}a_0}{e_{01}} \tag{4.5}$$

$$b_2 = \frac{b_3 - e_{33}a_3}{e_{32}} \tag{4.6}$$

Thus, the raw data measured at the receiver's reference plane is transformed to the DUT's reference planes. This calibration procedure indeed holds good not only for CW but also when characterizing the DUT under multi-tone excitation.

Vector Error-Correction Under W-CDMA Stimuli

Under W-CDMA excitation, the complex aperiodic signal captured by the receiver typically exhibits a continuous spectrum. Subsequently, error-correcting numerous frequency points (depending on the resolution bandwidth) in the relevant channels, namely, fundamental, lower- and upper sideband channels, become impractical, consuming much time during calibration and large-signal measurements. Besides, due to the continuously varying phase at these frequency points, real-time error correction poses another constraint. Hence, a simplified approach has been developed in this work.

With the underlying assumption of approximately constant frequency response of complex test-set parameters over 3.84 MHz bandwidth, three frequency points ($f_1 = f_c - \Delta f$, $f_2 = f_c$, $f_3 = f_c + \Delta f$), as shown in Figure 4.6, are calibrated, which follows the same procedure described for multi-tone case [68]. For vector error-correction, the complex raw data at these three frequencies are defined as follows:

- The magnitude of the measured vectors constitute the band powers (summation of powers of all frequency points within the specified band) of lower ACP band, the fundamental band and upper ACP band.
- The corresponding phase is measured at the respective centre frequency of each band $[\Phi(f_1), \Phi(f_2), \Phi(f_3)]$.

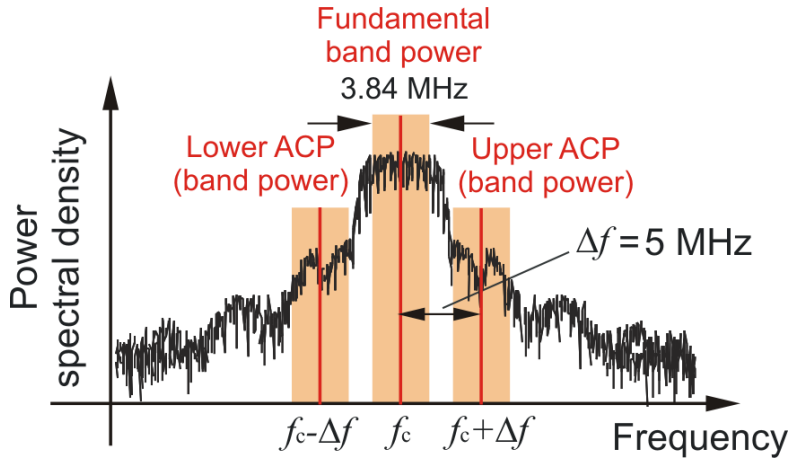

Figure 4.6 3GPP based UMTS spectral mask of a single-carrier W-CDMA spectrum depicting frequencies (f_c - Δf, f_c, f_c + Δf) at which vector error-correction is performed.

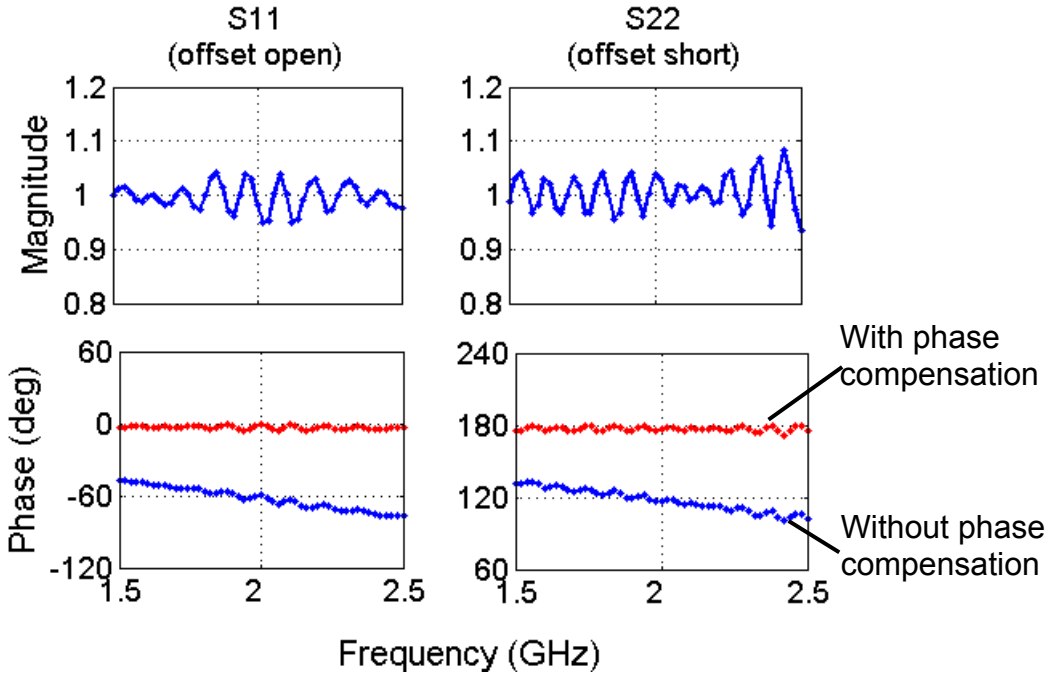

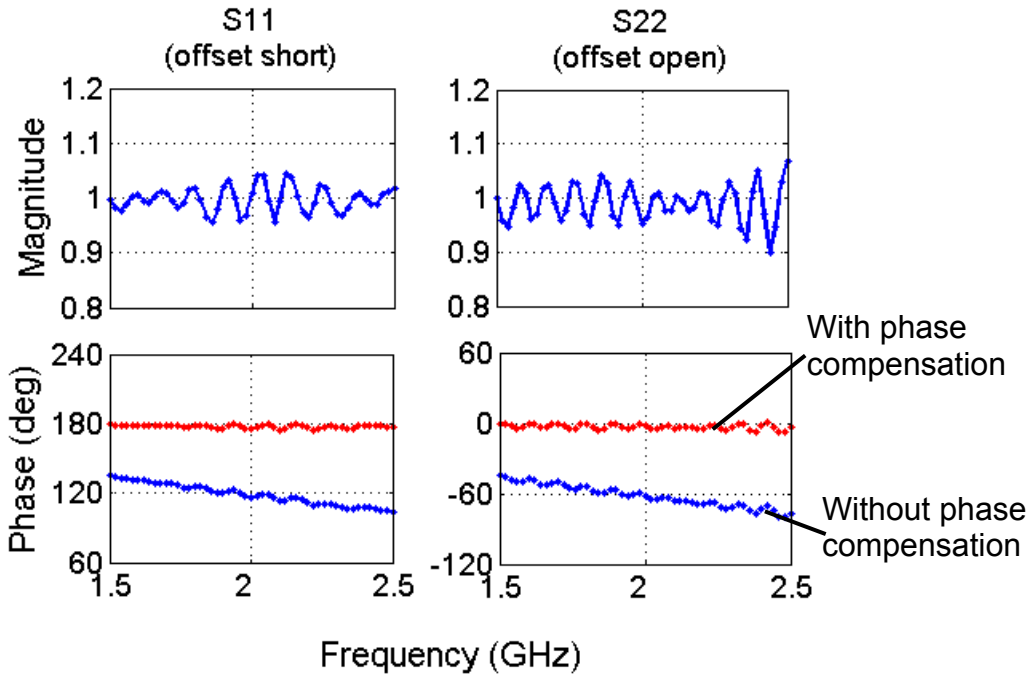

Figure 4.7 Calibrated 2-port complex ratio measurements using an adapter of length ℓ = 12.3 mm as DUT.

With the determination of all error-model parameters, the raw data measured during the large-signal measurements are error corrected by shifting the measured reference planes port 0 and port 3 to the calibrated reference planes port 1and port 2. Figure 4.7 illustrates the two-port reflection measurements conducted across the frequency range from 1.5 GHz to 2.5 GHz. An adapter of 12.3 mm length was used as an offset to verify the calibration under open and short terminations at both the input and output ports. A deviation of ±5% in magnitude and phase is observed, which is indeed acceptable for the current testbench application. A similar calibration procedure can be adopted for characterizing IMD and ACPR for multi-carrier W-CDMA stimuli, examples of which are discussed in chapter 5 and Appendix D. In this case the centre frequency of all relevant band are taken into account for calibration.

4.2 Termination Properties of IMD Based Testbench

The purpose of accurate IMD characterization is to measure distortion solely

resulting from the device. It is hence essential to assess the electrical properties of the measurement setup environment, which impact device inherent IMD behaviour. In this regard, Volterra series based IMD expressions can aid in localizing undesired distortion components that inhibit IMD measurements. The 3rd-order distortion current derived from Volterra series technique in Chapter 3 [equation (3.56)],

$$
\begin{aligned}
i_{ds,gm}(2\omega_1-\omega_2) = {} & \frac{3}{4}k_{3gm}v_{gs}(\omega_1)^2 v_{gs}(-\omega_2) \\
& + k_{2gm}v_{gs}(2\omega_1)v_{gs}(-\omega_2) + k_{2gm}v_{gs}(\omega_1-\omega_2)v_{gs}(\omega_1) \\
& + \frac{1}{2}k_{2gmgds}\begin{bmatrix} v_{ds}(2\omega_1)v_{gs}(-\omega_2) + v_{ds}(\omega_1-\omega_2)v_{gs}(\omega_1) \\ +v_{gs}(2\omega_1)v_{ds}(-\omega_2) + v_{gs}(\omega_1-\omega_2)v_{ds}(\omega_1) \end{bmatrix} \\
& + \frac{1}{4}k_{3gm2gds}\left[\, 2v_{gs}(\omega_1)v_{gs}(-\omega_2)v_{ds}(\omega_1) + v_{gs}(\omega_1)^2 v_{ds}(-\omega_2)\right] \\
& + \frac{1}{4}k_{3gmgds2}\left[\, 2v_{gs}(\omega_1)v_{ds}(-\omega_2)v_{ds}(\omega_1) + v_{ds}(\omega_1)^2 v_{gs}(-\omega_2)\right]
\end{aligned}
\tag{4.7}
$$

represents the lower IMD3 current contribution from nonlinear channel conductance G_m at the drain node. With the 2nd-order distortion restriction applied to the input, the IMD3 is not only influenced by the fundamental frequency components (ω_1, ω_2), but also by baseband (ω_1-ω_2) and 2nd-harmonic ($2\omega_1$) terms.

In (4.7), one of the dominant parameters, controlling $i_{ds,gm}(2\omega_1-\omega_2)$ current source, is the 3rd-order term $0.75k_{3gm}v_{gs}(\omega_1)^2v_{gs}(-\omega_2)$. In a 50Ω measurement setup environment, the voltage vectors $v_{gs}(\omega_1)$ and $v_{gs}(-\omega_2)$ are functions of the impedance across the fundamental tones ω_1 and ω_2, which is generally fixed to 50Ω. The voltage vectors [$v_{gs}(\omega)$, $v_{ds}(\omega)$] of the remaining terms in (4.7), identified by the 3rd and 2nd-order cross-terms ($k_{3gm2gds}$, $k_{3gmgds2}$, k_{2gmgds}) together with 2nd-order coefficient k_{2gm}, depend on the out-of-band termination properties, namely the envelope and second-harmonic zones.

It is important to note that during the RF operation of the device, the asymmetrical compression of the drain current waveforms along the loadline gives rise to even harmonics [56], [69]. Moreover, under modulated signal excitation, the even harmonics would also exist in the form of baseband components. As a result, the even harmonic terminations become relevant for nonlinear class of operation including class-AB, class-B, and class-C [70].

Under single-tone excitation, Figure 4.8 shows a typical example of drain current waveform of a 10 x 200 µm GaN HEMT (manufactured by Nitronex) measured using microwave transition analyser (MTA 71500A) in a 50Ω environment [54]. The relative magnitude of the harmonics generated by asymmetrical class-AB (biased at 20%I_{DSS}) and class-B waveforms are consistent with the Fourier series principle. It is evident that, as the quiescent bias is shifted from class-A towards class-B operation, the asymmetry in the drain current waveform becomes stronger generating both even and odd harmonics. As a result, it is interesting to systematically examine the factors influencing the out-of-band terminations of the measurement setup.

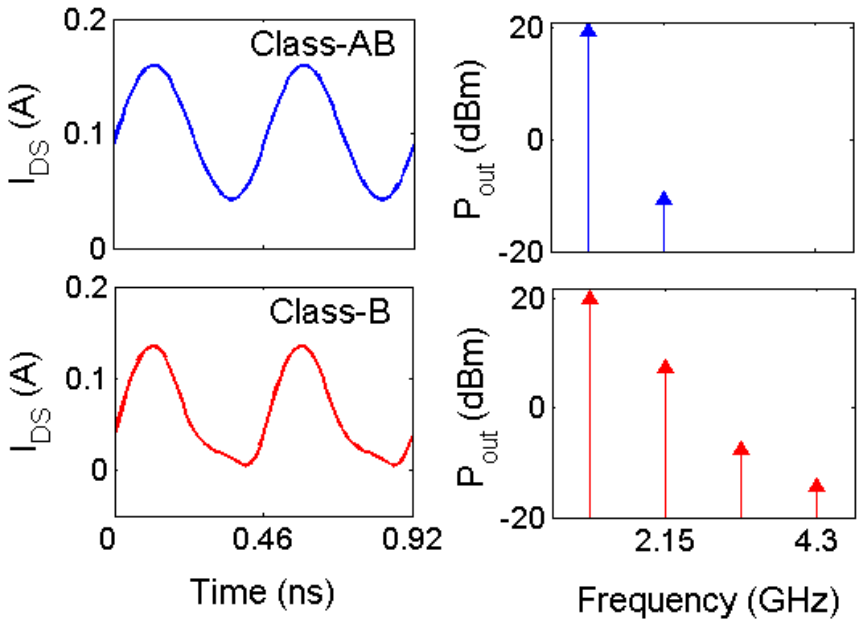

Figure 4.8 Measured time-domain output current waveform and spectral components under CW excitation of the analysed 2-mm GaN HEMT under class-AB (-1V, 15V, 20%I_{DSS}) and class-B (-1.5V, 15V) operation at f_c = 2.15 GHz.

Bias tees are one of the key components used in the measurement setup, which must be treated sensitively when dealing with broadband active device characterization. Commercially available bias tees only focus on wideband RF performance while completely neglecting its influence at baseband frequencies. In contrast, however, it is a common practice in the power amplifier architectures to design bias networks, which provide short at the envelope frequencies. This principle should be adopted even at the device-level characterization, which could eliminate $v(\omega_2-\omega_1)$ voltage vector. From the perspective of the measurement setup, an added advantage of following this strategy through bias tee design, would be to achieve repeatability of device specific IMD behaviour in all testbenches, eliminating any practical ambiguity caused by tuning the modulation bandwidth of the test signals.

4.3 RF Bias Network - Design Guidelines

Operating an RF FET device into partial or full conduction relies on supplying a constant DC bias to the gate and drain node of the active device through appropriate impedances. These requirements are fulfilled by the bias networks, which can be realized using inductances and capacitances either in lumped form or as distributed networks. The input-output terminating impedances of an RF active device is primarily determined by the bias circuit parameters. In FET devices, both, gate and drain bias networks have an overlapping role to isolate any leakage of RF signal into the bias supply line. This condition must be fulfilled without disrupting the device input and output matching and further preventing the device going unstable.

Gate Bias Network

Apart from providing a DC bias to the device's gate node, the gate bias network has to limit the gate current under breakdown conditions (drain-to-gate or gate-to-source), when the device is overdriven. Further, FET devices

often encounter problems of instability, when operating at higher quiescent point giving rise to oscillations. In other words, the input impedance of the device tends to exhibit negative resistance, leading to signal leakage into the DC path [29], [71]. In order to eliminate the negative resistance, a resistor is placed in the DC path, which is typically estimated as $R = 400/P_{sat}$, where P_{sat} is the saturated output power of the device [72]. Due to very low gate current flowing through the gate bias supply, there is negligible voltage drop across the resistor, thereby not affecting the gate voltage applied to the FET device. Resistive gate biasing also avoids memory effects at the input, but at high modulation frequencies, gate impedance starts to decrease due to the C_{gs} nonlinearity [14].

Drain Bias Network

In drain bias circuits, the traditional technique of implementing a high value inductor still holds good for applications involving signals with constant envelope schemes. In such cases, the baseband distortion component modulating along the DC path is totally absent. However, the requirements tend to escalate with the increase in signal complexity, placing stringent restrictions on the conventional drain bias network design. In other words, with the introduction of non-constant envelope signal, as was discussed in Chapter 2, a second-order distortion component arises at the baseband frequency because of the active device's nonlinearity. Consequently, the bias network has to satisfy two parallel requirements. The impedance offered by the DC path of the bias network must be high enough to exhibit an open at the RF and low enough (ideally short) to suppress any low frequency components, resulting in DC supply modulation, entering the DC path. Because of the vastness of bias network design subject, the following section will mainly focus on drain biasing issues and its relevance towards IMD/ACPR characterization under broadband multi-carrier stimuli for UMTS applications.

4.3.1 Characterization Testbench - Baseband and RF Perspective

Until recently, the RF bias tees were used mainly to provide the DC bias for the active device during characterization. But with the introduction of broadband measurement setups, an additional function of the bias tee is to provide a fixed baseband impedance (preferably short) for the entire operational frequency range [73]. Particularly, in terms of reliable CAD model verification of IMD, baseband short preserves repeatability and consistency of IMD characterized in different testbenches. In this context, since each of the commercially manufactured bias tees exhibit distinct baseband response, the broadband distortion measurements performed using different bias tees becomes a subject of debate. For this reason, two commercially available RF bias tees namely, HP11612A manufactured by Hewlett-Packard [74] and AU0616 manufactured by Auriga [75] are investigated as shown in Figure 4.9 and Figure 4.10 in order to understand their primary drawback in characterizing broadband intermodulation distortion.

Figure 4.9 shows a photograph, the equivalent circuit and reflection measurement of a commercial RF bias tee HP11612A. The tapered inductor coil along the DC path [Figure 4.9(a)], which is equivalent to a distributed network, is specified to deliver a wide stopband characteristics from 400 MHz to 26.5 GHz. The blocking capacitor is placed in series with the RF line to prevent DC voltage across the load termination. To avoid any influence from the baseband components on the device's IMD response, it is necessary to provide a short termination (Γ_L = -1) at the device input/output port across envelope frequencies. Figure 4.9(c) illustrates the baseband reflection coefficient Γ_L of HP11612A measured using Rohde & Schwarz vector network analyser (VNA) of type ZVR-E (9 kHz - 4 GHz) [76].

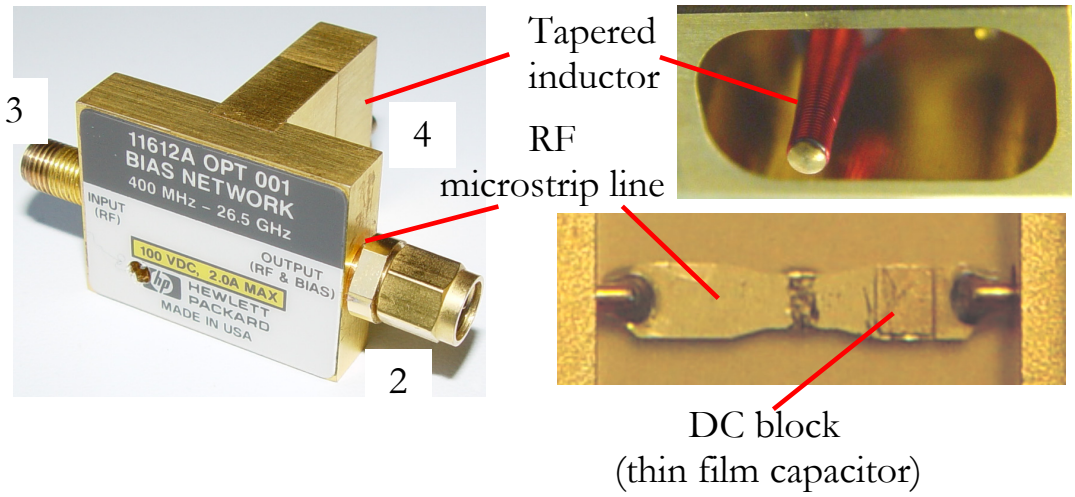

(a)

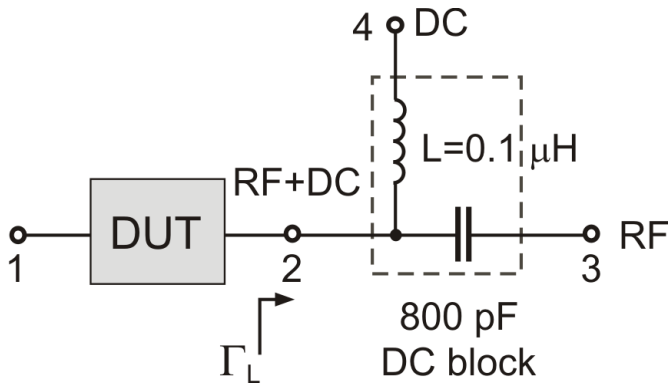

(b)

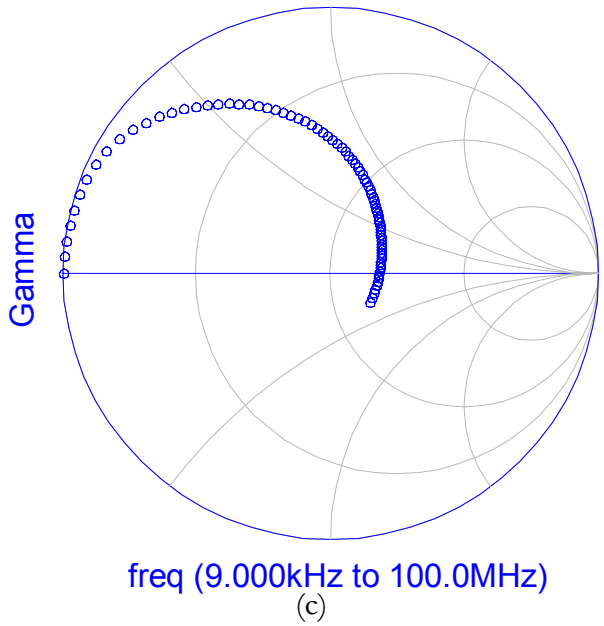

(c)

Figure 4.9 (a) Photograph of a commercial RF bias tee of type HP11612A (0.4 - 26.5 GHz, V_{max} = 100V, I_{max} = 2A) manufactured by Hewlett-Packard [74], (b) schematic, (c) measured baseband Γ_L using VNA with DC port grounded.

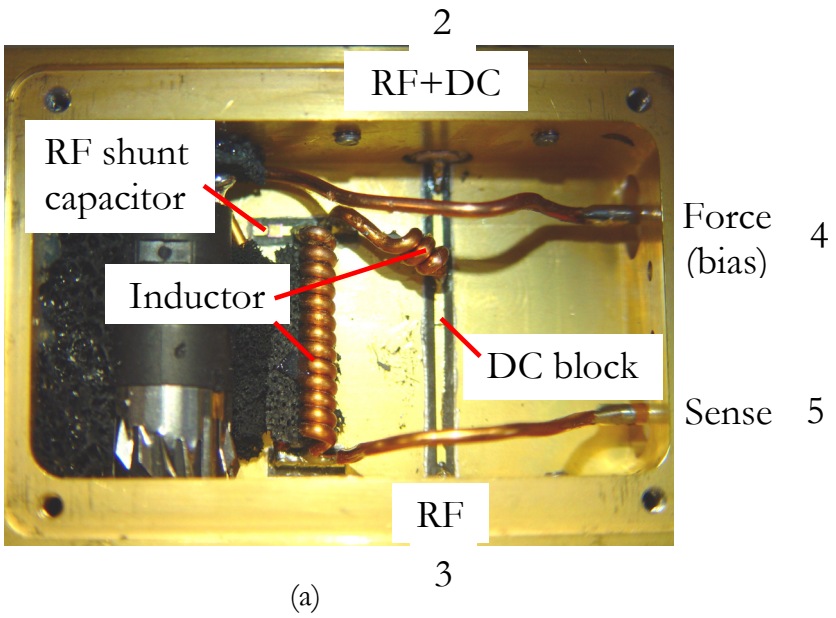

(a)

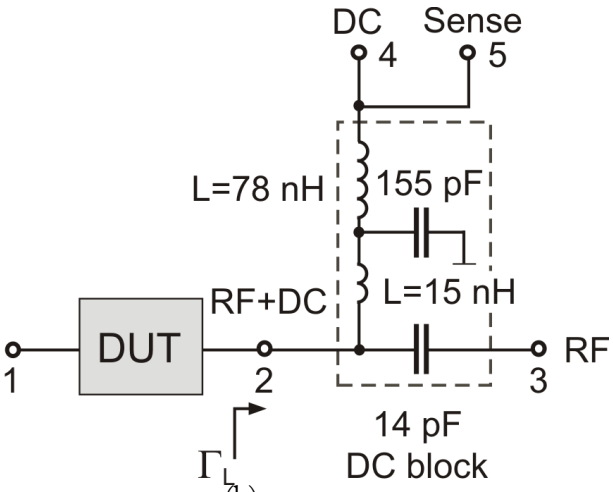

(b)

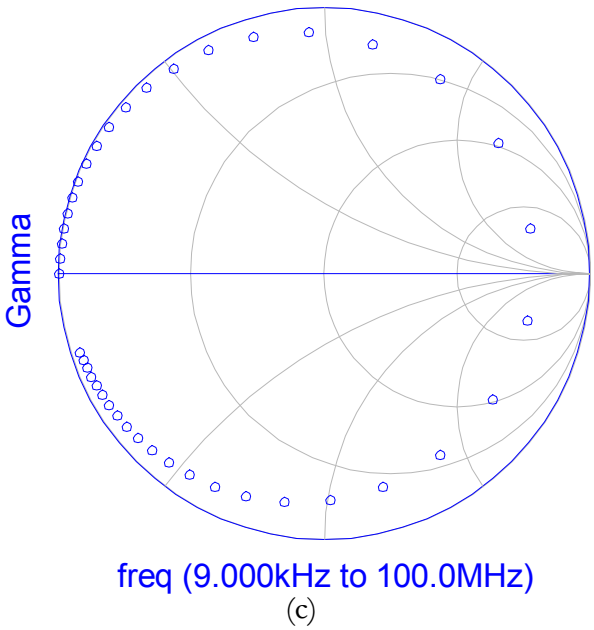

(c)

Figure 4.10 (a) Photograph of a commercial RF bias tee of type AU0616 (1 - 7 GHz, V_{max} = 50V, I_{max} = 15A) manufactured by Auriga [75], (b) schematic, (c) measured baseband Γ_L using VNA with DC port grounded.

From Figure 4.9(c), it is evident that for broadband measurements, the condition for the baseband $\Gamma_L = -1$ is no longer fulfilled. This is clearly due to the high inductance in series with the DC port (port 4) meant to realize wide RF bandwidth coupled with a high DC block capacitance. A similar conclusion can be made taking an example of another commercial RF bias tee AU0616, a photograph, equivalent circuit and the reflection measurement of which is shown in Figure 4.10. AU0616 has an additional port 5 to sense the bias voltage apart from the traditional force or bias port (port 4) through which the DC is fed to the DUT. As depicted by the equivalent schematic in Figure 4.10(b), AU0616 implements a stopband filter for an operational bandwidth from 1 GHz to 7 GHz, comprising an RF capacitor shunting the inductor. The values of the lumped components were extracted by optimisation from S-parameter measurement data.

Practically, the external electrical parameters impose limitations in retaining the true properties of bias tees. Gallou *et al.* [16], for the first time, experimentally demonstrated that the non-ideal DC bias feed, constituting the biasing cable and the DC source, add series impedance to the biasing circuit. This might well explain the reason for obtaining an optimal complex baseband termination, published by Sevic *et al.* [77], through envelope load-pull measurements performed on LDMOS. The reported results demonstrated excellent sideband asymmetry suppression, simultaneously reducing lower and upper ACPR with $Z_{L,env} = (55 - j80)\Omega$, contradicting commonly held belief that the envelope termination should be approximately zero at the input/output device reference plane. Consequently, it becomes questionable to conclude the device nonlinearity as the sole cause of spectral distortion. Before analysing the impact of baseband termination on GaN HEMT's IMD behaviour, the reflection coefficient Γ_L of the bias tees was measured at the baseband frequencies as shown in Figure 4.11(a). HP11612A RF commercial bias tee was measured along with the DC bias feed, which constituted the

biasing cable (length of 2.5m was used) and DC source. It was confirmed that the DC source indeed has negligible influence. It can be seen from Figure 4.11(b) that at 10 MHz (M1), for example, Z_L = (155 + j239.8)**Ω**, which is clearly a non-zero complex impedance.

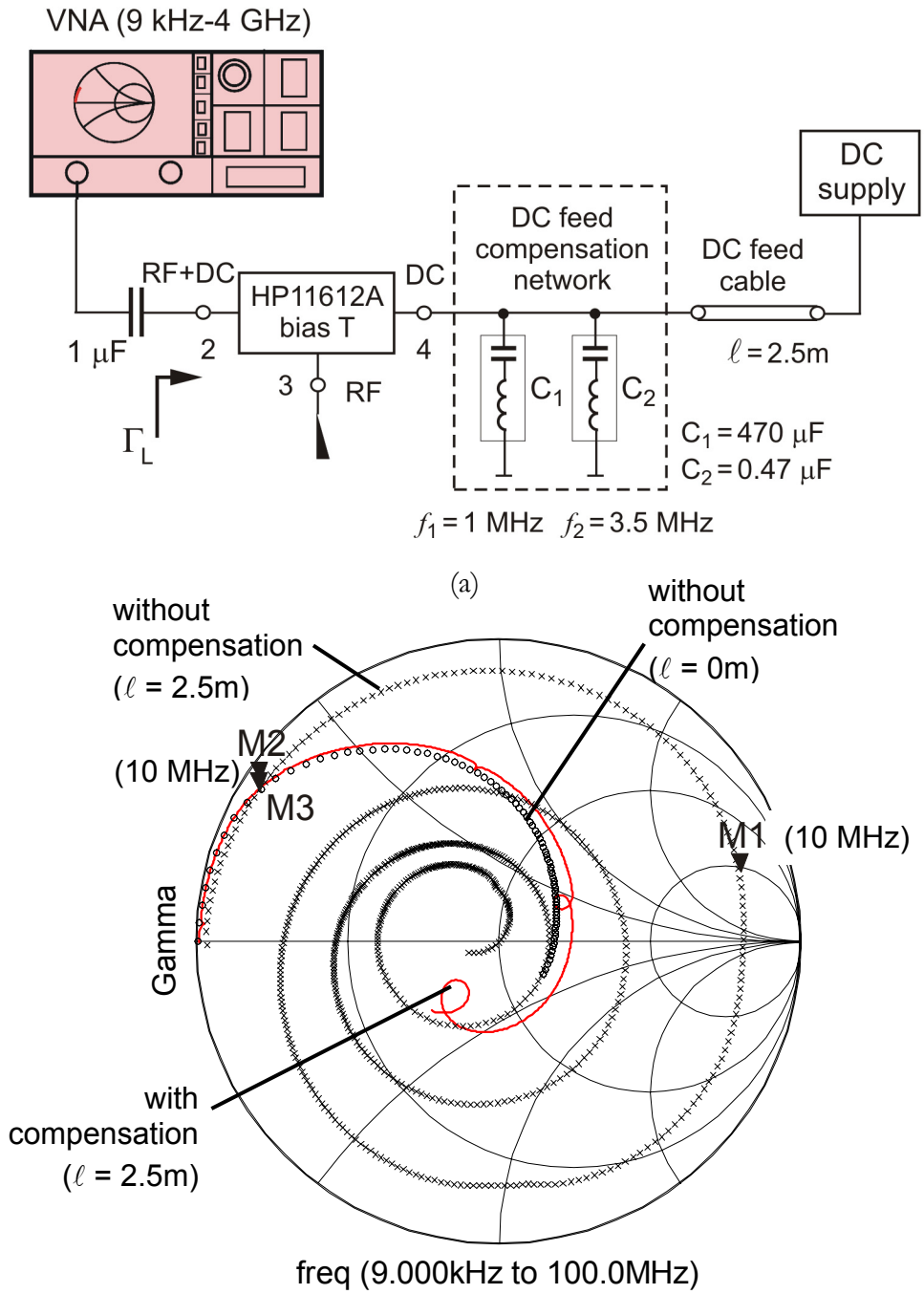

Figure 4.11 Baseband Γ_L measurement of HP 11612A bias tee together with the DC bias feed (without and with capacitive compensation) using VNA [73].

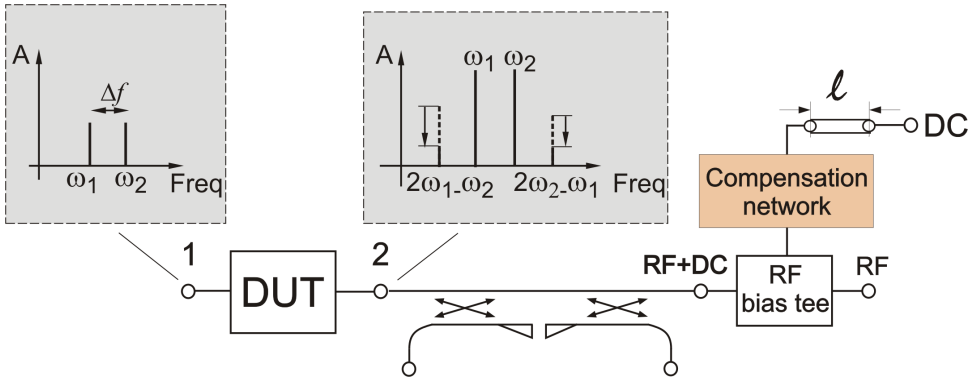

Figure 4.12 Measurement setup optimised to eliminate DC feed induced uncertainties.

This additional series impedance offered by the DC feed was eliminated through bias compensation of drain bias tee, as illustrated in Figure 4.12. This network constitutes two shunt capacitances (C_1 = 470 μF electrolytic capacitor, C_2 = 0.47 μF ceramic capacitor), whose series resonance frequency (SRF) is in the range of the modulation bandwidth of interest. Hence, these capacitors have a dual role of filtering low frequency components originating from the nonlinear device and to decouple undesired impedance of the imperfect DC feed. The series resonance frequency can be expressed as

$$f_{SR} = \frac{1}{2\pi\sqrt{L_S C}} \tag{4.8}$$

where L_S accounts for the parasitic inductance of the capacitor [78]. From the frequency response of the capacitor, f_{SR} can be determined at the point where the net reactance ($\sqrt{X_L - X_C}$) across the capacitor becomes approximately zero. In other words, from the phase characteristics of the transmission response (S_{21} or S_{12}), the zero crossing indicates the f_{SR} value. For C_1 and C_2, the f_{SR} was measured as 1 MHz and 3.5 MHz, respectively. As shown in Figure 4.11(b), an improved Γ_L was obtained, indicating the minimum achievable limit which reflects the inherent bias tee characteristics. At 10 MHz (M2), the load impedance is reduced to Z_L = (1.4 + j13.6)Ω, which is approximately in agreement with the bias tee's baseband response when the DC port is terminated with a short (ℓ = 0).

To examine the impact of the baseband termination properties, distortion analysis was carried out on an 8 x 500 μm GaN HEMT [manufactured by Ferdinand-Braun-Institute for High Frequency Technique (FBH), Berlin]. However, before analysing the large-signal distortion characteristics, it is important to get a general idea about the bias conditions which sensitise the bias network properties.

Pulsed I(V) characteristics provide a simple method of allowing the loadline to be mapped without RF measurement [79]. Hence, pulsed DC characterization of a 4-mm GaN HEMT was performed using Accent DiVA D265EP system [80]. Figure 4.13 illustrates the pulsed I(V) characteristics together with the extracted drain current values and the corresponding higher order derivatives along an ideal 50Ω loadline. In order to derive a reliable higher order derivatives of I(V) characteristics, a dense grid of drain current curves is often measured to avoid discontinuity problems, especially around the sub-threshold region (turn-on zone). Tracing G_{m2} curve in Figure 4.13(b) across the device turn-on zone ($G_{m2} \neq 0$, implying significant 2^{nd}-order distortion contribution), and referring to (4.7), it is evident that the impact of envelope termination is critical for nonlinear FET operation comprising of class-AB, class-B and class-C bias conditions.

Two-tone characterization was performed at f_c = 2.1 GHz, with 9 MHz tone spacing biased at deep class-AB with V_{DS0} = 15V. Figure 4.14 shows the measured fundamental power, IMD characteristics, and IMD asymmetry curves for -3.5V and -3.6V gate bias voltages. Due to high baseband termination before compensation, monotonically increasing IMD curves ($IMDU_{(w/o\ comp)}$, $IMDL_{(w/o\ comp)}$) can be seen in Figure 4.14(a). However, with the implementation of drain bias compensation, the envelope distortion component contributing to the overall IMD is eliminated. As a result, a dramatic reduction in lower and upper IMD is observed in Figure 4.14(a-b).

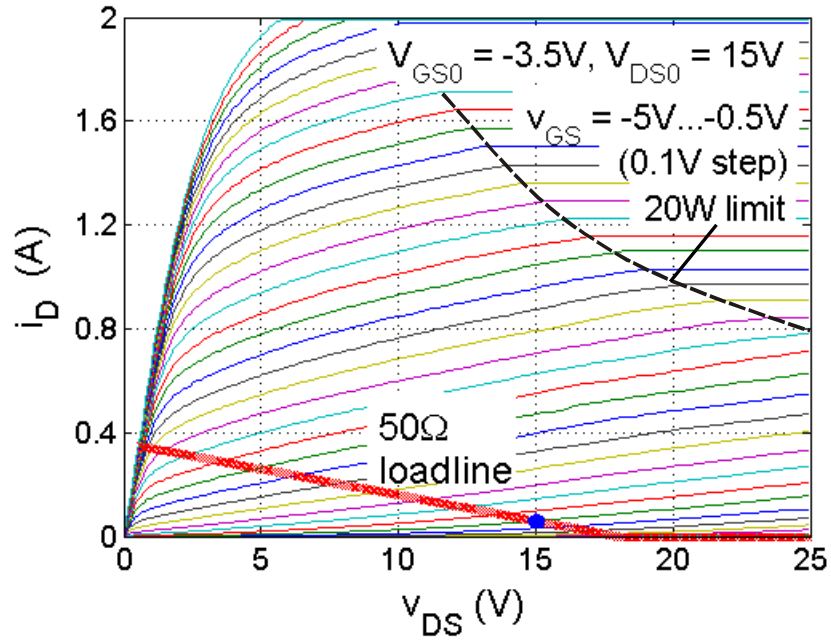

(a)

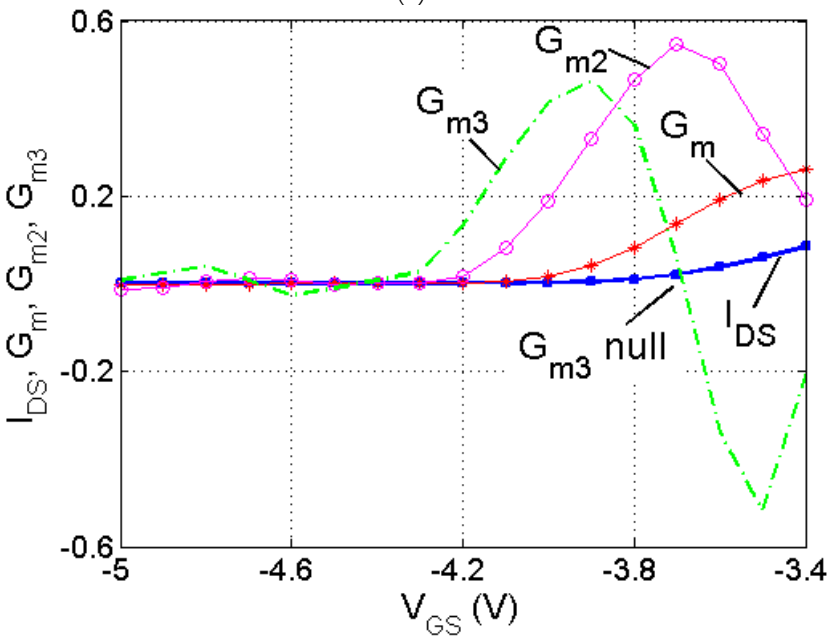

(b)

Figure 4.13 (a) Measured pulsed DC I(V) characteristics of an 8 x 500 µm GaN HEMT mounted on copper bar, (b) extracted Taylor series coefficients of the drain current along the 50Ω loadline. Quiescent bias of V_{GS0} = -3.5V and V_{DS0} = 15V with 1 ms pulse width and at 1 ms pulse repetition period.

Further, typical IMD properties like large-signal IMD sweet-spot with a double minima, which are sensitive to quiescent bias, is revealed in the upper IMD characteristics with a maximum of 40 dB IMD3 suppression. Interestingly, the compensation effect is also reflected on the peak output power performance, which is increased by 3 dB and 2.5 dB at 3-dB compression point (Pin ≈ 18 dBm) for gate bias of -3.5V and -3.6V, respectively. This demonstrates almost two-fold increase in output power only by baseband optimisation.

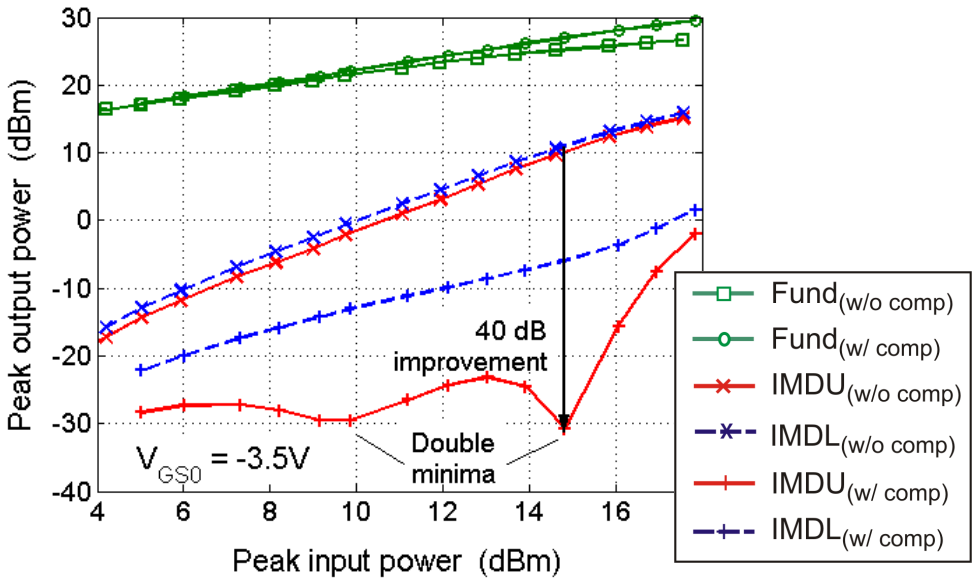

(a)

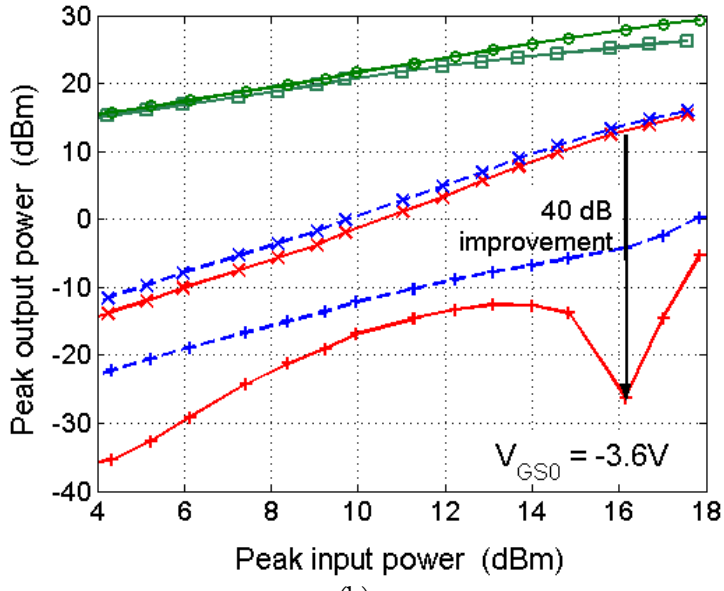

(b)

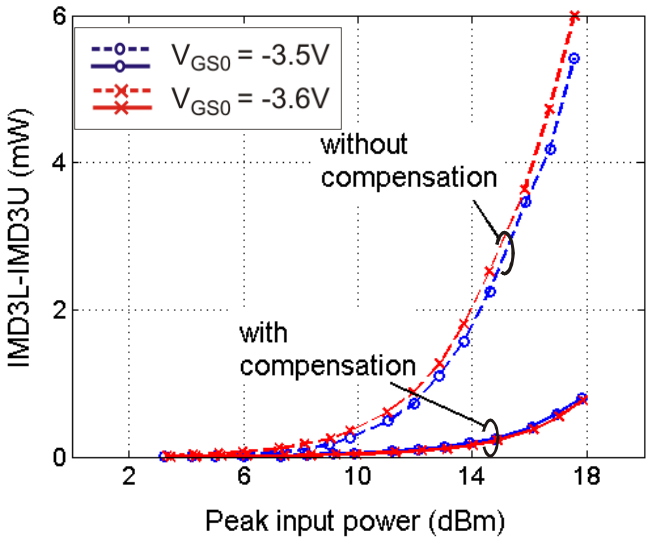

(c)

Figure 4.14 Two-tone characterization of 4-mm GaN HEMT depicting linearity and memory-effect improvement after baseband compensation.

Impact of DC Feed Length on IMR Measurements

Incorporating the compensation network into the measurement setup, the influence of DC feed on IMR and ACPR characteristics was investigated by varying the feed cable lengths, which is analogous to envelope load-pulling. Figure 4.15 illustrates IMR/ACPR and IMD/ACP asymmetry curves of the measured 3.2-mm gate width GaN HEMT [manufactured at the Fraunhofer Institute for Applied Solid-State Physics (IAF), Freiburg] biased for class-AB operation (-3V, 25V, 4%I_{DSS}). The DUT was characterized under two-tone (Δf = 5 MHz) [Figure 4.15(a-b)], single-carrier [Figure 4.15(c-d)] and two-carrier W-CDMA (Δf = 15 MHz) [Figure 4.15(e-f)] stimuli for different cable lengths varying from 0.5m to 2.7m.

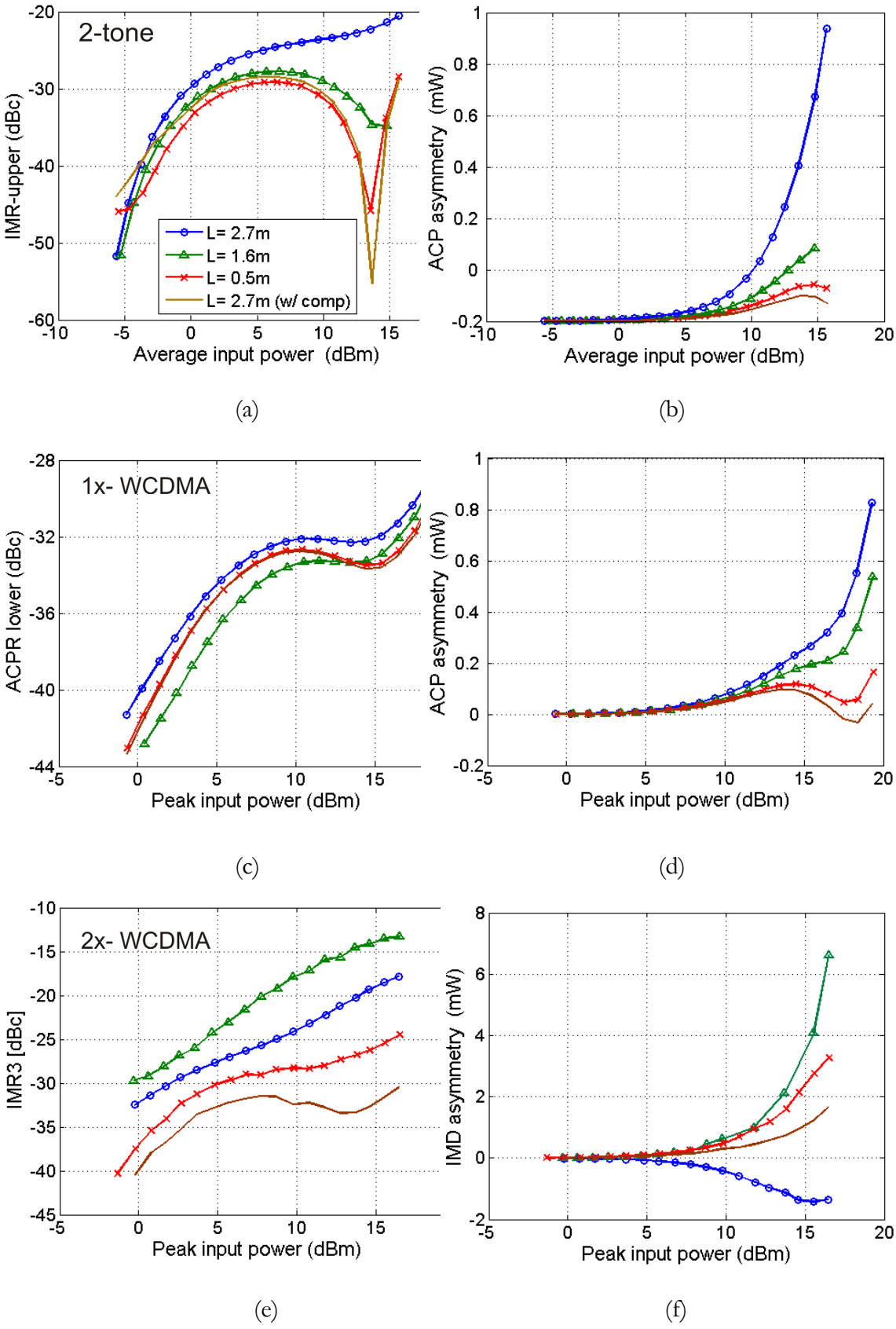

Figure 4.15 Measured lower and upper-IMR3 and IMD3 asymmetry of a 3.2-mm GaN HEMT for varying DC feed cable length [68].

Table 4.1 In-band distortion of 3.2-mm GaN HEMT without and with DC feed compensation.

	W/o DC feed compensation	*W/ DC feed compensation*
2-tone (Δf = 5 MHz) at $P_{out, peak}$= 33 dBm		
IMR (dBc)	-25.32	-58.27
ΔIMD (mW)	3.03	0.49
1x W-CDMA at $P_{out, peak}$= 30 dBm		
ACPR (dBc)	-31.97	-33.64
ΔACP (mW)	0.267	0.076
2x W-CDMA (Δf=15 MHz) at $P_{out, peak}$= 30 dBm		
IMR (dBc)	-20.28	-33.34
ΔIMD (mW)	-1.13	0.75

The dip in IMR3 curve observed in Figure 4.13(a) after drain compensation is thus a principally expected device property, which is now revealed since the bias tee with the baseband trap has considerably suppressed the IF distortion component contribution, which was co-existing with the in-band IMD. The shortest cable with a length of 0.5m offers comparable performance with drain bias compensated case. This indicates the need to use shorter cables while characterizing distortion in active devices. However, in case of single-carrier W-CDMA, the variation in ACPR characteristics is not pronounced in comparison with two-tone excitation due to the dominant higher order IMD products within the sidebands. This issue is addressed in detail in Chapter 5 and Appendix D. Nevertheless, as shown in Figure 4.15(d), the ACP asymmetry behaviour drastically improves with the reduction in cable length demonstrating a strong suppression of memory-effects [68]. In contrast, a distinct variation in IMR behaviour in Figure 4.15(e) is observed under two-carrier W-CDMA similar to the two-tone case. It is interesting to note that the IMR curve for a cable length of 2.7m is lower compared to the IMR measured using 1.6m cable length. This is because the baseband termination imposed by the bias tee at 15 MHz for a cable length of 2.7m [(15.45 - j58.05)Ω seen in Figure 4.11(b)] increases when the cable length reduces to 1.6m. A summary of the measurement results is tabulated in Table 4.1.

Figure 4.16 illustrates a principle impedance characteristics of a commercial RF bias tee across relevant frequency zones, whose baseband impedance increases monotonically due to the typical inductor component. Additionally, the DC feed of length $l < \lambda/4$, which represents an inductor for baseband frequencies, imposes an electrical offset short. The RF band, however, remains constant, providing 50Ω across both zone 1 and zone 2. Nevertheless, despite solving the DC feed problem through capacitive compensation mechanism, the inherent inductor apparently posed restriction in achieving lower impedance value at envelope frequencies, encouraging to design in-house bias tees relevant for characterizing FET devices for UMTS applications.

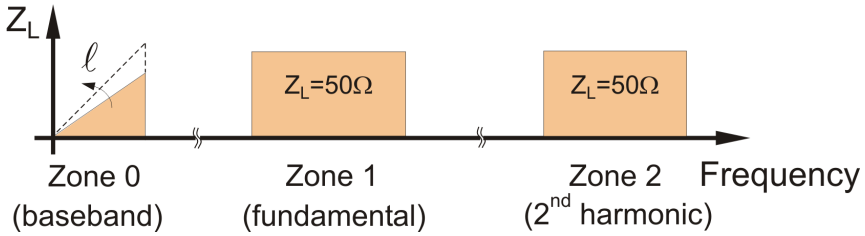

Figure 4.16 Principle IF and RF impedance response of a typical commercial RF bias tee in a 50Ω environment with a monotonically increasing IF impedance.

The design goal of an RF bias tee is shown in Figure 4.17, which shows a broadband short for zone 0 frequencies and a 50Ω for RF. However, there are practical difficulties as shown in Figure 4.17 in achieving the desired IF and RF termination properties. As regard to the baseband, the bandwidth of the short termination is limited by the series resonance frequency f_{SR} of the decoupling capacitors. Consequently, for higher modulation bandwidths, the inductance of the DC supply cable become critical. Further, the bandwidth of zone 1 termination is limited by impedance along the bias path, which should provide a high impedance for RF frequencies. Although, it is practically difficult to obtain a stopband response across zone 2, it has been proved that the impact of zone 0 termination on device IMD behaviour is more critical than zone 2 termination (Figure 5.6 of Chapter 5) [10]. With these design goal,

bias tees of different topologies were investigated at the drain terminal preserving primarily wideband 50Ω response around the operating carrier frequency.

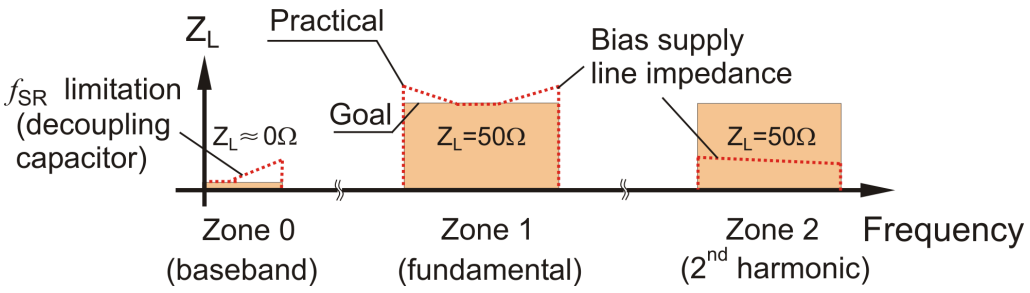

Figure 4.17 Design goal of an in-house bias tee depicting optimised IF and RF impedance response in a 50Ω environment.

4.3.2 Key Design Challenges

Before proceeding towards bias tee design, it is necessary to carefully select relevant circuit components, which is governed to an extent by the type of application under consideration. The objective is to establish an RF testbench to incorporate test signals with modulation bandwidth primarily fulfilling 20 MHz UMTS-LTE applications and further extended up to 100 MHz to demonstrate its application for future 4G schemes. This essentially means reinforcing (i) low envelope termination across 100 MHz bandwidth and (ii) constant 50Ω impedance over at least 300 MHz bandwidth around carrier frequency, taking into account even the IMD sidebands.

Envelope traps can be established by implementing a large video bypass capacitor with rather small inductance. Typically, a tantalum capacitor of 10 μF with 1.2 nH parasitic inductance, can be used, which presents an impedance of (0.15+j0.75)Ω and (0.84+j15.7)Ω at 100 MHz and 2.14 GHz, respectively [81]. However, in this work, monolithic ceramic capacitors of 1 μF and 10 μF (Murata GRM32 series) were used to achieve a broadband envelope trap. For determining the bandwidth, it is necessary to evaluate the

associated series resonance frequency (4.8). Using the models available from Murata design kit, the S-parameter simulation of 1 μF and 10 μF capacitors were performed in ADS®. Figure 4.18 illustrates the phase of the transmission coefficient S_{21} across the baseband from DC to 50 MHz. The series resonance frequency f_{SR} of the two capacitors can hence be determined by the zero-crossing of the phase of S_{21}, which are respectively 6 MHz and 2 MHz. Further, when both the capacitors are combined, the resonance property is still sustained.

Indeed, the lumped components being frequency dependent, cannot maintain a fixed low impedance for a wider frequency bandwidth. One possibility of enhancing the bandwidth is to consider decoupling capacitors with low quality factor $Q = |X_C - X_L| / R$, exhibiting significant parasitic inductance. However, the series resonance characteristics of the decoupling capacitors are strongly affected, restricting the realizable lower limits of the impedance at envelope frequencies. Nevertheless, another approach is to use several capacitors in parallel to facilitate the extended bypass frequency coverage.

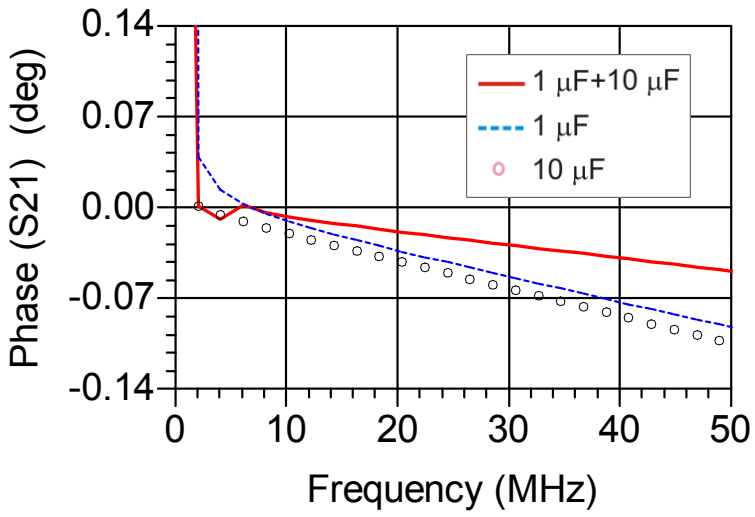

Figure 4.18 Evaluation of f_{SR} from the simulated phase of transmission coefficient S_{21} for various baseband decoupling capacitors.

Figure 4.19 illustrates the equivalent circuits and the corresponding photographs of the in-house designed drain bias circuit topologies realized on a plastic substrate (Taconic ADD TLX-9, ε_r = 2.51, h = 0.381 mm). Figure 4.19(a) shows a lumped inductor based bias tee, similar to the commercial RF bias tee configuration, which is designed with a reduced inductor value (L = 15 nH) to minimize overall baseband impedance [82]. Decoupling capacitors of 1 μF and 10 μF, which are implemented in all the in-house bias tee design, are shunted at the DC port to provide a baseband short. Further, as shown in Figure 4.19(b), a low impedance λ/4 short-circuited shunt stub (SCSS) of width w = 4.2 mm was designed to improve the envelope termination. The 22 pF bypass capacitor (AVX 0603 series) provides a narrowband short for λ/4 line at the carrier frequency, which is transformed to an open. Indeed this is achieved at the cost of RF bandwidth reduction due to low impedance λ/4 transmission line. Stubs of uniform microstrip transmission line with an electrical length of λ/4, generally, do not provide sufficient RF bandwidth [83]. A radial stub, on the other hand, exhibits a virtual ground at one end of λ/4 line, by transforming from open to short around the desired carrier frequency. Figure 4.19(c) shows the equivalent circuit and the photograph of λ/4 open-circuited radial stub based bias tee. The radial stub (l = 13 mm, w_i = 50 μm, a = 60°) provides a virtual ground at RF for the 50Ω λ/4 line (w = 1.05 mm).

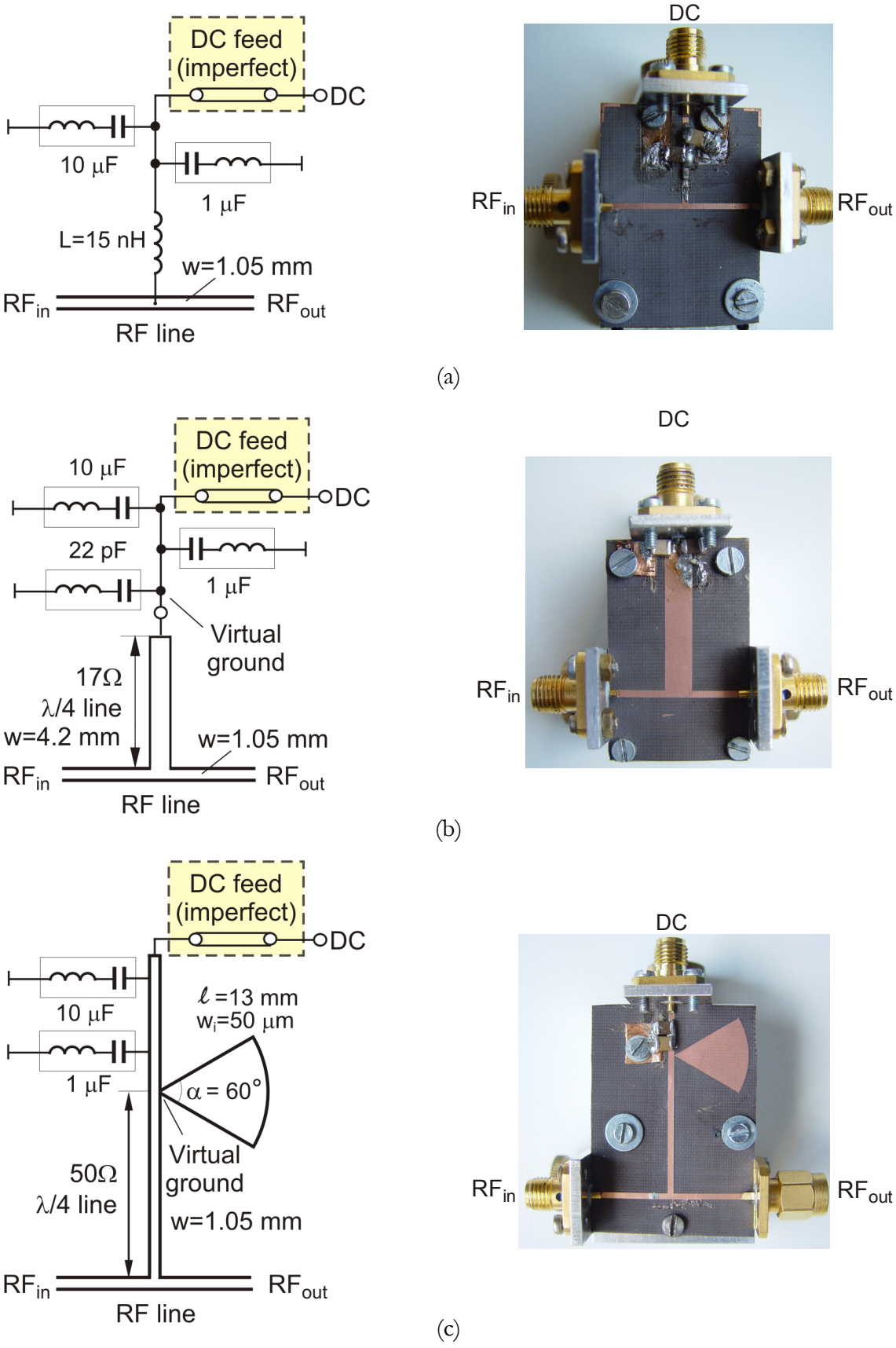

Figure 4.19 In-house designed drain bias tee schematics based on (a) lumped inductor, (b) low impedance quarterwave short-circuited shunt stub, and (c) quarterwave open-circuited radial stub.

Most literatures commonly discuss the RF bias tee performance characteristics in terms of the return loss, focussing mainly on the magnitude of the reflection coefficient ($|\Gamma|$). As a thumb rule, $|\Gamma|$ should be less than -10 dB at the operating frequency. However, additionally the circuits present a reactive impedance over the entire frequency band, which is generally ignored. As a result, this reactive impedance contributes towards electrical memory-effects, when presented across IMD products. For this reason, it is vital to examine the RF characteristics of the bias tee in impedance domain rather than restricting the specifications only to $|\Gamma|$ response.

Figure 4.20 illustrates the impedance of the commercial (HP11612A) and in-house RF bias tees under inspection measured using VNA measured across the baseband [Figure 4.20(a)], fundamental [Figure 4.20(b-c)], and 2^{nd}-harmonic [Figure 4.20(d-e)] frequencies. The baseband impedances of the respective bias tee variants are measured taking into account even the electrical effects of the DC feed (biasing cable, DC source having negligible influence). Since the research focus is towards UMTS basestation power amplifier applications, RF bandwidth was mainly considered around an operating frequency of 2.15 GHz. In Figure 4.20(b) and Figure 4.20(d), the commercial bias tee (Figure 4.9) demonstrates excellent RF response of constant 50Ω with negligible reactance as seen in Figure 4.20(c) and Figure 4.20(e). Such performance of the RF bias tee is indeed preferred mainly, when the DUT is characterized under CW excitation. However, with the increase in test signal complexity, constituting multiple carriers, the envelope impedance response of the bias tee becomes critical. From Figure 4.20(a), it can be observed that at 10 MHz, for example, an impedance as high as 500Ω is measured for the commercial bias tee (Figure 4.9). The reason is evident because of the DC feed length of the cable (l = 2.5m), which was taken into account while measuring bias tee characteristics.

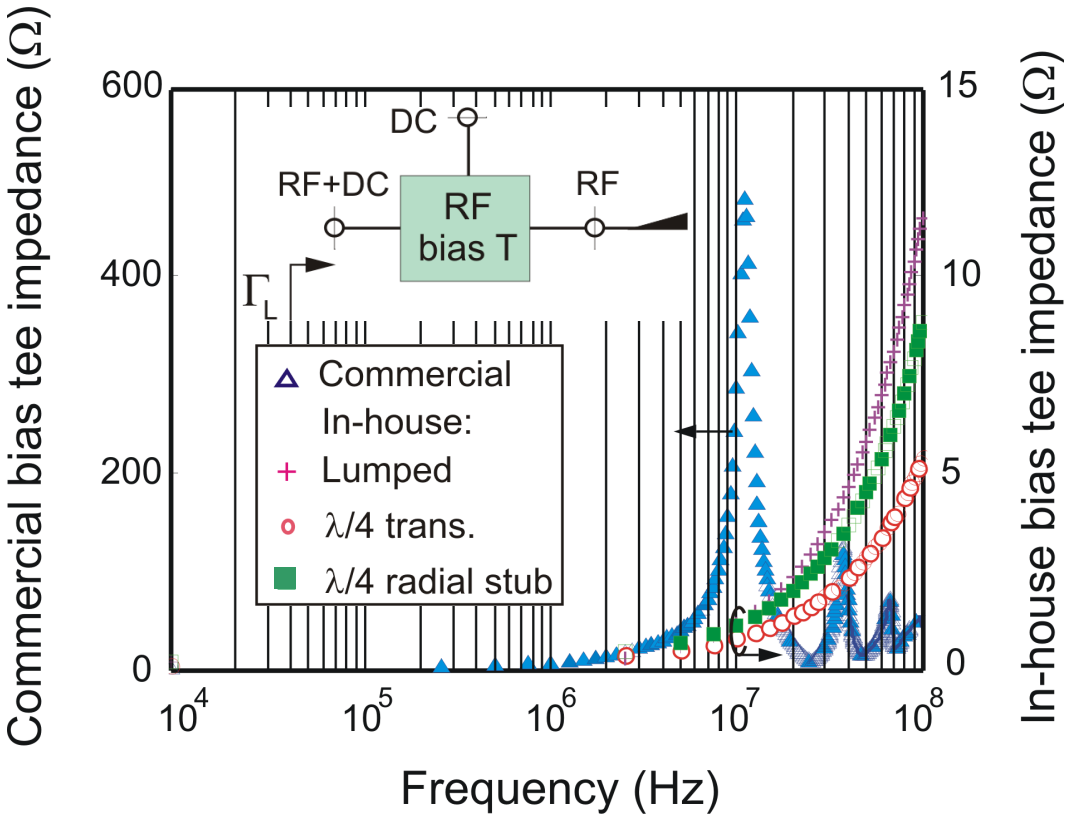
Commercial bias tee impedance (Ω)
In-house bias tee impedance (Ω)
600
400
200
0
15
10
5
0
DC
RF+DC
RF
RF
bias T
Γ_L
Commercial
In-house:
Lumped
λ/4 trans.
λ/4 radial stub
10^4
10^5
10^6
10^7
10^8
Frequency (Hz)

(a)

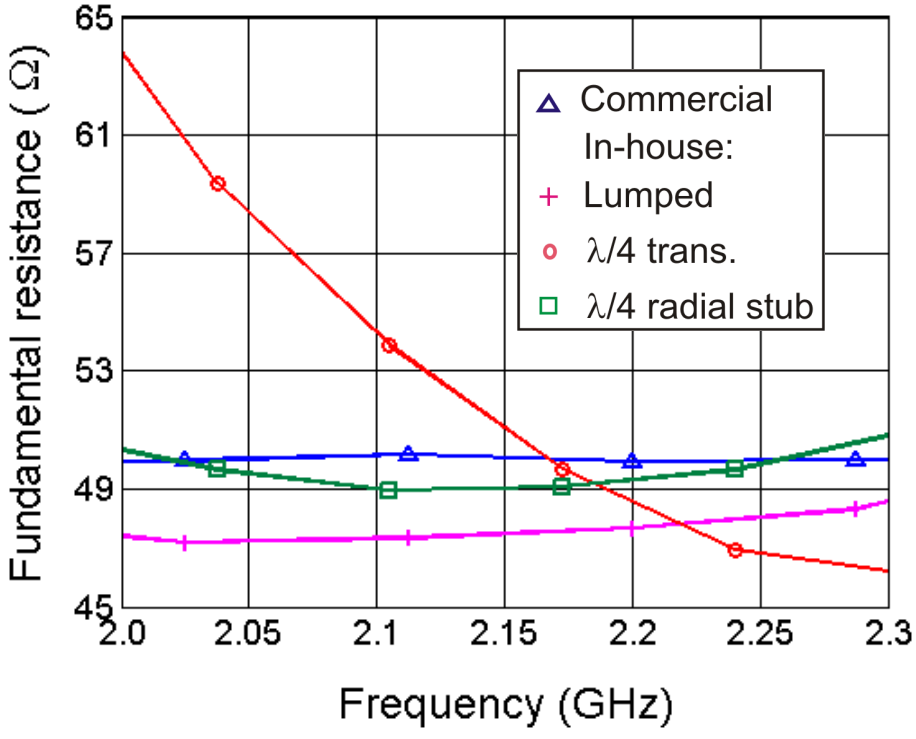
Fundamental resistance (Ω)
65
61
57
53
49
45
Commercial
In-house:
Lumped
λ/4 trans.
λ/4 radial stub
2.0
2.05
2.1
2.15
2.2
2.25
2.3
Frequency (GHz)

(b)

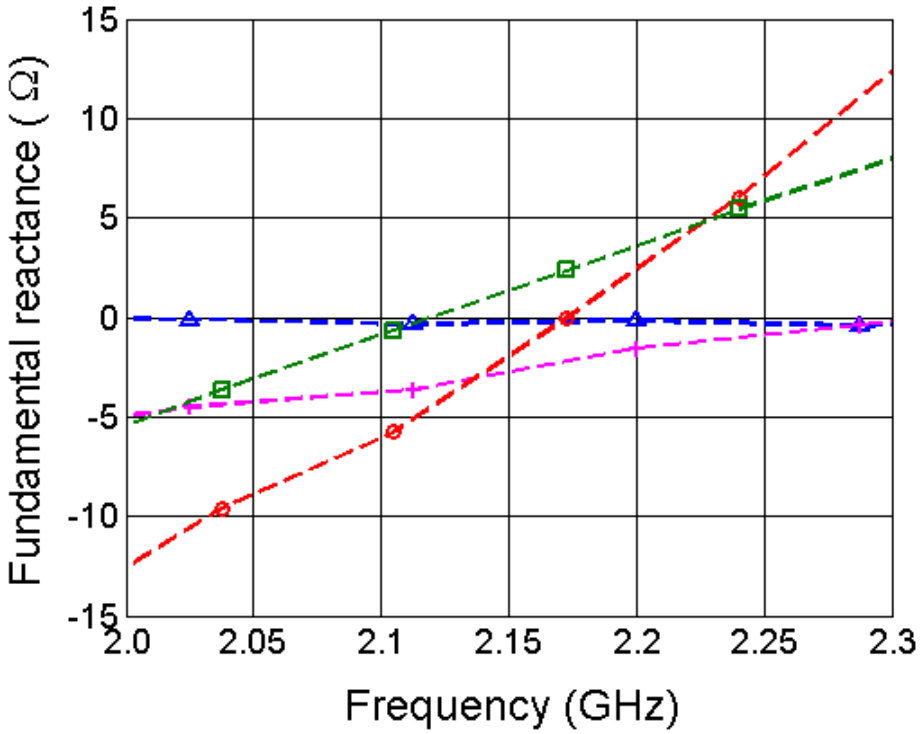
Fundamental reactance (Ω)
15
10
5
0
-5
-10
-15
2.0
2.05
2.1
2.15
2.2
2.25
2.3
Frequency (GHz)

(c)

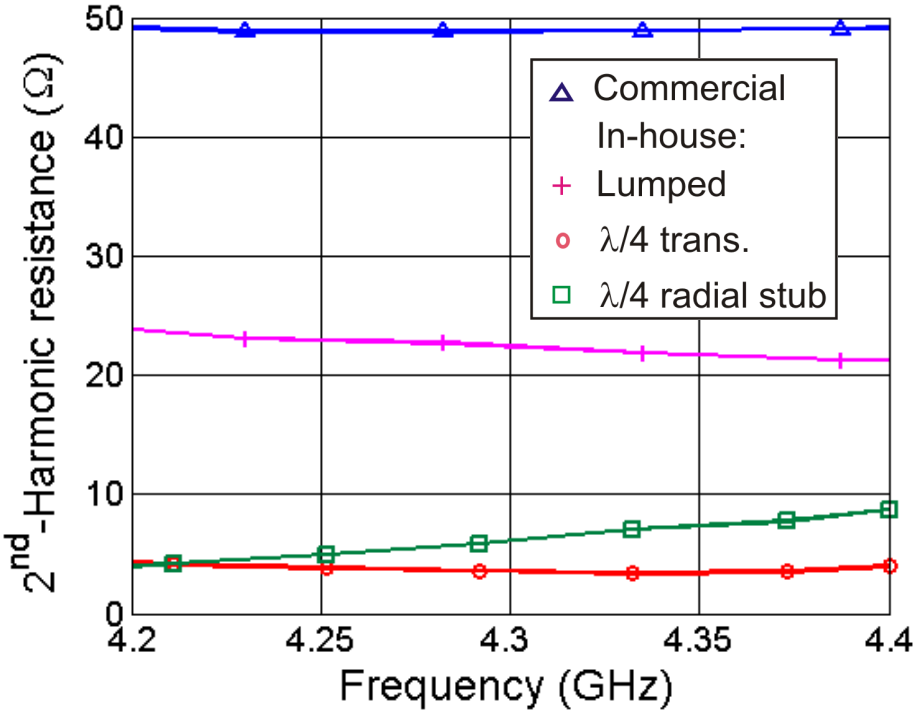
2nd-Harmonic resistance (Ω)
50
40
30
20
10
0
4.2
4.25
4.3
4.35
4.4
Frequency (GHz)
Commercial
In-house:
Lumped
λ/4 trans.
λ/4 radial stub

(d)

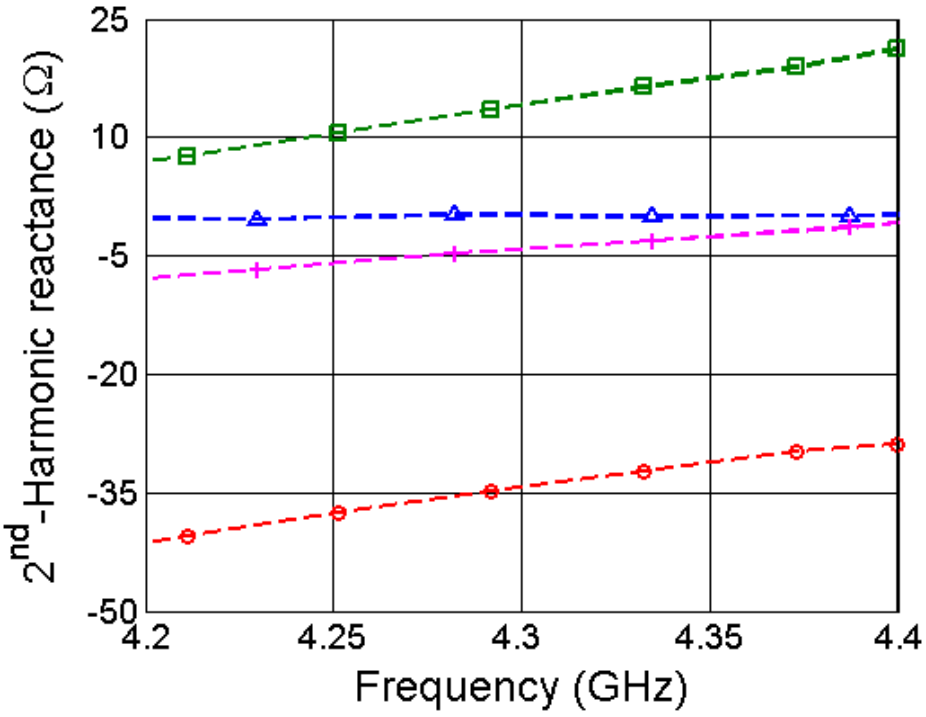

(e)

Figure 4.20 Impedance response of the implemented bias tees across (a) baseband, (b-c) fundamental, and (d-e) second-harmonic frequencies, measured using VNA.

It is evident from Figure 4.20(a) that for the lumped inductor based bias tee [Figure 4.19(a)], the decoupling capacitors (1 μF and 10 μF) have successfully held the impedance to a rather constant value with a maximum value of 12Ω measured at 100 MHz within the considered frequency range from DC to 100 MHz. In contrast, the λ/4 short-circuited shunt stub demonstrates an excellent baseband impedance of 5Ω at 100 MHz. In a two-tone signal environment, besides the fundamental frequencies, the RF impedance across the lower and upper IMD3 components should also be principally taken into account during the bias tee design. In this regard, the 22 pF bypass capacitor (AVX 0603 series) provides a narrowband short at f_c = 2.16 GHz for λ/4 line, which is transformed to an open resulting in a real 50Ω along the RF line as shown in Figure 4.20(b). Consequently, the non-negligible resistive and reactive impedance across the lower and upper IMD would force the DUT to

exhibit pronounced memory-effect behaviour, which is addressed in Section 4.4. It is important to note that even a small parasitic inductance, associated with either the bypass capacitor or improper ground contact introducing via inductance, can mistune the resonance of λ/4 line as shown in Figure 4.21 resulting in a non-50Ω load termination.

In case of λ/4 open-circuited radial stub based bias tee [Figure 4.19(c)], a maximum IF impedance of 9Ω is measured at 100 MHz as shown in Figure 4.20(a), which is comparable to 5Ω offered by λ/4 line based bias tee. Further, in Figure 4.20(b-c), a broadband 50Ω resistive impedance is measured with nearly constant low reactance, which is comparable to the commercial bias tee impedance properties. Subsequently, λ/4 open-circuited radial stub based bias tee can be accepted as an optimum solution, which satisfies low out-of-band termination and constant broadband 50Ω at the fundamental frequency with inevitably minimum reactive term. For practical power amplifier design applications, the above analysis underlines the importance of individually designing and experimentally verifying the bias network to inspect whether they meet the desired specifications.

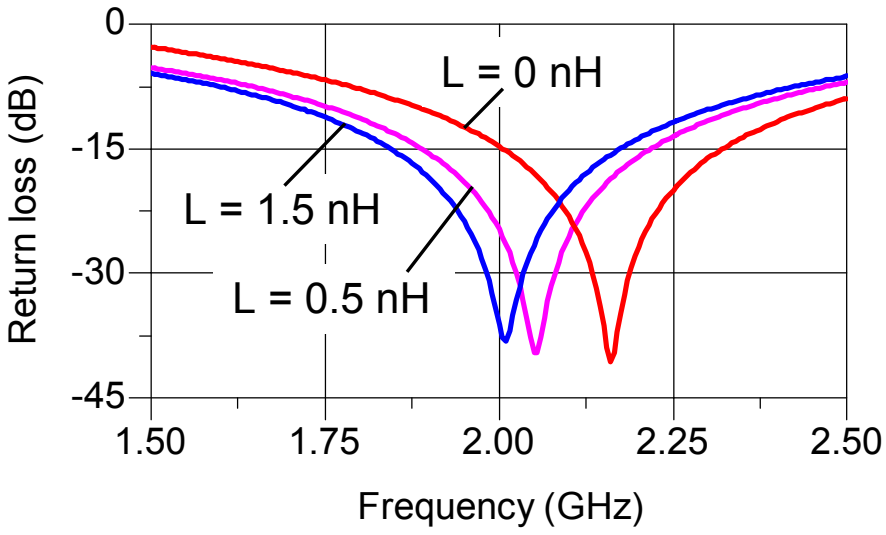

(a)

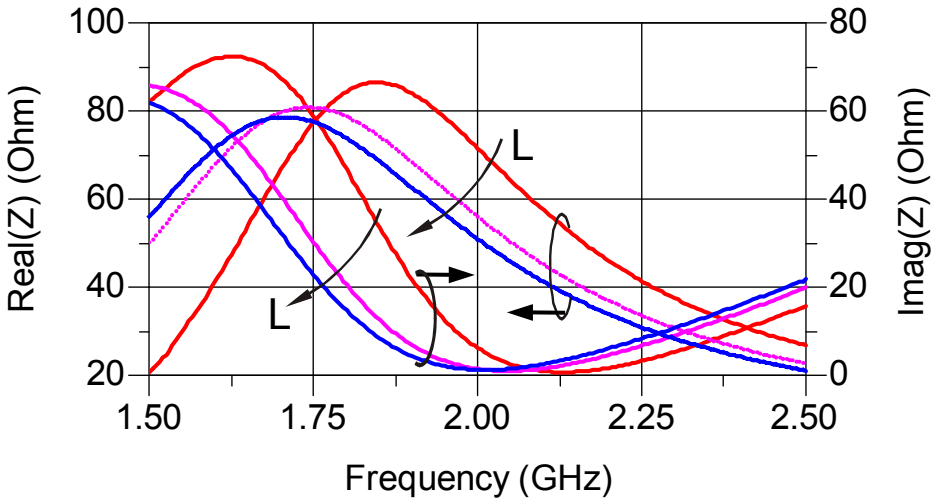

(b)

Figure 4.21 Effect of the parasitic inductance of the RF bypass capacitor (22 pF, AVX 0603 series) on λ/4 short-circuited shunt stub resonance, (a) return loss, (b) impedance response.

From Figure 4.20(d-e), it is rather interesting to note the second-harmonic termination of a radial stub based bias tee response, which is typically expected to exhibit a short. Its practical implications on active device characterization is not only on sideband distortion suppression but also potentially enhances overall efficiency. This can be principally achieved only when the short is presented at the device reference plane, which equally holds good for the baseband termination.

In reality, following the conventional measurement setup [54-55], [61] the RF bias tee is placed at an offset position subsequent to the directional coupler as shown in Figure C1.1(a-b) of Appendix C. To obtain an insight into realistic out-of-band terminations in a 50Ω environment, the electrical offset length l caused by of the insertion of the directional coupler between the RF bias tee and the device reference plane. The input impedance of a short-circuited transmission line is given by

$$jX = jZ_0 \tan \beta l \tag{4.9a}$$

with

$$\beta = \frac{2\pi}{\lambda_g} = 2\pi \frac{f_0 \sqrt{\varepsilon_{eff}(f_0)}}{c_0} \tag{4.9b}$$

where $\varepsilon_{eff}(f_0)$ is the effective dielectric constant at frequency f_0 and c_0 is the free space velocity. Assuming the value of $\varepsilon_{eff} = 2.51$ (PTFE) at 2.15 GHz, Figure 4.22 illustrates the impedance transformation on a short-circuited transmission line (4.9a) at 100 MHz and 4.2 GHz, exemplifying baseband and second-harmonic traps, respectively. Consequently, adverse impedance transformation leading to difficulties in interpreting measurement results, could be avoided by placing the bias tee physically closer to the drain terminal of the FET device. However, during on-wafer measurements, the physical length of the probes of the wafer practically limit the realizable termination properties of the bias tees.

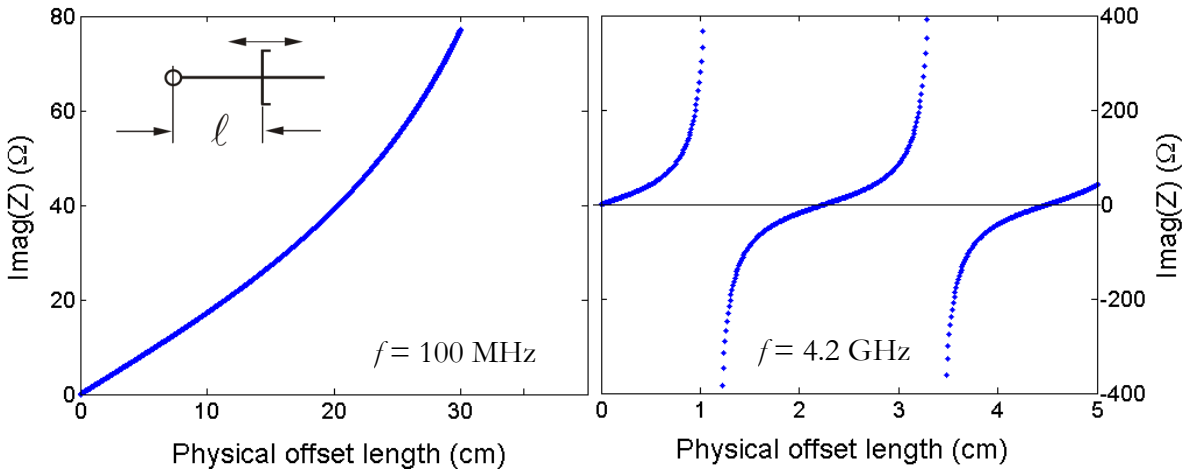

(a) (b)

Figure 4.22 Impedance transformation on a short-circuited transmission line at (a) 100 MHz and (b) 4.2 GHz.

4.4 Broadband Bias Tee Evaluation

4.4.1 Memory-Effect Characterization

Electrical memory-effect behaviour of 0.5-mm GaN HEMT [manufactured at the Fraunhofer Institute for Applied Solid-State Physics (IAF), Freiburg] was investigated to experimentally validate an optimal bias tee scheme. Figure 4.23(a-b) shows the photograph and the block diagram of an optimised characterization testbench. Figure 4.23(c) shows the memory-effect characterization results performed using different bias tee configurations shown in Figure 4.19. The two-tone characterization has been traditionally used for extracting signal bandwidth dependent spectral nonlinearities. Hence, by sweeping the carrier spacing between the two carriers from 200 kHz to 80 MHz, complex power waves, measured using dual-channel Agilent 89600 VSA, were vector error-corrected. The device was biased for class-AB operation (-4.2V, 25V, I_{DS0} = 2%I_{DSS}) with f_c = 2.15 GHz. Noting from the block diagram in Figure 4.23(b), the impact of envelope termination is nearly insignificant for narrowband operation ($\omega_2 - \omega_1 << \omega_1$ or ω_2). It is evident that with $\lambda/4$ open-circuited radial stub, an improvement of 19 dB is achieved at 20 MHz carrier spacing compared to the commercial bias tee, which is consistent with the previously reported arguments. In comparison to the measurements performed using the conventional testbench, which is depicted in Figure C1.2(a) of Appendix C, Figure 4.23(c) shows an overall improvement in the IMD response with the modified testbench over the modulation bandwidth from 200 kHz to 80 MHz. Interestingly, using the commercial bias tee, a 14.5 dB reduction in IMD is observed by placing the bias tee physically closer to the device reference plane, emphasizing the need to modify the testbench configuration.

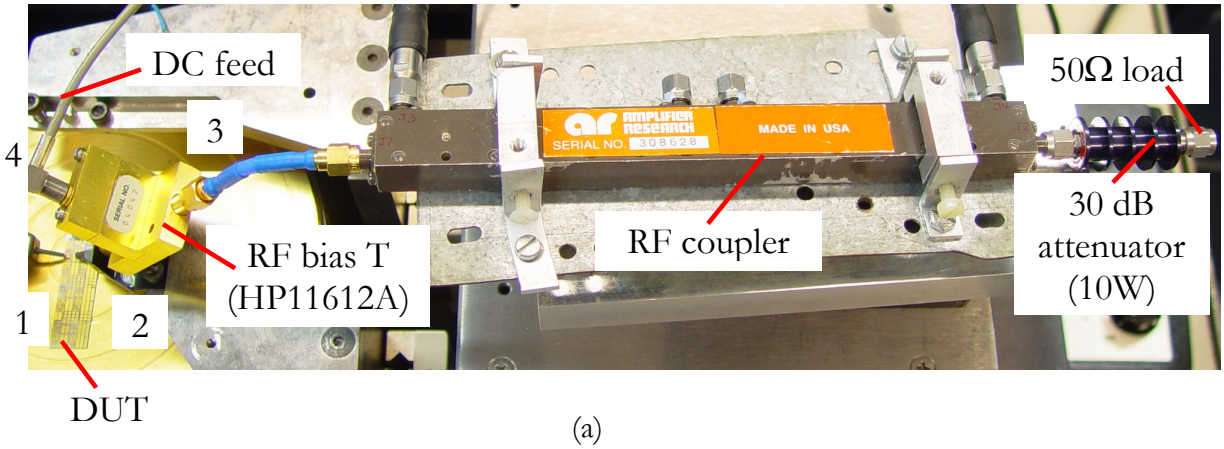

(a)

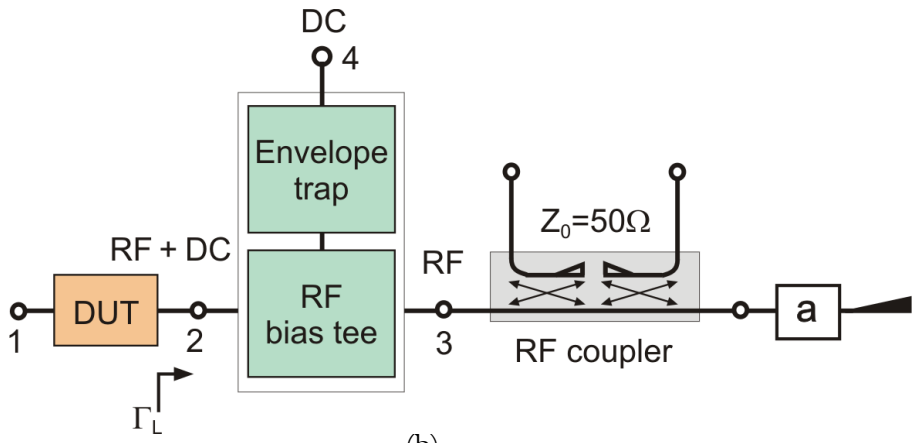

(b)

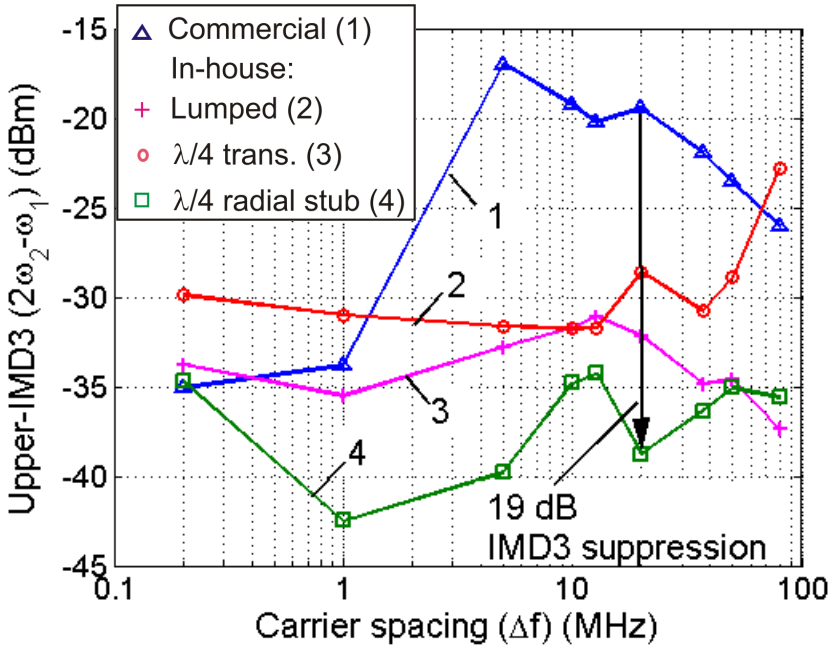

(c)

Figure 4.23 (a) Photograph of the modified testbench implementing commercial RF bias tee (HP11612A), (b) equivalent block diagram with in-house RF bias tee, (c) memory-effect characterization of a 0.5-mm GaN HEMT under the modified testbench conditions in a 50Ω environment [84].

Applying Volterra series modelling, which was discussed in Chapter 3, it is interesting to observe the distortion vectors affected by bias network properties. Thus, a further insight into the effect of baseband properties on IMD3 is gained by modelling third-order voltage phasors based on Volterra series on a 2 x 250 μm gate-width GaN HEMT. The carrier spacing was swept from 200 kHz to 80 MHz around f_c = 2.15 GHz at P_{in} = -16.5 dBm biased for class-AB (-4.25V, 25V, I_{DS0} = 2%I_{DSS}) operation, where the second-order distortion is dominant. Since the measured bias tee impedance values were discrete, for implementing these data into the simulation, it was essential to obtain the drain impedance response (IF and RF) with finer grid. Interpolation between the discrete measurement points enables simulations to be performed for intermediate frequencies. For efficient interpolation, an artificial neural network (ANN) based on multi-layer perceptron (MLP), was trained with the measured Z_L [85]. With input parameter being the frequency, the MLP constitutes a hidden layer (50 neurons) and an output layer (2 neurons for magnitude and phase of Z_L). Figures (4.24 - 4.27) demonstrate vectorially the individual contributions to total IMD3 from all the mixing products for each RF bias tee configuration separately.

From Figure 4.24, by using the commercial bias tee, clearly the cubic voltage vectors, which are functions of RF impedances, are held constant. This signifies the importance of maintaining a constant non-reactive 50Ω drain termination across the RF band. However, only the envelope component shows drastic changes, reflecting the envelope impedance behaviour. Consequently, memory-effect phenomena is evident with scattered IMD3 vectors, which is analogous to conclusions made from Figure 4.23(b). In contrast, with the in-house bias tees Figures (4.25 - 4.27), all the contributing vectors including the envelope component remain constant, demonstrating an improved memory-effect response. Among these, the radial stub based bias tee demonstrates minimized IMD response of 1 μV amplitude [Figure 4.27],

maintaining both magnitude and phase relatively constant over 80 MHz modulation bandwidth.

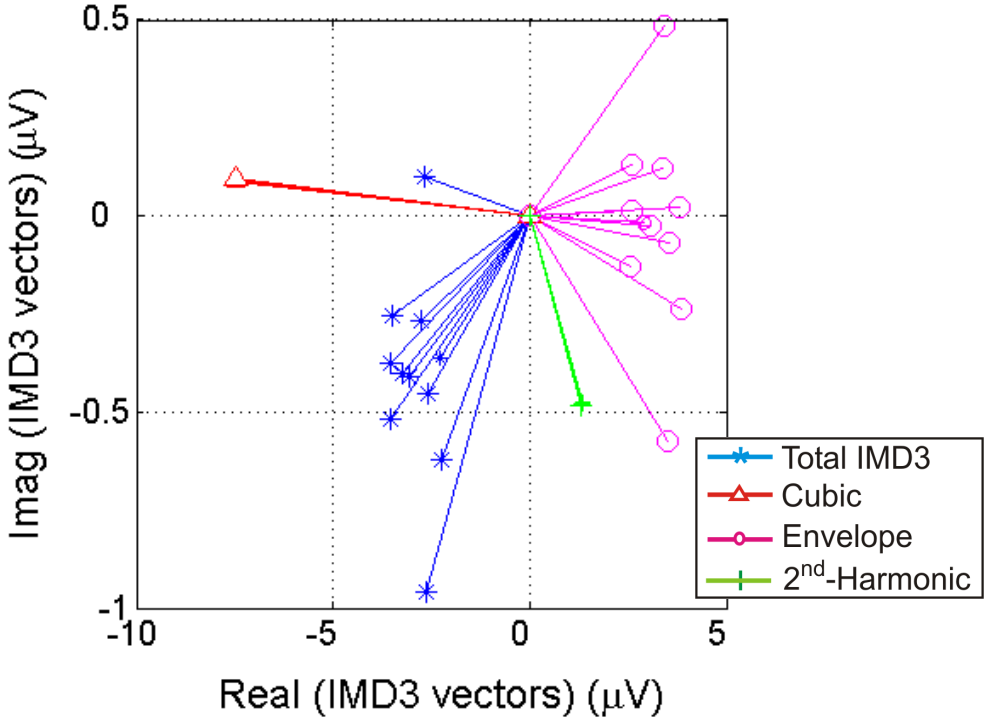

(a)

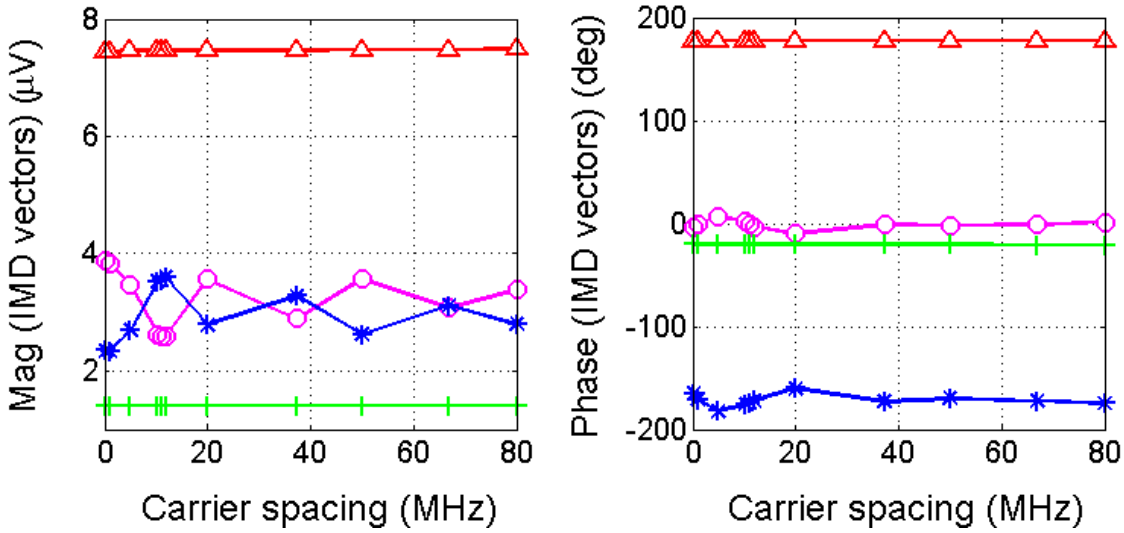

(b)

Figure 4.24 Commercial RF bias tee (HP 11612A) for device characterization of a 2 x 250 μm AlGaN/GaN HEMT, (a) voltage phasors, (b) magnitude and phase of complex upper-IMD simulated on the basis of Volterra series by varying carrier spacing Δf.

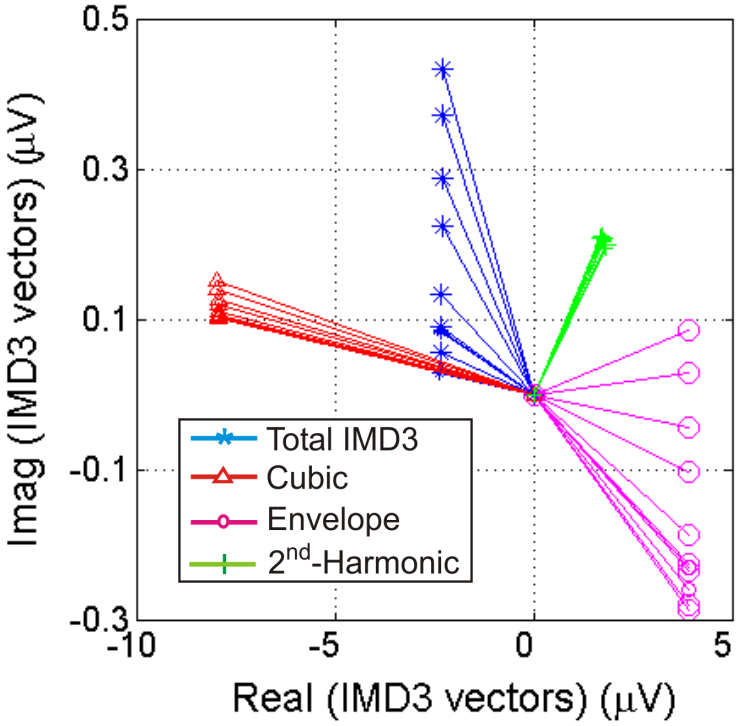

(a)

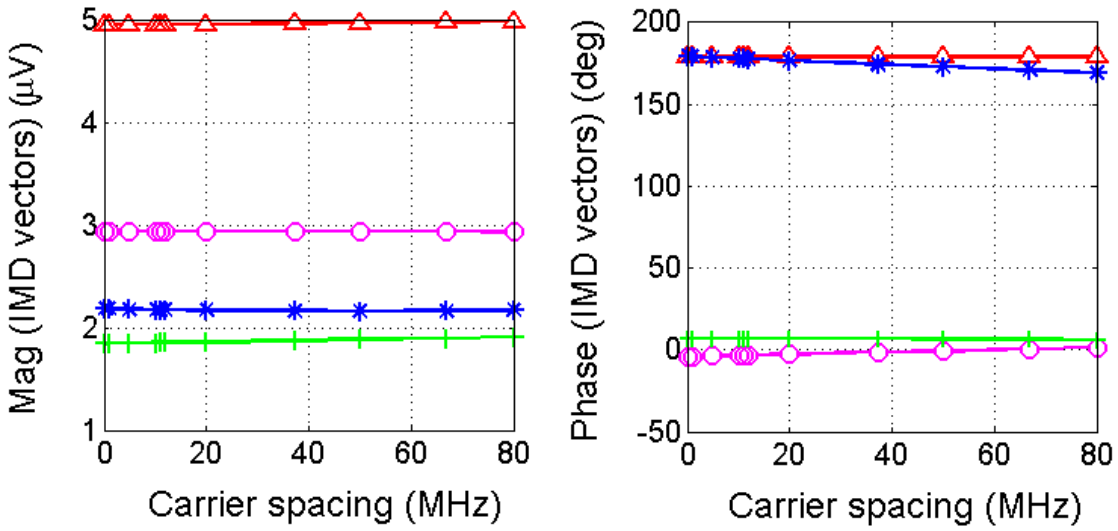

(b)

Figure 4.25 Lumped inductor based RF bias tee for device characterization of a 2 x 250 μm AlGaN/GaN HEMT, (a) voltage phasors, (b) magnitude and phase of complex upper-IMD simulated on the basis of Volterra series by varying carrier spacing Δf.

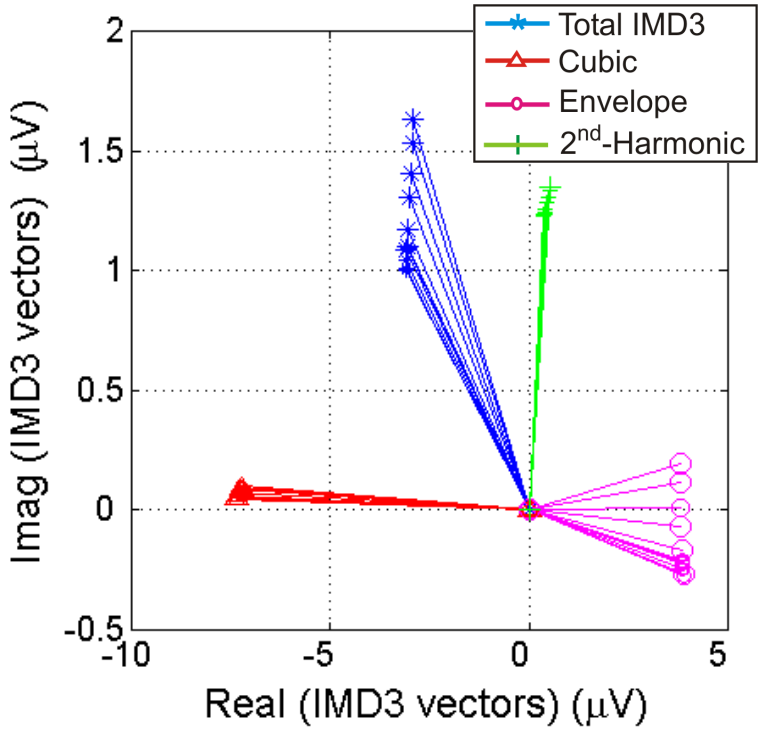

(a)

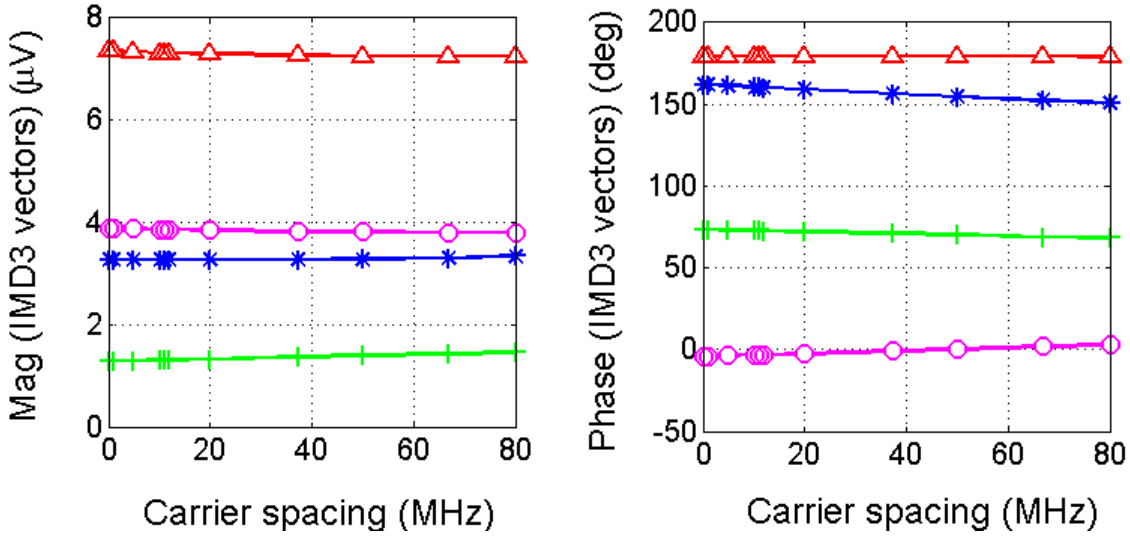

(b)

Figure 4.26 Quarterwave transformer based RF bias tee for device characterization of a 2 x 250 μm AlGaN/GaN HEMT, (a) voltage phasors, (b) magnitude and phase of complex upper-IMD simulated on the basis of Volterra series by varying carrier spacing Δf.

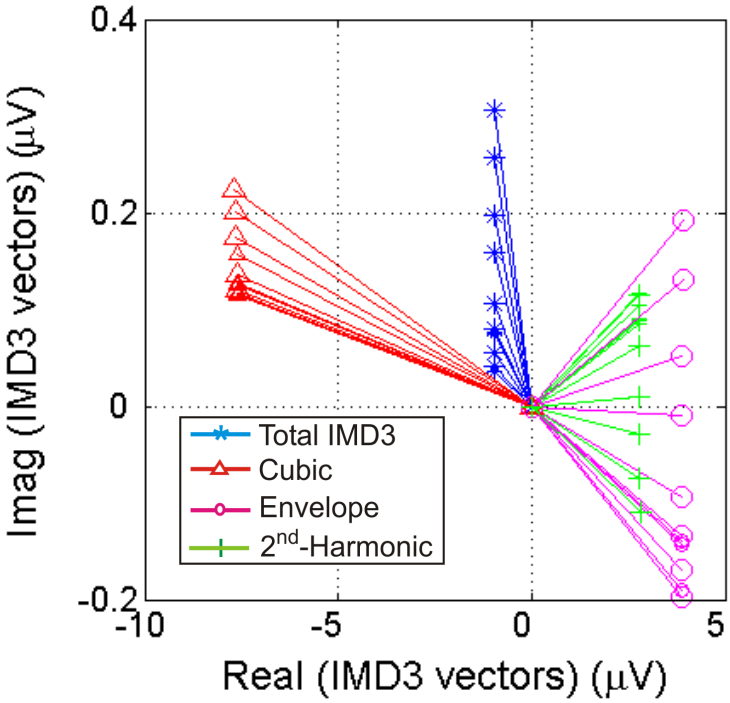

(a)

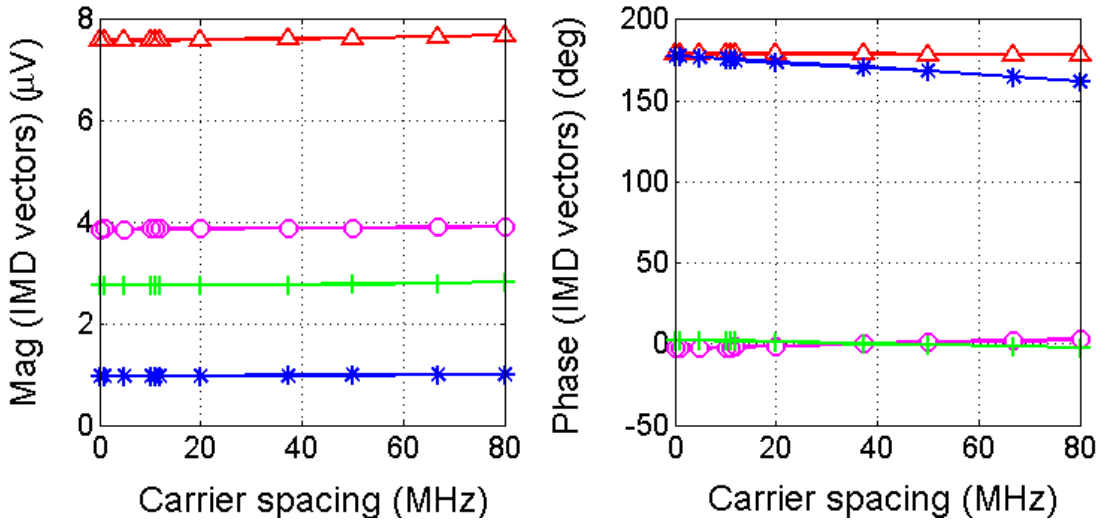

(b)

Figure 4.27 Radial stub based RF bias tee for device characterization of a 2 x 250 μm AlGaN/GaN HEMT, (a) voltage phasors, (b) magnitude and phase of complex upper-IMD simulated on the basis of Volterra series by varying carrier spacing Δf.

4.4.2 Load-Pull Characterization

It is the goal of every power amplifier designer to achieve high degree of linearity without compromising maximum available efficiency. Only an accurate and systematic characterization of active device coupled with a precise design methodology allows achievement of optimum FET performance. Experimental optimisation of bias and matching networks for high linear power amplifier design is one key advantage offered by source- and load-pull characterization apart from CAD model verification.

Sechi [86] has proposed a graphical technique that allows the designer to identify the optimum load termination for maximum power and efficiency at any predetermined value of IMD. In case of well behaved GaN based FET devices, the optimal load impedances determined from the closed contours of output power P_{out} and power added efficiency PAE, are normally in the proximity. However, when IMD contours are additionally taken into consideration, it becomes increasingly difficult to decide upon a single matching impedance, which satisfies maximum P_{out}, high PAE, and minimum IMD, simultaneously. In this context, it is important to investigate, for instance, to what extent the RF bias tee influence IMD load-pull measurements. With this intension, the performance of radial stub based bias tee was compared with the commercial bias tee.

Conventionally, passive tuners are used in a load-pull system to control impedances across the drain terminals. Using an automated in-house multi-harmonic mechanical slide tuner [87], two-tone fundamental load-pull characterization was conducted. Despite the fact that the tuner's reflection coefficient depends on frequency, it has been verified from tuner characterization that a maximum of 0.44° phase deviation can be expected for a bandwidth of 15 MHz around 2.15 GHz, which is acceptable for UMTS based source- and load-pull applications. This deviation, however, drastically increases as the tuner is moved away from the DUT reference plane. Hence,

even though the contours have been generated under two-tone excitation with 5 MHz carrier spacing, it is reasonable to assume that $\Gamma_L(\omega_1) \approx \Gamma_L(\omega_2) \approx \Gamma_L(\omega_0)$, where $\omega_0 = (\omega_1 + \omega_2)/2$. Moreover, based on GaAs FET devices, Ghannouchi *et al.* [57] have reported that there is negligible discrepancy between the P_{out}/PAE contours obtained from CW and two-tone characterization as long as the device is operated far below device compression point. Later on Hajji *et al.* [59] demonstrated that even with a gradual increase in the number of carriers from n = 2 to n = 8 (ΔPAR ≈ 6 dB), the optimal load termination remains approximately unchanged. Subsequently, this notion could be further extended to highly dynamic digitally modulated test signals (W-CDMA), which principally reproduces similar P_{out} contours across the complex $\Gamma_L(\omega)$ plane [88]. In other words, it can be concluded that concerning P_{out}/PAE, FET loading conditions are independent of the type of excitation signal used. In contrast, the discrepancy becomes significant, when the device is overdriven. This is a consequence of stronger gain compression behaviour, for example, under two-tone excitation, when compared to CW excitation, particularly in the region of optimal loading condition where maximum P_{out} is achieved [57].

Two-tone fundamental load-pull characterization was carried out on a 2-mm GaN HEMT (manufactured by Nitronex), operating in class-AB condition (-1.3V, 15V, I_{DS0} = 8%I_{DSS}) with 5 MHz carrier spacing. Figure 4.28 and Figure 4.29 depicts the P_{out} and PAE contours together with lower and upper IMD products over a wide range of complex $\Gamma_L(\omega_0)$ plane using both conventional and the modified testbench configuration. The conventional testbench implemented the commercial RF bias tee of type AU0616 while in the modified testbench the radial stub based in-house RF bias tee was used. With approximately same optimum load reflection coefficient [$\Gamma_{L,opt}(\omega_0)$] at the fundamental frequency, the maximum P_{out} and PAE in Figure 4.28(a) and Figure 4.29(a) are (28 dBm, 21%) and (27 dBm, 17.5%), respectively, measured corresponding to the lower fundamental tone (ω_1).

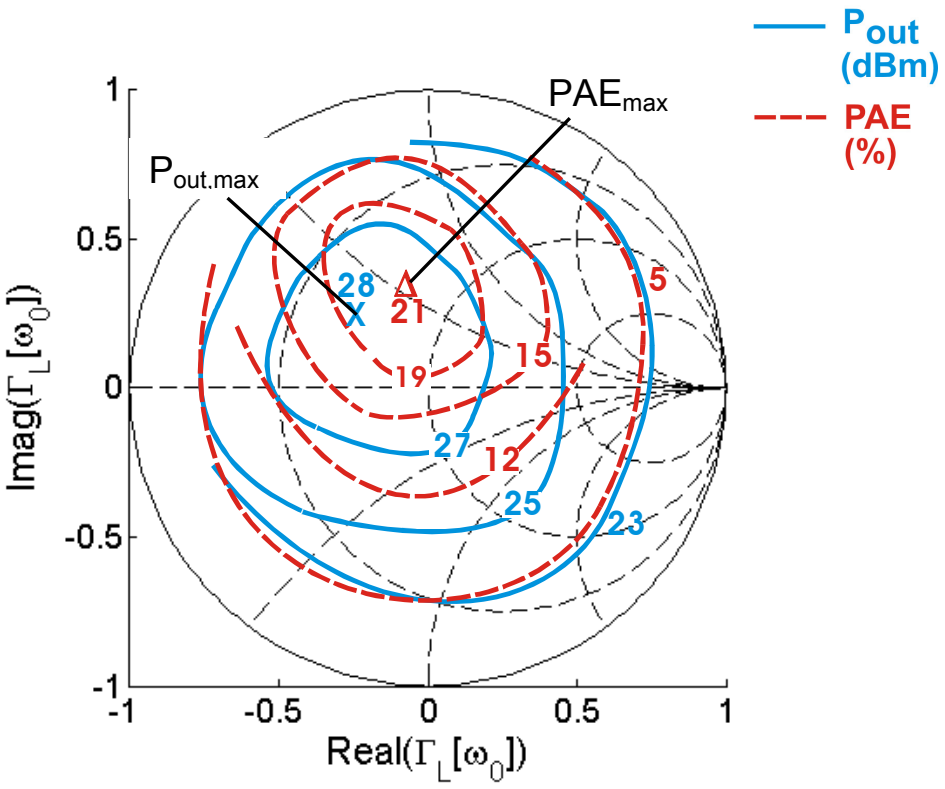

(a)

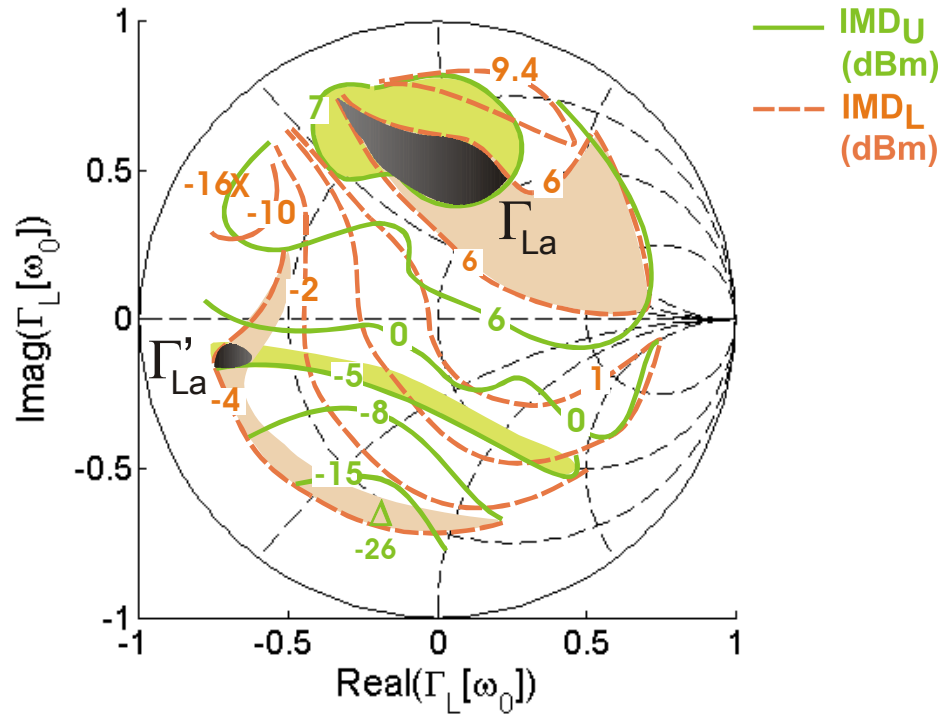

(b)

Figure 4.28 Fundamental load-pull characterization of a 2-mm GaN HEMT under 2-tone stimuli using a commercial RF bias tee (AU0616) in a conventional testbench [29]. (a) Output power and PAE contours, (b) upper and lower-IMD contours.

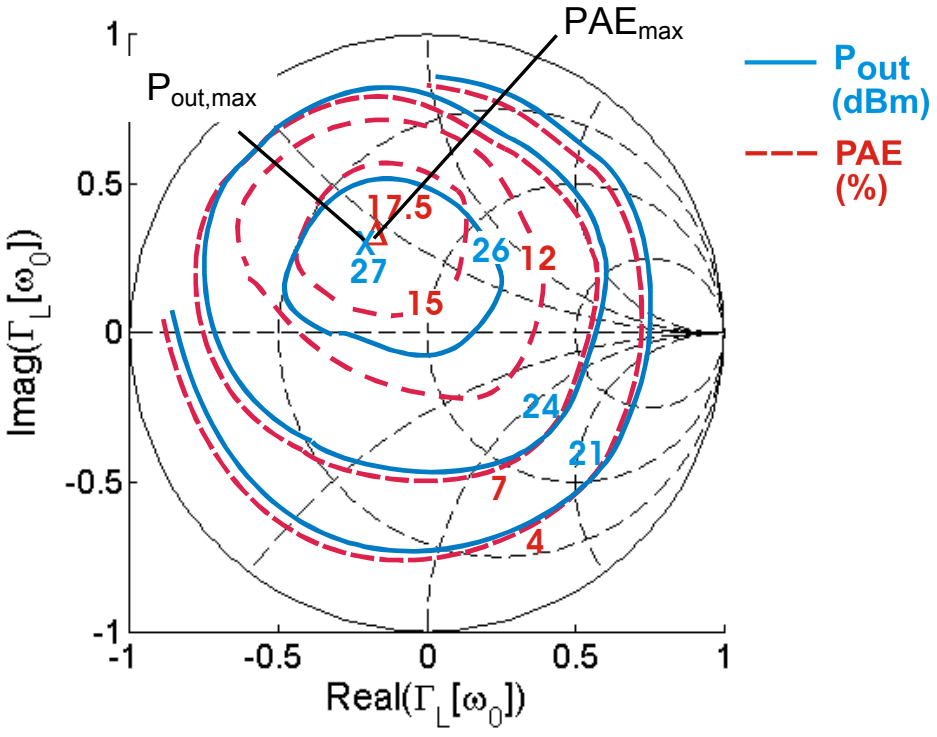

(a)

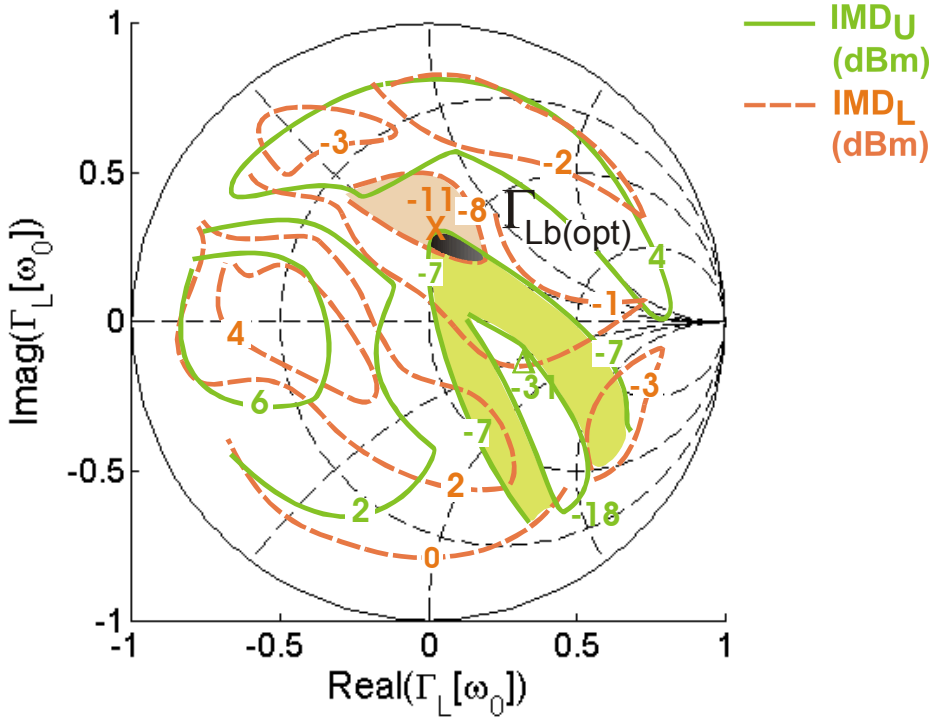

(b)

Figure 4.29 Fundamental load-pull characterization of a 2-mm GaN HEMT under 2-tone stimuli using a radial stub based in-house RF bias tee in the modified testbench [29]. (a) Output power and PAE contours, (b) upper and lower-IMD contours.

The power amplifiers that are used in telecommunication systems are often designed from the standpoint of high efficiency being the main design goal. Hence, in practice, it is common to choose $\Gamma_{L,opt}$ for attaining maximum P_{out} and PAE, independent from the IMD response. For instance, by visual inspection of contours in Figure 4.28(b) measured using a conventional testbench, one possibility is to choose Γ'_{La} (shaded overlapping contours of upper and lower IMD), which delivers relatively good linearity with -4 dBm IMD at the cost of poor PAE of 5% indicated in Figure 4.28(a). On the other hand, relying on the external linearization techniques, where up to 20 dB IMD cancellation is expected for basestation power amplifier applications [89], it is preferable to trade-off linearity (IMD ~ 6 dBm) at Γ_{La} shown in Figure 4.28(b), gaining maximum P_{out} and PAE. However, considering contours in Figure 4.29(b) measured using the modified testbench, at Γ_{Lb} = j0.24, where P_{out} and PAE in Figure 4.29(a) are approximately 27 dBm and 17%, respectively, 14 dB IMD suppression is obtained for approximately the same fundamental load termination.

Only under narrowband test signal environments, the commercial RF bias tee can be implemented together with the bias compensation network by following the modified testbench configuration as an alternative. On the other hand, the applicability of the proposed optimum in-house RF bias tee in load-pull measurements is limited to only fundamental tuning. This is similar to the fixed impedance method [90], which gives no possibility to perform second-harmonic tuning since the bias tee offers complete reflection of the second-harmonic component within the design frequency range. The importance of accurate IMD characterization under broadband conditions is hence demonstrated, supporting a straightforward application rule for power amplifier design through which a unique identification of optimal load can be achieved yielding high P_{out}, PAE and linearity simultaneously.

4.5 Drain Bias Sensing

Practically, when a nonlinear active device is characterized using multi-carrier excitation, due to the non-zero bias supply impedance, voltage modulation is sensed at the output biasing terminal. This unintentional drain bias modulation would in turn add to the device's in-band distortion. Even under narrowband stimuli ($\omega_2 - \omega_1 << \omega_1$ or ω_2), modulating bias can lead to device temperature modulation causing additional distortion [15-16]. Drain bias sensing is one of the few possibilities to experimentally demonstrate the implications of baseband termination at the low frequency beat [29]. Through bias sensing, it is possible to measure the envelope component (ω_2- ω_1), for example, under two-tone stimulus, which principally affects the resultant IMD under class-AB operation for wide carrier spacing. Consequently, this quick-shot test aids to localize and interpret the source of electrical memory-effect behaviour observed in IMD characteristics by sweeping the carrier spacing.

A typical test setup for sensing drain modulation is illustrated in Figure 4.30. Under modulated stimuli, the drain bias supply voltage waveforms were measured at the 'sense' port of the bias tee using 350 MHz Agilent 54641A digital oscilloscope. The compensation network, which is indicated in Figure 4.30, was installed in order to decouple the DC feed at baseband frequencies. Under two-tone excitation, a 8 x 500 μm gate width GaN HEMT [manufactured by (FBH), Berlin] was biased for class-AB operation (-3.5V, 15V, I_{DS0} = 3%I_{DSS}) with carrier frequency sweep from 200 kHz to 80 MHz at a peak input power of P_{in} = 15 dBm. The 'force' port of the commercial RF bias tee (AU0616) mainly provides DC bias to the DUT. The reason for using Auriga bias tee was to exploit the additional bias sensing feature provided in Auriga at the DC feed port, which is not available in HP11612A manufactured by Hewlett-Packard. As shown in Figure 4.31, the baseband impedances were comparable between the two commercial bias tees.

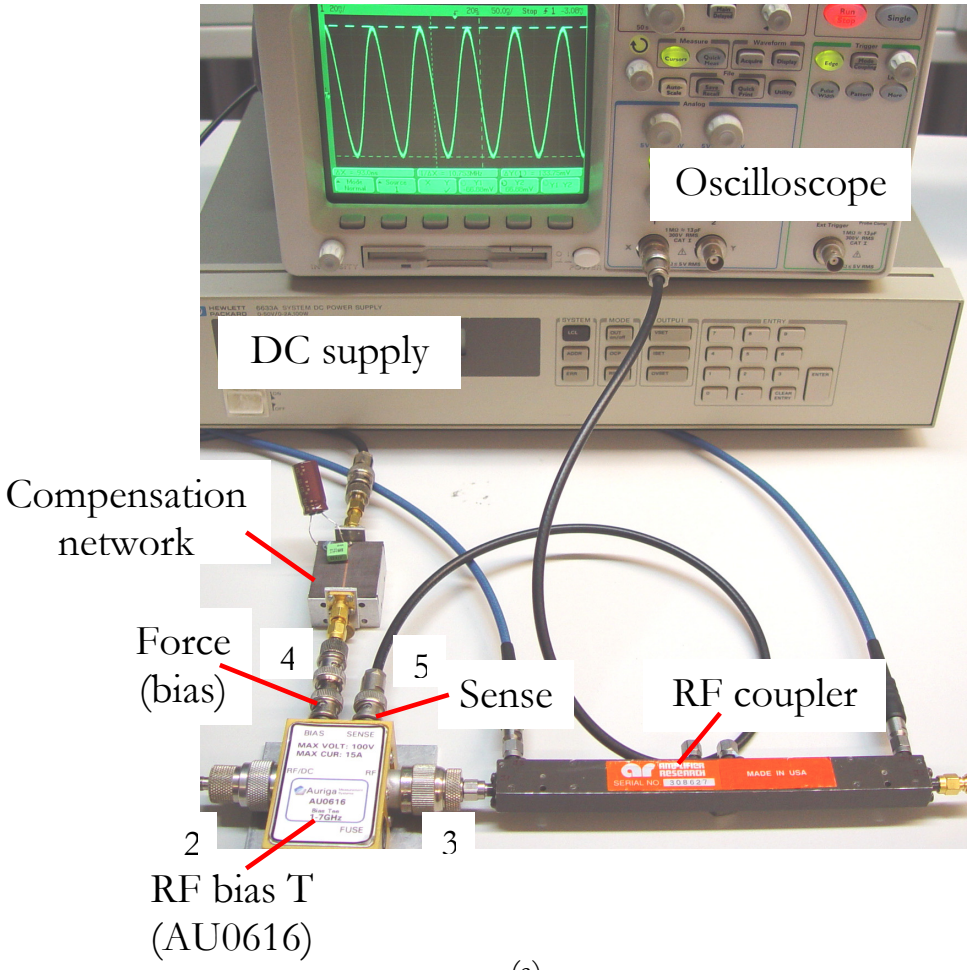

(a)

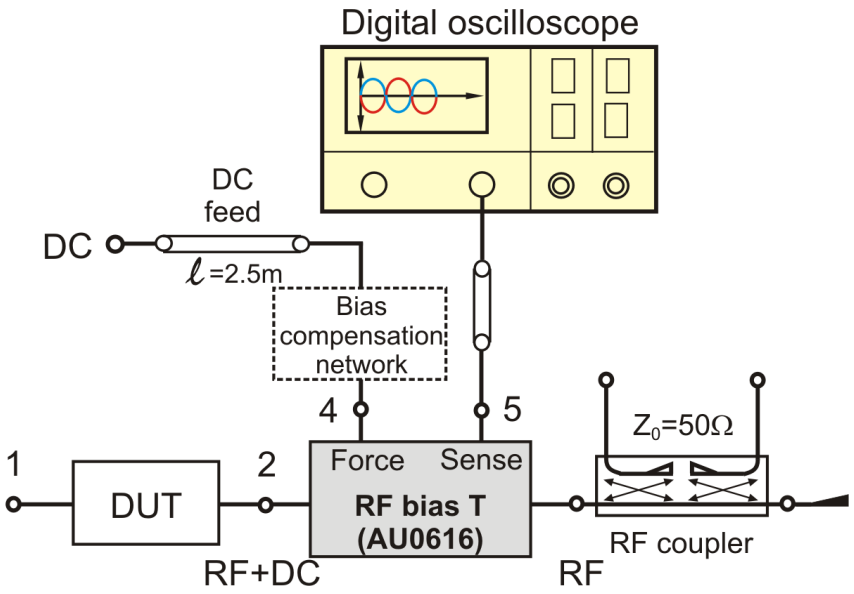

(b)

Figure 4.30 Drain bias sensing - quick shot test for imperfect DC feed. (a) photograph of the bias sensing setup, (b) equivalent block diagram.

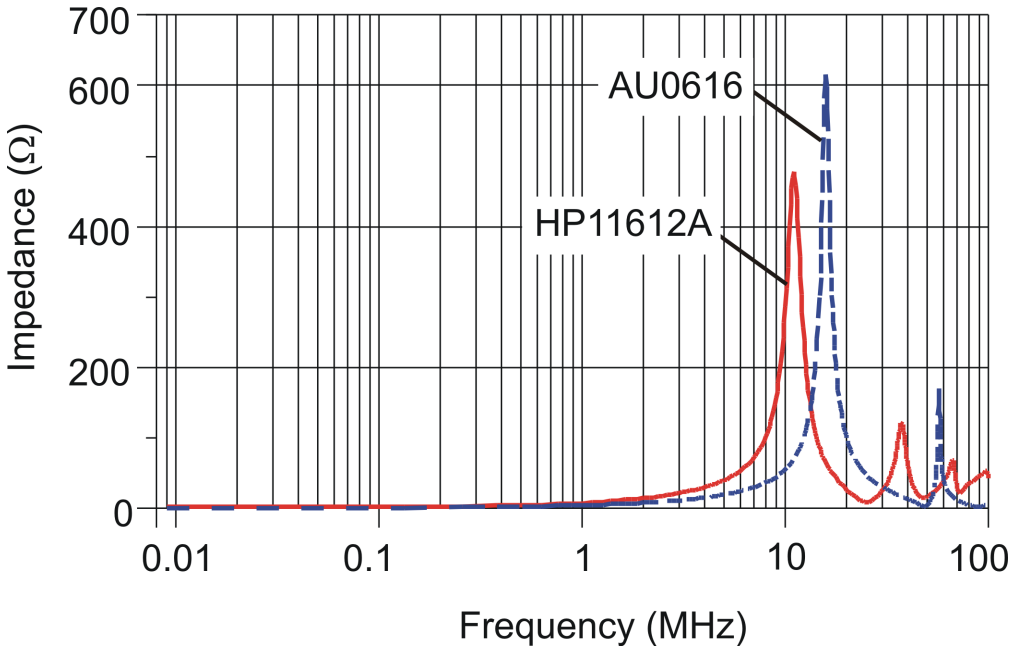

Figure 4.31 Measured baseband impedance magnitude of commercial RF bias tees of type HP11612A and Auriga AU0616 without DC feed compensation.

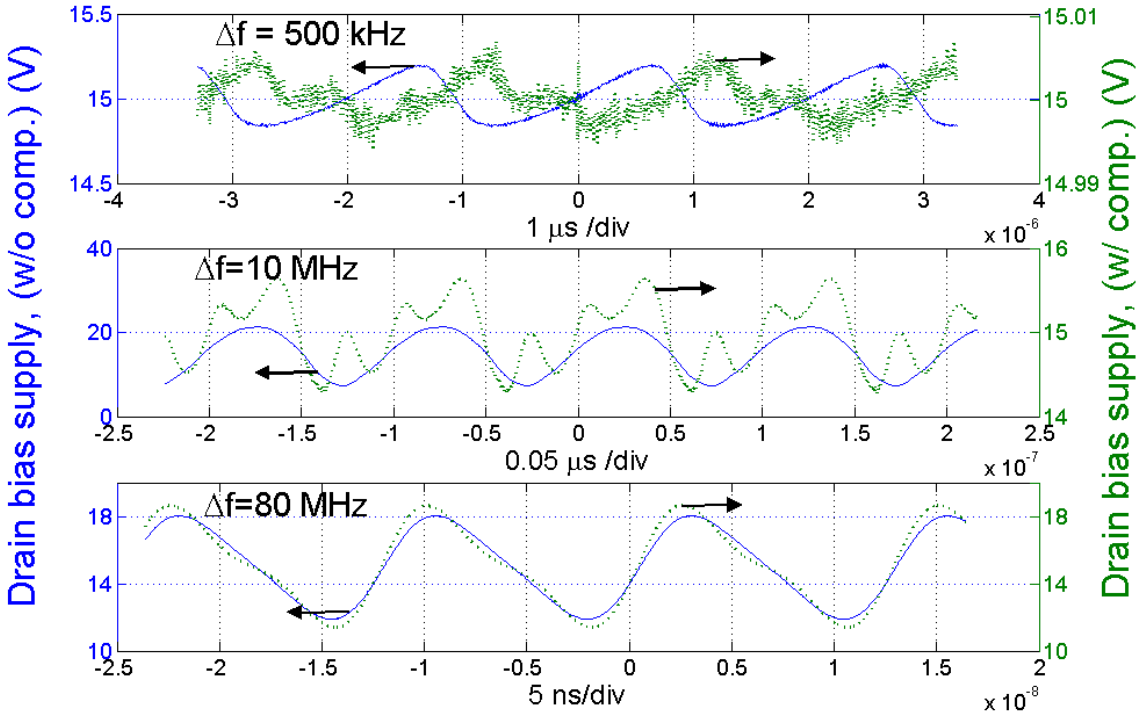

Figure 4.32 Bias sensing for characterizing drain supply modulation [73].

Figure 4.32 depicts the measured envelope voltage waveforms without and with drain bias compensation. The signal waveforms show typical ripple characteristics indicating the presence of higher baseband harmonics other than ω_2- ω_1 component, which is effectively suppressed by the compensation network. However, the decoupling capacitors [series resonance frequency f_{SR1} = 1 MHz, f_{SR2} = 3.5 MHz as shown in Figure 4.11(a)] effectively suppress the voltage modulation until 30 MHz bandwidth, above which, the inductance of the DC feed together with the bias tee inductance dominate the baseband reactive impedance. This is because the inherent inductance implemented in the RF bias tee along the DC path.

Drain Modulation Index

In order to compare such effects quantitatively, a novel FoM is defined below, known as drain modulation index (DMI) [73] normalized to 1Ω

$$DMI(\Delta f) = \frac{v_{peak}(\Delta f) / I_{DS,DC}}{1\Omega} \tag{4.10}$$

The drain modulation index can be used to characterize the extent of drain bias supply modulation $v_{peak}(\Delta f)$ caused by the baseband impedance when the device is self-biased with a DC drain current $I_{DS, DC}$. Figure 4.33 illustrates the drain modulation index characteristics computed from the drain supply modulation measurements shown in Figure 4.32.

Following the behaviour of the baseband response of the AU0616 bias tee in Figure 4.31, the frequency, at which modulation index is maximum, has been shifted from 15 MHz to 50 MHz after compensation. The reason is indeed because of the cancellation of the inductive behaviour presented by the short-circuited transmission line (DC feed) imposed by the compensation network. Subsequently, at 15 MHz, peak drain bias supply voltage has reduced to 20% after compensation, implying an 80% improvement in baseband dependent

distortion. Thus, a broadband compensation could eliminate resonance out of the usable bandwidth.

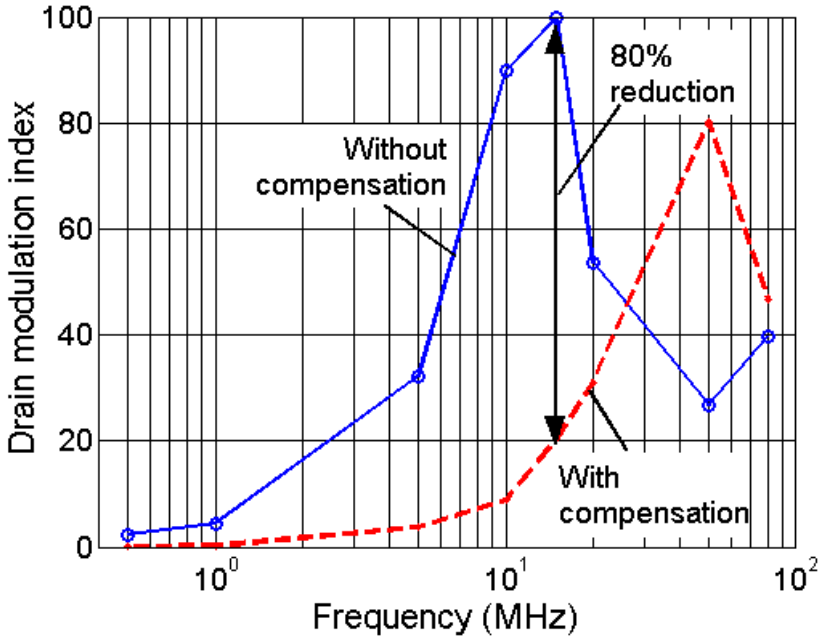

Figure 4.33 Drain modulation index [73].

The baseband performance of a commercial RF bias tee (AU0616) was compared with an in-house bias tee to emphasize the need for a compensation network at the DC bias port. Hence, a quarterwave transformer based bias tee, which delivered an excellent baseband performance as shown in Figure 4.20(a), was considered for measuring voltage modulation waveform. A 2 x 250 μm GaN HEMT [manufactured at the Fraunhofer Institute for Applied Solid-State Physics (IAF), Freiburg] was characterized under two-tone stimuli for measuring drain bias supply voltage waveforms by sweeping Δf from 200 kHz to 80 MHz. The device was biased for class-AB operation (-4.25V, 25V, I_{DS0} = 2%I_{DSS}). Figure 4.34 shows the voltage waveforms measured along the drain supply using a commercial and an in-house bias tee at two-tone carrier spacing of 5 MHz, 20 MHz and 80 MHz. Until 20 MHz, the envelope voltage waveforms measured using in-house bias tee has significantly suppressed the drain bias supply to less than 7 mV while it is 1.06V in case of commercial bias tee, which again emphasizes the importance of baseband characteristics of

the measurement setup when performing linearity analysis of active devices.

The relevance of memory-effect on high power large size GaN HEMTs is an interesting subject of discussion. Theoretically, for high power FET devices, the degree of nonlinearity cannot be restricted to three at P_{1dB}. In other words, in reality the baseband spectrum constitutes not only the first IF harmonic ($\Delta\omega = \omega_2 - \omega_1$) but also its higher harmonics IF(n.$\Delta\omega$) (n = 2.3…). This presents a serious issue concerning bandwidth dependent short-term electrical memory-effect, where it is not sufficient to suppress only IF($\Delta\omega$) but even its higher harmonics [91]. In terms of the bias tee design, all the envelope frequencies of concern [at least until IF(2$\Delta\omega$)] should be suppressed by a low impedance termination [4]. This is indeed critical under realistic test signals, which may have baseband components that extend from DC to several MHz.

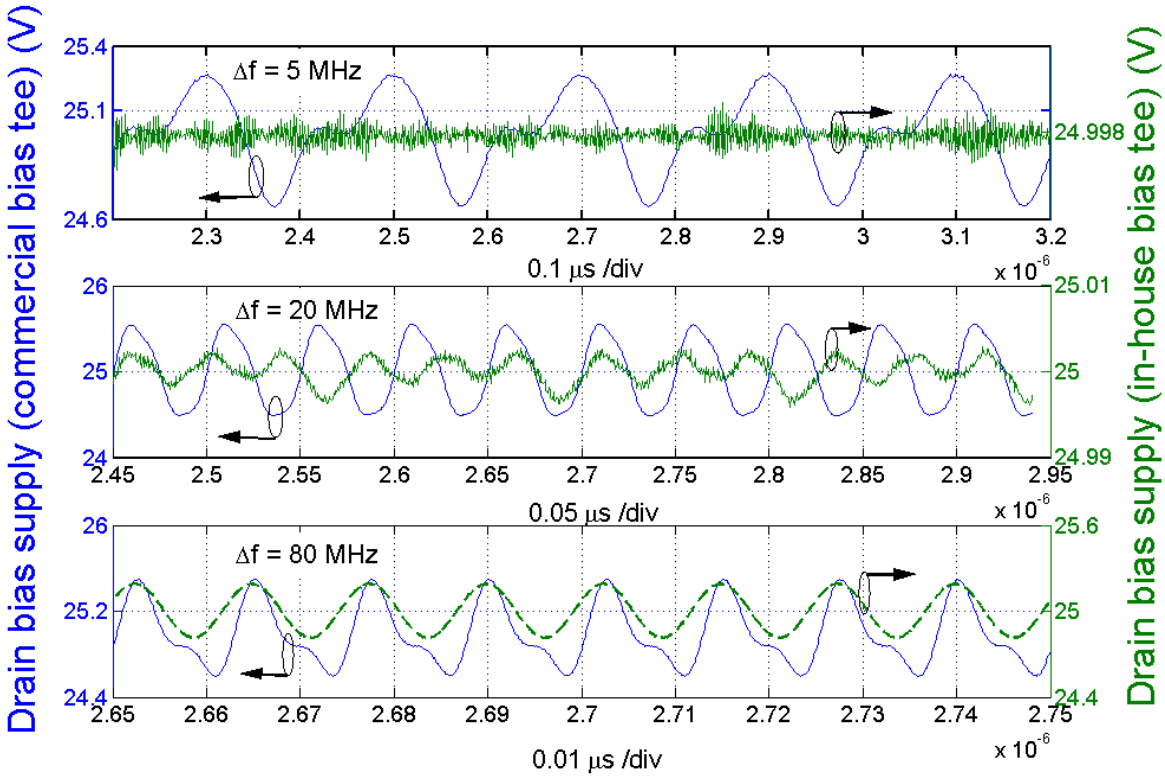

Figure 4.34 Sensing drain bias voltage modulation from an on-wafer characterized 0.5-mm GaN HEMT using commercial Auriga AU0616 and in-house bias tees. The IF voltage waveforms are measured for 5 MHz, 20 MHz and 80 MHz carrier spacing [82].

Through drain bias sensing, the IF harmonics of 3.2-mm GaN HEMT [manufactured at the Fraunhofer Institute for Applied Solid-State Physics (IAF), Freiburg] were measured using a commercial (HP11612A) and λ/4 open-circuited radial stub based in-house bias tee as shown in Figure 4.35. the device was biased for class-AB operation (-3V, 25V, I_{DS0} = 7%I_{DSS}). The in-house bias tee has proved its relevance over a broad bandwidth by mitigating IF harmonics at the baseband, emphasizing the importance of broadband envelope termination characteristics of the measurement setup. Interestingly, for the commercial bias tee case, the peak IMD value at 5 MHz carrier spacing observed in Figure 4.35, is indeed seen for 0.5-mm GaN HEMT shown in Figure 4.23(c). This signifies the persistent influence of bias network's property on the IMD behaviour independent of the active device being characterized.

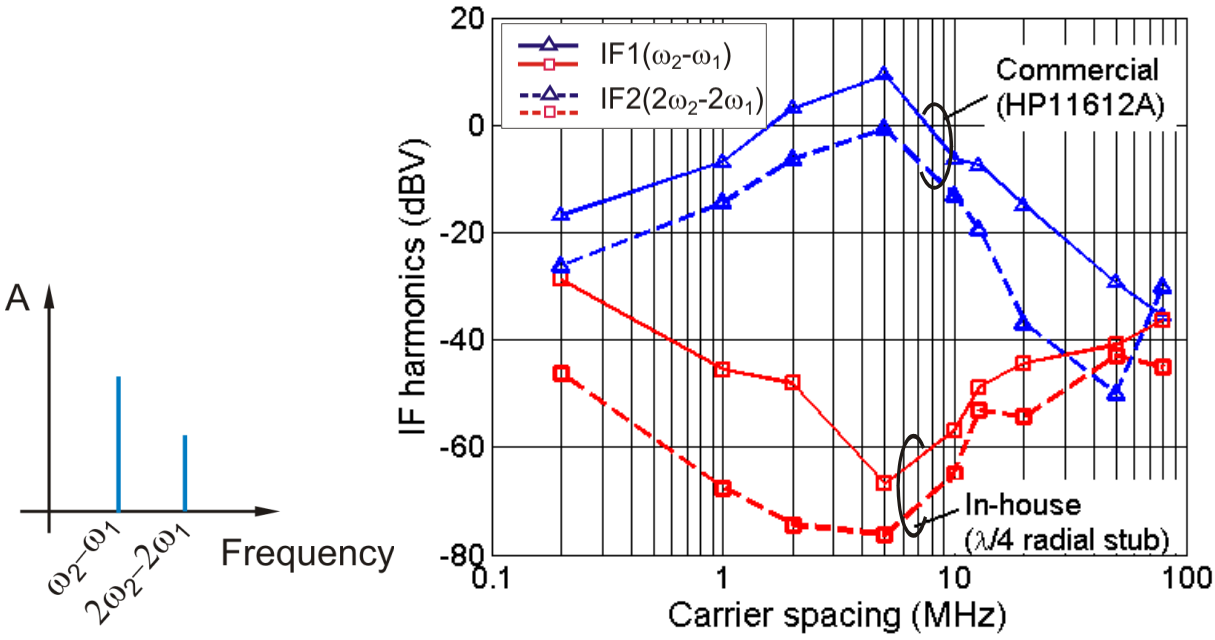

(a) (b)

Figure 4.35 IF harmonic characterization of a 3.2-mm GaN HEMT under two-tone excitation, (a) output baseband spectra (b) validation of broadband low baseband termination of in-house bias tee in comparison with commercial RF bias tee.

Chapter 5
IMD Sweet-Spots

Single-stage power amplifiers have been traditionally operated under class-A or class-AB configuration with sufficient back-off in order to restrict the RF output signal swing within the linear amplification limit. However, the benefit of obtaining high linearity is concealed by poor efficiency performance limiting power amplifier applications. In contrast, high efficiency power amplifiers are forced to operate in a nonlinear mode, where the RF output signal is clipped resulting in highly distorted output signal.

To suppress such distortions, linearization techniques have been developed, which rely on either adding external circuits to the power amplifier, or simply improving its design. However, since the first technique involves several drawbacks like cost, size, effective bandwidth, and even degradation of overall efficiency due to additional linearization circuitries, there is a growing interest in directly optimizing the actual power amplifier linearity, which is sometimes termed as device-level linearization [10], [92-93].

One possible way to achieve this design goal is to rely on a specific bias point and power operation condition to produce so-called *sweet-spots*, which appear as local minima in the intermodulation distortion characteristics near the

region where PAE is maximum [10], [94-95]. Over the years, research efforts have been devoted to investigate the causes and mechanisms responsible for causing sweet-spots in IMD characteristics of the active devices.

The existence of large-signal IMD sweet-spot was reported initially by Blanco [96]. Its behaviour was later comprehensively discussed by Carvalho and Pedro [95]. The applicability of such low current large-signal IMD sweet-spot for effectively improving linearity-efficiency trade-off was successfully demonstrated by Malaver *et al.* [94] through an envelope tracking class-B MESFET power amplifier.

5.1 Origin

The IMD measured at the output of a power amplifier has its origin mainly from the intrinsic active device's nonlinearity. As shown in Figure 5.1, the device output and transfer characteristics can be categorized into two regions, namely, quasi-linear and strongly nonlinear regimes, which are essentially the hard-clipping limits.

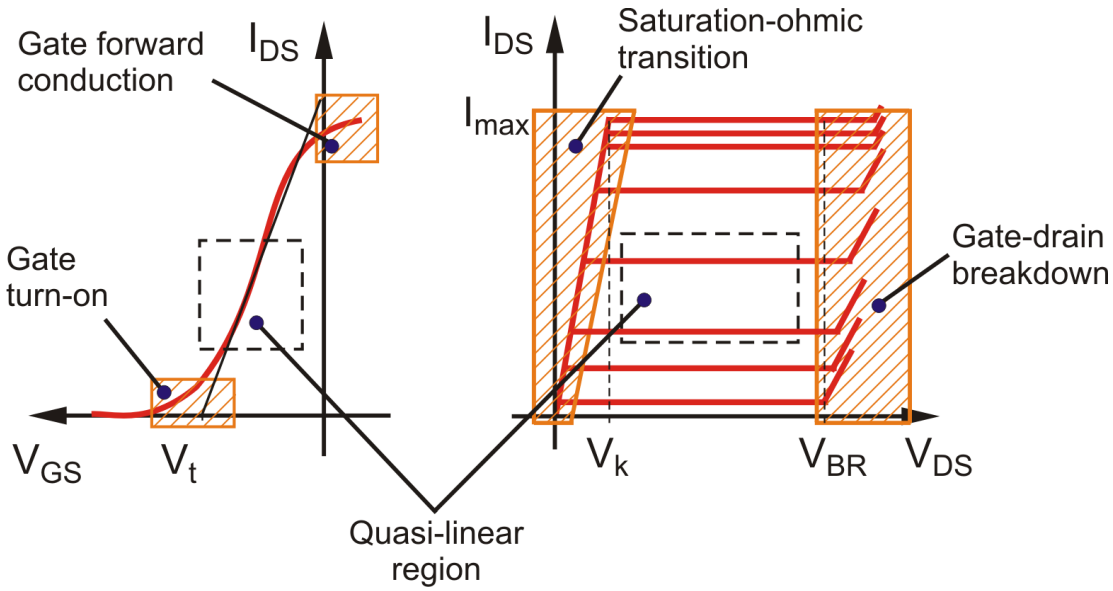

Figure 5.1 Schematic of an active device I(V) characteristics depicting the dominant nonlinear regions.

The major nonlinearities of FET resulting in hard-clipping have four distinct origins [97]. Among them, two nonlinear regimes are controlled by gate bias, namely, hard turn-on and gate-forward conduction zones, identified with the threshold V_t or pinch-off V_{pi} voltage and channel saturation current I_{max}, respectively. Interestingly, they reflect two extreme conditions or states of depletion region under reverse and forward gate bias, respectively. The drain bias related nonlinear regimes include saturation-to-ohmic transition zone defined by the knee voltage V_k and the gate-channel junction or gate-drain breakdown V_{BR} due to high reverse gate-drain bias. The interaction between the RF loadline with these dominant nonlinear zones has adverse effect on the output current and voltage waveforms, which inturn brings about distinct behaviour in IMD curves.

5.1.1 Small-Signal Sweet-Spot

In small-signal regime, as a first approximation, distortion products can be directly related to the third-order derivative of nonlinear drain-source current G_{m3} [94-95]. In typical MESFETs having Gaussian doping profile, it has been reported that for a particular gate bias, the depletion layer edge occurs near the transition between the zones of increasing and decreasing carrier concentration. This creates a perturbation on the transconductance G_m curve described by G_{m3} nulling [97]. In this regard, small-signal IMD sweet-spot is generally associated with the G_{m3} null.

As an example, Figure 5.2 illustrates the contours of G_{m3} null or small-signal IMD sweet-spots derived from the measured static I(V) characteristics of a 1.2-mm GaAs HEMT (manufactured by TriQuint Semiconductor). It is evident that the G_{m3} null appearing at higher transconductance zone becomes relevant for improving class-A linearity in small-signal amplifier applications.

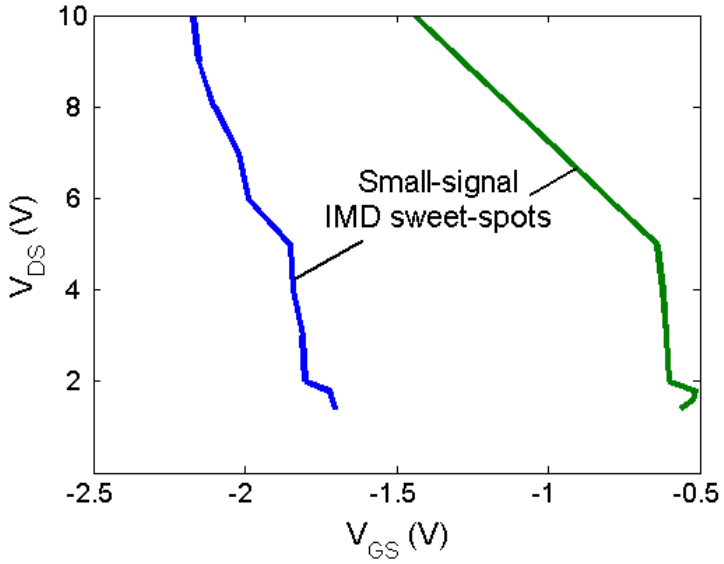

Figure 5.2 Contours of dual-bias dependent small-signal IMD sweet-spot measured from a 1.2-mm GaAs HEMT.

5.1.2 Large-Signal Sweet-Spot

Two distinct behaviours, namely, the fundamental output power and IMD curves of a 0.5-mm gate width GaN HEMT [manufactured at the Fraunhofer Institute for Applied Solid-State Physics (IAF), Freiburg] are depicted in Figure 5.3. The DUT is biased to demonstrate large-signal quasi-linear (class-A) and nonlinear (class-C) operation in a 50Ω environment.

In case of class-A operation, although the RF swing in the linear zone is assumed not to enter the dominant nonlinear regions as shown in Figure 5.1, residual nonlinearity is inevitable in which case the distortion products of the third-order dominate the device's in-band IMD performance. This results in a constant gain over a wide range of input power as shown in Figure 5.3 until the transistor enters saturation, causing gain compression and phase delay at high output power level. In this regard, IMD3 increases monotonously with a constant 3 dB/dB, the reason why third-order intercept point (IP3) is determined under class-A operating condition. IP3 is the most widely used figure of merit (FoM) to characterize the nonlinear behaviour of a device. IP3

is a point of intersection of the extrapolated 1 dB/dB slope line of the output fundamental power and 3 dB/dB slope line of the IMD3 power [10], [95].

On the contrary, under nonlinear class of operation, which in this case is class-C, the device typically exhibits gain expansion followed by compression characteristics, resulting in a low distortion local minimum termed as large-signal IMD sweet-spot as indicated in Figure 5.3. At low input power levels, the measured 1.3 dB/dB slope of IMD3 signifies the influence of higher degree contributors (for example fifth-degree, seventh-degree and so on) apart from dominant third-degree. With respect to the IP3 FoM, the definition holds good only when the IMD3 is not affected by any large-signal effects. In other words, under low drain current biasing conditions, where the IMD curves do not present a 3 dB/dB slope, it becomes meaningless to define IP3 [98]. However, Vaitkus *et al.* [99] for instance, defined IP3 by biasing the HFET device in nonlinear regimes (class-AB, class-B and class-C), which is principally misleading.

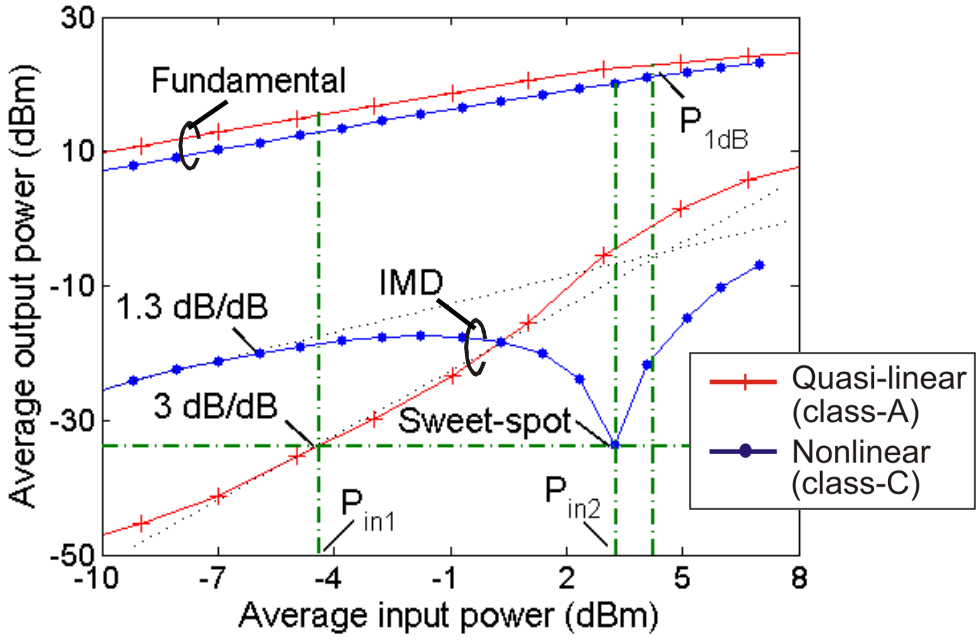

Figure 5.3 Typical measured output power and in-band IMD3 characteristics of a 0.5-mm GaN HEMT under two-tone excitation in a 50Ω environment.

For a fixed IMD value of -33 dBm in Figure 5.3, there are two possibilities of operating the transistor either under class-A bias condition backing-off from input P_{1dB} of 4 dBm by approximately 8 dB (P_{in1}), which results in P_{out} = 15 dBm. Alternately, under class-C bias condition, IMD of -33 dBm is achieved at P_{in2} with an apparent advantage of higher P_{out} = 20 dBm, which would clearly boost the overall efficiency compared to the former. Thus, by strategically placing the IMD minima close to P_{1dB} a highly linear and efficient amplifier design can be realized.

Carvalho and Pedro [95] have mathematically formulated the overall IMD behaviour by integrating the small-signal and the large-signal distortion contributions in a closed-form analytical expression. Accordingly, on the basis of Volterra series technique, which defines the third-order [$H_3(\omega)$] and fifth-order [$H_5(\omega)$] kernels, the small-signal part of the IMD current expression can be represented as [95]

$$\begin{aligned} SS_{Iout}(2\omega_2-\omega_1) = {} & \frac{3A^3}{8} H_3(\omega_2,\omega_2,-\omega_1)e^{j(2\phi_2-\phi_1)} \\ & + \frac{50A^5}{32} H_5(\omega_2,\omega_2,-\omega_1,\omega,-\omega)e^{j(2\phi_2-\phi_1)} \end{aligned} \tag{5.1}$$

with an assumption of describing small-signal IMD behaviour using fifth-degree Taylor series within quasi-linear range of operation.

Large-signal IMD contribution is expressed by the two sinusoidal input describing function $TSIDF_{Iout}(A, 2\omega_2-\omega_1)$, which reads

$$TSIDF_{Iout}(2\omega_2-\omega_1) = \frac{2j}{AT_1T_2} \int_{-T_1/2}^{T_1/2} \int_{-T_2/2}^{T_2/2} f_{NL}\left[V_{in}(t)\right] \cdot e^{j\omega_1 t_1} e^{-j2\omega_2 t_2} dt_1 dt_2 \tag{5.2}$$

where

$$V_{in}(t) = A\sin(\omega_1 t) + A\sin(\omega_2 t) \tag{5.3}$$

Equation (5.2) represents the Fourier transform of the input-output transfer function $I_{out} = f_{NL}(V_{in})$ at $2\omega_2-\omega_1$. In the case of low input excitation, the

small-signal IMD (5.1) becomes dominant, while the large-signal IMD starts to dominate the overall IMD, when the signal swing enters nonlinear regime. The phase of the small-signal IMD is determined by the bias condition (operating class), in which the smooth turn-on behaviour, depicted in Figure 4.13(b) of Chapter 4, along the loadline becomes very critical. While the RF swing along the loadline approaches saturation-to-ohmic transition zone, the phase of (5.2) tends to 180°. Consequently, for a certain input power level, partial cancellation between the small-signal and large-signal IMD can be expected depending on their respective phase resulting in a notch or IMD sweet-spot. Subsequently, for a fixed loading condition, the occurrence and the position of sweet-spots are mainly determined by the transconductance characteristics, which indeed varies with the semiconductor device technology. External controllable parameters include the operating point of the transistor (V_{GS0}, V_{DS0}), input power level, load termination and even the test signal type.

For understanding the impact of transconductance characteristics on the sweet-spot behaviour, a Curtice-quadratic GaN FET model was used to simulate IMD curves in a 50Ω environment by varying the parameter that controls the transconductance behaviour. Figure 5.4(a) shows the transfer characteristics for different transconductance behaviour and the corresponding IMD3 characteristics is illustrated in Figure 5.4(b). Inspecting Figure 5.4(b), following aspects can be incurred:

- From the linearity point of view, as the abrupt turn-on behaviour reduces, the overall IMD reduces at higher input power levels, though an opposite trend is observed for low signal levels. The former can be indeed explained in the terms of the suppression of higher order drain current derivatives due to rather smooth or flat G_m behaviour.
- The sweet-spot behaviour gradually diminishes as the turn-on behaviour drastically increases. This is attributed to the absence of phase cancellation between the small-signal and large-signal IMD. The

phase of the large-signal IMD principally tends to 180° regardless of the property of G_m characteristics. However, it is important to note that the phase of the small-signal IMD is determined by the phase of G_{m3}. In this regard, class-AB operation is typically proved to be an imprecise region wherein it is difficult to determine the phase of the small-signal IMD [93]. Moreover, the bias dependent G_{m3} is very sensitive to the G_m characteristics [93], [95]. All these factors impose strong limitation on the possible IMD cancellation phenomenon.

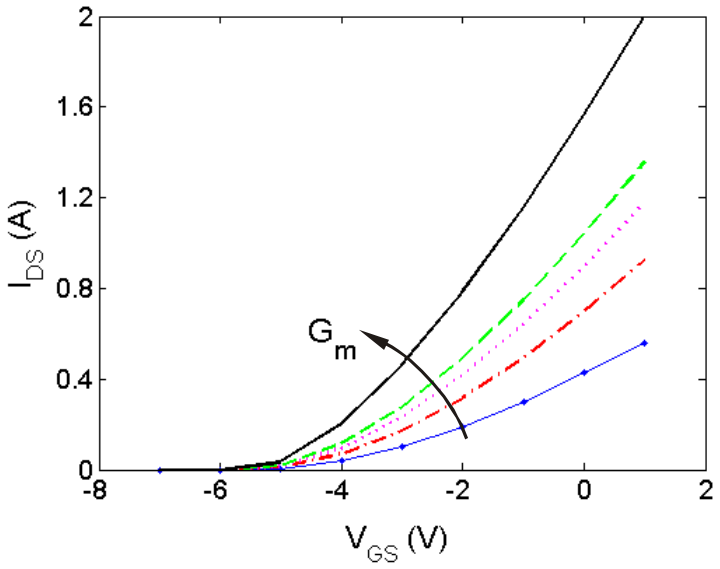

(a)

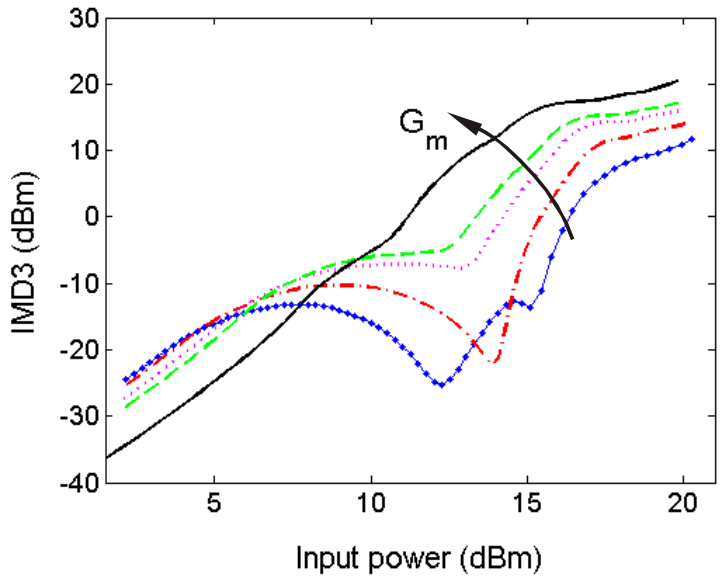

(b)

Figure 5.4 FET transfer characteristics impacting IMD sweet-spot properties under class-AB operating condition.

5.2 Bias and Load Termination

Carlvalho and Pedro [93] have also reported that out of the two possibilities of large-signal sweet-spots occurrence, the first occurs, when the gate terminal is biased either below pinch-off voltage (class-C) or in the vicinity above pinch-off voltage (deep class-AB) evolving towards higher efficiency region. The second appears when the transistor is biased at gate forward conduction (triode region). However, the latter affects the transistor reliability under large-signal operation limiting this region to only small-signal applications. Since it is of high interest to study the first case, two-tone simulation was conducted using in-house developed transistor model [100] of 1.2-mm GaAs HEMT (manufactured by TriQuint Semiconductors). Figure 5.5 demonstrates the loci of large-signal sweet-spot superimposed onto the lower and upper IMR contours with drain voltage V_{DS0} fixed at 9V (saturation region).

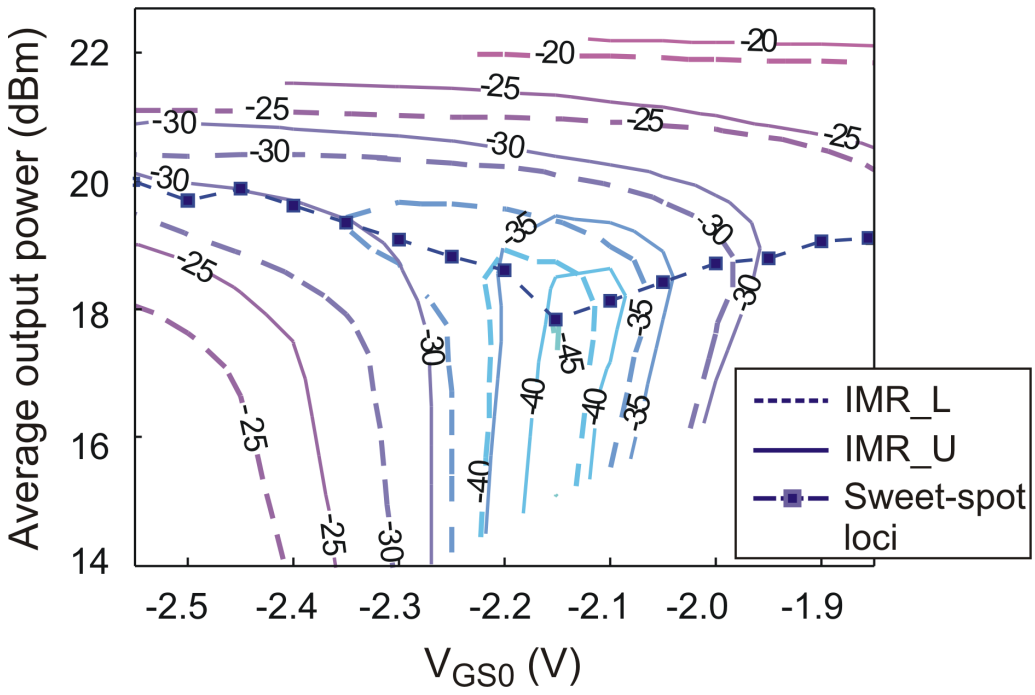

Figure 5.5 Simulation of two-tone excited IMR contours of 1.2-mm GaAs HEMT depicting large-signal IMD sweet-spot loci in a 50Ω environment.

With the pinch-off voltage of -2.2V, which was determined from the DC I(V) characteristics of the analysed 1.2-mm GaAs HEMT, clearly the IMD sweet-spots moves into the desired operating condition for higher efficiency and output power. From the contour plot, an optimum gate biasing of V_{GS0} = -2.15V can be chosen guaranteeing higher efficiency, which yields an IMR of -45 dBc at 3 dB back-off (from the 1 dB compression point) with $P_{out,\,avg}$ = 18 dBm. The drain bias has indeed a strong influence on the transistor gain. Hence, with the dual bias control, the gain can be held constant by which the output power could virtually vary linearly with the input power [94].

Thus, these effects demonstrate the general principle that the IMD characteristics of the device can be tailored according to the needs that an application demands. Subsequently, a power amplifier designer is encouraged to operate at higher input power levels in a very power-efficient mode, while simultaneously maintaining high linearity condition. Malaver *et al.* [94] arrived at a similar conclusion attaining -46 dBc ACPR at 25 dBm output power. The overall efficiency of 22% was achieved for class B MESFET based amplifier following IS-95 QPSK signal specifications, which imposes ACPR < -45 dBc.

Both the fundamental and out-of-band load terminations have strong influence on the IMD sweet-spot behaviour. This gives an added advantage in designing highly linear power amplifier for which the fundamental is terminated by an optimum load ($R_{L,opt}$ for $P_{out,max}$), and the harmonics, including the baseband, are optimally tuned for achieving reduced IMD at P_{1dB}. This is, in particular, relevant for amplifier classes operating beyond pinch-off, where linearity is highly essential. In other words, performing out-of-band load-pull is meaningful only, when the DUT is operating in a nonlinear mode and generating harmonic components. Thus, it becomes essential to analyse the effects of out-of-band termination on large-signal IMD sweet-spot behaviour taking a 1.2-mm GaAs HEMT as an example.

Simulations were carried out in ADS® using a validated in-house GaAs HEMT model [100], biased at V_{GS0} = -2.55V, V_{DS0} = 9V for class-C operation under two-tone stimulus having f_c = 2.15 GHz and Δf = 200 kHz. Table 5.1 illustrates different load-pulling conditions of baseband and second-harmonic frequency zones with variable load reflection coefficients $\Gamma_L(\omega) = \{1, j, -1, -j\}$, which includes purely resistive $[\Gamma_L(\omega) = (1, -1)]$ and reactive $[\Gamma_L(\omega) = (j, -j)]$ termination properties. Corresponding simulated results of the fundamental and upper IMD characteristics are shown in Figure 5.6(a-b) for variable baseband load impedance and Figure 5.6(c-d) for variable second-harmonic load impedance.

As a well accepted power amplifier design rule for linearity enhancement, Figure 5.6(a-b) shows that baseband short provides excellent IMD performance independent of second-harmonic termination properties. In the compression region, in particular, significant changes are observed for different envelope terminations. This indeed signifies the dominance of even-order nonlinearities as the RF loadline enters saturation-to-linear (ohmic) transition zone. On the other hand, with high baseband impedance the sweet-spot behaviour vanishes making the device more nonlinear. In this regard, experimental results are presented in Section 5.3.2 demonstrating the complexity in recovering the large-signal sweet-spot behaviour under realistic characterization testbench scenario.

Figure 5.6(c) depicts an interesting IMD behaviour under baseband short wherein the linearity is further enhanced by terminating the second-harmonic with Z_L = -j50Ω $[\Gamma_L(2\omega_0) = -j]$. This shows that, when the bias and matching networks are experimentally optimised for linear power amplifier design, especially when performing out-of-band load-pull measurement, envelope load-pulling must be followed by harmonic load-pulling, giving a better possibility to obtain high linearity. However, with the baseband short, it can

be concluded that the second-harmonic termination has no significant influence on the device IMD behaviour. Further, as expected, Figure 5.6(d) shows that a high baseband termination ceases any impact from second-harmonic load condition. Hence, practically it is not meaningful to perform second -harmonic load-pull when a high baseband impedance is imposed at the device drain node, implying a careful design of broadband characterization testbench.

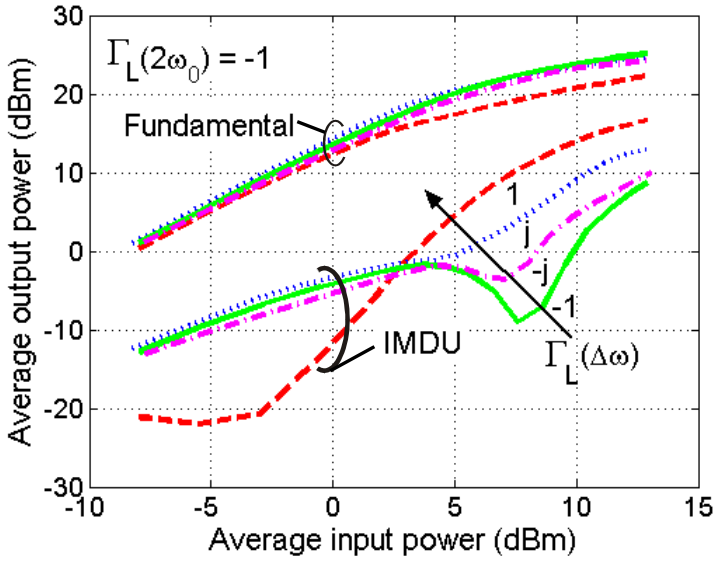

(a)

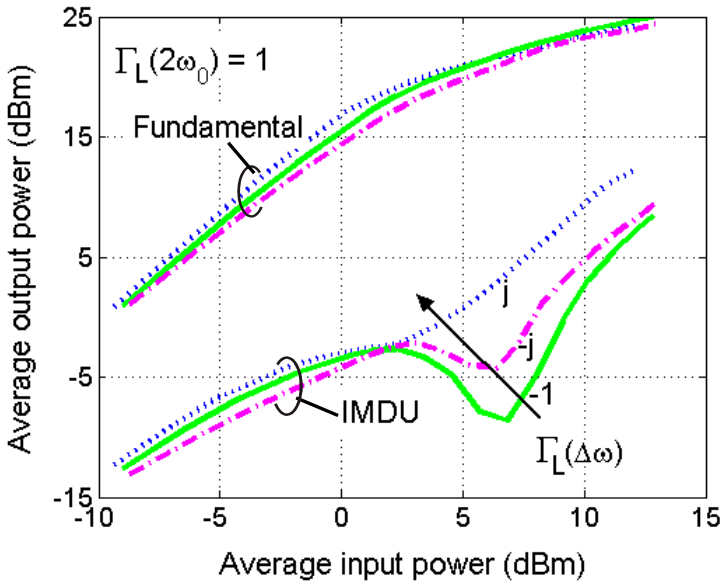

(b)

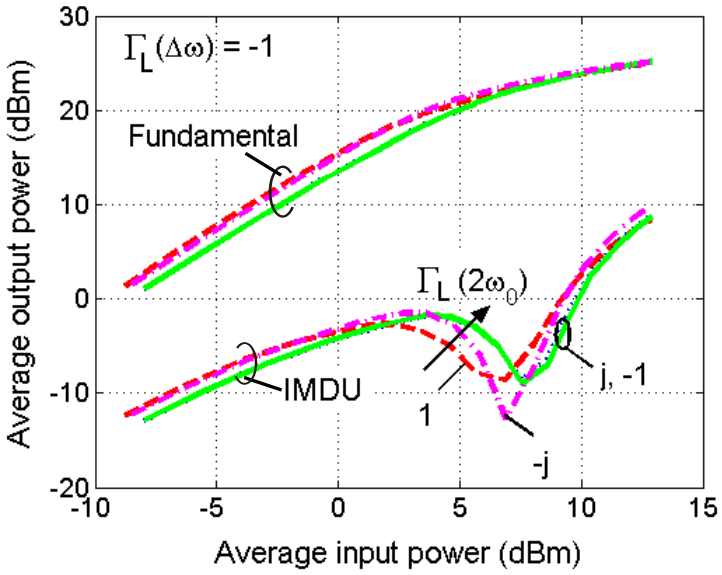

(c)

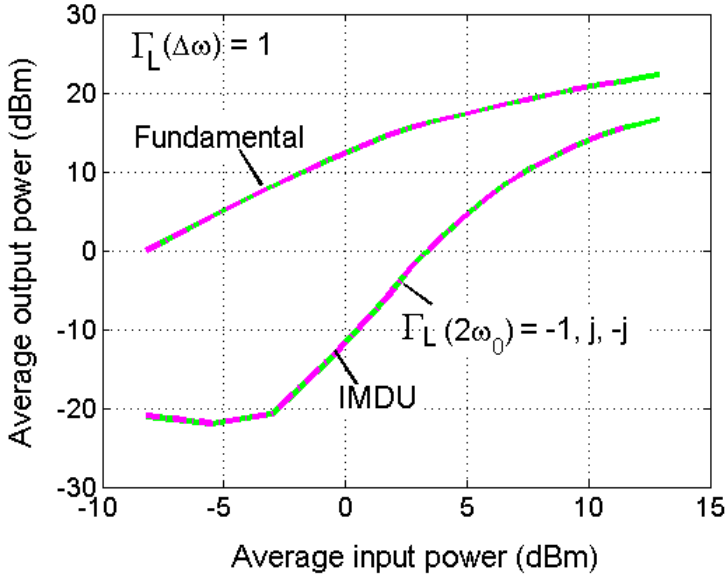

(d)

Figure 5.6 Simulated fundamental output power and IMD3 of 1.2-mm GaAs HEMT for variable out-of-band load-pulling, (a, b) baseband; (c, d) second-harmonic.

Table 5.1 Load-pulling out-of-band termination with $Z_L(\omega_0) = 50\Omega$ under two-tone stimulus.

Load termination settings	$\Gamma_L(\omega_0)$ *at baseband*	$\Gamma_L(2\omega_0)$ *at 2nd-harmonic*
(a)	variable	$1\angle 180°$
(b)	variable	$1\angle 0°$
(c)	$1\angle 180°$	variable
(d)	$1\angle 0°$	variable

5.3 Sweet-Spot Reproducibility

Analysis of device sensitive sweet-spot mechanism needs reliable large-signal IMD measurements. With the background of establishing a reliable RF characterization testbench, which was presented in Chapter 4 [Figure 4.23(a)], the true IMD sweet-spot behaviour in GaN HEMTs can be investigated for its consistency in high linear power amplifier design applications. On the other hand, GaAs HEMTs, which are practically accepted to be matured semiconductor technology, are additionally considered as a reference to evaluate the sweet-spot reproducibility in GaN HEMTs.

5.3.1 Statistical Process Consistency Evaluation

Until recently, importance was given only to saturation property of the $I_{DS}(v_{GS})$ transfer characteristics in FET devices to improve the fundamental P_{out} or PAE predictions. However, recent research activities from active device modelling community have revealed that the smooth turn-on property of the transfer characteristics has direct impact on the overall intrinsic distortion behaviour [17]. Underlining this fact, a statistical evaluation of pinch-off voltage V_{pi}, which defines the turn-on behaviour, was carried out on 14 samples of 1.2-mm GaAs HEMTs (manufactured by TriQuint Semiconductors) and 6 samples of 2-mm GaN HEMT (manufactured by Nitronex) for examining their respective process consistency.

In order to obtain an unambiguous and consistent definition of V_{pi}, a zero crossing of the third-derivative of drain-source current [G_{m3} null as shown in Figure 4.13(b) of Chapter 4] was determined for all the devices under investigation, which is located close to the position of the ideal threshold. Static-DC characterization was hence performed on GaAs and GaN HEMTs using Accent's dynamic I(V) analyser (DiVA) D265EP system [80]. As an outcome of the experimental analysis depicted in Figure 5.7, GaAs HEMTs

demonstrated a mean pinch-off voltage of V_{pi} = -2.225V with a standard deviation of 0.024V, while GaN HEMT exhibited a mean value of V_{pi} = -1.44V with a standard deviation of 0.14V. This significant deviation of V_{pi} in the less matured GaN HEMTs indicate a poor repeatability performance, which should have a clear impact on the large-signal sweet-spot characteristics.

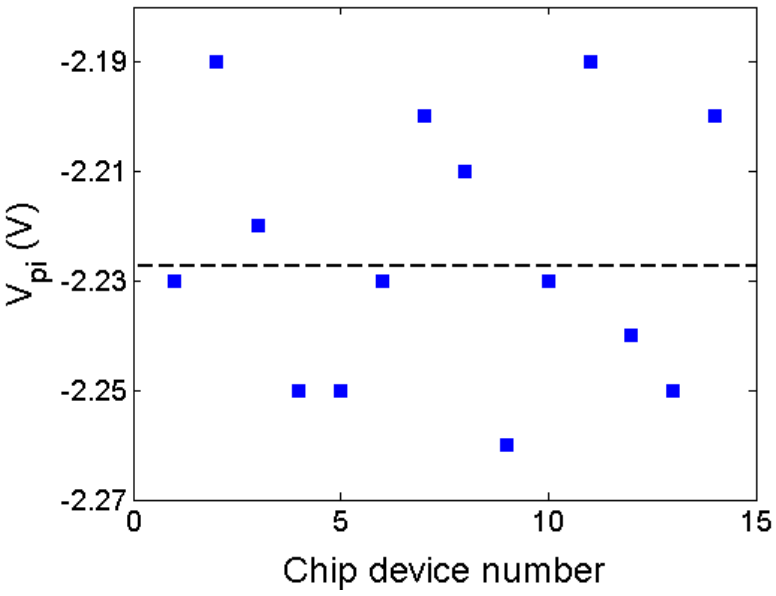

(a)

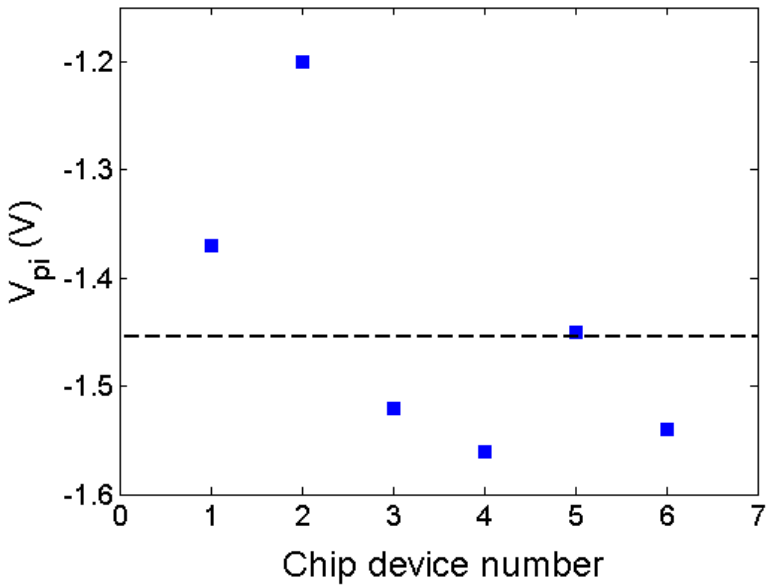

(b)

Figure 5.7 Statistical process consistency evaluation of (a) GaAs HEMT, (b) GaN HEMT chip devices for analysing the repeatability of pinch-off voltage V_{pi}.

5.3.2 Experimental Characterization of Large-Signal IMD Sweet-Spots

5.3.2.1 Two-Tone Stimuli

Taking into account only the first three devices (1, 2 and 3), the observed deviation in their respective pinch-off voltages was related to sweet-spot reproducibility at large-signal levels. Under two-tone stimuli (f_c = 2.15 GHz, Δf = 5 MHz), the IMD characteristics of GaAs and GaN HEMTs were measured as illustrated in Figures 5.8 and 5.9.

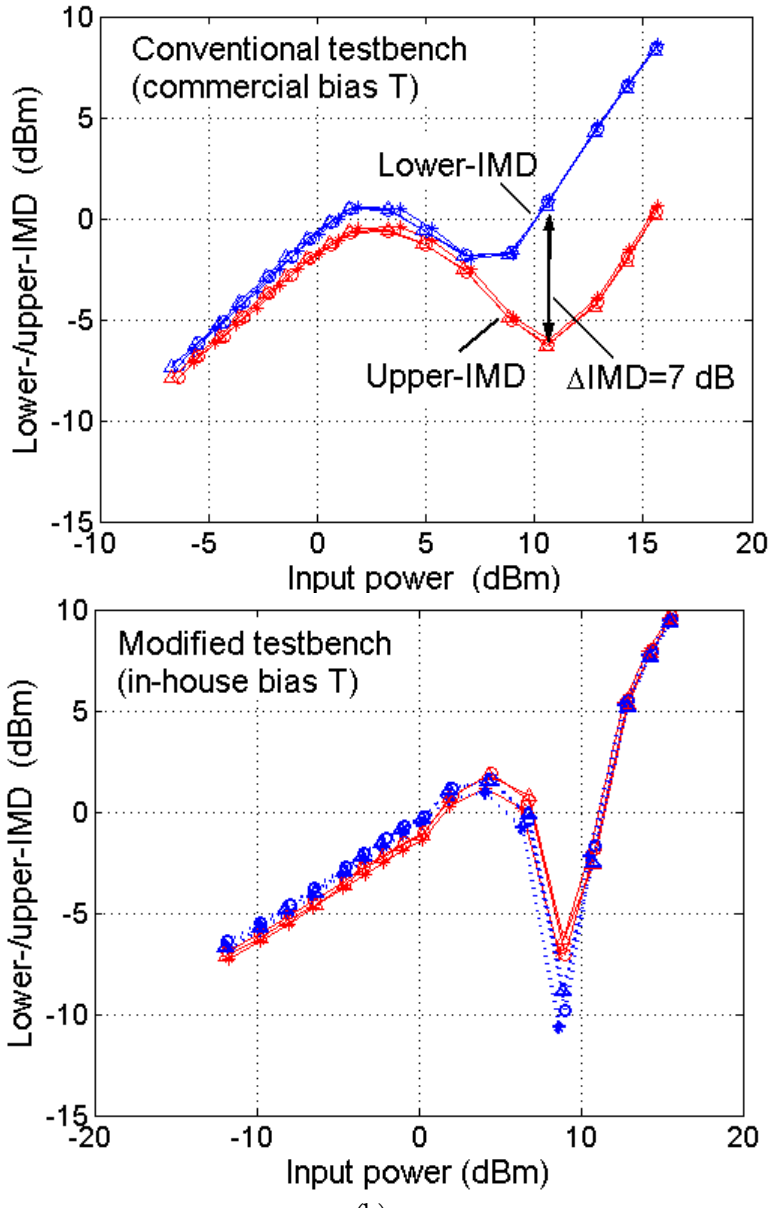

(b)

Figure 5.8 Experimental evaluation of sweet-spot reproducibility in three GaAs HEMT devices (1, 2, 3) biased for class-C operation (-2.6V, 9V).

As shown in Figure 5.8(a), GaAs HEMT, biased for class-C operation (-2.6V, 9V), primarily delivers good sweet-spot reproducibility in both, conventional and modified testbench (Section 4.4 of Chapter 4) conditions [84]. However, a strong IMD asymmetry of 7 dB is observed with the conventional testbench (see Figure C1.1 of Appendix C) using commercial RF bias tee of type HP11612A manufactured by Hewlett-Packard. In this case, it is necessary to minimize the measured IMD asymmetry before conducting any further analysis on the sweet-spot. This would require the optimisation of out-of-band terminations (especially zone 0) enabling reliable comparison of sweet-spot behaviour between two semiconductor technologies. As a result, with the improved testbench (see Figure 4.23 of Chapter 4), the asymmetry between lower and upper IMD is eliminated as shown in Figure 5.8(b) together with remarkable IMD suppression.

Figure 5.9 shows similar results in case of GaN HEMT, which was biased for class-C operation (-1.6V, 15V). Referring to the upper and lower IMD characteristics measured using conventional testbench, no sweet-spots are observed due to the non-zero baseband termination as reported in [95]. Additionally, the sweet-spot reproducibility becomes more dramatic as shown in Figure 5.9(a). This is in accordance with the pinch-off voltage inspected in Figure 5.7(b). However, with the modified setup, the low distortion sweet-spot behaviour is revealed and its variation is in agreement with the experimentally determined pinch-off voltages [10]. It is important to note that the signal bandwidth of the stimulus signal has major influence on the sweet-spot behaviour, wherein memory-effect is strongly pronounced [101].

Large-signal IMD sweet-spot is a phase cancellation phenomena that occurs between small-signal and large-signal IMD behaviour. The phase of the small-signal IMD is determined by G_{m3} corresponding to the bias condition (operating class), in which case the smooth turn-on behaviour becomes very critical. In particular, for class-C operation, the phase of the small-signal IMD

($\angle G_{m3}$) is principally zero. While the phase of the large-signal IMD tends to 180°, when the RF swing along the loadline approaches saturation-to-ohmic transition. Consequently, the cancellation of IMD due to phase change results in sweet-spot characteristics for a particular input drive level.

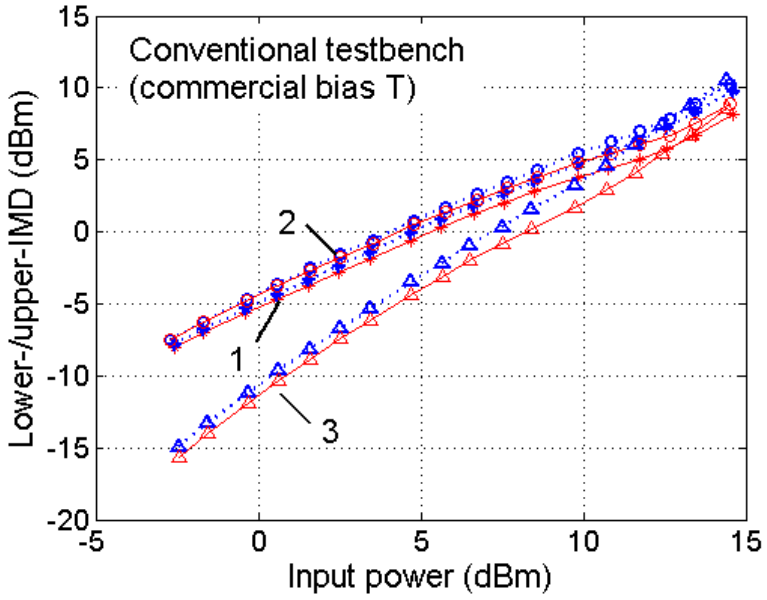

(a)

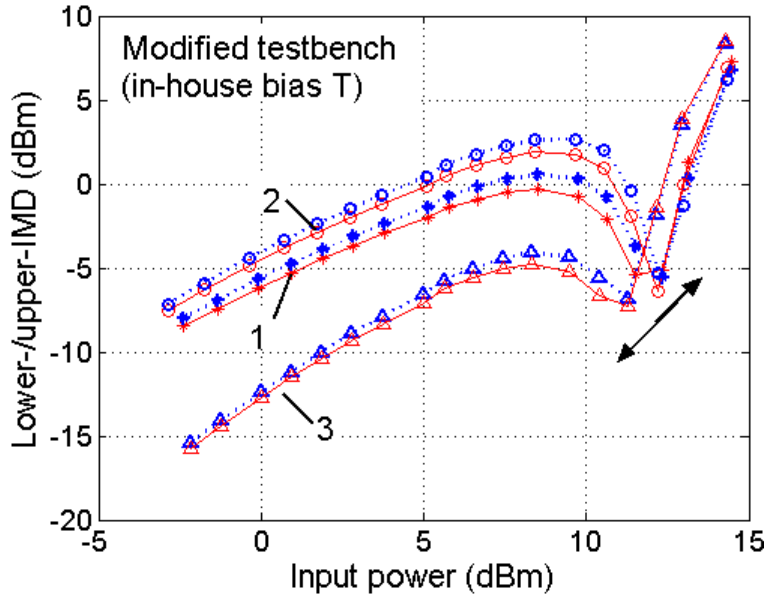

(b)

Figure 5.9 Experimental evaluation of sweet-spot reproducibility in three GaN HEMT devices (1, 2, 3) biased for class-C operation (-1.6V, 15V).

In the present scenario, under class-C operation, even though the gate voltage was fixed to -1.6V for all the three GaN HEMT devices, device 2 is deeply reverse biased compared to device 1 and 3 as shown in Figure 5.7(b). This is because of the variation in turn-on behaviour of these devices. As a result, under a fixed 50Ω load, for the cancellation phenomena to occur in the IMD characteristics of device 2, a larger input drive is essential to enter into saturation-to-ohmic zone. The trend of sweet-spot occurrence in Figure 5.9(b) clearly follows the pinch-off behaviour shown in Figure 5.7(b).

5.3.2.2 Multi-Carrier W-CDMA Stimuli

It is known that the correlation between two-tone stimulated IMR and ACPR under digitally modulated excitation are generally weak [102]. Nevertheless, it is of high interest for high linear power amplifier design to know to what extent can the dynamic ACPR characteristics sustain sweet-spots based on single-carrier W-CDMA excitation. From the UMTS application point of view, implementing W-CDMA modulation technique, there is scepticism on the consistency of sweet-spot occurrence. Thus, uncertainty is still prevailing among several researchers, whether sweet-spot characteristics could be utilized for practical applications. In order to analyse this issue, again GaAs and GaN technologies were considered to obtain more transparency in the device's behaviour in response to complex dynamic stimulus.

Figure 5.10 shows the ACPR measurements performed on GaAs and GaN HEMTs under 3GPP single-carrier W-CDMA (Test Model 1, 32 DPCH). Interestingly, as illustrated from the measurement results in Figure 5.10(a), 1.2-mm GaAs HEMT (manufactured by TriQuint Seminconductors) is vulnerable to the out-of-band optimisation, due to the modified testbench. Consequently, 3 dB reduction in ACPR and marginal asymmetry improvement is obtained. However, the situation changes dramatically in case of GaN HEMT devices as seen in Figures 5.10(b-c). Two GaN HEMT

devices [2-mm device: Nitronex; 0.5-mm device: Fraunhofer Institute for Applied Solid-State Physics (IAF), Freiburg] were considered for achieving meaningful conclusion on ACPR characteristics in GaN HEMTs. Despite different process technologies, only ACPR asymmetry seen in Figures 5.10(b-c) has been suppressed without any hint of sweet-spot behaviour.

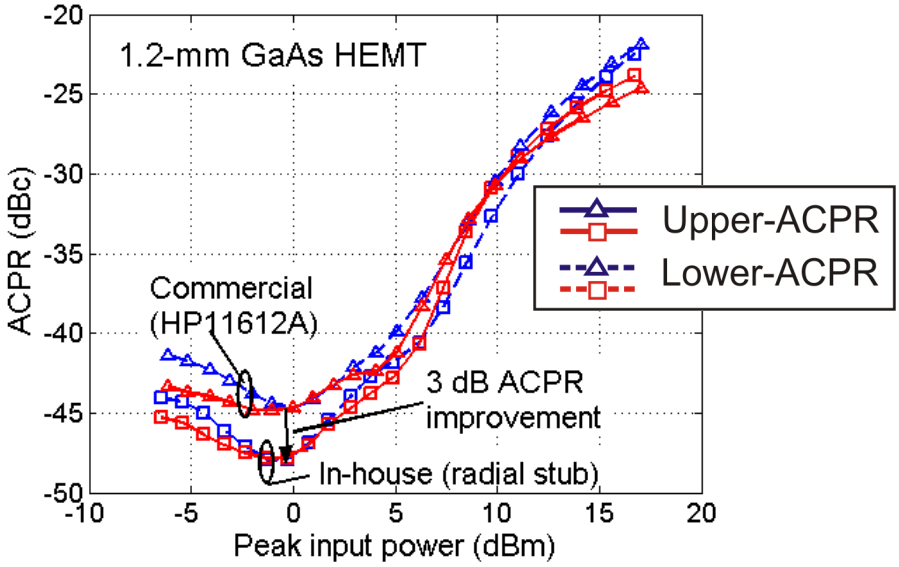

(a)

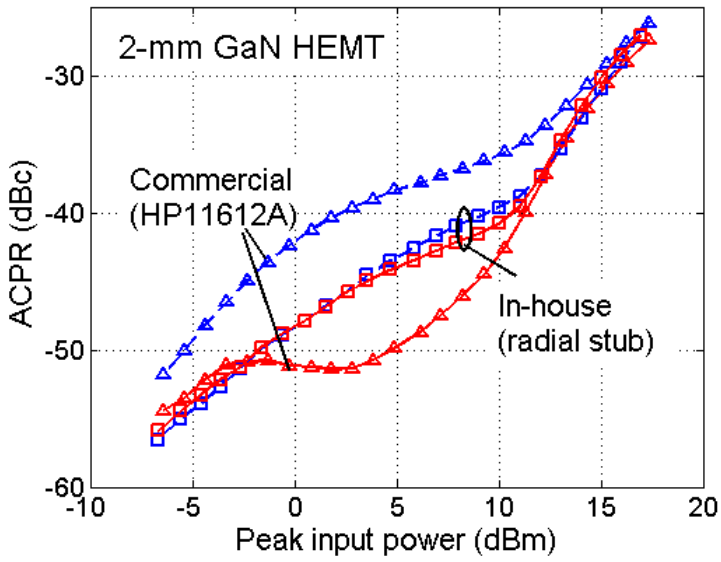

(b)

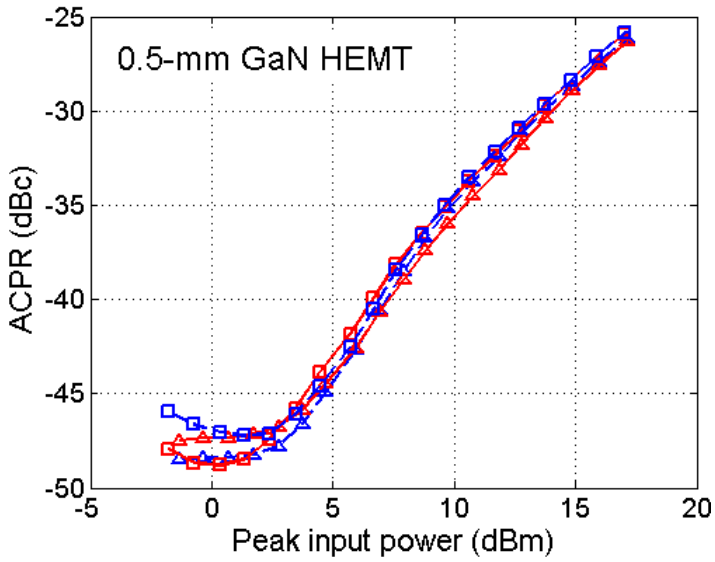

(c)

Figure 5.10 ACPR performance comparison for 3GPP Test Model 1, 32 DPCH 1 x WCDMA around 2.15 GHz carrier frequency for (a) 1.2-mm GaAs HEMT biased at V_{GS0} = -2.6V, V_{DS0} = 9V, (b) 2-mm GaN HEMT biased at V_{GS0} = -1.6V, V_{DS0} = 15V, and (c) 0.5-mm GaN HEMT biased at V_{GS0} = -4.2V, V_{DS0} = 25V.

In case of GaAs HEMT, one possible reason for the improvement in ACPR characteristics could be that only the third-order distortion products are predominant in the adjacent channels, whose impact is directly reflected from optimum out-of band load termination. In contrast, GaN HEMTs are significantly prone to higher order distortion products co-existing at the same frequencies, where third-order products are suppressed (Figure D1.1 in Appendix D). Hence, no change occurs in sideband distortion despite optimising out-of-band termination.

To appreciate the observed difference in ACPR performance between GaAs and GaN HEMT semiconductor technologies, it becomes meaningful to study their corresponding nonlinear I_{DS} characteristics, which is the primary cause dominating overall distortion [103]. The measured transconductance characteristic of 1.2-mm GaAs HEMT, as shown in Figure 5.11(a), has a typical constant G_m region unlike GaN HEMTs seen in Figure 5.11(b-c).

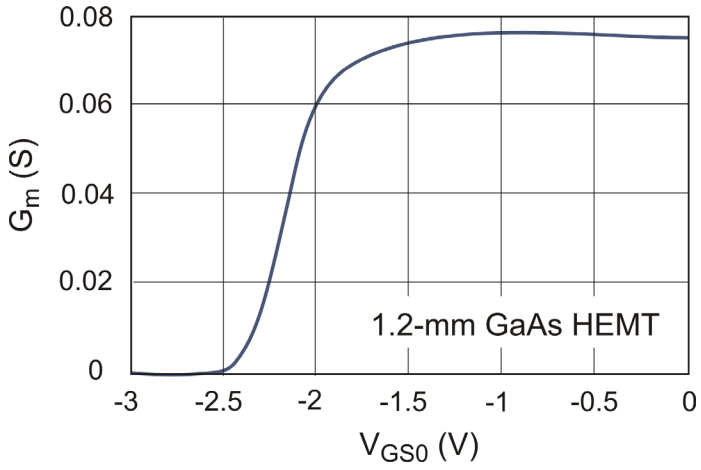

(a)

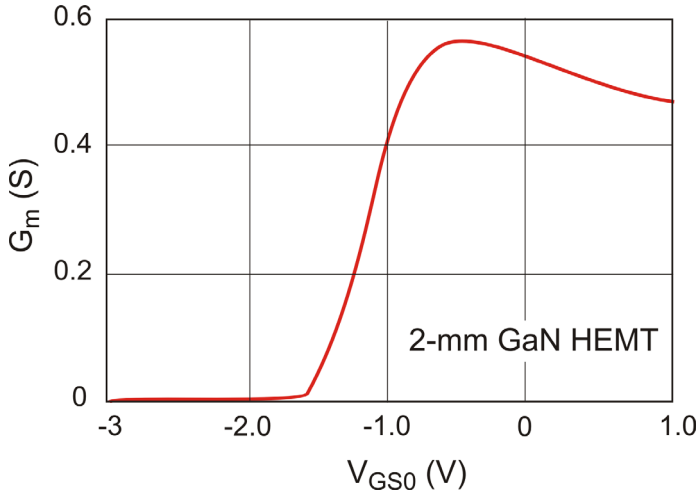

(b)

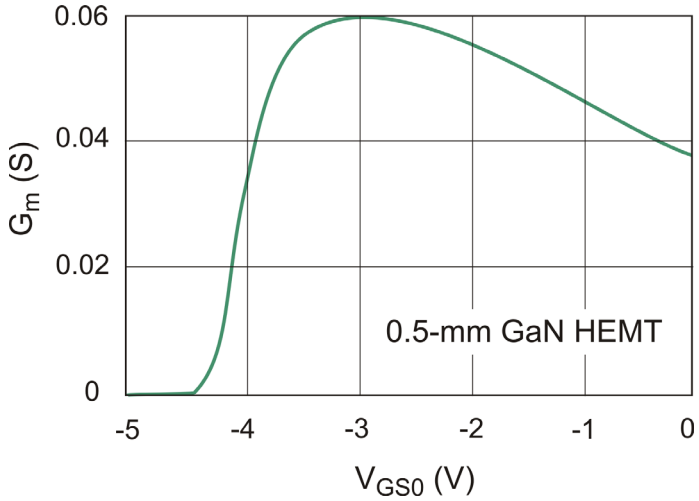

(c)

Figure 5.11 Comparison of typical transconductance characteristics G_m of GaAs and GaN HEMT devices derived from pulsed-DC measurements.

Subsequently, in case of GaAs HEMT, due to the constant G_m behaviour under large-signal operating conditions, the higher order derivatives (5^{th}, 7^{th} and so on) of nonlinear I_{DS} become negligible compared to the dominant third-derivative (G_{m3}). This clearly explains the unique ACPR performance in GaAs HEMTs, wherein 3 dB reduction was measured as shown in Figure 5.10(a) with optimised out-of-band load termination. Thus, the technological change in GaAs HEMT and GaN HEMT on ACPR performance from transconductance characteristics perspective has been deciphered by means of a reliable RF characterization testbench. The measured sweet-spot phenomenon principally demonstrate the fact that the device characteristics could be tailored suitably to increase the linearity of highly efficient power amplifier classes.

From the perspective of multi-carrier W-CDMA applications based on GaN HEMT technology, a 0.5-mm GaN HEMT [manufactured by Fraunhofer Institute for Applied Solid-State Physics (IAF), Freiburg] was driven by two-carrier W-CDMA signal (Test Model 1, 32 DPCH) with Δf = 15 MHz around f_c = 2.15 GHz (V_{GS0} = -4.2V, 2%I_{DSS}, V_{DS0} = 25V). The measured IMR3 characteristics using a conventional and the modified measurement setup are shown in Figure 5.12.

The sweet-spot occurrence is evident when in-house RF bias tee is implemented in the modified testbench. In this case, the third-order intermodulation distortion ratio (IMR3) requirement of -45 dBc or lower becomes more vital because of its wide spread interference with the adjacent channels. The dip in IMR3 is thus a fundamental device property, which is now revealed since the bias tee has provided a wide baseband and second-harmonic short termination. These results are in agreement with the published work of Vare and Hopper [104], who also demonstrated IMD sweet-spots using an LDMOS device characterized under two-carrier W-CDMA test signal

(Figure D1.3 in Appendix D). However, there was a significant memory-effect with more than 10 dB IMD imbalance at the regions, where sweet-spot occurred. In the present work, it can be seen from Figure 5.12 that the IMD3 asymmetry has reduced to less than 0.5 dB at the local minima using the in-house bias tee. Similar to two-tone stimulus, in recent years, two-carrier W-CDMA has proved to be an optimal excitation signal to investigate the behaviour of large-signal IMD sweet-spot.

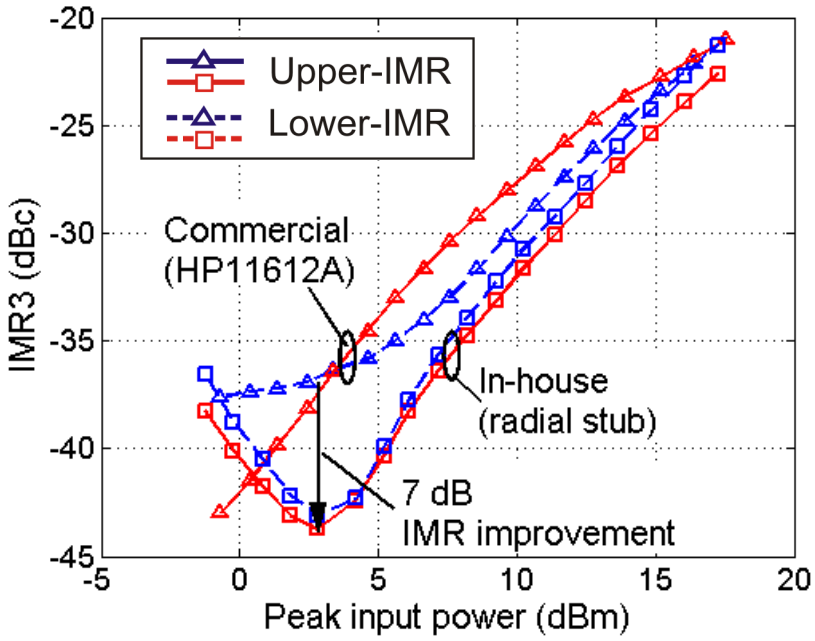

Figure 5.12 Two-carrier W-CDMA stimulus based IMD3 characterization of a 0.5-mm GaN HEMT in a 50Ω environment.

For practical applications, depending on the peak-to-average ratio (PAR) of the signal considered, IMD sweet-spot can be appropriately positioned for a specific back-off operation by tuning the fundamental load termination. By implementing the optimised bias network for broadband amplifier design, the linearity performance will be hence enhanced at required bias conditions minimizing the linearizer design complexity or even eliminating the need for external linearization.

Chapter 6
Conclusion and Future Work

Key strategies to explore the possibilities of improving linearity and efficiency of basestation power amplifiers at higher output power are still under development. With the former issue, intensive research activities have been initiated worldwide, to reduce IMD in power devices. Besides the benefits of high linearity and efficiency offered by upcoming GaN devices, due to rapidly developing broadband multi-standard air interfaces with multi-carrier solutions, the situation has become even more challenging to meet the 3GPP specifications. Meeting the requirements of increased mobile users have led to the use of single carrier with wider spectrum or multi-carrier solution with each carrier possessing a narrowband spectrum. With the advent of future 3G UMTS-LTE, which incorporates OFDM for downlink having scalable bandwidths ranging from 1.25 to 20 MHz, the complexity of satisfying telecommunication linearity requirements would rapidly escalate. In this thesis, a new approach, based on Volterra series technique, has been analysed for identification and minimization of distortion sources in GaN HEMT devices. Application rules have been developed to experimentally decipher device inherent IMD in GaN HEMTs.

The benefit of Volterra series technique has been widely acknowledged over the years in an effort to understand IMD generation mechanism by identifying dominant distortion contributors. Volterra model of a weakly nonlinear FET equivalent circuit is based on the polynomial models of I(V) and C(V) nonlinearities. These comprise the transconductance $G_m(v_{gs}, v_{ds})$, the channel conductance $G_{ds}(v_{gs}, v_{ds})$, the gate-source capacitance $C_{gs}(v_{gs})$ and also the gate-drain capacitance $C_{gd}(v_{gs}, v_{ds})$, which are the key nonlinearities that shape the device's IMD. In this research work, analytical equations describing third-order IMD contribution from each nonlinear FET equivalent circuit element has been derived. The multitude of different mixing mechanisms causing distortion has been demonstrated, stressing on the need to include second-order terms contributing towards total IMD product. From the IMD vectorial analysis conducted on an 8 x 125 μm GaN HEMT, it was found that the third-order voltage phasor associated with the feedback capacitance C_{gd} was one of the dominant distortion causing vectors.

Taking the benefit of gate field-plate structure, which effectively increases C_{gd}, it was demonstrated through simulation that by scaling C_{gd} to 150%, the device linearity improved by around 3 dB. The demonstrated 3 dB linearity improvement is, indeed, significant in terms of the present telecommunication demands, emphasizing the applicability of Volterra series technique for developing GaN HEMT technology for higher linearity performance.

At this point, it is rather difficult to quantitatively generalize the IMD improvement. This is because, for a given transistor technology, the amount of distortion suppression depends on the methodology of fabrication, structure type, device characterization environment and importantly the extrinsic (frequency dependent) and intrinsic (bias dependent) small-signal equivalent circuit parameter extraction procedure. Following the same reasoning, the depiction of individual distortion contributors having unique vectorial pattern cannot be generalized. However, in the context of GaN

based semiconductor technology, which is still immature, the distortion patterns distinctly vary from device-to-device in spite of undergoing the same technology processing. Furthermore, it is important to note that the distortion pattern of IMD phasor is independent of the input power level since it is known that by following Volterra series technique, the IMD level increases linearly with 3 dB/dB slope.

Obtaining an accurately working transistor device model involves mainly three phases, namely (a) data acquisition, (b) model extraction based on the data acquired, (c) accurate large-signal device characterization for reliable model verification. With respect to the model verification phase, this thesis has stressed upon the need for precise characterization of broadband distortion in GaN HEMT devices. Reliable large-signal device characterization is also necessary for comprehensive experimental optimisation of power amplifier design through multi-harmonic source- and load-pulling. A fully calibrated frequency-domain measurement setup was developed using dual-channel vector signal analyser (VSA) as receiver. The availability of the second measurement channel in Agilent's 89600 series VSA, which is phase locked to the first channel, expanded the capability to provide real-time relative phase measurements. A large-signal vector error-correction technique was hence established for calibrating the measurement system under multi-tone and W-CDMA test signal environment.

In a broadband measurement environment, it is imperative to realize a constant load termination at the active device reference plane. In this regard, bias tees are among the key components whose design must be treated sensitively for linearity characterization. Commercial RF bias tees fail to fulfil this requirement, especially when modulated test signals are used. The bias tee's inherent inductor along the DC feed imposes high baseband impedance forcing IMD measurements dependent on the signal bandwidth. The solution of implementing a compensation network constituting shunt capacitors was

proposed, which functions as an envelope trap for decoupling the undesired DC feed and DC power supply. With respect to the RF bias tee design criteria, the emphasis is given to a short IF termination mainly because of two reasons:

- First, it is simpler to realize a baseband short, decoupling all undesirable effects influenced by external electrical parameters.
- Secondly, it is necessary to standardize broadband distortion measurements. This implies, in a 50Ω environment broadband distortion measurements become reproducible independent of the testbench configuration. This reduces the ambiguity commonly observed when validating broadband IMD prediction of the device model.

The intension to determine an optimal drain bias tee led to systematic development of many bias tee variants. Among those, the wide bandwidth λ/4 open-circuited radial stub based bias tee was validated experimentally as optimal bias network design through memory-effect and IMD load-pull characterization of GaN HEMT. Further, for evaluating the reliability of the measurement setup from baseband perspective, drain bias sensing was treated as a quick-shot test by analysing the drain supply voltage waveforms.

From the industrial perspective, when realizing a complex power amplifier architecture, tackling critical issues of biasing becomes one of the major sub-problem in reaching final design goal. Within the framework of FET based applications, principally, the bias network design procedure should be independent of the transistor technology and the class of operation. Nevertheless, in practice, the influence of bias network configuration on achieving targeted specification, should be carefully evaluated before proceeding towards establishing routine mass production.

Another outcome of this research work was in achieving transparency on the uncertainties involved in implementing conventional measurement setup

configuration for broadband IMD characterization. Experimental memory-effect characterization results showed that the common practice of placing the RF bias tees at an offset from the device reference plane imposes restrictions in characterizing true device IMD behaviour. The modified testbench configuration indeed reflected an amplifier environment where the bias tee was placed close to the device reference plane. With the improved broadband testbench, the statistical process consistency of two different semiconductor technologies, namely GaAs and GaN HEMTs, were investigated, focusing on their respective sweet-spot behaviours. Also the cause for not achieving IMD sweet-spot under real stimuli in GaN HEMTs, which is often speculated, was justified by comparing its transconductance characteristics with the matured GaAs HEMT technology. Nevertheless, under multi-carrier W-CDMA stimuli, the experimental results on GaN HEMTs have justified the practical applicability of IMD sweet-spots in UMTS basestation power amplifier design, which would minimize the complexity of external linearization techniques. The proposed IMD measurement technique, hence, represents a further refinement in the state-of-the-art of source- and load-pull for precise evaluation of intrinsic linearity in GaN HEMTs for 3G broadband applications.

Future work

With the development of GaN HEMT technology still in its early stages, this work has made an appeal that Volterra series analysis is a powerful tool for improving GaN device technology. As an extension to the present work, the most immediate requirement is to primarily provide experimental validation of linearity improvement in GaN HEMTs with the field-plate structures. As the technology progresses, more detailed RF analysis is, however, required to accurately evaluate and optimize the device performance. Nevertheless, the developed Volterra series technique can further provide more heuristic facts

that may accelerate the development of GaN HEMT technology, some of which are envisaged as follows:

- It is of greater significance to conduct experiments and IMD3 simulations on devices having different field-plate dimensions and to analyse the trend of linearity behaviour. In other words, field-plate length can be scaled to study its gradual impact on device's IMD behaviour.
- Linearity and RF gain are in a trade-off relationship as it has been proved in case of GaAs FETs. Increasing the feedback capacitance through field-plate technology can improve the device linearity but would definitely degrade the RF gain. Consequently, this trade-off relationship cannot be solved by a simple optimisation of feedback capacitance. Nevertheless, the demerit of gain in field-plate based GaN devices could be partially compensated when the device is operated at higher drain voltages. This aspect could be analysed from the vectorial pattern modelled by Volterra series technique.
- For a given device technology, analysing the interaction between different nonlinearities and their dependence on bias voltages and termination impedance plays an important role in designing highly linear and efficient power amplifier. In this thesis work, theoretical and experimental investigation of the impact of drain bias network on GaN HEMT's IMD performance were performed. However, it is also meaningful to examine the effect of source termination, in general, and gate bias network, in particular, on GaN HEMT's linearity property.
- It is essential to understand the behaviour of distortion in GaN HEMT based power amplifiers exhibiting memory-effects and to investigate the means to cancel these bandwidth dependent distortion by tuning relevant impedance termination. In this case the question arises, whether the sources causing memory-effects and the solution to cancel

such effect, can be a standardized for all devices manufactured from the same process technology. In other words, the simulated distortion vectors could be investigated so as to be a representative behavioural pattern for many devices fabricated from the same process technology. Moreover, this could probably prove to be a rigorous test for examining the maturity of the device technology.

- In this work, it was shown that in case of GaN HEMTs, the fifth-order intermodulation distortion (IMD5) product had significant impact on overall linearity performance. Hence, Volterra series technique can be applied for treating IMD5 in order to gain deeper insight into the distortion generation mechanism.

To extend Volterra series for large-signal IMD prediction, power S-parameter characterization (ratio measurements under large-signal excitation) could be adopted. This is particularly useful to closely investigate the cancellation behaviour causing large-signal IMD sweet-spots. Relating such cancellation phenomena to the device physics could be a further challenging task.

For reliable distortion characterization of future UMTS-LTE systems, device-level linearity issues resulting from out-of-band terminations should be carefully analysed. GaN HEMTs are generally characterized using source- and load-pull measurement techniques to determine the optimum loading conditions for maximum gain, output power, efficiency, and ACPR, which are assessed under various complex load conditions. The signals used in these tests are frequently CW or two-tone signals. However, such experimental analysis is incomplete without evaluating device's parametric performance and related gradients across the impedance plane under realistic telecommunication signals. For instance, W-CDMA based source- and load-pull characterization of GaN HEMTs will be of great importance for the UMTS basestation power amplifier designers. However, the interpretation of the measured source- and load-pull contours under realistic stimuli often

become difficult. To avoid such difficulties, it would be meaningful to carry out source- and load-pull measurements involving the following steps:

- CW characterization by sweeping the carrier frequency across the fundamental bandwidth of the digitally modulated signal, which is application specific.
- Two-tone characterization by sweeping the tone spacing around a fixed centre frequency, so that the entire bandwidth of interest is characterized.
- The procedure can be extended to multi-tone stimuli, for example three-tone, before proceeding towards real stimuli.

Appendix A

FET Based IMD3 Phasors

The following part of the Appendix presents essential equations in order to compute the final IMD3 voltage vectors at the drain node. Next step is to solve the drain voltage phasor of lower IMD $(2\omega_1 - \omega_2)$ or upper IMD $(2\omega_2 - \omega_1)$, which is expressed in terms of the incremental input gate-source voltage $v_{gs}(\omega)$ as a summation of mixing products arising from cubic $[\sum_{n=1}^{7} v_{cubic(n)}(2\omega_1 - \omega_2)]$, envelope $[\sum_{n=1}^{21} v_{E(n)}(2\omega_1 - \omega_2)]$ and second-harmonic $[\sum_{n=1}^{21} v_{H(n)}(2\omega_1 - \omega_2)]$ components.

Lower IMD3 vectors: 3rd-order cubic terms

$$v_{d3cubic1}(2\omega_1 - \omega_2) = k_{3cgs} \cdot TF_{GSD}(2\omega_1 - \omega_2) \cdot \left[\frac{3}{4} \cdot j(2\omega_1 - \omega_2)\right] \cdot v_{gs}(\omega_1)^2 \cdot \overline{v_{gs}(\omega_2)}$$

$$v_{d3cubic2}(2\omega_1 - \omega_2) = \frac{3}{4} \cdot k_{3gm} \cdot TF_{DSD}(2\omega_1 - \omega_2) \cdot v_{gs}(\omega_1)^2 \cdot \overline{v_{gs}(\omega_2)}$$

$$v_{d3cubic3}(2\omega_1-\omega_2)=\frac{1}{2}k_{3gm2gds}\cdot TF_{DSD}(2\omega_1-\omega_2)\cdot\left[2\cdot TF(\omega_1)+\overline{TF(\omega_2)}\right]\cdot v_{gs}(\omega_1)^2\overline{v_{gs}(\omega_2)}$$

$$v_{d3cubic4}(2\omega_1-\omega_2)=\frac{1}{2}k_{3gmgds2}\cdot TF_{DSD}(2\omega_1-\omega_2)\cdot\left[2\cdot\overline{TF(\omega_2)}\cdot TF(\omega_1)+TF(\omega_1)^2\right]\cdot v_{gs}(\omega_1)^2\cdot\overline{v_{gs}(\omega_2)}$$

$$v_{d3cubic5}(2\omega_1-\omega_2)=\frac{3}{4}\cdot k_{3gds}\cdot TF_{DSD}(2\omega_1-\omega_2)\cdot TF(\omega_1)^2\cdot\overline{TF(\omega_2)}\cdot v_{gs}(\omega_1)^2\cdot\overline{v_{gs}(\omega_2)}$$

$$v_{d3cubic6}(2\omega_1-\omega_2)=\frac{3}{4}\cdot k_{3cgd}\cdot j(2\omega_1-\omega_2)\cdot TF_{GDD}(2\omega_1-\omega_2)\cdot\left[(TF(\omega_1)-1)^2\cdot\overline{(TF(\omega_2)-1)}\right]\cdot v_{gs}(\omega_1)^2\cdot\overline{v_{gs}(\omega_2)}$$

The additional in-band 3rd-order IMD voltage vectors generated by extending the analysis to 5th-degree are given below:

$$v_{d3cubic7}(2\omega_1-\omega_2)=\frac{k_{5cgs}}{16}TF_{GSD}(2\omega_1-\omega_2)\cdot\left\{30\cdot v_{gs}(\omega_2)\cdot\overline{v_{gs}(\omega_2)}+20v_{gs}(\omega_1)\cdot\overline{v_{gs}(\omega_1)}\right\}\cdot v_{gs}(\omega_1)^2\cdot\overline{v_{gs}(\omega_2)}\cdot j(2\omega_1-\omega_2)$$

$$v_{d3cubic8}(2\omega_1-\omega_2)=\frac{k_{5gm3gds2}}{8}TF_{DSD}(2\omega_1-\omega_2)\cdot\left\{3\cdot\overline{TF(\omega_2)}^2+12\cdot\overline{TF(\omega_2)}\cdot TF(\omega_1)+6\overline{TF(\omega_2)}\cdot TF(\omega_2)+3\cdot TF(\omega_1)^2\right\}\cdot v_{gs}(\omega_1)^2\cdot v_{gs}(\omega_2)\cdot\overline{v_{gs}(\omega_2)}^2$$

$$v_{d3cubic9}(2\omega_1-\omega_2)=\frac{k_{5gm2gd3}}{8}TF_{DSD}(2\omega_1-\omega_2)\cdot\left\{6\cdot\overline{TF(\omega_1)}\cdot\overline{TF(\omega_2)}+6\cdot\overline{TF(\omega_1)}\cdot TF(\omega_1)^2+2\cdot TF(\omega_1)^3\right\}\cdot v_{gs}(\omega_1)^3\cdot v_{gs}(\omega_2)\cdot\overline{v_{gs}(\omega_2)}$$

$$v_{d3cubic10}(2\omega_1-\omega_2)=\frac{k_{5gm}}{16}TF_{DSD}(2\omega_1-\omega_2)\cdot\left\{30\cdot v_{gs}(\omega_2)\cdot\overline{v_{gs}(\omega_2)}\cdot+20\cdot v_{gs}(\omega_1)\cdot\overline{v_{gs}(\omega_1)}\right\}\cdot v_{gs}(\omega_1)^2\cdot\overline{v_{gs}(\omega_2)}\cdot$$

$$v_{d3cubic11}(2\omega_1-\omega_2)=\frac{k_{5gds}}{16}TF_{DSD}(2\omega_1-\omega_2)\cdot\left\{30\cdot TF(\omega_1)^2TF(\omega_2)\cdot\overline{TF(\omega_2)}^2 v_{gs}(\omega_2)\cdot\overline{v_{gs}(\omega_2)}\cdot+20\cdot TF(\omega_1)^3\cdot\overline{TF(\omega_1)}\cdot\overline{TF(\omega_2)}\cdot v_{gs}(\omega_1)\cdot\overline{v_{gs}(\omega_1)}\right\}\cdot v_{gs}(\omega_1)^2\overline{v_{gs}(\omega_2)}$$

$$v_{d3cubic12}(2\omega_1-\omega_2)=\frac{k_{5cgd}}{16}TF_{GDD}(2\omega_1-\omega_2)\cdot j(2\omega_1-\omega_2)\cdot\{30\cdot(TF(\omega_1)-1)^2 (TF(\omega_2)-1)\cdot\overline{(TF(\omega_2)-1)}^2 v_{gs}(\omega_2)\cdot\overline{v_{gs}(\omega_2)}\cdot+20\cdot(TF(\omega_1))^3 \cdot\overline{(TF(\omega_1)-1)}\cdot\overline{(TF(\omega_2)-1)}\cdot v_{gs}(\omega_1)\cdot\overline{v_{gs}(\omega_1)}\}\cdot v_{gs}(\omega_1)^2\overline{v_{gs}(\omega_2)}$$

$$v_{d3cubic13}(2\omega_1-\omega_2)=\frac{k_{5cgd3cgs2}}{16}TF_{GDD}(2\omega_1-\omega_2)\cdot j(2\omega_1-\omega_2)\cdot\{3\cdot(TF(\omega_1)-1)^2 \cdot(TF(\omega_2)-1)+12\cdot(TF(\omega_1)-1)\cdot\overline{(TF(\omega_2)-1)}+6\cdot(TF(\omega_1)-1)^2 \cdot\overline{(TF(\omega_2)-1)}+6\cdot\overline{(TF(\omega_2)-1)}^2\cdot(TF(\omega_1)-1)+3\cdot\overline{(TF(\omega_2)-1)}^2 \cdot(TF(\omega_2)-1)\}\cdot v_{gs}(\omega_1)^2 v_{gs}(\omega_2)\overline{v_{gs}(\omega_2)}^2$$

$$v_{d3cubic14}(2\omega_1-\omega_2)=\frac{k_{5cgd2cgs3}}{16}TF_{GDD}(2\omega_1-\omega_2)\cdot j(2\omega_1-\omega_2)\cdot\{6\cdot(TF(\omega_1)-1)^2 +6\cdot(TF(\omega_1)-1)\cdot\overline{(TF(\omega_1)-1)}+6\cdot(TF(\omega_1)-1)\cdot\overline{(TF(\omega_2)-1)} +2\cdot\overline{(TF(\omega_1)-1)}\cdot\overline{(TF(\omega_2)-1)}\}\cdot v_{gs}(\omega_1)^3 v_{gs}(\omega_2)\overline{v_{gs}(\omega_2)}$$

Lower IMD3 vectors: envelope mixing terms

$$v_{dE1}(2\omega_1-\omega_2)=k_{2cgs}^2\cdot j(2\omega_1-\omega_2)\cdot TF_{GDS}(2\omega_1-\omega_2) \cdot\overline{TF_{GDS}(\omega_2-\omega_1)}\cdot v_{gs}(\omega_1)^2\overline{v_{gs}(\omega_2)}$$

$$v_{dE2}(2\omega_1-\omega_2)=k_{2gm}k_{2cgs}\cdot\left[j(2\omega_1-\omega_2)\cdot TF_{GDS}(2\omega_1-\omega_2)\cdot\overline{TF_{GDS}(\omega_2-\omega_1)} +j(\omega_1-\omega_2)\cdot TF_{DSD}(2\omega_1-\omega_2)\cdot\overline{TF_{GSGS}(\omega_2-\omega_1)}\right]\cdot v_{gs}(\omega_1)^2\overline{v_{gs}(\omega_2)}$$

$$v_{dE3}(2\omega_1-\omega_2)=k_{2gds}\cdot k_{2cgs}\left[j(2\omega_1-\omega_2)\cdot TF_{GSD}(2\omega_1-\omega_2) \cdot\overline{TF_{DSGS}(\omega_2-\omega_1)}\cdot\overline{TF(\omega_1)}+j(\omega_1-\omega_2)\cdot TF_{DSD}(2\omega_1-\omega_2) \cdot\overline{TF_{GSGS}(\omega_2-\omega_1)}\cdot\overline{TF(\omega_1)}\right]\cdot v_{gs}(\omega_1)^2\cdot\overline{v_{gs}(\omega_2)}$$

$$v_{dE4}(2\omega_1-\omega_2)=k_{2gmgds}\cdot k_{2cgs}\left[j(2\omega_1-\omega_2)\cdot TF_{GSD}(2\omega_1-\omega_2)\cdot\overline{TF_{DSGS}(\omega_2-\omega_1)} \cdot\left(\overline{TF(\omega_2)}+TF(\omega_1)\right)+j(\omega_1-\omega_2)\cdot TF_{DSD}(2\omega_1-\omega_2)\cdot \left\{\overline{TF_{GSDS}(\omega_2-\omega_1)}+TF(\omega_1)\cdot\overline{TF_{GSGS}(\omega_2-\omega_1)}\right\}\right]v_{gs}(\omega_1)^2\cdot\overline{v_{gs}(\omega_2)}$$

$$v_{dE5}(2\omega_1-\omega_2)=k_{2cgs}\cdot k_{2cgd}\cdot j(2\omega_1-\omega_2)\cdot j(\omega_1-\omega_2)\cdot\left[TF_{GSD}(2\omega_1-\omega_2)\right.$$
$$\cdot\overline{TF_{DSGS}(\omega_2-\omega_1)}\cdot\left(TF(\omega_1)-1\right)\cdot\left(\overline{TF(\omega_2)-1}\right)+TF_{GDD}(2\omega_1-\omega_2)$$
$$\left.\cdot TF_{GSGD}\cdot\left(TF(\omega_1)-1\right)\right]v_{gs}(\omega_1)^2\overline{v_{gs}(\omega_2)}$$

$$v_{dE6}(2\omega_1-\omega_2)=k_{2gm}^2\cdot TF_{DSD}(2\omega_1-\omega_2)\cdot\overline{TF_{DSGS}(\omega_2-\omega_1)}\cdot v_{gs}(\omega_1)^2\overline{v_{gs}(\omega_2)}$$

$$v_{dE7}(2\omega_1-\omega_2)=k_{2gm}k_{2gds}\cdot TF_{DSD}(2\omega_1-\omega_2)\cdot TF(\omega_1)\cdot\left[\overline{TF_{DSGS}(\omega_2-\omega_1)}\right.$$
$$\left.\cdot\overline{TF(\omega_2)}+TF_{DSDS}(\omega_2-\omega_1)\cdot v_{gs}(\omega_1)^2\overline{v_{gs}(\omega_2)}\right.$$

$$v_{dE8}(2\omega_1-\omega_2)=k_{2gm}\cdot k_{2gmds}\cdot TF_{DSD}(2\omega_1-\omega_2)\cdot\left[\overline{TF_{DSGS}(\omega_2-\omega_1)}\cdot\left(TF(\omega_2)\right.\right.$$
$$\left.+TF(\omega_1)\right)+\overline{TF_{DSGS}(\omega_2-\omega_1)}+TF(\omega_1)\cdot\overline{TF_{DSGS}(\omega_2-\omega_1)}\Big]$$
$$\cdot v_{gs}(\omega_1)^2\cdot\overline{v_{gs}(\omega_2)}$$

$$v_{dE9}(2\omega_1-\omega_2)=k_{2gm}\cdot k_{2cgd}\cdot\Big[j(\omega_1-\omega_2)\cdot TF_{DSD}(2\omega_1-\omega_2)\cdot\overline{TF_{GDGS}(\omega_2-\omega_1)}\cdot$$
$$\left[\overline{TF(\omega_2)-1}\right]\cdot\left[TF(\omega_1)-1\right]+TF_{GDD}(2\omega_1-\omega_2)\cdot j(2\omega_1-\omega_2)\cdot\overline{TF_{DSGS}(\omega_2-\omega_1)}\cdot$$
$$\left[TF(\omega_1)-1\right]\Big]\cdot v_{gs}(\omega_1)^2\cdot\overline{v_{gs}(\omega_2)}$$

$$v_{dE10}(2\omega_1-\omega_2)=k_{2gmds}\cdot k_{2gds}\cdot\frac{1}{2}TF_{DSD}(2\omega_1-\omega_2)\Big[\overline{TF_{DSGS}(\omega_2-\omega_1)}\cdot\overline{TF(\omega_2)}$$
$$\cdot TF(\omega_1)+\overline{TF_{DSGS}(\omega_2-\omega_1)}\cdot\overline{TF(\omega_2)}\cdot TF(\omega_1)^2+TF(\omega_1)$$
$$\overline{TF_{DSGS}(\omega_2-\omega_1)}\Big]\cdot\left[\overline{TF(\omega_2)}+TF(\omega_1)\right]\cdot v_{gs}(\omega_1)^2\overline{v_{gs}(\omega_2)}$$

$$v_{dE11}(2\omega_1-\omega_2)=k_{2gmgds}^2\cdot TF_{DSD}(2\omega_1-\omega_2)\cdot\left[\overline{TF_{DSDS}(\omega_2-\omega_1)}\cdot\left[TF(\omega_1)+\overline{TF(\omega_2)}\right]\right.$$
$$\left.+\overline{TF_{DSGS}(\omega_2-\omega_1)}\cdot TF(\omega_1)\cdot\left[TF(\omega_1)+\overline{TF(\omega_2)}\right]\right]\cdot v_{gs}(\omega_1)^2\overline{v_{gs}(\omega_2)}$$

$$v_{dE12}(2\omega_1-\omega_2)=k_{2gmds}\cdot k_{2cgd}\cdot TF_{DSD}(2\omega_1-\omega_2)\cdot j(\omega_1-\omega_2)\cdot\left[\overline{TF_{GDDS}(\omega_2-\omega_1)}\right.$$
$$\cdot\left[\overline{TF(\omega_2)-1}\right]\cdot\left[TF(\omega_1)-1\right]+\overline{TF_{GDGS}(\omega_2-\omega_1)}\cdot TF(\omega_1)+j(2\omega_1-\omega_2)$$
$$\cdot TF_{DSGD}(\omega_2-\omega_1)\cdot TF_{GDD}(2\omega_2-\omega_1)\cdot\left[TF(\omega_1)-1\right]\cdot\left[TF(\omega_1)+\overline{TF(\omega_2)}\right]\Big]$$
$$\cdot v_{gs}(\omega_1)^2\cdot\overline{v_{gs}(\omega_2)}$$

$$v_{dE13}(2\omega_1-\omega_2)=k_{2gds}^2\cdot TF_{DSD}(2\omega_1-\omega_2)\cdot\overline{TF_{DSDS}(\omega_2-\omega_1)}\cdot TF(\omega_1)^2\cdot\overline{TF(\omega_2)}$$
$$\cdot v_{gs}(\omega_1)^2\overline{v_{gs}(\omega_2)}$$

$$v_{dE14}(2\omega_1-\omega_2)=k_{2\,gds}\cdot k_{2\,gds}\cdot\Big[j(\omega_1-\omega_2)\cdot TF_{DSD}(2\omega_1-\omega_2)\cdot\overline{TF_{GDDS}(\omega_2-\omega_1)}\cdot\overline{[TF(\omega_2)-1]}[TF(\omega_1)-1]+j(2\omega_1-\omega_2)\cdot TF_{GDD}(2\omega_1-\omega_2)\cdot[TF(\omega_1)-1]\cdot\overline{TF(\omega_2)}\Big]\cdot\overline{TF_{DSGD}(\omega_2-\omega_1)}\cdot TF(\omega_1)\cdot v_{gs}(\omega_1)^2\cdot\overline{v_{gs}(\omega_2)}$$

$$v_{dE15}(2\omega_1-\omega_2)=k_{2cgd}^2\cdot j(2\omega_1-\omega_2)\cdot j(\omega_1-\omega_2)\cdot TF_{GDD}(2\omega_1-\omega_2)\cdot\overline{TF_{GDGD}(\omega_2-\omega_1)}\cdot[TF(\omega_1)-1]^2\cdot\overline{[TF(\omega_2)-1]}\cdot v_{gs}(\omega_1)^2\overline{v_{gs}(\omega_2)}$$

$$v_{dE16}(2\omega_1-\omega_2)=k_{2cgs}\cdot k_{2cgdcgs}\cdot j(2\omega_1-\omega_2)\Big\{\frac{j}{2}(\omega_1-\omega_2)\cdot\big(TF_{GDS}(2\omega_1-\omega_2)\cdot\overline{TF_{GDGS}(\omega_2-\omega_1)}\cdot[[TF(\omega_1)-1]+[TF(\omega_2)-1]]+TF_{GDD}(2\omega_1-\omega_2)\cdot\overline{TF_{GSGD}(\omega_2-\omega_1)}\big)+[TF(\omega_1)-1]\cdot\frac{j}{2}(\omega_1-\omega_2)\cdot TF_{GDD}(2\omega_1-\omega_2)\cdot\overline{TF_{GSGS}(\omega_2-\omega_1)}\Big\}\cdot v_{gs}(\omega_1)^2\cdot\overline{v_{gs}(\omega_2)}$$

$$v_{dE17}(2\omega_1-\omega_2)=k_{2\,gm}\cdot k_{2cgdcgs}\cdot\Big\{\frac{j}{2}(\omega_1-\omega_2)\cdot\big(\overline{TF_{DSGS}(\omega_2-\omega_1)}\cdot[TF(\omega_1)-1]+\overline{TF_{DSGD}(\omega_1-\omega_2)}\big)TF_{GDD}(2\omega_1-\omega_2)+\frac{j}{2}(\omega_1-\omega_2)\cdot TF_{DSD}(2\omega_1-\omega_2)\cdot\overline{TF_{GDGS}(\omega_2-\omega_1)}\cdot\big([TF(\omega_1)-1]+\overline{[TF(\omega_2)-1]}\big)\cdot v_{gs}(\omega_1)^2\cdot\overline{v_{gs}(\omega_2)}$$

$$v_{dE18}(2\omega_1-\omega_2)=k_{2\,gds}\cdot k_{2cgdcgs}\cdot\Big\{\frac{j}{2}(\omega_1-\omega_2)\cdot TF_{DSS}(2\omega_1-\omega_2)\cdot\overline{TF_{GDDS}(\omega_2-\omega_1)}\cdot TF(\omega_1)\cdot\big([TF(\omega_1)-1]+\overline{[TF(\omega_2)-1]}\big)+\frac{j}{2}(2\omega_1-\omega_2)\cdot\Big(\overline{TF_{DSGS}(\omega_2-\omega_1)}\cdot[TF(\omega_1)-1]\cdot TF(\omega_1)+\overline{TF_{DSGD}(\omega_2-\omega_1)}\cdot TF(\omega_1)\cdot\overline{TF(\omega_2)}\Big)\cdot v_{gs}(\omega_1)^2\cdot\overline{v_{gs}(\omega_2)}$$

$$v_{dE19}(2\omega_1-\omega_2)=k_{2\,gmgds}\cdot k_{2cgdcgs}\cdot\Big\{\frac{j}{2}(\omega_1-\omega_2)\cdot TF_{DSD}(2\omega_1-\omega_2)\cdot\big([TF(\omega_1)-1]+\overline{[TF(\omega_2)-1]}\big)\cdot\Big(\overline{TF_{GDDS}(\omega_2-\omega_1)}+\overline{TF_{GDDS}(\omega_2-\omega_1)}\cdot TF(\omega_1)\Big)+\frac{j}{2}(2\omega_1-\omega_2)\cdot TF_{GDD}(2\omega_1-\omega_2)\cdot\Big(\overline{TF_{DSGS}(\omega_2-\omega_1)}\cdot[TF(\omega_1)-1]\cdot\big[TF(\omega_1)+\overline{TF(\omega_2)}\big]+\overline{TF_{DSGD}(\omega_2-\omega_1)}\cdot\big[TF(\omega_1)+\overline{TF(\omega_2)}\big]\Big)\Big\}\cdot v_{gs}(\omega_1)^2\cdot\overline{v_{gs}(\omega_2)}$$

$$v_{dE20}(2\omega_1-\omega_2)=k_{2cgdcgs}k_{2cgd}\cdot j(2\omega_1-\omega_2)\cdot\frac{j}{2}(\omega_1-\omega_2)\cdot TF_{GDD}(2\omega_1-\omega_2)$$
$$\cdot\left\{\overline{TF_{GDGD}(\omega_2-\omega_1)}\cdot TF(\omega_1)\cdot\left(\left[TF(\omega_1)-1\right]+\left[\overline{TF(\omega_2)-1}\right]\right)\right.$$
$$\left.+TF_{GDGS}(\omega_2-\omega_1)\cdot\left(\left[TF(\omega_1)-1\right]+\left[\overline{TF(\omega_2)-1}\right]\right)\right\}\cdot v_{gs}(\omega_1)^2\overline{v_{gs}(\omega_2)}$$

$$v_{dE21}(2\omega_1-\omega_2)=k_{2cgdcgs}^2\cdot\frac{j}{2}(2\omega_1-\omega_2)\cdot\frac{j}{2}(\omega_1-\omega_2)\cdot TF_{GDD}(2\omega_1-\omega_2)\cdot$$
$$\left\{\overline{TF_{GDGS}(\omega_2-\omega_1)}\cdot\left[TF(\omega_1)-1\right]+\overline{TF_{GDGD}(\omega_2-\omega_1)}\right\}\cdot\left(\left[TF(\omega_1)-1\right]\right.$$
$$\left.+\left[\overline{TF(\omega_2)-1}\right]\right)v_{gs}(\omega_1)^2\overline{v_{gs}(\omega_2)}$$

Lower IMD3 vectors: 2nd-harmonic mixing terms

$$v_{dH1}(2\omega_1-\omega_2)=k_{2cgs}{}^2\cdot j(2\omega_1-\omega_2)\cdot j\omega_1\cdot TF_{GDS}(2\omega_1-\omega_2)$$
$$\cdot TF_{GSGS}(2\omega_1)\cdot v_{gs}(\omega_1)^2\cdot\overline{v_{gs}(\omega_2)}$$

$$v_{dH2}(2\omega_1-\omega_2)=k_{2gm}\cdot k_{2cgs}\cdot\left[\frac{j}{2}(2\omega_1-\omega_2)\cdot TF_{GDS}(2\omega_1-\omega_2)\cdot TF_{DSGS}(2\omega_1)\right.$$
$$\left.+j\omega_1\cdot TF_{DSD}(2\omega_1-\omega_2)\cdot TF_{GSGS}(2\omega_1)\right]\cdot v_{gs}(\omega_1)^2\cdot\overline{v_{gs}(\omega_2)}$$

$$v_{dH3}(2\omega_1-\omega_2)=k_{2gds}\cdot k_{2cgs}\cdot\left[\frac{j}{2}(2\omega_1-\omega_2)\cdot TF_{GSD}(2\omega_1-\omega_2)\cdot TF_{DSGS}(2\omega_1)\right.$$
$$\cdot TF(\omega_1)^2+j(\omega_1)\cdot TF_{DSD}(2\omega_1-\omega_2)\cdot TF_{GSGS}(2\omega_1)\cdot\left.\overline{TF(\omega_2)}\right]$$
$$\cdot v_{gs}(\omega_1)^2\cdot\overline{v_{gs}(\omega_2)}$$

$$v_{dH4}(2\omega_1-\omega_2)=k_{2gmgds}\cdot k_{2cgs}\cdot\left[j(2\omega_1-\omega_2)\cdot TF_{GSD}(2\omega_1-\omega_2)\cdot TF_{DSGS}(2\omega_1)\right.$$
$$\cdot TF(\omega_1)+j\omega_1\cdot TF_{DSD}(2\omega_1-\omega_2)\cdot\left[TF_{GSDS}(2\omega_1)+TF_{GSGS}(2\omega_1)\cdot\overline{TF(\omega_2)}\right]\Big]$$
$$v_{gs}(\omega_1)^2\cdot\overline{v_{gs}(\omega_2)}$$

$$v_{dH5}(2\omega_1-\omega_2)=k_{2cds}\cdot k_{2cgs}\cdot j(2\omega_1-\omega_2)\cdot j\omega_1\cdot\left[TF_{GSD}(2\omega_1-\omega_2)\cdot TF_{DSGS}(2\omega_1)\right.$$
$$\cdot\left(TF(\omega_1)-1\right)^2+TF_{GDD}(2\omega_1-\omega_2)\cdot TF_{GSDS}(2\omega_1)\cdot\left.\left(\overline{TF(\omega_2)}-1\right)\right]$$
$$\cdot v_{gs}(\omega_1)^2\cdot\overline{v_{gs}(\omega_2)}$$

$$v_{dH6}(2\omega_1-\omega_2)=k_{2gm}{}^2\cdot\frac{1}{2}\cdot TF_{DSD}(2\omega_1-\omega_2)\cdot TF_{DSGS}(2\omega_1)\cdot v_{gs}(\omega_1)^2\cdot\overline{v_{gs}(\omega_2)}$$

$$v_{dH7}(2\omega_1-\omega_2)=k_{2gm}k_{2gds}\cdot\frac{1}{2}\cdot TF_{DSD}(2\omega_1-\omega_2)\cdot\left[TF_{DSGS}(2\omega_1)\cdot TF(\omega_1)^2\right.$$
$$\left.+TF_{DSDS}(2\omega_1)\cdot\overline{TF(\omega_2)}\right]\cdot v_{gs}(\omega_1)^2\cdot\overline{v_{gs}(\omega_2)}$$

$$v_{dH8}(2\omega_1-\omega_2)=k_{2gm}\cdot k_{2gmds}\cdot\left[TF_{DSD}(2\omega_1-\omega_2)\cdot TF_{DSGS}(2\omega_1)\cdot TF(\omega_1)_2\right)$$
$$+\frac{1}{2}TF_{DSD}(2\omega_1-\omega\cdot\left(TF_{DSDS}(2\omega_1)\cdot+TF_{DSDS}(2\omega_1)\cdot\overline{TF(\omega_2)}\right)\Big]$$
$$\cdot v_{gs}(\omega_1)^2\cdot\overline{v_{gs}(\omega_2)}$$

$$v_{dH9}(2\omega_1-\omega_2)=k_{2gm}\cdot k_{2cgd}\cdot\left[j(\omega_1)\cdot TF_{DSD}(2\omega_1-\omega_2)\cdot TF_{GDGS}(2\omega_1)\right.$$
$$\cdot\left[TF(\omega_1)-1\right]^2+\frac{j}{2}(2\omega_1-\omega_2)TF_{GDD}(2\omega_1-\omega_2)\cdot TF_{DSDS}(2\omega_1)$$
$$\left.\cdot\left[\overline{TF(\omega_2)}-1\right]\right]\cdot v_{gs}(\omega_1)^2\cdot\overline{v_{gs}(\omega_2)}$$

$$v_{dH10}(2\omega_1-\omega_2)=k_{2gmds}\cdot k_{2gds}\cdot\left[\frac{1}{2}\cdot TF_{DSD}(2\omega_1-\omega_2)\cdot\left(TF_{DSDS}(2\omega_1)\right.\right.$$
$$+TF_{DSGS}(2\omega_1)\cdot\overline{TF(\omega_2)}\Big)\cdot TF(\omega_1)^2+TF_{GDD}(2\omega_1-\omega_2)\cdot TF_{DSDS}(2\omega_1)$$
$$\left.\cdot TF(\omega_1)\cdot\overline{TF(\omega_2)}\right]\cdot v_{gs}(\omega_1)^2\cdot\overline{v_{gs}(\omega_2)}$$

$$v_{dH11}(2\omega_1-\omega_2)=k_{2gmgds}^2\cdot TF_{DSD}(2\omega_1-\omega_2)\left[TF_{DSDS}(2\omega_1)+TF_{DSGS}(2\omega_1)\right.$$
$$\left.\cdot\overline{TF(\omega_2)}\right]\cdot v_{gs}(\omega_1)^2\cdot\overline{v_{gs}(\omega_2)}$$

$$v_{dH12}(2\omega_1-\omega_2)=k_{2gmds}\cdot k_{2cgd}\cdot\left\{j(\omega_1)\cdot TF_{DSD}(2\omega_1-\omega_2)\left[TF_{GDDS}(2\omega_1)+\right.\right.$$
$$TF_{GDGS}(2\omega_1)\cdot\overline{TF(\omega_2)}\Big]\cdot\left(TF(\omega_1)-1\right)^2+j(2\omega_1-\omega_2)TF_{GDD}(2\omega_1-\omega_2)$$
$$\left.TF_{DSGD}(2\omega_1-\omega_2)TF(\omega_1)\overline{\left(TF(\omega_2)-1\right)}\right\}v_{gs}(\omega_1)^2\cdot\overline{v_{gs}(\omega_2)}$$

$$v_{dH13}(2\omega_1-\omega_2)=k_{2gmgds}^2\cdot\frac{1}{2}\cdot TF_{DSD}(2\omega_1-\omega_2)TF_{DSDS}(2\omega_1)TF(\omega_1)^2\cdot\overline{TF(\omega_2)}$$
$$\cdot v_{gs}(\omega_1)^2\cdot\overline{v_{gs}(\omega_2)}$$

$$v_{dH14}(2\omega_1-\omega_2)=k_{2gds}\cdot k_{2cgd}\cdot\left\{j(\omega_1)\cdot TF_{DSD}(2\omega_1-\omega_2)TF_{GDDS}(2\omega_1)\cdot\overline{TF(\omega_2)}\right.$$
$$\cdot\left(TF(\omega_1)-1\right)^2+\frac{j}{2}(2\omega_1-\omega_2)TF_{GDD}(2\omega_1-\omega_2)TF_{DSGD}(2\omega_1-\omega_2)$$
$$\left.TF(\omega_1)^2\overline{\left(TF(\omega_2)-1\right)}\right\}v_{gs}(\omega_1)^2\cdot\overline{v_{gs}(\omega_2)}$$

$$v_{dH15}(2\omega_1-\omega_2)=k_{2cgd}^2\cdot j(2\omega_1-\omega_2)\cdot j(\omega_1)\cdot TF_{GDD}(2\omega_1-\omega_2)TF_{GDGD}(2\omega_1)$$
$$\cdot\left(TF(\omega_1)-1\right)^2\cdot\overline{\left(TF(\omega_2)-1\right)}\cdot v_{gs}(\omega_1)^2\cdot\overline{v_{gs}(\omega_2)}$$

$$v_{dH16}(2\omega_1-\omega_2)=k_{2cgs}k_{2cgdcgs}\cdot j(2\omega_1-\omega_2)\cdot j(\omega_1)\cdot\{TF_{GSD}(2\omega_1-\omega_2)$$
$$TF_{GDGS}(2\omega_1)\cdot\left(TF(\omega_1)-1\right)+\frac{1}{2}\cdot TF_{GDD}(2\omega_1-\omega_2)\left[TF_{GSGS}(2\omega_1)\right.$$
$$\left.\cdot\overline{\left(TF(\omega_2)-1\right)}+TF_{GSGD}(2\omega_1)\right]\}\cdot v_{gs}(\omega_1)^2\cdot\overline{v_{gs}(\omega_2)}$$
$$v_{dH17}(2\omega_1-\omega_2)=k_{2gm}k_{2cgdcgs}\cdot\{j(\omega_1)\cdot TF_{DSD}(2\omega_1-\omega_2)TF_{GDGS}(2\omega_1)$$
$$\cdot\left(TF(\omega_1)-1\right)+\frac{1}{4}\cdot TF_{GDD}(2\omega_1-\omega_2)\left[TF_{DSGS}(2\omega_1)\cdot\overline{\left(TF(\omega_2)-1\right)}\right.$$
$$\left.+TF_{DSGD}(2\omega_1)\right]\}\cdot v_{gs}(\omega_1)^2\cdot\overline{v_{gs}(\omega_2)}$$
$$v_{dH18}(2\omega_1-\omega_2)=k_{2gds}k_{2cgdcgs}\cdot\{j(\omega_1)\cdot TF_{DSD}(2\omega_1-\omega_2)TF_{GDDG}(2\omega_1)\cdot\overline{TF(\omega_2)}$$
$$\cdot\left(TF(\omega_1)-1\right)+TF_{GDD}(2\omega_1-\omega_2)\frac{j}{4}(2\omega_1-\omega_2)\left[TF_{DSGS}(2\omega_1)\right.$$
$$\left.\cdot\overline{\left(TF(\omega_2)-1\right)}\cdot TF(\omega_1)^2+TF_{DSGD}(2\omega_1)\cdot TF(\omega_1)^2\right]\}\cdot v_{gs}(\omega_1)^2$$
$$\cdot\overline{v_{gs}(\omega_2)}$$
$$v_{dH19}(2\omega_1-\omega_2)=k_{2gmgds}k_{2cgdcgs}\cdot\{j(\omega_1)\cdot TF_{DSD}(2\omega_1-\omega_2)\cdot\left(TF(\omega_1)-1\right)$$
$$\left[TF_{GDDS}(2\omega_1)+TF_{GDGS}(2\omega_1)\cdot\overline{TF(\omega_2)}\right]+TF_{GDD}(2\omega_1-\omega_2)\frac{j}{2}$$
$$(2\omega_1-\omega_2)\left[TF_{DSGS}(2\omega_1)\cdot\overline{\left(TF(\omega_2)-1\right)}\cdot TF(\omega_1)+TF_{DSGD}(2\omega_1)\right.$$
$$\left.\cdot TF(\omega_1)^2\right]\}\cdot v_{gs}(\omega_1)^2\cdot\overline{v_{gs}(\omega_2)}$$
$$v_{dH20}(2\omega_1-\omega_2)=k_{2cgd}\cdot k_{2cgdcgs}\cdot j(2\omega_1-\omega_2)\cdot j(\omega_1)\cdot TF_{GDD}(2\omega_1-\omega_2)$$
$$\{TF_{GDGD}(2\omega_1)\cdot\left[\overline{\left(TF(\omega_2)-1\right)}+\frac{1}{2}\cdot\left(TF(\omega_1)-1\right)\right]+TF_{GDGS}(2\omega_1)$$
$$\cdot\overline{\left(TF(\omega_2)-1\right)}\cdot\left(TF(\omega_1)-1\right)^2\}\cdot v_{gs}(\omega_1)^2\cdot\overline{v_{gs}(\omega_2)}$$

$$v_{dH21}(2\omega_1-\omega_2)=k_{2cgdcgs}^2\cdot j(2\omega_1-\omega_2)\cdot j(\omega_1)\cdot TF_{GDD}(2\omega_1-\omega_2)\cdot\{TF_{GDGS}(2\omega_1)$$
$$\cdot\overline{\left(TF(\omega_2)-1\right)}\cdot\left(TF(\omega_1)-1\right)+TF_{GDGD}(2\omega_1)\cdot\left(TF(\omega_1)-1\right)\}\cdot v_{gs}(\omega_1)^2$$
$$\cdot\overline{v_{gs}(\omega_2)}$$

Appendix B

Measurement Accuracy Enhancement Criteria

During large-signal device and/or power amplifier characterization, it is indeed desired to obtain a reliable measurement data. Following aspects have been observed and hence implemented for enhancing the frequency-domain measurement accuracy.

As the analyser consists of active components (e.g. mixers) in its signal path, there is a risk that the analyser can also generate distortion products when overdriven, resulting in invalid measurements. In order to ensure linear operation of the internal mixers avoiding any overload conditions, the in-built step attenuators integrated within the two channels of the receiver are set automatically corresponding to the amount of signal power measured. On the other hand attenuator values must be set low enough such that the desired distortion products to be measured are well above the noise floor. By setting the relevant trigger events corresponding to the type of test signal characterized, it is possible to measure a signal component having a stable amplitude and phase at a predefined frequency point.

Concerning dynamic range improvement when measuring intermodulation ratio (IMR) in case of multi-tone excitation, it is very important to use distortion-free RF-signal source which avoids any unwanted noise at the output. It is highly preferred to use a step attenuator at the output of the driver amplifier to maintain a constant power level at the amplifier's output while allowing an adjustable RF power level at the DUT. This will further keep the IMD generated by the RF source constant as the power level is varied while enhancing the quality of IMD and memory-effect characterization of the measurement setup [105].

By time averaging, which is simply a process of integration or low-pass filtering, a significant improvement in the dynamic range can be achieved for precise measurement spectral components close to the receiver's detectable noise level. A further refinement is possible by decreasing the resolution bandwidth which, however, increases in sweep time during measurements. Although modern VSAs are extremely versatile, still challenges exist at the instrumentation level in improving the dynamic range of the analog-to-digital converter (ADC) and the frequency bandwidth of the internal mixers.

Appendix C

Pitfalls in Characterizing Device Inherent IMD

When characterizing a FET device under 50Ω environment, a constant broadband load presented by an RF bias tee is assumed at the device reference plane. However, in reality, following the conventional measurement setup, the RF bias tee is placed at an offset position subsequent to the directional coupler as shown in Figure C1.1(a-b). Under two-tone stimulus, memory-effect behaviour of 0.5-mm GaN HEMT under a conventional testbench was investigated by sweeping the tone spacing from 200 kHz to 80 MHz. The device was biased for class-AB operation (-4.2V, 25V, I_{DS0} = 2%I_{DSS}) with f_c = 2.15 GHz.

Figure C1.2(a) illustrates the measured upper IMD3 and the corresponding IMD asymmetry is seen in Figure C1.2(b). However, the measured IMD results shown in Figure C1.2(a) do not reflect the theoretical interpretation discussed in Section 4.3.1 of Chapter 4 over a wide range of bandwidth though in-house design provides an optimum out-of-band termination compared to the commercial bias tee. This leads to a misinterpretation of IMD results, for instance, when reaching the broadband limits. As illustrated in Figure 4.22 of Chapter 4, the directional coupler imposes an offset to the

terminations presented by the bias tee. Hence, as illustrated in Figure 4.23 of Chapter 4, to avoid any adverse impedance transformation, the bias tee and the directional coupler positions, at the output, must be interchanged.

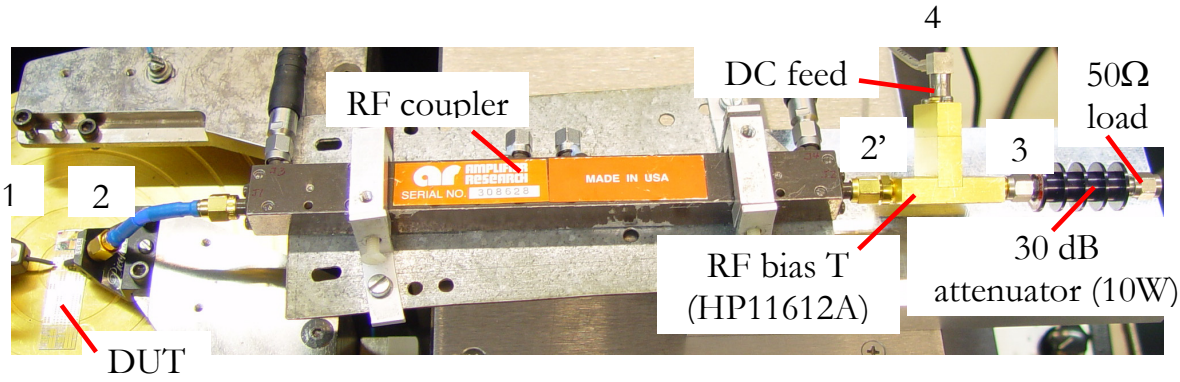

(a)

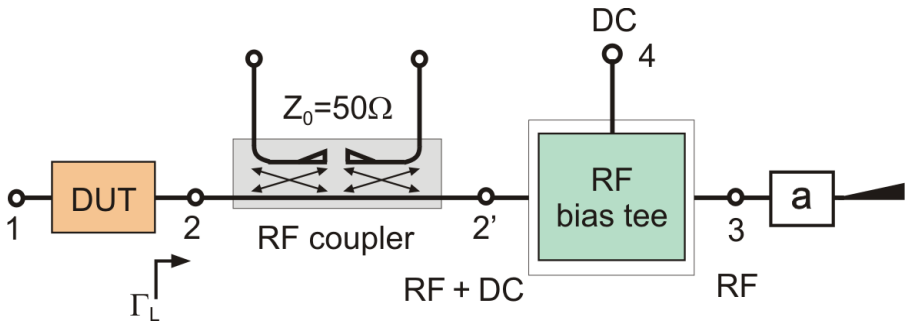

(b)

Figure C1.1 (a) Photograph of a conventional testbench implementing commercial RF bias tee (HP11612A), (b) equivalent block diagram.

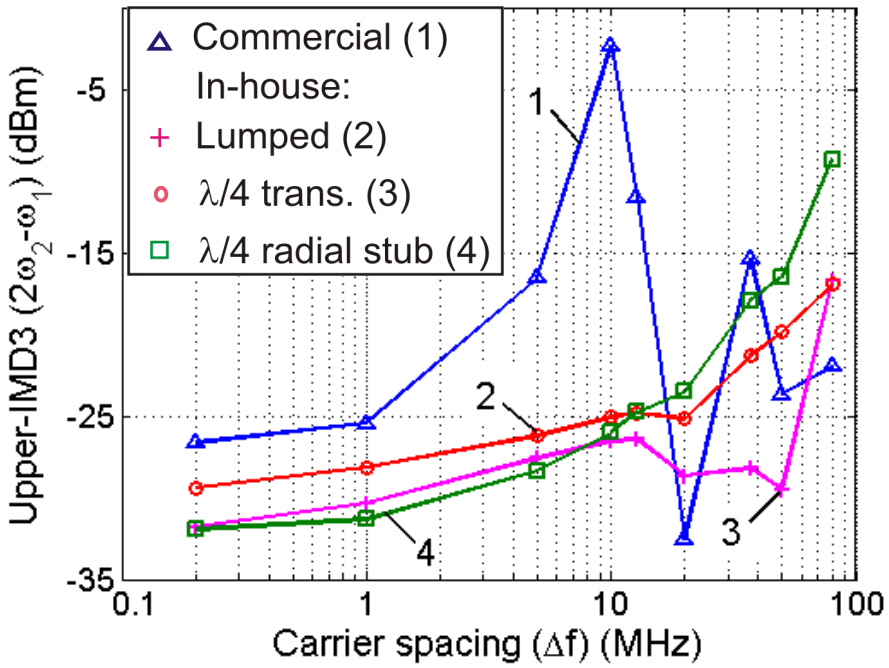

(a)

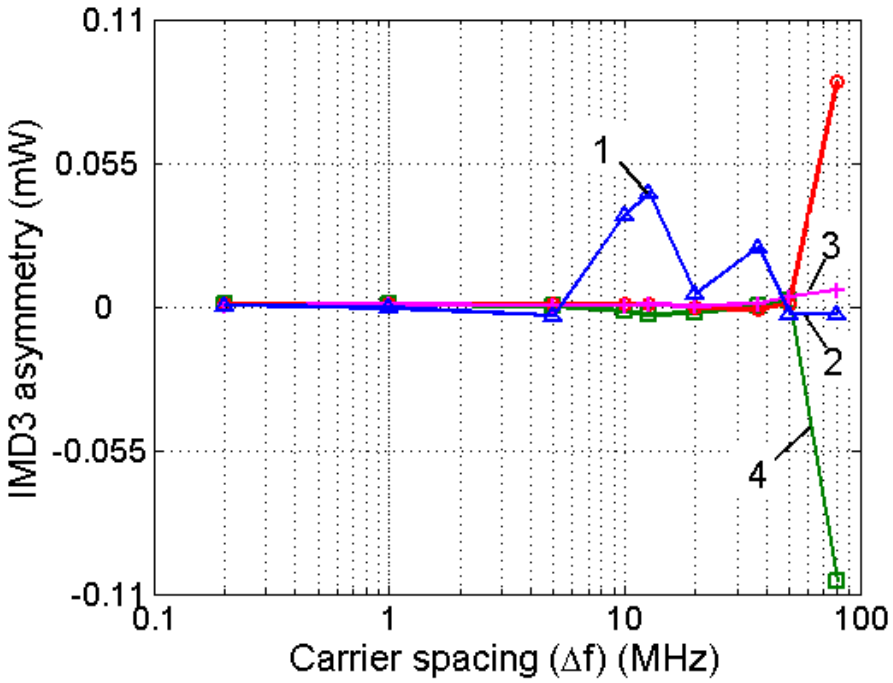

(b)

Figure C1.2 Memory-effect characterization of a 0.5-mm GaN HEMT under a conventional testbench conditions with different bias tee configurations in a 50Ω environment, (a) upper IMD measured by varying the carrier spacing from 200 kHz to 80 MHz and (b) IMD asymmetry.

Reliability of Model Verification

Significant deviation in CAD model prediction of IMD compared with the measured results is commonly encountered. This is more common, when the bias point shifts towards low-current quiescent conditions (typically deep class-AB, class-B and class-C) where the practical termination properties sensitise IMD measurements. The effort to assess and optimize relevant termination properties of the testbench affecting distortion measurements has been well acknowledged by model verification results shown in Figure C1.3. Here a typical scenario of 2-mm GaN HEMT model prediction is illustrated under class-C bias condition depicting sweet-spot behaviour in a 50Ω environment [106]. The trend of the simulated curves show improved agreement with the measurements obtained from the optimised testbench.

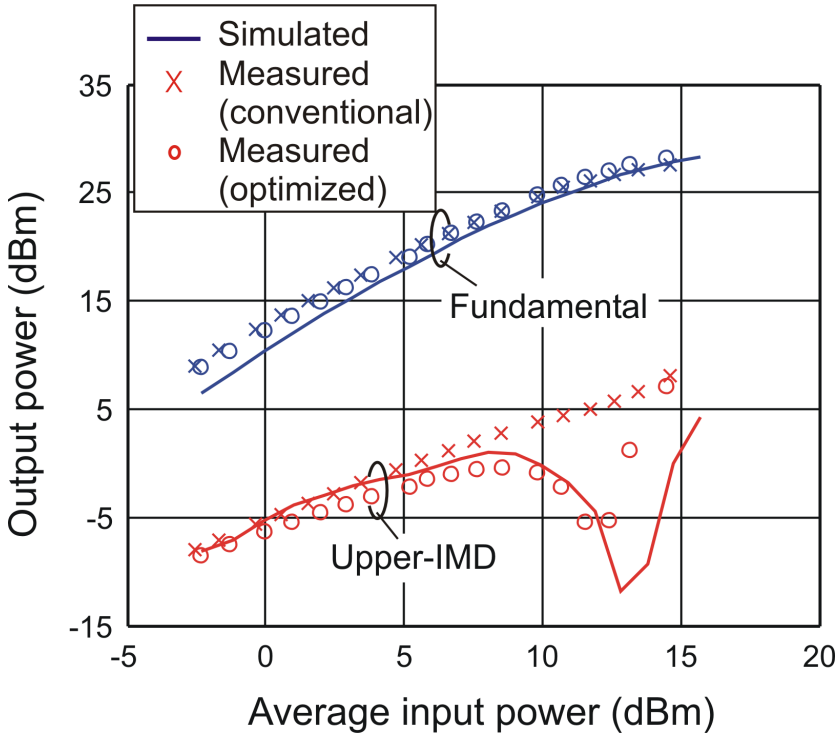

Figure C1.3 RF testbench optimization for reliable model verification.

Appendix D

Correlation Between IMR and ACPR Characteristics

Since two-tone characterization has been traditionally used to characterize nonlinearity of both active and passive RF components, its correlation with the currently implemented complex digitally modulated test signal are highly desirable. This is well described by Carvalho and Pedro [9] providing compact formulas relating the distortion figures of merit (FoMs) encountered under modern test signal and well established two-tone stimulus.

For assessing the nonlinear distortion performance of a FET device under real telecommunication test signal, each combination of two sinusoidal components of the continuous spectrum may be interpreted as two-tone excitation. Further, these multi-tones can be categorized, for convenience, into multiple two-tone signals with variable carrier spacing up to 3.84 MHz (focusing on UMTS application as example). Taking into account the 3.84 MHz adjacent channel bandwidth, which is used to compute adjacent channel power ACP, typically both third-order and fifth-order mixing products (also higher order) impact ACPR characterization [102], [107]. This is illustrated in Figure D1.1, which considers two cases of two-tone excited nonlinear output spectrum with carrier spacing Δf_1 (dotted) and Δf_2 (solid) depicting the

superposition of IMD3 and IMD5 products onto the W-CDMA spectral mask. Table D1.1 gives the boundary conditions of the carrier spacing which produce third-order and fifth-order products occurring simultaneously within the sidebands under consideration. As a result the fundamental property of IMD3 observed under two-tone excitation no longer prevails under digitally modulated test signals.

Table D1.1 Carrier spacing Δf limits for IMD3 and IMD5 mixing products falling into the adjacent channel bandwidth of 3.84 MHz.

Stimuli	3rd-order (IMD3)	5th-order (IMD5)
2-tone	2.053 MHz $\leq \Delta f \leq$ 4.613 MHz	1.232 MHz $\leq \Delta f \leq$ 2.768 MHz

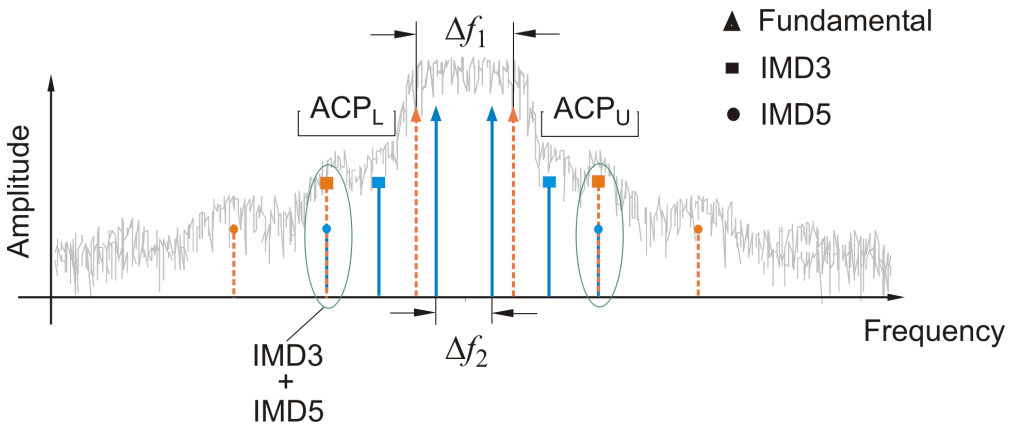

Figure D1.1 Notional two-tone excited discrete nonlinear output spectrum superimposed onto a 1 x WCDMA excited nonlinear output spectrum.

Considering the analogy of multi-tone excited nonlinear output spectrum, each distortion product in the sideband is dominated by its lowest order component, for instance, third-order mixing product for typical $2\omega_2$-ω_1 case. This is true at the small-signal excitation regime. However, when the excitation level increases, higher order contributions start to dominate over the lower order components. Moreover, each of the sidebands at the output is a result of vectorial sum of many mixing products of order $\geq 2n+1$, where n is

the total number of input tones or carriers [107]. Depending on the phase of individual mixing products occurring at a given frequency, the voltage vectors may interfere in a constructive or destructive manner. Consequently, above certain power levels the IMD3 behaviour under two-tone stimuli can no longer be correlated to the sidebands of multi-tone/digitally modulated signals. Moreover, from the perspective of nonlinear output spectrum of digitally modulated signals, wherein the input spectral components typically have randomised phase (equivalent to having uncorrelated tones), integrated distortion power in the sidebands will never tend to null condition [107]. This is one of the cause for not reproducing low distortion IMD sweet-spots in realistic applications, which otherwise is prominent under two-tone excitation.

To demonstrate this particular condition, a 4-mm GaN HEMT [manufactured by Ferdinand-Braun-Institute for High Frequency Technique (FBH), Berlin] is characterized under three-tone excitation with uniform amplitude and zero phase offset at f_c = 2.1 GHz with (V_{GS0} = -3.7V, V_{DS0} = 15V, Δf_{offset} = 1.5 MHz) in a uniform 50Ω environment.

To get an insight into the evolution of such behaviour, the 3rd-order upper and lower IMD tones ($\pm\omega_4$, $\pm\omega_5$), resulting from three-tone characterization, are shown in Figure D1.2. Although, a pronounced sweet-spot occurs at $\omega_4=2\omega_3-\omega_2$ (or $\omega_3+\omega_2-\omega_1$ where ω_1, ω_2, ω_3 are the input tones) for P_{in} = 17 dBm, the drastic increase in the distortion at $\omega_5=2\omega_3-\omega_1$ for higher input power level, cancels the former effect, resulting in a diminished sweet-spot characteristics in ACP curve. This phenomenon can be hence extrapolated to complex ACP characteristics generation under W-CDMA excitation, which would then explain the absence of pronounced sweet-spots. Nevertheless, the possibility of a pronounced sweet-spot digitally modulated signal increases only when the higher order distortion products (IMD5, IMD7, and so on) diminish which is the key for sweet-spot application in UMTS basestation power amplifiers. In

other words, devices with weak fifth-order nonlinearities may exhibit reasonable correlation between IMR and ACPR characteristics, which in most of the cases is device technology dependent.

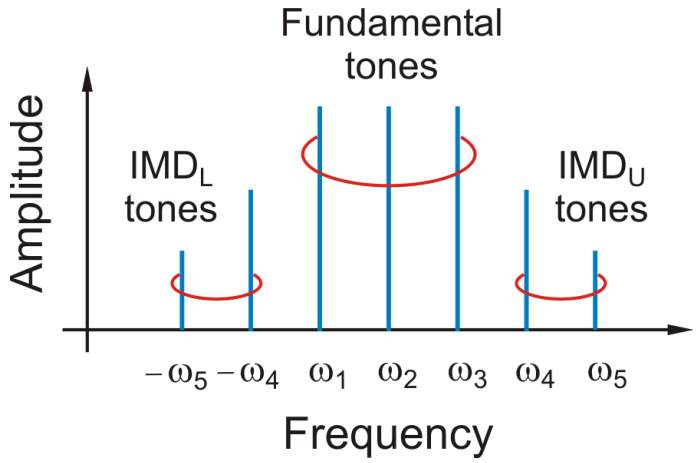

(a)

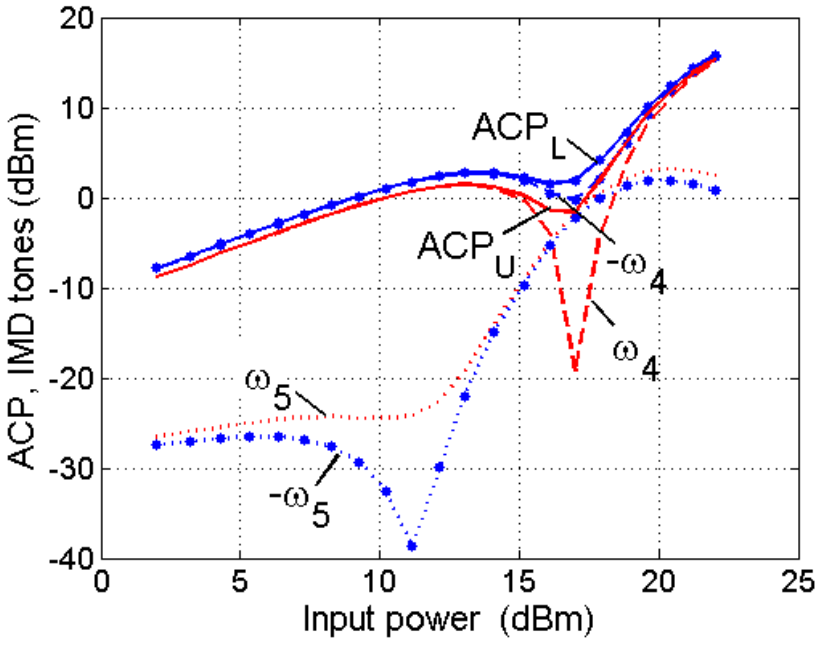

(b)

Figure D1.2 Insight into the evolution of sideband distortion resulting in weak sweet-spot behaviour under three-tone excitation in a uniform 50Ω environment.

In contrast, under two-carrier digitally modulated signal, only third-order products fall into the IMD zone, as can be seen in Figure D1.3, whose behaviour could be rather compared with two-tone IMD3 characteristics.

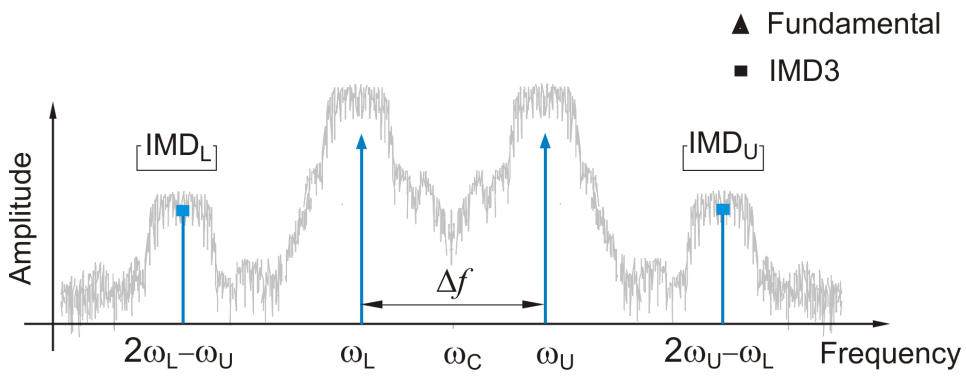

Figure D1.3 Notional two-tone excited discrete nonlinear output spectrum superimposed onto 2x WCDMA excited nonlinear output spectrum.

References

[1] S. C. Cripps, *RF Power Amplifiers for Wireless Communications*, Norwood, MA: Artech House, 1999.

[2] 3GPP Technical Specifications, *www.3GPP.org*

[3] *Towards Global Mobile Broadband — Standardising the Future of Mobile Communications with LTE (Long Term Evolution)*, white paper from UMTS Forum, February 2008, *www.umts-forum.org*

[4] P. B. Kenington, *High Linearity RF Amplifier Design*, Norwood, MA: Artech House, 2000.

[5] N. Wongkomet and P. Gray, *Efficiency Enhancement Technique for RF CMOS Power Amplifier*, EECS Department, University of California, Berkeley, Tech. Rep. UCB/EECS-2006-74, May 2006.

[6] Y. F. Wu, A. Saxler, M. Moore, R. P. Smith, S. Sheppard, P. M. Chavarkar, T. Wisleder, U. K. Mishra, and P. Parikh, "30-W/mm GaN HEMTs by Field Plate Optimization," *IEEE Electron Device Letters*, Vol. 25, No. 3, pp. 117-119, March 2004.

[7] T. Reveyrand, C. Mazière, J. M. Nebus, R. Quere, A. Mallet, L. Lapierre, and J. Sombrin, "A Calibrated Time Domain Envelope Measurement System for the Behavioral Modeling of Power Amplifiers," *Gallium Arsenide Applications Symposium (GAAS)*, pp. 23-27, Milano, September 2002.

[8] J. C. Pedro and N. B. Carvalho, "On the Use of Multi-Tone Techniques for Assessing RF Component's Intermodulation Distortion," *IEEE Trans. Microwave Theory and Tech.*, Vol. 47, No. 12, pp. 2393-2402, December 1999.

[9] N. B. Carvalho and J. C. Pedro, "Compact Formulas to Relate ACPR and NPR to Two-Tone IMR and IP3," *Microwave Journal*, Vol. 42, No. 12, pp. 70-84, December 1999.

[10] J. C. Pedro and N. B. Carvalho, *Intermodulation Distortion in Microwave and Wireless Circuits*, Norwood, MA: Artech House, 2003.

[11] J. M. Golio, *The RF and Microwave Handbook*, Boca Raton, CRC Press, 2001.

[12] W. Bösch and G. Gatti, "Measurement and Simulation of Memory Effects in Predistortion Linearizers," *IEEE Trans. Microwave Theory and Tech.*, Vol. 37, pp. 1885-1890, December 1989.

[13] V. Meghdadi, J. P. Cances, F. R. Chevallier, and J. M. Dumas, "Method for the Simulation of a Nonlinear Amplifier with Envelope Memory Effect," *USA Patent*, 6.216.100, April 2001.

[14] J. Vuolevi, T. Rahkonen, and J. Manninen, "Measurement Technique for Characterizing Memory Effects in RF Power Amplifiers," *IEEE Trans. Microwave Theory and Tech.*, Vol. 49, No. 8, pp. 1383-1389, August 2001.

[15] J. Vuolevi and T. Rahkonen, *Distortion in Power Amplifiers*, Norwood, MA: Artech House, 2003.

[16] N. Le Gallou, J. M. Nebus, E. Ngoya, and H. Buret, "Analysis of Low Frequency Memory and Influence on Solid State HPA Intermodulation Characteristics," *IEEE MTT-S Int. Microwave Sym.* Dig., pp. 979-982, May 2001.

[17] S. C. Cripps, *Advanced Techniques in RF Power Amplifier Design*, Norwood, MA: Artech House, 2002.

[18] J. C. Pedro and J. Perez, "Accurate Simulation of GaAs MESFET's Intermodulation Distortion Using a New Drain-Source Current Model," *IEEE Trans. Microwave Theory and Tech.*, Vol. 44, No.1, pp. 25-33, January 1994.

[19] P. Wambacq and W. Sansen, *Distortion Analysis of Analog Integrated Circuits*, Norwell, MA: Kluwer, 1998.

[20] S. Narayanan, "Transistor Distortion Analysis Using Volterra Series Representation," *Bell Sys. Tech. Journal.*, pp. 991-1024, May-June 1967.

[21] J. Vuolevi and T. Rahkonen, "Extraction of a Nonlinear AC FET Model Using Small-Signal S-Parameters," *IEEE Trans. Microwave Theory and Tech.*, Vol. 50, No. 5, pp. 1311-1315, May 2002.

[22] T. Y. Yum, L. Chiu, C. H. Chan, and Q. Xue, "High-Efficiency Linear RF Amplifier - A Unified Circuit Approach to Achieving Compactness and Low Distortion," *IEEE Trans. Microwave Theory and Tech.*, Vol. 54, No. 8, pp. 3255-3266, August 2006.

[23] V. W. Leung, J. Deng, P. S. Gudem, and L. E. Larson, "Analysis of Envelope Signal Injection for Improvement of RF Amplifier Intermodulation Distortion," *IEEE Proceedings of the Custom Integrated Circuits Conference*, pp. 133-136, October 2004.

[24] S. L. G. Chu, J. Huang, W. Struble, G. Jackson, N. Pan, M. J. Schindler, and Y. Tajima, "A Highly Linear MESFET," *IEEE MTT-S Int. Microwave Symp. Dig.*, pp.

725-728, July 1991.

[25] J. C. Pedro, "Evaluation of MESFET Nonlinear Intermodulation Distortion Reduction by Channel-Doping Control," *IEEE Trans. Microwave Theory and Tech.*, Vol. 45, No.11, pp. 1989-1997, November 1997.

[26] Y. Nakasha, M. Nagahara, Y. Tateno, H. Takahashi, T. Igarashi, K. Joshin, J. Fukaya, and M. Takikawa, "A Low-Distortion and High Efficiency E-mode GaAs Power FET Based on a New Method to Improve Device Linearity Focused on gm Value," *Int. Electron Devices Meeting (IEDM) Technical Digest*, pp. 405-408, 1999.

[27] S. A. Maas, "How to Model Intermodulation Distortion," *IEEE MTT-S Int. Microwave Symp. Dig.*, pp. 149-151, 1991.

[28] S. A. Maas, *Nonlinear Microwave and RF Circuits*, Norwood, MA: Artech House, 2003.

[29] S. C. Cripps, *RF Power Amplifiers for Wireless Communications*, Norwood, MA: Artech House, 2006.

[30] I. E. Zhigalov, V. N. Il'in, and V. N. Lantsov, "Broader Possibilities for Use of the Volterra-Series Formalism in CAD Programs," *Radioelectron. and Commun. Syst.*, Vol. 28, No. 9, pp. 47-51, 1985.

[31] A. Heiskanen and T. Rahkonen, "A 5th Order Multi-Tone Volterra Simulator with Component-Level Output," *IEEE International Symposium on Circuits and Systems (ISCAS)*, Vol. 3, pp. 591-594, 2002.

[32] S. A. Maas and A. Crosmun, "Modelling the Gate I/V Characteristic of a GaAs MESFET for Volterra-Series Analysis," *IEEE Trans. Microwave Theory and Tech.*, Vol. 37, No.7, pp. 1134-1136, November 1989.

[33] V. D. Dimitriev and A. I. Silyutin, "A Method of Designing Broadband Nonlinear Circuits Based on a Modification of the Nonlinear Current Method," *Radioelectron. and Commun. Syst.*, Vol. 29, No. 11, pp. 50-55, 1986.

[34] V. Krozer and H. Hartnagel, "Large-Signal Analysis of Nonlinear Microwave Circuits Using Modified Volterra Series," *International Workshop on Integrated Nonlinear Microwave and Millimeterwave Circuits (INMMiC)*, pp. 197-211, Duisburg, October 1990.

[35] J. P. Aikio and T. Rahkonen, "Detailed Distortion Analysis Technique Based on Large-Signal Voltage and Current Spectra," *IEEE Trans. Microwave Theory and Tech.*, Vol. 53, No. 10, pp. 3057-3066, October 2005.

[36] A. Jarndal and G. Kompa, "A New Small-Signal Modeling Approach Applied to GaN Devices," *IEEE Trans. Microwave Theory and Tech.*, Vol. 53, No.11, pp. 3440-3448, November 2005.

[37] G. Dambrine, A. Cappy, F. Heliodore, and E. Playez, "A New Method for Determining the FET Small-Signal Equivalent Circuit," *IEEE Trans. Microwave Theory and Tech.*, Vol. 36, No. 7, pp. 1151-1159, July 1988.

[38] E. S. Mengistu, *Large-Signal Modeling of GaN HEMTs for Linear Power Amplifier Design*, Doctoral Thesis, Department of High Frequency Engineering, University of Kassel, Kassel, Germany, January 2008.

[39] N. B. Carvalho and J. C. Pedro, "Large- and Small-Signal IMD Behavior of Microwave Power Amplifiers," *IEEE Trans. Microwave Theory and Tech.*, Vol. 47, No. 12, pp. 2364-2374, December 1999.

[40] R. Pucel, "Profile Design for Distortion Reduction in Microwave Field Effect Transistors," *Electronics Letters*, Vol. 14, No. 6, pp. 204-206, March 1978.

[41] R. Williams and D. Shaw, "Graded Channel FET's: Improved Linearity and Noise Figure," *IEEE Trans. Electron Devices*, Vol. ED-25, No. 6, pp. 600-605, June 1978.

[42] Y. Ando, Y. Okamoto, K. Hataya, T. Nakayama, H. Miyamoto, T. Inoue, and M. Kuzuhara, "12 W/mm Recessed-Gate AlGaN/GaN Heterojunction Field-Plate FET," *Int. Electron Devices Meeting (IEDM) Tech. Dig.*, pp. 563-566, December 2003.

[43] A. Chini, D. Buttari, R. Coffie, L. Shen, S. Heikman, A. Chakraborty, S. Keller, and U. K. Mishra, "Power and Linearity Characteristics of Field-Plated Recessed-Gate AlGaN/GaN HEMTs," *IEEE Electron Device Letters*, Vol. 25, No. 5, pp. 229-231, May 2004.

[44] Y. Hori, M. Kuzuhara, Y. Ando, and M. Mizuta, "Analysis of Electric Field Distribution in GaAs Metal-Semiconductor Field Effect Transistor with a Field-Modulating Plate," *J. Appl. Phys.*, Vol. 87, pp. 3483-3487, April 2000.

[45] Y. Ando, Y. Okamoto, H. Miyamoto, T. Nakayama, T. Inoue, and M. Kuzuhara, "10-W/mm AlGaN/GaN HFET with a Field Modulating Plate," *IEEE Electron Device Letters*, Vol. 24, No. 5, pp. 289-291, May 2003.

[46] A. Asano, Y. Miyoshi, K. Ishikura, Y. Nashimoto, M. Kuzuhara, and M. Mizuta, "Novel High Power AlGaAs/GaAs HFET with a Field-Modulating Plate Operated at 35V Drain Voltage," *Int. Electron Devices Meeting (IEDM) Technical*

Digest, pp. 59-62, 1998.

[47] Y. F. Wu, A. Saxler, M. Moore, R. P. Smith, S. Sheppard, P. M. Chavarkar, T. Wisleder, U. K. Mishra, and P. Parikh, "30-W/mm GaN HEMTs by Field Plate Optimization," *IEEE Electron Device Letters*, Vol. 25, No. 3, pp. 117-119, March 2004.

[48] E. R. Srinidhi, A. Jarndal, and G. Kompa, "A New Method for Identification and Minimization of Distortion Sources in GaN HEMT Devices Based on Volterra Series Analysis," *IEEE Electron Device Letters*, Vol. 28, No. 5, pp. 343-345, May 2007.

[49] Y. Kim, T. M. Roh, and B. Kim, "A Novel Higher Order Extending Method in a MESFET Channel Current Model for Volterra Series Analysis," *Microwave and Optical Technology Letters*, Vol. 20, No. 5, pp. 292-295, March 1999.

[50] A. Heiskanen, J. Aikio, and T. Rahkonen, "A 5th Order Volterra Study of a 30W LDMOS Power Amplifier," *IEEE International Symposium on Circuits and Systems (ISCAS)*, Vol. 4, pp. 616-619, May 2003.

[51] E. R. Srinidhi and G. Kompa, "Investigation of IMD3 in GaN HEMT Based on Extended Volterra Series Analysis," *Proc. of European Microwave Integrated Circuits (EuMIC) Conference*, pp. 52-55, Munich, Germany, October 2007.

[52] W. Kruppa and K. F. Sodomsky, "An Explicit Solution for the Scattering Parameters of a Linear Two-Port Measured With an Imperfect Test Set," *IEEE Trans. Microwave Theory and Tech.*, Vol. 19, No. 1, pp. 122-123, January 1971.

[53] U. Lott, "Measurement of Magnitude and Phase of Harmonics Generated in Nonlinear Microwave Two-Ports," *IEEE Trans. Microwave Theory and Tech.*, Vol. 37, No. 10, pp. 1506-1511, October 1989.

[54] F. van Raay and G. Kompa "A 40 GHz Large-Signal Double-Reflectometer Waveform Measurement System Designed for Load-Pull Applications," *Proc. of 26th European Microwave Conference (EuMC)*, pp. 657-661, Prague, Czech Republic, September 1996.

[55] J. Benedikt, R. Gaddi, P. J. Tasker, and M. Goss, "High-Power Time-Domain Measurement System with Active Harmonic Load-Pull for High-Efficiency Basestation Amplifier Design," *IEEE Trans. Microwave Theory and Tech.*, Vol. 48, pp. 2617-2624, December 2000.

[56] P. McGovern, D. J. Williams, P. J. Tasker, J. Benedikt, J. Powell, K. P. Hilton, R.

S. Balmer, T. Martin, and M. J. Uren, "Single-Tone and Two-Tone Time-Domain Large Signal Characterization of GaN HFETs Operated in Class A," *IEEE MTT-S Int. Microwave Sym. Dig.*, pp. 825-828, June 2004.

[57] F. M. Ghannouchi, G. Zhao, and F. Beauregard, "Simultaneous Load-Pull of Intermodulation and Output Power Under Two-Tone Excitation for Accurate SSPA's Designs," *IEEE Trans. Microwave Theory and Tech.*, Vol. 43, pp. 929-934, June 1994.

[58] M. I. Khalil, "Characterizing Intermodulation Distortion of High-Power Devices," *High Frequency Electronics*, Vol. 6, No. 7, pp. 26-33, July 2007.

[59] R. Hajji, F. Beauregard, and F. M. Ghannouchi, "Multitone Power and Intermodulation Load-Pull Characterization of Microwave Transistors Suitable for Linear SSPA's Design," *IEEE Trans. Microwave Theory and Tech.*, Vol. 45, No. 7, pp. 1093-1099, July 1997.

[60] Agilent Technologies, *Agilent E4438C ESG Vector Signal Generator*, Data Sheet, *www.agilent.com/find/esg*.

[61] R.S. Tucker and P. D. Bradley, "Computer-Aided Error Correction of Large-Signal Load-Pull Measurements," *IEEE Trans. Microwave Theory and Tech.*, Vol. 32, No. 3, pp. 296-301, March 1984.

[62] M. Sipilä, K. Lehtinen, and V. Porra, "High-Frequency Periodic Time-Domain Waveform Measurement System," *IEEE Trans. Microwave Theory and Tech.*, Vol. 36, No. 10, pp. 1397-1405, October 1988.

[63] M. Demmler, B. Hughes, and A. Cognata, "A 0.5-50 GHz On-wafer, Intermodulation, Load-Pull and Power Measurement System," *IEEE MTT-S Int. Microwave Sym. Dig.*, Vol. 3, pp. 1041-1044, May 1995.

[64] A. Ahmed, *Analysis, Modeling and Linearization of Nonlinearity and Memory Effects in Power Amplifiers Used for Microwave and Mobile Communications*, Doctoral Thesis, Department of High Frequency Engineering, University of Kassel, Kassel, Germany, March 2005.

[65] Agilent Technologies, *89640S VXI-based 2.7 GHz RF Vector Signal Analyzer*, *www.agilent.com*.

[66] D. Rytting, "Network Analyzer Error Models and Calibration Methods," *RF and Microwave Measurements for Wireless Applications* (ARFTG/NIST Short Course Notes), 1996.

[67] S. Rehnmark, "On the Calibration Process of Automatic Network Analyzer Systems," *IEEE Trans. Microwave Theory and Tech.*, Vol. 22, No. 4, pp. 457-458, April 1974.

[68] E. R. Srinidhi, R. Ma, and G. Kompa, "Application Rules for Accurate IMD Characterization in GaN HEMT's," *Proc. of German Microwave Conference (GeMIC)*, pp. 171-174, March 2008.

[69] J. G. Leckey, J. A. C. Stewart, and A. D. Patterson, "Analysis of HEMT Harmonic Generation Using a Vector Nonlinear Measurement System," *IEEE MTT-S Int. Microwave Sym. Dig.*, Vol. 3, pp. 1739-1742, June 1996.

[70] D. J. Williams, J. Leckey, and P. J. Tasker, "Envelope Domain Analysis of Measured Time Domain Voltage and Current Waveforms Provide for Improved Understanding of Factors Effecting Linearity," *IEEE MTT-S Int. Microwave Sym. Dig.*, Vol. 2, pp. 1411-1414, June 2003.

[71] Fujitsu, "150-W, 2.11 - 2.17 GHz Push-Pull Compact Amplifier for IMT-2000 Base-Station Application," Application Note 008.

[72] R. Basset, "High Power GaAs FET Device Bias Considerations," Fujitsu Compound Semiconductor Inc., Application Note 010.

[73] E. R. Srinidhi, R. Ma, A. Z. Markos, and G. Kompa, "Optimization of Broadband Drain Modulation in GaN HEMT Devices," *IEEE Proc. of Radio and Wireless Symposium (RWS)*, pp. 81-84, Orlando, FL, January 2008.

[74] Agilent Technologies, *Operating and Service Manual of 11612A Bias Network*, March 2000.

[75] Auriga Measurement Systems, LLC, *http://www.auriga-ms.com/bteemain.shtml*.

[76] Rohde & Schwarz, *www.rohde-schwarz.de/*

[77] J. F. Sevic, K. L. Burger, and M. B. Steer, "A Novel Envelope-Termination Load-Pull Method for ACPR Optimization of RF/Microwave Power Amplifier," *IEEE MTT-S Int. Microwave Symposium Dig.*, pp. 723-726, June 1998.

[78] R. Fiore, "Capacitors in Broadband Applications," *Applied Microwave and Wireless*, pp. 40-53, May 2001.

[79] P. McGovern, P. J. Tasker, J. Powell, K. P. Hilton, R. S. Balmer, T. Martin, and M. J. Uren, "Analysis of DC-RF Dispersion in AlGaN/GaN HFET's Using Pulsed I-V and Time-Domain Waveform Measurements," *IEEE MTT-S Int. Microwave Symposium*, pp. 503-506, Long Beach, CA, June 2005.

[80] Accent Optical Technologies, www.accentopto.com

[81] J. Cha, I. Kim, S. Hong, B. Kim, J. S. Lee, and H. S. Kim, "Memory Effect Minimization and Wide Instantaneous Bandwidth Operation of a Base Station Power Amplifier," *Microwave Journal*, Vol. 50, No. 1, pp. 66-82, January 2007.

[82] E. R. Srinidhi, R. Ma, and G. Kompa, "Volterra Series Based Distortion Analysis for Optimization of Out-of-Band Terminations in GaN HEMT Devices," *IEEE Electron Device Letters*, Vol. 29, No. 1, pp. 24-27, January 2008.

[83] G. Kompa, *Practical Microstrip Design and Applications*, Norwood, MA: Artech House, 2005.

[84] E. R. Srinidhi, B. Wittwer, R. Ma, and G. Kompa, "Key Aspects for Characterizing Device Inherent IMD in GaN HEMTs," *Proc. of 38th European Microwave Conference (EuMC)*, pp. 1117-1120, Amsterdam, The Netherlands, October 2008.

[85] E. R. Srinidhi, A. Ahmed, and G. Kompa, "Power Amplifier Behavioural Modelling Strategies Using Neural Network and Memory Polynomial Models," *Microwave Review Journal*, Vol. 12, No.1, pp. 15-20, June 2006.

[86] F. N. Sechi, "Design Procedure for High-Efficiency Linear Microwave Power Amplifiers," *IEEE Trans. Microwave Theory and Tech.*, Vol. 28, pp. 1157-1163, November 1980.

[87] C. Curran, B. Wittwer, E. R. Srinidhi, and G. Kompa, "Highly Integrated Multi-Harmonic Tuner for Broadband High Power Source/Load-Pull System," *Proc. of German Microwave Conference (GeMIC)*, pp. 179-181, Hamburg, Germany, March 2008.

[88] J. A. Garcia, J. M. Zamanillo, and M. O'Droma, *Characterization and Modelling Approaches for Advanced Linearization Techniques*, Research Signpost, 2005.

[89] S. C . Cripps, "Ignoring the Obvious: Possibilities for On-Chip Linearization of RFIC Power Amplifiers," *Proc. of Gallium Arsenide Applications Symposium (GAAS)*, pp. 23-27, Milano, Italy, September 2002.

[90] G. Simpson, "Harmonic Load-Pull with High Gamma Tuners," *Microwave Journal*, pp. 232-242, May 2008.

[91] A. Alghanim, J. Lees, T. Williams, J. Benedikt, and P. J. Tasker, "Investigation of Electrical Base-Band Memory Effects in High-Power 20W LDMOS Power Amplifiers," *Proc. of 37th European Microwave Conference (EuMC)*, pp. 48-51, Munich,

Germany, October 2007.

[92] P. Colantonio, J. A. Garcia, F. Giannini, E. Limiti, E. Malaver, and J. C. Pedro, "High Linearity and Efficiency Microwave PAs," *12th European Gallium Arsenide and Other Compound Semiconductors Application Symposium (GAAS)*, pp. 183-186, Amsterdam, 2004.

[93] J. C. Pedro and N. B. Carvalho, "A Unified Theory for Nonlinear Distortion Characteristics in Different Amplifier Technologies," *Microwave Journal*, Vol. 48, No. 4, pp. 62-78, April 2005.

[94] E. Malaver, J. A. García, A. Tazón, and A. Mediavilla, "Improving the Linearity-Efficiency Trade-Off in FET Power Amplifiers Using Large-Signal IMD Sweet-Spots," *Microwave and Optical Technology Letters*, Vol. 41, pp. 327-331, May 2004.

[95] N. B. Carvalho and J. C. Pedro, "Large- and Small-Signal IMD Behaviour of Microwave Power Amplifiers," *IEEE Trans. Microwave Theory and Tech.*, Vol. 47, No. 12, pp. 2364–2374, December 1999.

[96] C. Blanco, "Gain Expansion and Intermodulation in a MESFET Amplifier," *IEE Electron. Lett.*, Vol. 15 , No. 1, pp. 31-32, January 1979.

[97] J. C. Pedro and J. Perez, "Design Techniques for Low Intermodulation Distortion Amplifiers," *Microwave Journal*, Vol. 37, No. 5, pp. 94-104, May 1994.

[98] S. C. Cripps, "The Intercept Point Deception," *IEEE Microwave Magazine*, Vol. 8, No. 1, pp. 44-50, February 2007.

[99] R. Vaitkus, V. Nair, and S. Tehrani, "A Low-Current Linearity Sweet-Spot in HFETs," *IEEE MTT-S Int. Microwave Symposium Dig.*, pp. 523-526, 1995.

[100] A. Jarndal, *Large-Signal Modeling of GaN Device for High Power Amplifier Design*, Doctoral Thesis, Department of High Frequency Engineering, University of Kassel, Kassel, Germany, November 2006.

[101] N. B. Carvalho and J. C. Pedro, "A Comprehensive Explanation of Distortion Sideband Asymmetries," *IEEE Trans. Microwave Theory and Tech.*, Vol. 50, No. 9, pp. 2090-2101, September 2002.

[102] J. F. Sevic, G. R. Simpson, and M. B. Steer, *Automated Large-Signal Load-Pull Characterization of Adjacent-Channel Power Ratio for Digital Wireless Communication Systems*, Application Note 5C-047, Maury Microwave Corporation, September 2000.

[103] M. J. Bailey, "Intermodulation Distortion in pHEMTs and an Extension of the

Classical Theory," *IEEE Trans. Microw. Theory and Tech.*, Vol. 48, No. 1, pp. 104-110, January 2000.

[104] A. D. Vare and R. Hopper, *Power Amplifiers Devices for UMTS*, Roke Manor Research Ltd, pp. 4.1-4.8, October 2002.

[105] K. Barkley, "Two-Tone IMD Measurement Techniques", *RF Design Magazine*, pp. 36-52, June 2001.

[106] A. Z. Markos, *Analysis, Design and Efficiency Enhancement of GaN RF Power Amplifiers*, Doctoral Thesis, Department of High Frequency Engineering, University of Kassel, Kassel, Germany, November 2008.

[107] J. C. Pedro and N. B. Carvalho, "Inferring Nonlinear Distortion Performance of Power Amplifiers Subject to Telecommunications Signals from Two-Tone Measurements," *IEEE MTT-S Int. Microwave Symp.*, WE3D-6, pp. 817-820, Long Beach, CA, June 2005.

Publications of the Author

[1] E. R. Srinidhi, R. Ma, and G. Kompa, "Improved Large-Signal Measurement Technique for Reliable IMD Characterization in GaN HEMTs," *Proc. of the European Microwave Association Journal.* (accepted for publication)

[2] E. R. Srinidhi, B. Wittwer, R. Ma, and G. Kompa, "Key Aspects for Characterizing Device Inherent IMD in GaN HEMTs," *Proc. of 38th European Microwave Conference (EuMC)*, pp. 1117-1120, Amsterdam, The Netherlands, October 2008.

[3] E. R. Srinidhi, R. Ma, and G. Kompa, "Application Rules for Accurate IMD Characterization in GaN HEMTs," *Proc. of German Microwave Conference (GeMIC)*, pp. 171-174, March 2008.

[4] E. R. Srinidhi, R. Ma, and G. Kompa, "Volterra Series Based Distortion Analysis for Optimization of Out-of-Band Terminations in GaN HEMT Devices," *IEEE Electron Device Letters*, Vol. 29, No. 1, pp. 24-27, January 2008.

[5] E. R. Srinidhi, R. Ma, A. Z. Markos, and G. Kompa, "Optimization of Broadband Drain Modulation in GaN HEMT Devices," *IEEE Proc. of Radio and Wireless Symposium (RWS)*, pp. 81-84, Orlando, FL, January 2008.

[6] E. R. Srinidhi and G. Kompa, "Investigation of IMD3 in GaN HEMT Based on Extended Volterra Series Analysis," *Proc. of European Microwave Integrated Circuits (EuMIC) Conference*, pp. 52-55, Munich, Germany, October 2007.

[7] E. R. Srinidhi, A. Jarndal, and G. Kompa, "A New Method for Identification and Minimization of Distortion Sources in GaN HEMT Devices Based on Volterra Series Analysis," *IEEE Electron Device Letters*, Vol. 28, No. 5, pp. 343-345, May 2007.

[8] E. R. Srinidhi, B. Bunz, B. Wittwer, and G. Kompa, "Multi-Tone Based AM-AM and AM-PM PA Characterization," *Proc. of TARGET DAYS Tutorial*, Via Frascati, Italy, October 2006.

[9] E. R. Srinidhi, A. Ahmed, and G. Kompa, "Power Amplifier Behavioral Modeling Strategies Using Neural Network and Memory Polynomial Models," *Microwave Review Journal*, Vol. 12, No. 1, pp. 15-20, June 2006.